

Marcin Froissart, BEng, MSc
Institute of Fluid-Flow Machinery, Polish Academy of Sciences
in Gdańsk

Centre of Flow and Combustion
Energy Conversion Department

Modelling of cooling of thermally highly loaded components using Thermal FSI method

Doctoral dissertation submitted to the Scientific Council
of the Institute of Fluid-Flow Machinery,
Polish Academy of Sciences in Gdańsk

Supervisor of the dissertation:
Tomasz Ochrymiuk, BEng, PhD, DSc

Gdańsk, *December 2023*

mgr inż. Marcin Froissart
Instytut Maszyn Przepływowych w Gdańsku
Polskiej Akademii Nauk
Ośrodek Przepływów i Spalania
Zakład Konwersji Energii

Modelowanie chłodzenia elementów wysokoobciążonych termicznie przy użyciu metody Thermal FSI

Rozprawa doktorska przedłożona Radzie Naukowej
Instytutu Maszyn Przepływowych im. Roberta Szewalskiego
Polskiej Akademii Nauk w Gdańsku

Promotor rozprawy:
dr hab. inż. Tomasz Ochrymiuk

Gdańsk, *grudzień 2023*

I would like to express my sincere thanks to my supervisor Prof Tomasz Ochrymiuk for his unwavering support, guidance and shared knowledge throughout the years of studies.

I would like also to thank my Colleagues from the Energy Conversion Department for inspiring atmosphere, readiness for support and teamwork in promoting the development of Polish energy industry.

This research was done thanks to The National Centre for Research and Development and Norway, which co-financed this project under the Norwegian Financial Mechanisms 2014-2021. Project title is "nCO2PP - Negative CO2 emission gas power plant" [contract number: NOR/POLNORCCS/NEGATIVE-CO2-PP/0009/2019-00].

Pragnę złożyć serdeczne podziękowania
mojemu promotorowi
prof. Tomaszowi Ochrymiukowi
za nieocenioną pomoc, wsparcie, życzliwość,
wrozumiałość i przekazaną wiedzę.
Chciałbym także podziękować moim
Koleżankom i Kolegom z Zakładu Konwersji
Energii za miłą atmosferę, gotowość do pomocy
oraz wspólną pracę na rzecz rozwoju polskiej
energetyki.
Specjalne podziękowania chciałbym złożyć
Narodowemu Centrum Badań i Rozwoju oraz
Norwegii, która współfinansowała ten project
w ramach Funduszy Norweskich 2014-2021.
Tytuł projektu to "nCO2PP - Negative CO2
emission gas power plant" [numer kontraktu:
NOR/POLNORCCS/NEGATIVE-CO2-
PP/0009/2019-00].

ABSTRACT

Rapid civilisation development in the last century was driven by the massive consumption of fossil fuels. Very cheap energy sources such as coal or oil have improved the life quality globally, but at the cost of unprecedented greenhouse gasses emission. Taking into account that fossil fuels resources are limited, it should be acknowledged that they need to be replaced at some point with renewable energy sources. This is a very expensive process, but crucial to avoid abrupt shortage of energy supply in the peak of civilization development.

Research presented in this thesis is a part of the project "nCO₂PP - Negative CO₂ emission gas power plant", which is aimed at sewage sludge gasification and synthetic gas utilization inside the wet combustion chamber (WCC) powering gas turbine. The advantages of such cycle is utilisation of toxic wastes, power generation and carbon dioxide storage, which was initially trapped in the sewage.

Efficiency improvement of heat engines is equally important as sustainable management of energy sources. Based on the thermodynamic description of gas turbine operation (Brayton cycle), inlet temperature increase improves engine efficiency leading to the fuel savings. On the other side, outlet temperature is restricted by the strength of turbine components. Thermal FSI (Fluid-Solid Interaction) method is a proper choice for the analysis of actively cooled gas turbine components, as it offers precise prediction of structural temperature. In contrast to that, separate CFD and CSD analyses are less accurate, which introduces the necessity of wider safety margins and reduction of nominal temperature of heat engines.

The research hypothesis is formulated as follows: "It is possible to describe relationships between thermo-mechanical parameters and changes in composite structure of highly loaded components of gas turbines such as combustion liner. This will take into account the occurrence of such complex phenomena as the transpiration of the coolant through the micropores of the ceramics and evaporation at the inner wall of the combustion chamber. It is also possible to predict the process of damage evolution of ceramic matrix composite (component durability) with known load parameters. Description of such physical mechanisms and phenomenon is necessary to control deterioration effects".

The task formulated in this thesis is original and forms an important step in the design process improvement. The research hypothesis was confirmed using the Thermal FSI method, which enables heat transfer modelling between fluid and solid within one model operating on consistent mesh at interfaces. As a consequence, boundary layer temperature variation influences solid temperature and vice versa. The other element of the research hypothesis confirmation was application of GRI-Mech 3.0 combustion model and DPM (Discrete Phase Modelling) model, which links droplet evaporation (discrete phase) with continuous phase. From the solid side, it was crucial to model composite structure of liner, as it enabled application of Tsai-Wu failure criterion at the later stage.

Presented Thermal FSI approach is of a greater importance when modelling actively cooled components such as combustion chamber, where solid wall is washed simultaneously with cold and hot flow. On top of that, it was proved that consistent mesh at fluid/solid interferences improves considerably analysis convergence, so it should be always used instead of coarse and non-consistent mesh.

Especially important step in the model build was determination of thermal expansion coefficient of CMC (Ceramic Matrix Composite) material in an experimental way. This is a key parameter enabling the proper prediction of thermal stresses, which dominates in structures heavily heated and cooled at the same time. Due to the complex internal structure of CMC liner, measured thermal expansion coefficient is non-linear. It is caused

by the fact, that heat it conducted better along the fibres than through the porous matrix. Additionally, weak contact between fibres and matrix can be easily broken, which adds additional non-linearity into thermal expansion behaviour.

The final result of Thermal FSI analysis is the distribution of Tsai-Wu inverse reserve factor within the domain of CMC liner. Region located at the proximity of flame has Tsai-Wu inverse reserve factor exceeding one. It means that some regions of liner are expected to be cracked, which does not disqualifies the experiment. It should be noted, that presented results refer to the prototype, so project assumptions will be verified at the later stage of the design process. Combustion chamber analysis at the highly loaded conditions is a key requirement from the thermodynamic and economic point of view.

Detailed description of Thermal FSI model geometry, boundary conditions and results was supplemented by deep and wide study of mathematical models. From the CFD (Computational Fluid Dynamics) side this is the turbulence, combustion, water evaporation and porous medium model. From the CSD (Computational Solid Dynamics) side this is the elastic model of isotropic and orthotropic materials (composite). Thermal FSI method integrates CFD and CSD analyses into one numerical model.

It should be highlighted, that CMC material was developed by research institutions as a response to the necessity of having material able to withstand high temperatures like monolithic ceramic, but non-brittle at the same time. CMC material is employed mainly in aerospace and space industry, but it can be found in other sectors as well. Due to the fact that CMC manufacturing methods is a modern technology developed by only few companies worldwide, the experimental data is not easily accessible in the public domain. WHIPOX is a commercial name of CMC material developed by the German Institute of Aviation. Its porous structure was designed to reduce brittleness in the extremely high temperatures, so available publications ignore WHIPOX behaviour in the wet condition. The key innovative element of presented research is the WHIPOX ability to enable transpiration cooling of liners. This application is present in the literature, but it is much less common than mixing enhancement and flame stability methods. Another important subject widely explored in the literature are active cooling systems based on the cooling films application.

The literature review was made inside the appropriate chapters. Presented thesis is based on nine main steps, which were taken to confirm research hypothesis. They are listed below.

1. Verification of research methods is based on Thermal FSI model generation and cross-check of numerical results against experimental data. The first model contains 3D Tay combustion chamber geometry with cold air flow. It was successfully verified based on the axial and circumferential velocity plots at the control section. The second model calculates temperature and pressure distribution at the midspan of internally cooled NASA C3X vane. After the comparison of several turbulence models, it was found that $k - \omega$ SST model generates most accurate results. For that reason it was employed in the further Thermal FSI modelling (Chapter 3).
2. 3D steady CFD analysis of wet combustion chamber taking into account oxi-fuel combustion of methane, water droplet evaporation inside the flame and transpiration cooling. Based on the cyclic symmetry assumption, geometry was reduced to the 120° sector. The decision about the geometry selection was based on the several parametric models, aimed at mixing intensity maximization and flattening of outlet temperature profile (Chapters 5.7).

3. Liner 3D CSD model generation using CMC material is a key enabler of further component durability analysis. Steady and transient assessments supported the fibres winding angle optimisation and proved that model was built in a robust way (Chapter 5.2-5.4).
4. Experimental assessment of heat expansion coefficient of CMC material in the laboratory of Institute of Fluid-Flow Machinery at Polish Academy of Sciences. This parameter has a key role in the prediction of stress distribution inside the liner, which is heavily heated and cooled at the same time. Measurements revealed, that non-linear heat transfer coefficient can be interpolated with two constants - one below and one above 100°C (Chapter 5.1).
5. Build and analysis of steady and transient CSD models of wet combustion chamber assembly. In these cases temperature boundary conditions were applied arbitrarily to test model before conversion into Thermal FSI analysis (Chapter 5.5-5.6).
6. Build and analysis of Thermal FSI model consisting both solid and fluid domains is the key element of presented thesis. Thanks to this approach all physical phenomena are coupled with each other, so all of them are taken into consideration in every iteration of numerical solution (Chapter 5.8).
7. Liner temperature comparison between CFD and Thermal FSI models reveals noticeable differences. This is driven by the boundary layer behaviour, which exchanges heat with the wall in the Thermal FSI method (Chapter 5.9).
8. CMC liner durability analysis was performed using Tsai-Wu failure criterion. These results are directly applicable to the prototype durability. However, the more complex model the higher uncertainty of obtained results (Chapter 5.8).
9. Proposal of analysis' method improvement to take into account material properties modification when pores are filled with non-compressible fluid. In such a case liner became stiffer when loaded rapidly, because fluid will not be able to outflow the pore in a very short period of time. As a consequence of that, trapped liquid is able to carry hydrostatic load applied to the pore (Chapter 5.10).

STRESZCZENIE

Rozwój cywilizacyjny człowieka w ciągu ostatniego wieku znacznie przyspieszył za sprawą masowego wykorzystania paliw kopalnych. Bardzo tanie źródła energii w postaci węgla i ropy naftowej doprowadziły do polepszenia jakości życia ludzi na całym świecie, jednak skutkiem ubocznym spalania jest intensywna emisja gazów cieplarnianych. Biorąc pod uwagę, że te zasoby energetyczne są ograniczone, należy jak najszybciej ograniczyć ich zużycie i przestawić się na źródła energii odnawialnej. Proces ten jest bardzo kosztowny, lecz konieczny, aby uniknąć scenariusza nagłego wyczerpania zasobów energetycznych w szczytowym rozwoju cywilizacyjnym.

Badania przedstawione w tej rozprawie są częścią projektu badawczego "nCO2PP - Negative CO2 emission gas power plant", którego założenie polega na zgazowaniu osadów ściekowych i spalaniu gazu syntetycznego w mokrej komorze spalania napędzającej turbinę. Zaletą takiego rozwiązania jest utylizacja niebezpiecznych odpadów, produkcja energii elektrycznej oraz sekwestracja i zmagazynowanie dwutlenku węgla zawartego początkowo w ściekach.

Zwiększenie wydajności silników cieplnych jest równie ważne jak zrównoważona gospodarka źródłami energii. Zgodnie z opisem termodynamicznym obiegu porównawczego turbiny gazowej (obieg Braytona), wzrost temperatury wlotowej poprawia sprawność obiegu prowadząc do oszczędności paliwa. Z drugiej strony wysokość temperatury wlotowej jest ograniczona wytrzymałością oraz żywotnością komponentów turbinowych. Zastosowana metoda Thermal FSI idealnie nadaje się do obliczeń aktywnie chłodzonych elementów turbin gazowych, gdyż pozwala na dokładne wyznaczenie temperatury pracy struktury. Dla porównania metoda oddzielnych analiz CFD i CSD jest mniej dokładna, co skutkuje potrzebą wprowadzenia wyższych marginesów bezpieczeństwa i obniżeniu znamionowej temperatury pracy silników cieplnych.

Hipoteza badawcza brzmi: "Opis zależności pomiędzy parametrami termiczno mechanicznymi a zmianą kompozytowej struktury wysokoobciążonych elementów turbin gazowych takich jak liner komory spalania jest możliwy do określenia. Ta zależność powinna uwzględniać występowanie złożonych zjawisk takich jak przesiąkanie chłodziwa przez materiał porowaty oraz gwałtowne jego odparowanie na wewnętrznej powierzchni komory spalania. Jest także możliwe przewidywanie procesu degradacji porowatego ceramicznego kompozytu (trwałość komponentu) na podstawie rozkładu obciążeń. Opis tych zjawisk jest niezbędny do utrzymania kontroli nad procesami zniszczenia".

Zadanie postawione w rozprawie jest oryginalne i stanowi ważny krok w ulepszeniu procesu konstrukcyjnego. Hipotezę badawczą sprawdzono przy pomocy metody Thermal FSI (termiczne sprzężenie płynu z ciałem stałym), która pozwala na zamodelowanie przepływu ciepła pomiędzy płynem a ciałem stałym w ramach jednego modelu o spójnej siatce. Dzięki temu zmiana temperatury warstwy przyściennej wpływa na właściwości ciała stałego, a zmiana temperatury ciała stałego wpływa na parametry warstwy przyściennej. Kolejnym elementem sprawdzenia hipotezy badawczej było zastosowanie modelu procesu spalania GRI-Mech 3.0 oraz modelu DPM, który pozwala na odparowanie fazy dyskretniej (kropki wody) wewnątrz fazy ciągłej. Od strony ciała stałego, niezwykle ważne było zamodelowanie kompozytowej struktury wewnętrznej lineru, które pozwoliło na zastosowanie kryterium oszacowania zniszczenia Tsai-Wu.

Zaprezentowane kompleksowe podejście Thermal FSI jest szczególnie ważne podczas modelowania aktywnie chłodzonych elementów takich jak komora spalania, gdzie ścianka sąsiaduje bezpośrednio z gorącym i zimnym przepływem. Ponadto został potwierdzony fakt, że dopasowanie węzłów siatki na granicy płynu i ciała stałego znacznie ułatwia zbieżność analizy, więc zagęszczona i zarazem spójna siatka daje dokładniejsze i szybsze

rozwiązanie od zgrubnej i niespójnej.

Szczególnie ważnym etapem rozwoju modelu było określenie współczynnika rozszerzalności cieplnej materiału CMC (ceramiczny kompozyt) przy pomocy eksperymentu. Jest to kluczowy parametr pozwalający na prawidłowe odwzorowanie naprężeń termicznych, które dominują w konstrukcjach intensywnie podgrzewanych i chłodzonych. Ze względu na skomplikowaną strukturę wewnętrzną linera wykonanego z ceramicznego kompozytu, zaobserwowano nieliniowy współczynnik rozszerzalności cieplnej. Jest to spowodowane tym, że ciepło szybciej się rozchodzi wzdłuż jednolitych włókien niż w poprzek materiału porowatego. Poza tym, słaby kontakt pomiędzy włóknem a porowatym wypełnieniem może ulec odklejeniu, co jeszcze bardziej komplikuje zagadnienie rozszerzalności cieplnej.

Końcowym wynikiem analizy Thermal FSI jest rozkład współczynnika Tsai-Wu w domenie linera zbudowanego z materiału CMC. Rejon leżący najbliżej płomienia ma najwyższy współczynnik Tsai-Wu przekraczający jeden. Oznacza to, że według tego kryterium pewne rejony linera mogą ulec uszkodzeniu, co nie dyskwalifikuje eksperymentu. Należy wziąć pod uwagę, że przedstawione obliczenia opisują konstrukcję prototypową, więc na pewnym etapie procesu konstrukcyjnego nastąpi weryfikacja założeń projektowych. Obliczenia komory spalania dla wysokoobciążonych punktów pracy mają kluczowe znaczenie z termodynamicznego oraz ekonomicznego punktu widzenia.

Szczegółowy opis geometrii modelu Thermal FSI, jego warunków brzegowych oraz wyników został uzupełniony przez głębokie i szerokie studium modeli matematycznych. Od strony analizy CFD (Computational Fluid Dynamics) jest to modelowanie turbulencji, spalania, odparowania oraz przepływu przez materiał porowaty. Od strony CSD (Computational Solid Dynamics) jest to modelowanie elastycznego materiału izotropowego oraz ortotropowego kompozytu. Podejście Thermal FSI integruje analizę CFD oraz CSD w ramach jednego modelu.

Należy podkreślić, że materiał CMC (ceramiczny kompozyt) jest odpowiedzią instytutów badawczych na potrzebę stworzenia materiału odpornego na wysokie temperatury tak jak jednolita ceramika, ale pozbawionego jej głównej wady jaką jest kruchość. CMC znajduje zastosowanie głównie w przemyśle lotniczym i kosmicznym, ale używa się jego także w innych gałęziach przemysłu. Zaledwie kilka firm na świecie dysponuje technologią potrzebną do produkcji komponentów CMC, więc dane eksperymentalne dostępne w przestrzeni publicznej są mocno ograniczone. WHIPOX jest nazwą komercyjną materiału CMC opracowanego przez Niemiecki Instytut Lotnictwa. Jego porowata struktura została zaprojektowana z myślą o ograniczeniu kruchości w ekstremalnych temperaturach, więc dostępne publikacje pomijają zachowanie WHIPOXu w stanie mokrym. Elementem innowacyjnym przeprowadzonych badań jest wykorzystanie ceramicznej struktury porowatej do chłodzenia transpiracyjnego ciekłą wodą. Jest to zastosowanie obecne w literaturze, która jednak bardziej koncentruje się na intensyfikacji mieszania paliwa z utleniaczem i zapewnieniu stabilności płomienia. Innym ważnym tematem dostępnym w literaturze jest wydajność chłodzenia elementów silników cieplnych przy pomocy filmów chłodzących.

Przegląd literatury został zaprezentowany w poszczególnych rozdziałach. Poniższa rozprawa składa się z dziewięciu głównych kroków, które zostały wykonane w celu sprawdzenia hipotezy badawczej. Są one wyszczególnione poniżej.

1. Weryfikacja metod badawczych polegająca na zbudowaniu modelu Thermal FSI i porównaniu wyników względem pomiarów. Pierwszy użyty model jest oparty na trójwymiarowej geometrii komory spalania Tay, przez którą płynie zimne powietrze. Obliczony profil prędkości w przekroju kontrolnym jest bliski wynikom eksperymentalnym, co stanowi pozytywną weryfikację. Drugi model został zweryfikowany na podstawie rozkładu ciśnienia i temperatury na ścianie łopatkii kierowniczej NASA

C3X. Po porównaniu szeregu modeli turbulencji, najdokładniejsze wyniki dał model $k - \omega SST$, który to został użyty w późniejszych krokach analizy Thermal FSI (rozdział 3).

2. Budowa trójwymiarowej stacjonarnej analizy CFD mokrej komory spalania, biorącej pod uwagę spalanie metanu w czystym tlenie, odparowanie kropel wody wewnątrz płomienia i chłodzenie transpiracyjne. Ze względu na cykliczność geometrii, została ona zredukowana do sektora o kącie 120° . Wybór geometrii komory spalania został dokonany w oparciu o szereg modeli parametrycznych, mających na celu maksymalizację efektywności mieszania i ujednolicenie wylotowego profilu temperaturowego (rozdział 5.7).
3. Budowa trójwymiarowego modelu CSD linera zrobionego z kompozytowej ceramiki jest kluczowym elementem pozwalającym na późniejsze określenie stopnia zniszczenia linera. Analizy stacjonarne i niestacjonarne pozwoliły na optymalizację kąta splotu włókien oraz potwierdziły skuteczność modelu (rozdziały 5.2-5.4).
4. Eksperymentalne wyznaczenie współczynnika rozszerzalności cieplnej materiału CMC w laboratorium Instytutu Maszyn Przepływowych Polskiej Akademii Nauk. Ten parametr ma kluczowe znaczenie w określeniu stopnia naprężenia linera, ponieważ jest on jednocześnie poddawany intensywnemu nagrzewaniu oraz gwałtownemu chłodzeniu. Eksperyment potwierdził, że współczynnik rozszerzalności cieplnej może być przybliżony dwoma stałymi wartościami - poniżej i powyżej temperatury 100°C (rozdział 5.1).
5. Zbudowanie i przeanalizowanie złożeniowego modelu CSD w stanie stacjonarnym i niestacjonarnym. W tym przypadku temperaturowe warunki brzegowe zostały zadane arbitralnie, aby przeanalizować i przygotować złożenie do modelowania przy pomocy metody Thermal FSI (rozdział 5.5-5.6).
6. Zbudowanie i przeanalizowanie modelu Thermal FSI zawierającego w sobie domeny płynu i ciała stałego to najważniejszy element przeprowadzonych badań. Dzięki takiemu podejściu wszystkie zjawiska fizyczne są ze sobą sprzęgnięte, więc oddziałują na siebie w każdym numerycznym kroku prowadzącym do rozwiązania (rozdział 5.8).
7. Porównanie rozkładu temperatury na ścianie linera pomiędzy modelami CFD a Thermal FSI wskazuje, że są zauważalne znaczne różnice pomiędzy podejściem rozłącznym (CSD plus CFD), a zintegrowanym (Thermal FSI). Przyczyną jest zachowanie płynu przy ścianie, który w metodzie zintegrowanej jest termicznie sprzęgnięty ze ścianką (rozdział 5.9).
8. Określenie trwałości linera wykonanego z ceramiki kompozytowej (CMC) przy pomocy hipotezy wytrzymałościowej Tsai-Wu. Wyniki tej analizy mają bezpośrednie zastosowanie to określenia trwałości prototypu. Należy jednak zaznaczyć, że im bardziej skomplikowany model numeryczny, tym większa niepewność związana z otrzymanymi wynikami (rozdział 5.8).
9. Zaproponowanie modyfikacji metody obliczeniowej, która bierze pod uwagę zmianę właściwości mechanicznych porowatego linera, gdy jest on wypełniony nieściśliwym płynem. W takim przypadku liner staje się sztywniejszy pod wpływem gwałtownych zmian obciążeń, gdyż płyn wypełniający pory nie zdąży wypłynąć w krótkim czasie przenosząc część obciążenia hydrostatycznego (rozdział 5.10).

Contents

1	Introduction	13
1.1	Motivation	13
1.2	Aim and scope of the thesis	14
1.3	Ceramic Matrix Composite WHIPOX	17
1.4	Combustion chambers – industrial concepts	20
2	Modelling techniques	29
2.1	Numerical modelling – fluid domain	29
2.1.1	Model of turbulence	34
2.1.1.1	Mixing length model	35
2.1.1.2	Standard $k - \epsilon$ model	36
2.1.1.3	Standard $k - \omega$ model	39
2.1.1.4	Shear-Stress Transport (SST) $k - \omega$ model	40
2.1.2	Model of combustion	42
2.1.2.1	Homogenous mixture approach	43
2.1.2.2	Mass conservation of mixture	44
2.1.2.3	Momentum conservation of mixture	44
2.1.2.4	Energy conservation of mixture	47
2.1.2.5	Kinetics of reactions	47
2.1.2.6	Numerical integration of reacting mixture	50
2.1.3	Discrete phase modelling	53
2.1.3.1	The Euler-Lagrange approach	53
2.1.3.2	Particle motion theory	54
2.1.3.3	Laws for heat and mass exchange	54
2.1.4	Porous Media modelling	55
2.2	Numerical modelling – solid domain	57
2.2.1	Model of the isotropic elasticity	63
2.2.2	General model of the anisotropic materials	66
2.2.3	Classical laminate theory	66
2.2.4	Ply failure behaviour	76
2.2.5	Composite failure criteria	78
2.2.6	Maximum stress criterion	78
2.2.7	Maximum strain criterion	79
2.2.8	Tsai-Wu failure criterion	79
2.2.9	Tsai-Hill failure criterion	80
2.2.10	Hoffman failure criterion	81
2.2.11	Hashin strain criterion	81
2.2.12	Puck failure criterion	82
2.2.13	Specific numerical model for the WHIPOX	83

2.2.14	Methods' application	84
2.2.14.1	ANSYS ACP approach	84
2.2.14.2	Recent research advances	88
2.3	Numerical modelling - fluid-solid interaction	96
2.3.1	Description of the ALE kinematics	96
2.3.2	Time derivatives in the ALE formulation	98
2.3.3	The ALE form of balance equations	100
3	Method Validation	102
3.1	Method validation based on C3X vane	102
3.2	Method validation based on Tay combustor	107
4	Wet Combustion Chamber Models	110
4.1	Geometry	110
4.1.1	Actual assembly	110
4.1.2	Simplified assembly	111
4.1.3	Liner	113
4.1.4	Computational Fluid Dynamics Model	114
4.1.5	Fluid-Solid Interaction Model	114
4.2	Boundary conditions	116
4.2.1	Static liner	116
4.2.2	Transient liner	118
4.2.3	Static assembly – solid	119
4.2.4	Transient assembly – solid	121
4.2.5	Fluid-solid interaction model	122
4.2.6	Wet liner transient model	125
5	Results	131
5.1	Liner - validation case	131
5.2	Liner results – static	132
5.3	Liner cooled acceleration – transient	140
5.4	Liner non-cooled acceleration – transient	143
5.5	Solid assembly - static	144
5.6	Solid assembly - transient	148
5.7	CFD Analysis	152
5.8	Fluid-Solid Interaction	153
5.9	Fluid-Solid Interaction model advantage over CFD	159
5.10	Wet liner transient model	159
6	Summary	161
6.1	General conclusions	161
6.2	Detailed conclusions	162
6.3	Research hypothesis	164
6.4	Research objectives	165

Chapter 1

Introduction

1.1 Motivation

Sustainable development is a clear global trend in the international economy, which transforms lives of most countries in the world. Its main goal is to assure, that civilisation development is independent from the fossil fuels, which are source of pollution and will inevitably run out with the few centuries.

Technological development is a very strong tool in achieving sustainable targets such as reduction of fossil fuels dependency, waste recycling and improving environmental impact of every human activity. However, global transformation to fully renewable energy consumption is a complex process which needs enormous investments and requires decades to be finished. For that reason, both industrial and scientific projects need more precise analysis methods helping to improve modelling accuracy.

Thermal Fluid-Solid-Interaction (FSI) computational method offers significant advancements by solving thermal interaction between fluid and solid domains in the same step. An example of device which design can benefit from such approach is the gas turbine shown on Figure 1.1. The hottest part of it is an actively cooled combustion chamber, where hot flow interacts with coolant through the liner's wall. In such case wall thermal gradient is a function of hot and cold boundary layers and heat transfer coefficients. That complex interaction is very difficult to capture accurately in separate CFD (Computational Fluid Dynamics) and CSD (Computational Solid Dynamics) models.

Brayton cycle can be used as an idealised description of gas turbine thermodynamic cycle. It contains four stages as follows: isentropic compression, isobaric heating, isentropic expansion and isobaric heat rejection. Based on equation 1.1, gas turbine efficiency can be improved by increasing temperature at the combustion chamber outlet. For that reason



Figure 1.1: GE 9F AGP gas turbine [1]

Thermal FSI analysis is crucial, as it can help to find the optimum combustion chamber cooling system and reduce environmental impact of burned fuel.

$$\eta_{ideal} = 1 - \frac{T_4}{T_3} \quad (1.1)$$

where η_{ideal} is efficiency of ideal Brayton cycle, T_3 is temperature of combustion chamber outlet, T_4 is the ambient temperature.

High Pressure turbine stage is another region which design can be improved using Thermal FSI model. Highly turbulent flow through nozzle guide vanes and turbine blades requires utilization of proper turbulent model able to predict main flow and boundary layer. This highly non-uniform and anisotropic [2, 3] flow often separates from the solid, so $k - \omega$ SST viscous model was employed.

Apart from the cooling system application, efficiency and durability of gas turbine can be improved by adoption of Ceramic Matrix Composite (CMC) components. This new technology can be applied in various installations including jet engines, rockets or furnaces. Its main advantage over monolithic ceramic is resistance to brittleness while assuring equivalent temperature and corrosion protection. One of the main motivation of this thesis is to create and include orthotropic CMC component within Thermal FSI analysis and assess its ability to withstand the thermo-mechanical load.

1.2 Aim and scope of the thesis

The aim of the thesis is to confirm or disprove the research hypothesis: "It is possible to describe relationships between thermo-mechanical parameters and changes in composite structure of highly loaded components of gas turbines such as combustion liner. This will take into account the occurrence of such complex phenomena as the transpiration of the coolant through the micropores of the ceramics and evaporation at the inner wall of the combustion chamber. It is also possible to predict the process of damage evolution of ceramic matrix composite (component durability) with known load parameters. Description of such physical mechanisms and phenomenon is necessary to control deterioration effects".

Additionally, thesis is going to answer three main scientific questions below:

1. What is the effect of high temperature on the structure and mechanical properties of the combustion chamber liner made of ceramic material?
2. What is the impact of the evaporation process and the pressure surge on the structural and mechanical properties of the material during thermal load?
3. What is the relationship between thermo-mechanical load and deterioration of structural and mechanical properties?

This thesis is a part of Project "nCO2PP - Negative CO2 emission gas power plant", which is co-financed by Programme "Applied Research" under the Norwegian Financial Mechanisms 2014-2021. The idea behind this international project is to design power plant able to convert sewage sludge into electricity, which is shown on Figure 1.2. Wet Combustion Chamber (WCC) located at the top is fuelled by methane, which generates very high temperature in oxy-combustion process. For that reason, it was decided to equip combustor with Ceramic Matrix Composite (CMC) liner and liquid water cooling system able to withstand extreme temperature of the flame (about 3000°K). Other elements of the presented diagram are gas turbines, heat exchangers and pumps.

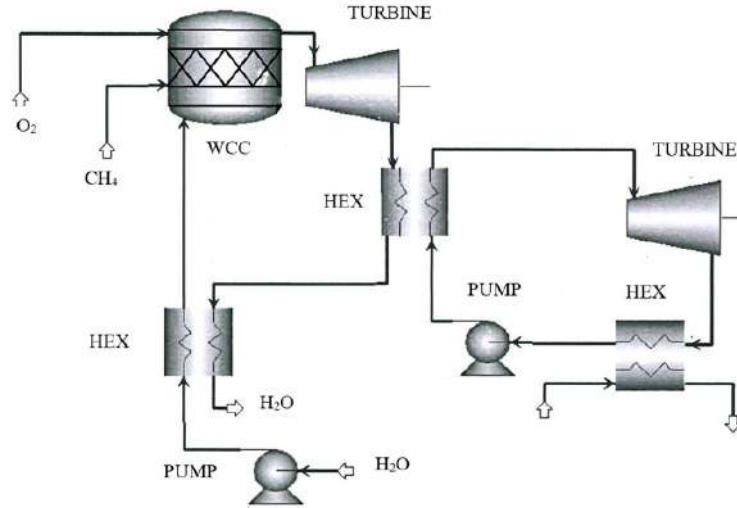


Figure 1.2: Layout of negative CO2 power plant (nCO2PP)

The scope of the thesis is focused on the design process of Wet Combustion Chamber and scientific methods able to support and improve it. Special attention is given to the Thermal FSI method, which is a significant step forward in comparison to application of separate CFD and CSD analyses. Its main advantage is the coupled approach, which captures impact of boundary layer to solid temperature and vice versa. That is especially important in the case of cooled components like combustion chamber, where metal temperature is a function of heat transfer coefficients on hot and cold sides.

Table 1.1 summarises scientific steps taken at the path of design process improvement.

First step is focused on the Thermal FSI method validation. That element is crucial, because it demonstrates that methods employed to design a prototype were successfully verified against experimental data gained from the similar component. 3D Rolls-Royce Tay CFD combustor chamber model was built and verified based on the cold flow velocity distribution. That was important from the flow structure point of view. Second verification model was the C3X NASA vane, which enabled Thermal FSI method verification against measured metal temperature and midspan pressure. That is a significant advancement over the CFD model, because heat transfer coefficient calculation was required to couple gas and metal temperature.

Second step contains the CFD model build and analysis of actual Wet Combustion Chamber geometry. Due to the fact, that this is the pre-prototype stage, no experimental measurements are available for comparison. Note that combustion and water evaporation models were coupled together to improve mixing prediction accuracy. That step marked an important milestone in the project, so results were presented at the international conference CPOTE 2022 (7th International Conference on Contemporary Problems of Thermal Engineering) and published in the Elsevier Energy Journal.

Third step is focused on the CMC (Ceramic Matrix Composite) CSD (Computational Solid Dynamics) modelling method. Since the CMC material has an orthotropic structure, nine elastic parameters are required to fully describe its mechanical properties (along and across the fibres). Another layer of complexity is added by the theta winding angle, which is explicitly modelled in a form of specifically oriented composite plies. A series of thermal load cases were analysed to demonstrate capability of created models.

Fourth step presented on Table 1.1 is focused on the CMC material properties refine-

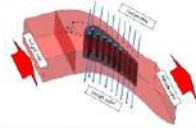
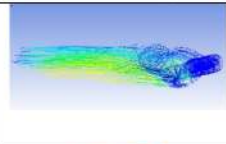
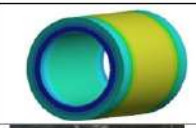

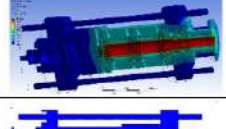
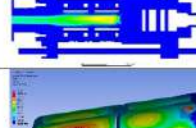
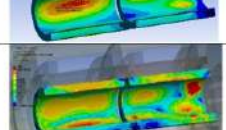
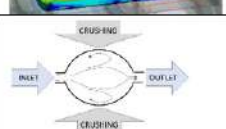

Step	Description	Chapters	Symbol
1	3D steady Thermal FSI method verification based on the literature (C3X NASA vane & Tay combustor).	3	
2	3D steady CFD analysis including combustion and cooling water evaporation (results presented at 7 th International Conference CPOTE and published in the ELSEVIER Energy Journal).	5.7	
3	3D steady/transient CSD Ceramic Matrix Composite models built and analysed (fibres theta angle optimisation).	5.2 – 5.4	
4	CMC thermal expansion coefficient measurement .	5.1	
5	3D steady/transient CSD assembly models built and analysed.	5.5 – 5.6	
6	3D Thermal FSI global model built and analysed.	5.8	
7	3D liner's temperature comparison – Thermal FSI vs. CFD .	5.9	
8	Assessment of composite durability using Tsai-Wu criterion.	5.8	
9	Wet porous CMC model proposal .	5.10	

Table 1.1: Research steps

ment. An experiment taken at the Institute of Fluid Flow Machinery PAS revealed actual thermal expansion coefficient for theta winding angle equal at 75° . It was found, that its non-linearity can be expressed by two independent thermal expansion coefficients, one applicable below 100°C temperature and another one above that threshold.

Fifth step is an advancement of CSD modelling, because the entire assembly is analysed altogether. The very important aspect is that isotropic and orthotropic components interact with each other through mechanical contacts. The most advanced analysis at this step is the transient assessment with conservative very rapid acceleration time equals to one second.

Sixth step contains the Thermal FSI analysis, which is the most complex case of all. Coupling CFD and CSD domains creates a synergy able to improve temperature prediction over the separate CFD and CSD approach. Properly captured heat transfer coefficients at the fluid/solid boundaries successfully interact with combustion and water evaporation algorithms.

Seventh step assesses the variation between CFD and Thermal FSI prediction of liners' temperature. Thermal FSI model is closer to the reality, because it takes into account proper heat transfer coefficient and coupled thermal properties at the fluid/solid boundary.

Eighth step is focused on the CMC liners' durability, which is calculated based on the Thermal FSI temperature distribution and Tsai-Wu failure criterion. Note that the obtained results should be taken with some uncertainty margin, which will be reduced along with experimental data generation.

The last step is a proposal of Thermal FSI method extension, which takes into account wet porous medium stiffening in a condition of rapid or vibratory load. In such conditions viscous non-compressible liquid is trapped inside the pore, because it has not enough time to outflow. As a consequence, it is able to carry hydrostatic load between pores' walls.

1.3 Ceramic Matrix Composite WHIPOX

WHIPOX is a Ceramic Matrix Composite (CMC) material, which combines properties of metals and ceramics in the unique way. It is a material which is better than metal above 800°C from the warp and corrosion perspective. It is also expected to address the pure ceramics brittleness limitation under mechanical/thermal load. WHIPOX structure consists of thousands oxide ceramics fibers embedded in the oxide ceramic matrix. This combination of both elements provide the unique mechanical and thermal properties: thermal shock proof, warp free, low heat capacity, oxidant and corrosion resistant. CMC material is presented on figure 1.3, where red arrows point photos with certain magnification scale [4].

Picture on the left shows ready cylindrical components, which can be made in different sizes and aspect ratios. Middle photo shows the composite structure at the linear basic scale of $100\mu\text{m}$, where adjacent plies are built at a different angle. Right photo shows detailed cross section, where circular fibers are solid and porous matrix fills cavity between them.

Monolithic oxide ceramics is not widely used in the industry, because of its inherent brittleness. Therefore many efforts have been made during the recent decades to overcome the problem of brittleness by reinforcing oxide matrices [7]. Many attempts were made to overcome that disadvantage, by application of reinforcement techniques. Most popular are addition of reinforcing elements like ZrO_2 [8], whiskers or chopped fibers [9] and continuous fibers, which are the most promising solution [10]. Although both constituents of CMC are brittle, the internal structure let them for a quasi-ductile deformation due

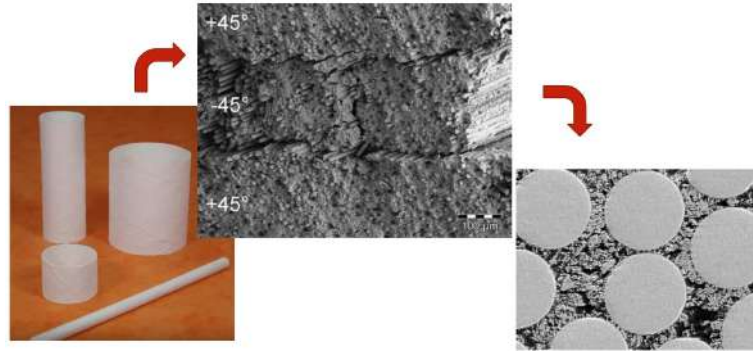


Figure 1.3: Ceramic matrix composite [5–7]

to the mechanisms like crack deflection, crack bridging or fiber pull-out [11]. This is schematically shown on the figure 1.4.

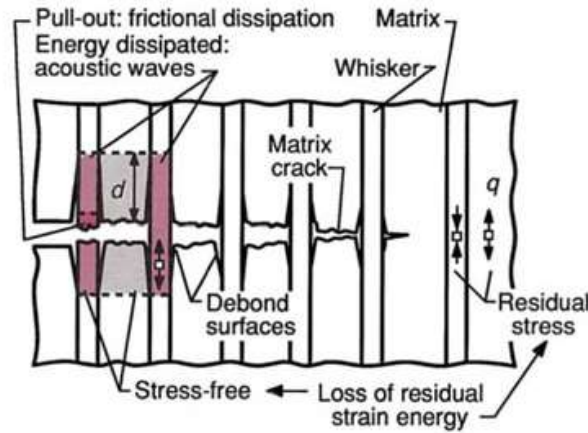


Figure 1.4: Crack bridging in fibre-reinforced composites [12]

Table 1.2 summarises differences between four types of ceramics based of strength at elevated temperatures, oxidation resistance, thermal shock resistance and graceful failure (crack) behaviour. It becomes apparent, that for the jet propulsion engines monolithic non-oxide ceramics is the worst option, as it is too brittle and easy to oxidise. Monolithic oxide ceramics is slightly better, because of its resistance to oxidation (it is already oxidised). Non-oxide CMC has clear advantage over monolithic options, as fibers add a protection against brittle failure under the thermal or mechanical load. The best option is application of oxide Ceramics Matrix Composite, as it is resistant against all four categories from 1.2.

Conventional CMC contains coated fibers and dense matrix around, which requires complex and expensive manufacturing process. In such solution, coating around fibers is required to ensure their protection (limitation of the destructive load transferred from the solid matrix into the fibers). Opposite design philosophy was applied to WHIPOX, which replaced costly coating process into the porous matrix, which is too weak to transfer significant load into the fibers. The comparison showing the difference is shown on figure 1.5. WHIPOX is manufactured by a continuous winding process [13], which is a unique method in comparison to its competitors. Its fibers are made from the commercially

	Monolithic non-oxide ceramics	Monolithic oxide ceramics	Non-oxide CMC	Oxide CMC
Sufficient strength at elevated temperature	+	◊	+	◊
Oxidation resistance	—	+	—	+
Thermal shock resistance	—	—	+	+
Graceful failure behavior	—	—	+	+

+ good,
 ◊ suitable,
 — insufficient

Table 1.2: Ceramics selection table [7]

available Nextel series, which can withstand up to 1200 °C [14].

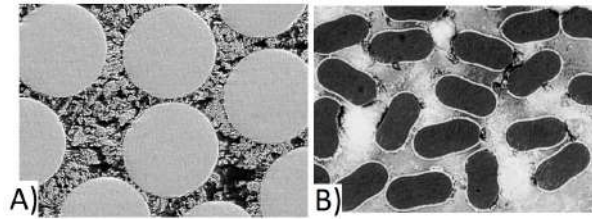


Figure 1.5: Matrix comparison, A) porous, B) dense with coating [7]

The WHIPOX manufacturing process fibers are sized and burned-off in a tube furnace. in the next stage bundles are separated apart and infiltrated with the water-based matrix slurry [7]. The infiltrated rovings are passed through the furnace to stabilize the matrix and are wound on plastic mandrels using a digitally-controlled process. On the next stage WHIPOX is removed from the mandrel in the moist stage which allows to form final shape (1.6). Last stage contains drying in air at temperature around 1300 °C.

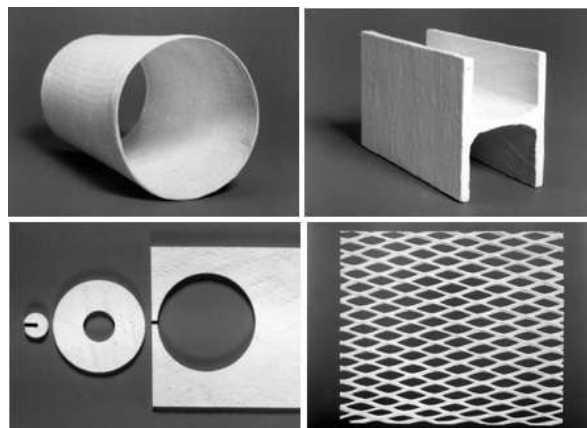


Figure 1.6: Examples of WHIPOX components [7]

One of the main manufacturing challenges is to obtain homogeneous matrix porosity and fiber distribution. According to the collected data, it is very likely to obtain fiber-rich

or matrix-rich areas, because the infiltration process is more effective in the outer areas of a sample than in the core [15]. However, the matrix-rich zones are the more challenging flaws, because they contain pores up to $100\mu m$ diameter. The winding process and internal structure of WHIPOX is presented on figure 1.7. A statistical method to determine internal agglomerations was recently developed by Schmucker et al. [16].

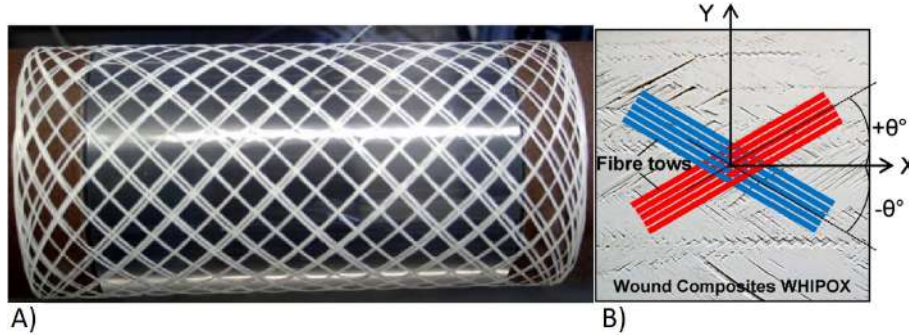


Figure 1.7: A) initial stage of winding, B) schematic winding structure [17]

Thermal shock resistance and improved fracture properties is the advantage of CMC oxide structure over monolithic and non-oxide ceramics. Thermal shock is driven by the very low thermal conductivity factor, so it causes a very localised damage. This was demonstrated during an experiment, where WHIPOX plate was locally heated by the solar furnace and an oxyacetylene torch. Results showed, that after multiple heating/cooling cycles no macroscopic deterioration was observed [18].

Separate experiment was conducted for the thermal aging. It included the impact of short-term firing (1h) into the microstructure stability and fracture behaviour of CMC. It contained Nextel 720 [14] fibers and an aluminosilicate matrix corresponding to phase composition of mullite plus minor amounts of silica-rich glass. It was concluded, that silica-rich matrix reacts with the Nextel 720 fibers leading to the new generation of mullite formed at the fibers [19].

1.4 Combustion chambers – industrial concepts

Combustion chamber is an essential component of gas turbine, where chemical energy of fuel is converted into thermal and kinetic energy of gas used downstream to power gas turbine. Gas turbines are used mainly in power plants and transportation industry. Their potential was recognised in the early 1900s, but its rapid development started in 1930s driven initially by military budgets in Great Britain and Germany. The development process is still ongoing, aiming at increasing outlet temperature, pollutant reduction and stability. A well designed combustor should maintain low pressure losses, high combustion efficiency, low emissions of smoke and pollutants, proper outlet temperature distribution, provide smooth ignition capability, be stable at wide air/fuel ratios. On top of that it should be cheap, capable to operate on multiple fuels and have proper shape and size.

Early industrial concepts of combustion chambers are presented graphically on Figure 1.8. The most basic concept a) is the straight duct connecting compressor and turbine. However, this simple arrangement is impractical, because the pressure loss incurred would be excessive [20]. The reason behind is too high velocity, which will cause an excessive pressure loss build in the compressor. To reduce this loss to an acceptable level, a diffuser

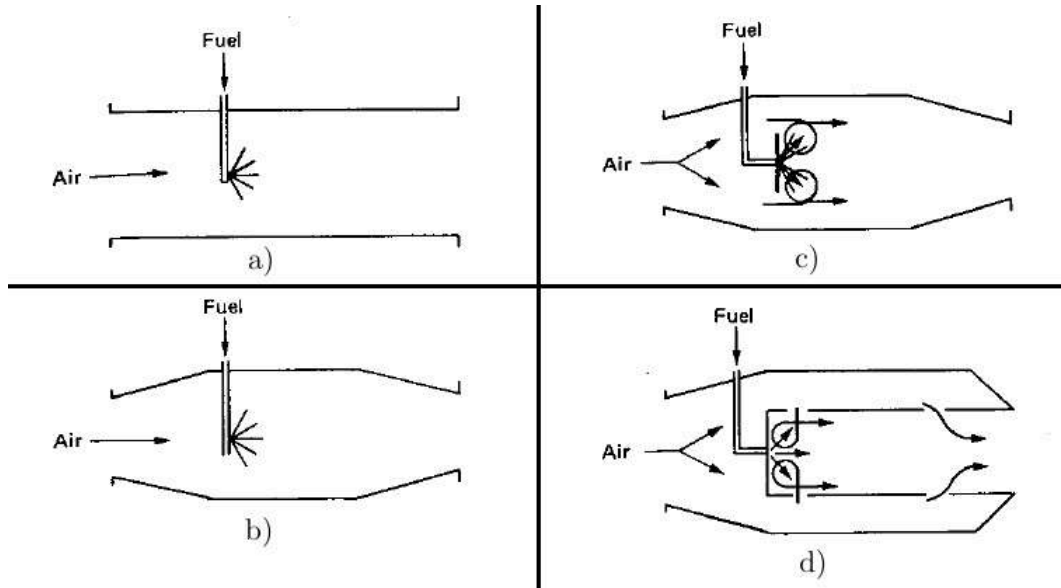


Figure 1.8: Evolution of conventional combustor [20]

should be applied to slow velocity by a factor of 5, which is shown on the concept b) on the Figure 1.8. However, this solution would blow the flame out, so a plain baffle should be applied to shelter and sustain the flame, which is shown on concept c). The disadvantage of this profile is that high air/fuel ratio at the level of 50 is far beyond of flammability limits of air-hydrocarbon mixtures. For that reason concept d) was introduced, where plain baffle was replaced with a perforated liner. Its function is to create stable conditions to deliver outlet gases at parameters required by the gas turbine.

Key elements of liner are shown on Figure 1.9. The primary zone was designed to create region of low velocity, where recirculation promotes sustained combustion. Such conditions are required to provide the continuous source of ignition for incoming fuel-air mixture.

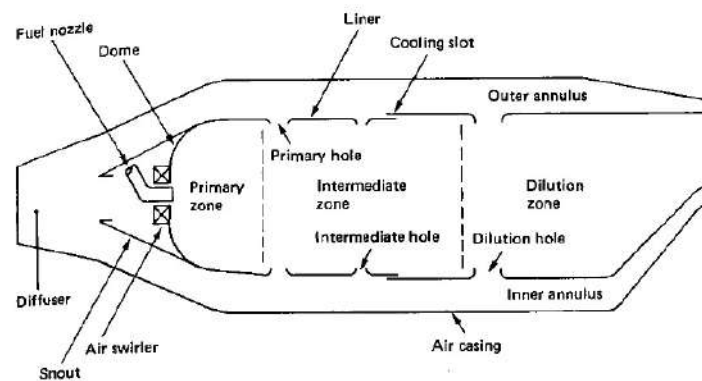


Figure 1.9: Key elements of combustor [20]

The intermediate zone has two functions to perform. On the ground it helps to recover primary zone dissociation losses of CO_2 into CO , which will be otherwise "frozen" in the dilution zone leading to combustion efficiency drop. At high altitudes, when reaction

intensity drops due to lower pressure, intermediate zone act as an extension of primary zone, which helps to improve efficiency. Dilution zone admits remaining 20 to 40% of air into the hot gas stream to ensure that outlet temperature and traverse meet turbine requirements.

Primary zone airflow patterns are presented on Figure 1.10. Concept a) is an opposite jets architecture creating partial obstacle for the flame and promoting mixing at the same time. Concept b) is another approach based on swirlers, which enhance mixing intensity by adding circumferential component to inlet gas velocity. Concept c) is a combined swirler-opposed jet arrangement. This is the most common solution, as it combines advantages of swirler and opposed jets. In this case swirling jet partially is recirculated with opposed jets, which creates spiral vortex between jets.

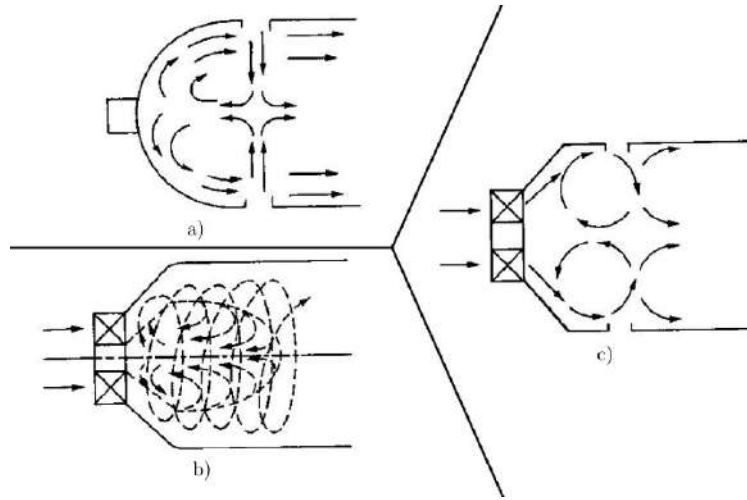


Figure 1.10: Primary zone airflow patterns [20]

Figure 1.11 presents wall cooling solutions, which were evolved over the years. The simple film cooling design was based on the cascade structure of rings, which were separated by rows on holes providing cool air to create protective film on internal side. More advanced solution protects liner with a convection and film, which was obtained with changing holes into slots. Another cooling solution takes an advantage of jet impingement technique [21, 22] supported by the protective film. In this case amount of cooling air is reduced, because of high heat transfer coefficient of impingement cooling. The most advanced solution is the transpiration system, where coolant actively cools down the wall itself and created protective film afterwards. This approach can save as much as 50 % of coolant flow.

An example of industrial combustor is presented on Figure 1.12. It contains all key elements required to stabilize flame and provide effective combustion. Diffuser reduces air speed to reduce pressure lost, injector supplies fuel which is airblast atomised, igniter and casing to create a passage for dilution air. The whole structure is optimised for weight and size reduction, as it needs to fit into the CF6 turbofan engine.

Over the last few decades, emissions environmental norms are becoming stricter, with special emphasis to nitrogen oxides, carbon monoxide, unburned hydrocarbons, sulphur oxides, particulates and smoke [23]. However, these requirements need to be met together with easy ignition, wide burning range and high combustion efficiency. Note, that primary zone requirement of alleviating smoke and nitric oxide cannot be achieved in the same

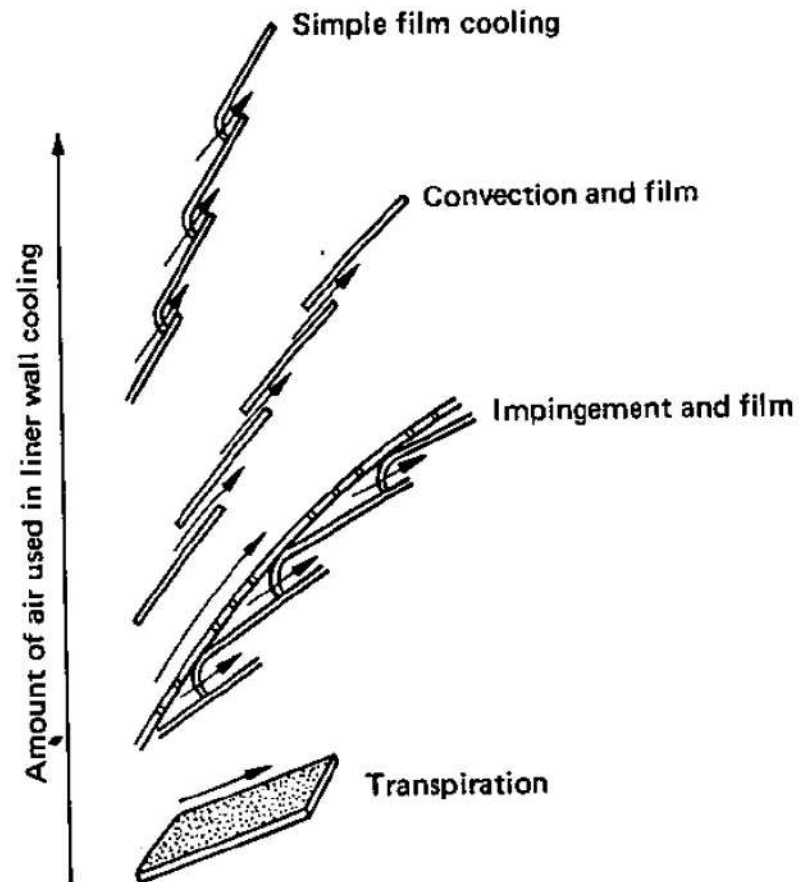


Figure 1.11: Wall cooling evolution [20]

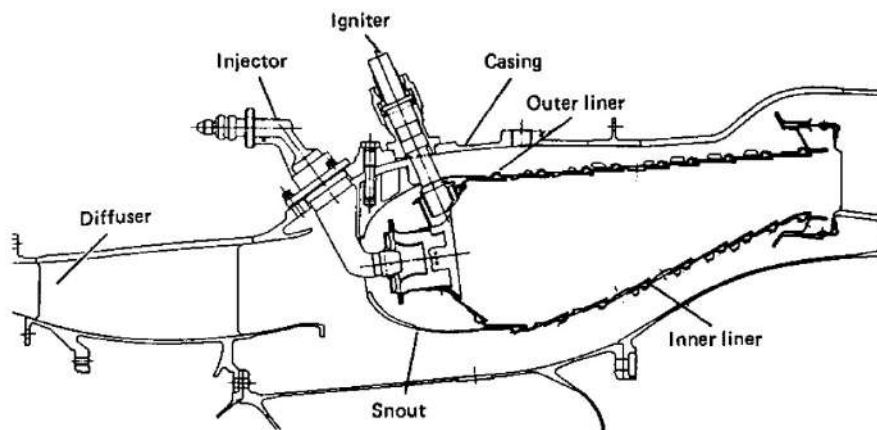


Figure 1.12: CF6-50 annular combustor (courtesy General Electric Company) [20]

time with carbon monoxide and unburned hydrocarbons reduction. For that reason, more sophisticated combustion chambers designs were created.

Figure 1.13 presents an example of design, integrating two separate zones, which are made to optimise specific aspects of combustion performance. The primary zone operates at equivalence ratio about 0.8 to reduce production of unburned hydrocarbons and carbon monoxide at low power. For higher load conditions, its role is a pilot source of heat for the downstream zone. In the Vorbix combustor example, conventional primary zone is supplied by 30 spray fuel atomizers and stabilized with swirled flow. The main burning zone is supplied with swirled air and fuel at low equivalence ratio through 60 swirl cups located on each side of the liner. Intense mixing between primary and secondary flows ensures rapid completion of combustion.

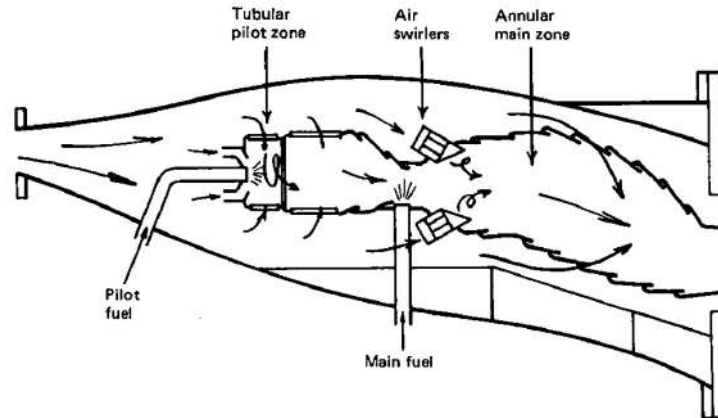


Figure 1.13: Vorbix combustor (courtesy Pratt and Whitney Aircraft Group) [20]

An alternative dual-zone design developed by General Electric Company is shown of Figure 1.14. The idea is consistent with Vorbix combustor, where pilot zone supplies engine at idle conditions and stabilizes flame at high-power flight stages like take off, climb or cruise.

Small engines combustors is a category, which needs to meet specific requirements like close coupling between compressor and turbine combined with low frontal area. For

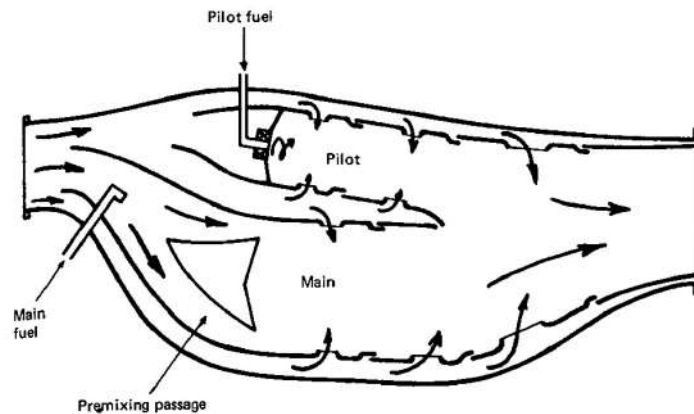


Figure 1.14: Radial two-stage combustor [20]

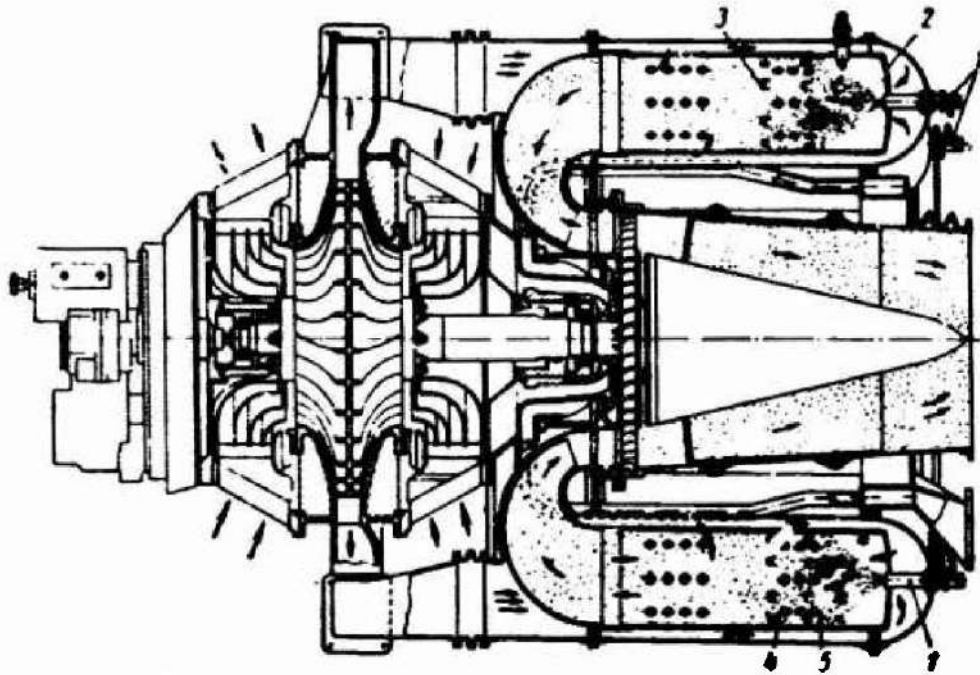


Figure 1.15: Aircraft gas turbine with reverse-flow sectional combustion chambers [24]

these reasons, most popular solutions are annular reverse-flow and radial-axial combustors. Figure 1.15 presents aircraft gas turbine powered by the annular reverse-flow combustor. Its advantages are short length, efficient utilization of the available volume and easy access to the fuel injectors. On the other hand, its main disadvantage is high surface-volume ratio of the liner, which poses significant cooling challenges. Furthermore, classical double-vertex primary zone pattern (balance) cannot be obtained, because the inner annulus suffers higher pressure loss than outer annulus.

Typical aircraft gas turbine engines are presented of Figure 1.16. Solution with centrifugal compressor is more compact than with axial one, but it requires more space inside the plane. Additionally, radial compressor airflow has to change flow direction rapidly, which causes higher pressure drop difficulties with flame stabilization. Due to the angled position of combustors, longer and heavier cone is required at the outlet.

One of the latest combustion chamber concepts enables pressure-gain combustion (PGC) [25], which is able to improve gas turbine efficiency. Taking into account, that 14% of global energy consumption is generated in gas turbines, so 1% efficiency improvement is an equivalent of 17300 commercial wind turbines. The idea behind PGC is to constrain gas expansion, causing a rise in stagnation pressure allowing work extraction by expansion to the initial pressure. Apart from improving thermodynamic cycle efficiency, PGC is able to reduce carbon dioxide emissions. That technology is based on detonative or isochoric (constant volume) combustion, where temperature ratio indicates fuel mass inlet. Based on research performed at NASA laboratory [25], power plant efficiency rises by 1.86%, which is accompanied with 2.97% power plant output increase.

Resonant pulse combustor (RPC) is presented on Figure 1.17. It is equipped with a valve system, which enables some part of reaction to be isochoric and cause pressure-gain. Due to the fact, that combustion pilot zone needs to be regularly opened to allow consistent flow, control valves open/close cycle is very fast - it lasts about 3 ms. The successful cycle

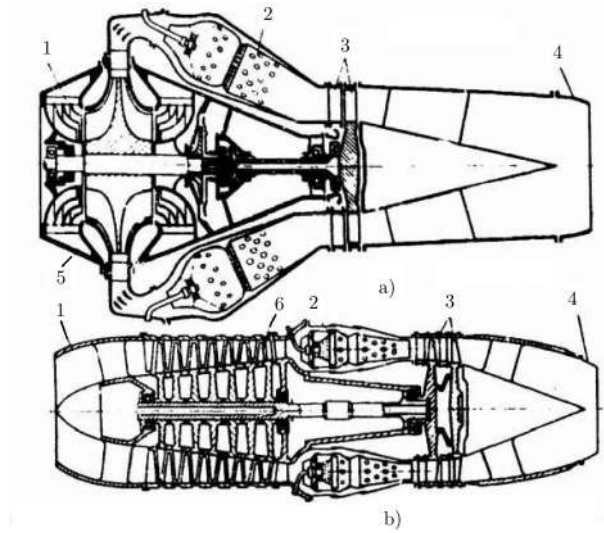


Figure 1.16: Diagram of arrangement of combustion chambers on a gas turbine engines, a) with centrifugal compressor b) with axial-flow compressor; 1-intake, 2-combustion chamber, 3-turbine, 4-outlet nozzle, 5-centrifugal compressor, 6-axial-flow compressor [24]

is driven by large vortex dynamics, efficient chemical kinetics and Helmholtz phenomena. Due to the high complexity of induced unsteady flow, model validation is an crucial development step. Note, that impulsive hot flow needs to be sooled and stabilized to not cause turbine damage. That could be done with efficient mixing in the ejector and adding bypass flow.

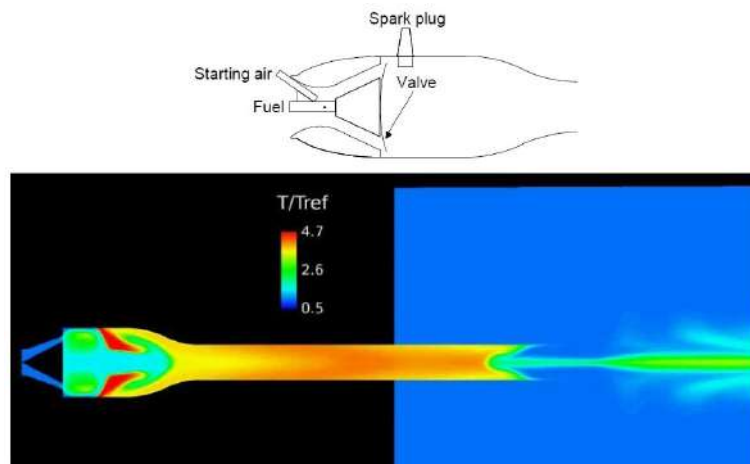


Figure 1.17: Resonant pulse combustor [25]

Figure 1.18 presents rotating detonation combustor, in which supersonic wave propagates circumferentially. This is a very robust solution, as self-sustained deflagration to detonation mechanism propagates without any obstacles. Due to the fact, that inlet fluid is supplied axially, circular velocity is very fast leading to very high frequency operation at the level of kHz, which can be heard as an audible screech. Once startup is completed, no ignition is needed, but inlet valve is required to prevent backflow. Additional advantage

of this type of combustor is that it supports non-premixed hydrogen combustion in air, which is supposed to be the dominant of fuel in the future.

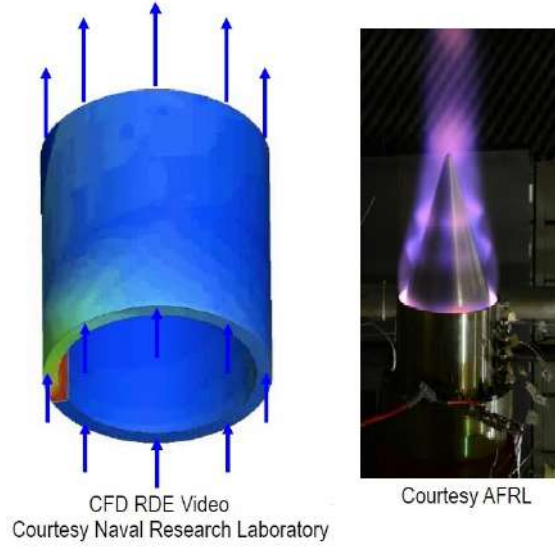


Figure 1.18: Rotating detonation combustor [25]

Figure 1.19 presents rotating detonation wave formed during hydrogen/air combustion. Normalized temperature contour in the middle plot reveals several regions of supersonic wave propagation. The hottest region is the shear mixing zone, which is directly attached to the detonation front. It is present due to the axial component of velocity, which keeps detonation in the lower section of chamber. Due to the fact that propagation velocity is supersonic, region in front of it is cold and non-burned.

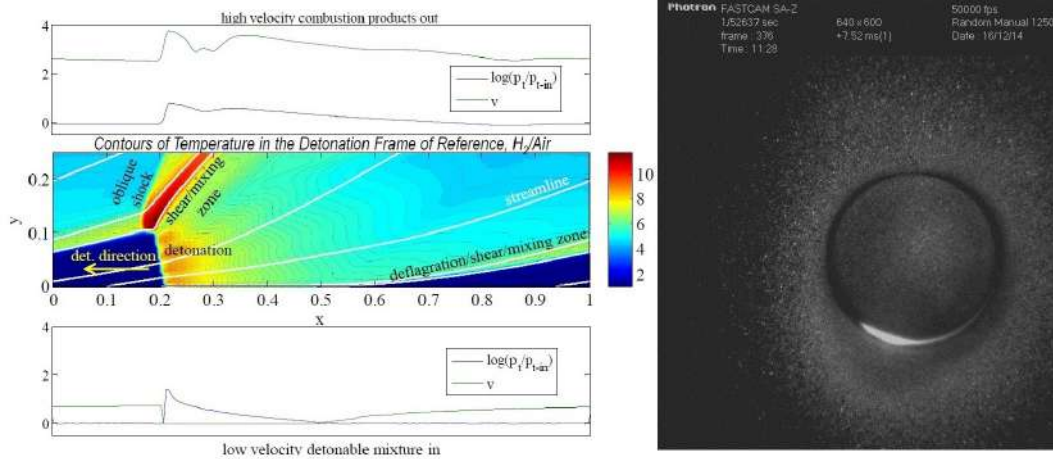


Figure 1.19: Rotating detonation wave [25]

White streamlines mark direction of flow, which is normal to the detonation zone. Lower graph presents inlet conditions, where detonation shock wave accelerates flow in

front of it. In contrast to that, top graph summarises outlet condition, where velocity plot is in the same phase with pressure. That is required to balance inlet velocity profile. Photo on the right was taken from the exhaust end of rotating detonation combustion chamber at the Department of Energy/National Energy Technology Laboratory. To capture rotation frequency of kHz, a high-speed camera was used, able to record 50000 frames per second. The thick bright region is the detonation wave, which leaves a thin tail behind at 25% of circumference. That is reflected in the temperature plot in the middle, where hot mixing zone follows the least resistance path to outlet.

Wet combustion chamber concept with transpiration cooling goes one step ahead in comparison to popular industrial solutions. However, to take the full advantage of CMC material resistance combination with transpiration cooling efficiency, available modelling methods need to be expanded and improved. That leads to many challenges, which can be overcome by extensive experimental programmes supported by advanced programming skills. Thermal FSI method offers very accurate stress predictions, which can be improved even more by taking into account more subtle phenomena like stiffness adjustment between dry and wet porous material.

Chapter 2

Modelling techniques

This chapter is focused on mathematical models, which are the backbone of the numerical methods applied in this thesis. Presented Thermal FSI model of wet combustion chamber captures complex interactions between physical phenomena occurring inside fluid and solid domains. It is therefore essential to systematize applied mathematical models using consistent notation. Furthermore, this knowledge is required to properly setup boundary conditions and post-process CFD and CSD components or results. From the CFD point of view, key phenomena are captured within the turbulent flow interacting with chemical reactions, discrete droplets and water evaporation phase change. On the other side, CSD isotropic and orthotropic domains are subject to thermal and mechanical loads. Both types of analyses are coupled within Thermal FSI model using ALE approach, which is briefly explained in this chapter.

2.1 Numerical modelling – fluid domain

The main difference between fluids and solids is the ability to sustain shear stresses when at rest. Without the motion fluid can carry only hydrostatic stress, so the velocity v_i is an essential independent variable when analysing fluid carrying shear load. An indicial notation of fluid velocity is shown on equation 2.1 [26].

$$v_i, \quad i = 1, 2, 3 \quad (2.1)$$

Fluid velocity is as important as displacement in the solid mechanics. For that reason general stresses in fluids are driven by the rates of strain, which can be defined according to equation 2.2.

$$\dot{\epsilon}_{ij} = \frac{1}{2} \left(\frac{\partial v_i}{\partial x_j} + \frac{\partial v_j}{\partial x_i} \right) \quad (2.2)$$

Above tensorial definition is an inconvenient form in the finite element analysis environment, so it was converted to the vector form presented on equation 2.3.

$$\dot{\underline{\epsilon}}^T = [\dot{\epsilon}_{11}, \dot{\epsilon}_{22}, \dot{\epsilon}_{33}, 2\dot{\epsilon}_{12}, 2\dot{\epsilon}_{23}, 2\dot{\epsilon}_{31}] \quad (2.3)$$

The stress-strain relations for a linear (newtonian) isotropic fluid require the definition of two constraints: μ (dynamic viscosity) and κ (volumetric viscosity) [26]. The first one links the deviatoric stresses τ_{ij} with deviatoric strain rates according to the equation 2.4.

$$\tau_{ij} \equiv \sigma_{ij} - \delta_{ij} \frac{\sigma_{kk}}{3} = 2\mu \left(\dot{\epsilon}_{ij} - \delta_{ij} \frac{\dot{\epsilon}_{kk}}{3} \right) \quad (2.4)$$

where quantity in brackets is known as the deviatoric strain, δ_{ij} is the Kronecker delta and repeated index is a summation presented on equation 2.5. Dynamic viscosity μ is analogous to the shear modulus in solid elasticity.

$$\sigma_{ii} \equiv \sigma_{11} + \sigma_{22} + \sigma_{33} \quad \text{and} \quad \dot{\epsilon}_{ii} \equiv \dot{\epsilon}_{11} + \dot{\epsilon}_{22} + \dot{\epsilon}_{33} \quad (2.5)$$

Volumetric viscosity κ relates mean stress changes and volumetric strain rates according to equation 2.6. It is an analogous parameter to bulk modulus in solid linear elasticity.

$$p = \frac{\sigma_{ii}}{3} = -\kappa \dot{\epsilon}_{ii} + p_0 \quad (2.6)$$

where p is a pressure and p_0 is the initial hydrostatic pressure independent of the strain rate.

Equation 2.7 is based on equations 2.4 and 2.6. It is also known as the 'constitutive' relation of fluids.

$$\sigma_{ij} = 2\mu \left(\dot{\epsilon}_{ij} - \frac{\delta_{ij} \dot{\epsilon}_{kk}}{3} \right) + \delta_{ij} \kappa \dot{\epsilon}_{kk} - \delta_{ij} p_0 = \tau_{ij} - \delta_{ij} p \quad (2.7)$$

An alternative form of equation 2.7 is given below.

$$\sigma_{ij} = 2\mu \dot{\epsilon}_{ij} + \delta_{ij} \left(\kappa - \frac{2}{3}\mu \right) \dot{\epsilon}_{ii} + \delta_{ij} p_0 \quad (2.8)$$

Quantity in brackets in equation 2.8 is also known as Lamé parameter (equation 2.9), but it is not recommended to change basic relation 2.7.

$$\kappa - \frac{2}{3}\mu \equiv \lambda \quad (2.9)$$

Although volumetric viscosity κ has theoretical meaning, there is little evidence about its existence (equation 2.10).

$$\kappa \dot{\epsilon}_{ii} \equiv 0 \quad (2.10)$$

Based on negligible effect of volumetric viscosity, constitutive equation 2.8 can be written in a form below.

$$\sigma_{ij} = 2\mu \left(\dot{\epsilon}_{ij} - \frac{\delta_{ij} \dot{\epsilon}_{kk}}{3} \right) - \delta_{ij} p = \tau_{ij} - \delta_{ij} p \quad (2.11)$$

Deviatoric stresses τ_{ij} from equation 2.11 can be written in a form of equation 2.12.

$$\tau_{ij} = 2\mu \left(\dot{\epsilon}_{ij} - \frac{\delta_{ij} \dot{\epsilon}_{kk}}{3} \right) = \mu \left[\left(\frac{\partial v_i}{\partial x_j} + \frac{\partial v_j}{\partial x_i} \right) - \delta_{ij} \frac{2}{3} \frac{\partial v_k}{\partial x_k} \right] \quad (2.12)$$

Mass conservation is one on the key laws which are used in computational fluid dynamics (CFD) models. Equation 2.13 adds three mass streams in cartesian directions to the mass accumulation/loss (density rate change) inside the control volume presented on Figure 2.1.

$$\frac{\partial \rho}{\partial t} + \frac{\partial}{\partial x_i} (\rho v_i) = \frac{\partial \rho}{\partial t} + \frac{\partial}{\partial x_1} (\rho v_1) + \frac{\partial}{\partial x_2} (\rho v_2) + \frac{\partial}{\partial x_3} (\rho v_3) = 0 \quad (2.13)$$

Equation 2.14 contains momentum conservation law in j^{th} directions, so stream momentums have to be in equilibrium with the stresses σ_{ij} and body forces ρf_j .

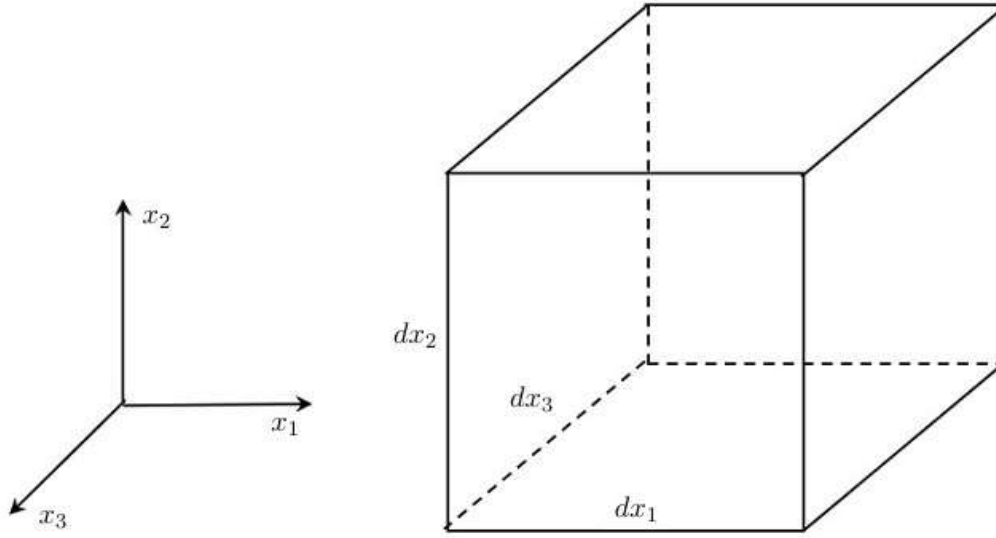


Figure 2.1: Infinitesimal control volume

$$\frac{\partial (\rho v_j)}{\partial t} + \frac{\partial}{\partial x_i} [(\rho v_j) v_i] - \frac{\partial}{\partial x_i} (\sigma_{ij}) - p f_j = 0 \quad (2.14)$$

Based on equation 2.11, momentum conservation law can be rewritten into the form below

$$\frac{\partial (\rho v_j)}{\partial t} + \frac{\partial}{\partial x_i} [(\rho v_j) v_i] - \frac{\partial}{\partial x_i} (\tau_{ij}) + \frac{\partial p}{\partial x_j} - p f_j = 0 \quad (2.15)$$

Note that mass and momentum conservation laws contains independent variables v_i (velocities), p (pressure) and ρ (density), so there is one variable too many to close these two equations. One possible solution is to assume, that flow is incompressible (constant density). In the more generic case, pressure, density and absolute temperature are related by the equation of state (equation 2.16).

$$\rho = \rho(p, T) \quad (2.16)$$

Which for an ideal fluid takes the form below

$$\rho = \frac{p}{RT} \quad (2.17)$$

where R is the universal gas constant and T is temperature.

The energy conservation law is an important supplement to the governing equations even if not coupled, because it provides additional information about the analysed flow. Equation 2.18 introduces e , which is an intrinsic energy per unit mass, which is dependent on the fluid pressure and temperature.

$$e = e(T, p) \quad (2.18)$$

Total energy includes intrinsic and kinetic energy per unit mass, which is shown on equation 2.19.

$$E = e + \frac{v_i v_i}{2} \quad (2.19)$$

Finally, enthalpy can be defined as [26]

$$h = e + \frac{p}{\rho} \quad \text{or} \quad H = h + \frac{v_i v_i}{2} = E + \frac{p}{\rho} \quad (2.20)$$

Energy transfer occurs with conduction (equation 2.21), convection and radiation, which is most often confined to boundaries.

$$q_i = -\lambda \frac{\partial}{\partial x_i} T \quad (2.21)$$

For the full picture of energy conservation law, heat sources need to be defined per unit volume q_H . They can exist due to the chemical reactions within the flow and must consider energy dissipation due to internal stresses (2.22).

$$\frac{\partial}{\partial x_i} (\sigma_{ij} v_j) = \frac{\partial}{\partial x_i} (\tau_{ij} v_j) - \frac{\partial}{\partial x_j} (p v_j) \quad (2.22)$$

The balance of energy in a unit volume can be written in a form of equation 2.23

$$\frac{\partial(\rho E)}{\partial t} + \frac{\partial}{\partial x_i} (\rho v_i E) - \frac{\partial}{\partial x_i} \left(k \frac{\partial T}{\partial x_i} \right) + \frac{\partial}{\partial x_i} (p v_i) - \frac{\partial}{\partial x_i} (\tau_{ij} v_j) - \rho f_i v_i - q_H = 0 \quad (2.23)$$

or in simplified equation 2.24.

$$\frac{\partial(\rho E)}{\partial t} + \frac{\partial}{\partial x_i} (\rho v_i H) - \frac{\partial}{\partial x_i} \left(k \frac{\partial T}{\partial x_i} \right) + \frac{\partial}{\partial x_i} (\tau_{ij} v_j) - \rho f_i v_i - q_H = 0 \quad (2.24)$$

Navier-Stokes equations are the basis of entire fluid mechanics, so their definition is crucial in further fluid considerations. Their general conservative form is shown on the equation 2.26 or 2.27.

$$\frac{\partial \mathcal{H}}{\partial t} + \nabla \mathcal{V} + \nabla \mathcal{G} + \mathcal{Q} = 0 \quad (2.25)$$

$$\frac{\partial \mathcal{H}}{\partial t} + \frac{\partial \mathcal{V}_i}{\partial x_i} + \frac{\partial \mathcal{G}_i}{\partial x_i} + \mathcal{Q} = 0 \quad (2.26)$$

in which equations 2.13, 2.15 and 2.23 provide entries to the vectors.

The vector of independent unknowns is shown below

$$\mathcal{H} = \begin{pmatrix} \rho \\ \rho v_1 \\ \rho v_2 \\ \rho v_3 \\ \rho E \end{pmatrix} \quad (2.27)$$

$$\mathcal{V}_i = \begin{pmatrix} \rho v_i \\ \rho v_1 u_i + p \delta_{1i} \\ \rho v_2 u_i + p \delta_{2i} \\ \rho v_3 u_i + p \delta_{3i} \\ \rho H v_i \end{pmatrix} \quad (2.28)$$

$$\mathcal{G}_i = \begin{pmatrix} 0 \\ -\tau_{1i} \\ -\tau_{2i} \\ -\tau_{3i} \\ -(\tau_{ij}v_j) - k\frac{\partial T}{\partial x_i} \end{pmatrix} \quad (2.29)$$

$$\mathcal{Q} = \begin{pmatrix} 0 \\ -\rho f_1 \\ -\rho f_2 \\ -\rho f_3 \\ -\rho f_i v_i - q_H \end{pmatrix} \quad (2.30)$$

where deviatoric stress τ_{ij} is given by equation 2.12.

$$\tau_{ij} = \mu \left[\left(\frac{\partial v_i}{\partial x_j} + \frac{\partial v_j}{\partial x_i} \right) - \delta_{ij} \frac{2}{3} \frac{\partial v_k}{\partial x_k} \right] \quad (2.31)$$

The complete Navier-Stokes equation can be converted to "Euler equation" if assumed that viscosity and heat conduction is equal to zero ($\tau_{ij} = k = 0$).

Presented equations are the basis for all fluid mechanics studies, so various alternative forms of them exists in the literature. However the above set of equations written in the conservation form convenient and meaningful conservation of important quantities. It should be noted that only equations written in the conservation form will yield the correct, physically meaningful results in problems where shock discontinuities are present.

Non-conservative form of Navier-Stokes equations are based on conservation forms of conservation laws below.

Conservation of mass:

$$\frac{\partial \rho}{\partial t} + \frac{\partial (\rho v_i)}{\partial x_i} = \frac{\partial \rho}{\partial t} + \rho \frac{\partial v_i}{\partial x_i} + v_i \frac{\partial \rho}{\partial x_i} = 0 \quad (2.32)$$

Conservation of momentum:

$$\frac{\partial (\rho v_i)}{\partial t} + \frac{\partial (\rho v_i v_j)}{\partial x_j} - \frac{\partial \tau_{ij}}{\partial x_j} + \frac{\partial p}{\partial x_i} = 0 \quad (2.33)$$

Conservation of energy:

$$\frac{\partial (\rho E)}{\partial t} + \frac{\partial (v_j \rho E)}{\partial x_j} - \frac{\partial}{\partial x_i} \left(k \frac{\partial T}{\partial x_i} \right) + \frac{\partial (v_j p)}{\partial x_j} - \frac{\partial (\tau_{ij} v_j)}{\partial x_j} = 0 \quad (2.34)$$

Rewriting the momentum equation with terms differentiated as [26]

$$\rho \frac{\partial v_i}{\partial t} + v_i \left(\frac{\partial \rho}{\partial t} + \rho \frac{\partial v_j}{\partial x_j} + v_j \frac{\partial \rho}{\partial x_j} \right) + \rho v_j \frac{\partial v_i}{\partial x_j} - \frac{\partial \tau_{ij}}{\partial x_j} + \frac{\partial p}{\partial x_i} = 0 \quad (2.35)$$

and submitting the equation 2.32 into the equation 2.35 gives the reduced momentum equation 2.36

$$\frac{\partial v_i}{\partial t} + v_j \frac{\partial v_i}{\partial x_j} - \frac{1}{\rho} \frac{\partial \tau_{ij}}{\partial x_j} + \frac{1}{\rho} \frac{\partial p}{\partial x_i} = 0 \quad (2.36)$$

In analogical way, the energy equation 2.34 can be rewritten with differentiated terms as

$$E \left(\frac{\partial \rho}{\partial t} + \rho \frac{\partial v_j}{\partial x_j} + v_j \frac{\partial \rho}{\partial x_j} \right) + \rho \frac{\partial E}{\partial t} + \rho v_j \frac{\partial E}{\partial x_j} - \frac{\partial}{\partial x_i} \left(k \frac{\partial T}{\partial x_i} \right) + \frac{\partial (v_i p)}{\partial x_i} - \frac{\partial (\tau_{ij} v_j)}{\partial x_i} = 0 \quad (2.37)$$

By submitting the continuity equation into the equation 2.37, reduced form of the energy equation can be obtained as below

$$\frac{\partial E}{\partial t} + v_j \frac{\partial E}{\partial x_j} - \frac{1}{\rho} \frac{\partial}{\partial x_i} \left(k \frac{\partial T}{\partial x_i} \right) + \frac{1}{\rho} \frac{\partial (v_i p)}{\partial x_i} - \frac{1}{\rho} \frac{\partial (\tau_{ij} u_j)}{\partial x_i} \quad (2.38)$$

2.1.1 Model of turbulence

The Reynolds Stress in the Reynolds-Averaged Navier Stokes (RANS) equations needs to be modelled to close the equation below [27]:

$$\frac{\partial (\rho \bar{v}_i)}{\partial t} + \frac{\partial (\rho \bar{v}_i \bar{v}_j)}{\partial x_j} = -\frac{\partial \bar{p}}{\partial x_i} + \frac{\partial}{\partial x_j} \left[\mu \left(\frac{\partial \bar{v}_i}{\partial x_j} + \frac{\partial \bar{v}_j}{\partial x_i} - \frac{2}{3} \delta_{ij} \frac{\partial \bar{v}_m}{\partial x_m} \right) \right] + \frac{\partial}{\partial x_j} \left(-\rho \overline{v'_j v'_i} \right) \quad (2.39)$$

where time-averaging is defined as

$$\bar{f} = \lim_{T \rightarrow \infty} \frac{1}{T} \int_0^T f(x_i, t) dt \quad (2.40)$$

instantaneous field is defined as the sum of the mean and fluctuating component, such as

$$p = \bar{p} + p' \quad \text{or} \quad v_i = \bar{v}_i + u'_i \quad (2.41)$$

and

$$\frac{\partial \rho}{\partial t} + \frac{\partial (\rho \bar{v}_i)}{\partial x_i} = 0 \quad (2.42)$$

Reynolds-averaged approach to turbulence modelling requires stresses $\left(-\rho \overline{v'_j v'_i} \right)$ from equation 2.39 to be appropriately modelled [28]. A common method is based on the Boussinesq hypothesis presented on equation 2.43, which relates Reynolds stresses to the mean velocity gradients. In such a case μ_t is the only variable required to close RANS equation.

$$-\rho \overline{v'_i v'_j} = \mu_t \left(\frac{\partial \bar{v}_i}{\partial x_j} + \frac{\partial \bar{v}_j}{\partial x_i} \right) - \frac{2}{3} \delta_{ij} \left(\rho k + \mu_t \frac{\partial \bar{v}_m}{\partial x_m} \right) \quad (2.43)$$

The disadvantage of the Boussinesq hypothesis is that it assumes μ_t is an isotropic scalar quantity, which is not right in all cases. However that assumption gives good results for shear flows dominated by only one of the turbulent shear stresses. This covers many technical flows, such as wall boundary layers, mixing layers, jets etc. [[28]].

Note that for simplicity, equations 2.39 and 2.43 are often presented with dropped overbar, so the same approach is going to be taken in this dissertation. Turbulence models described below were introduced to calculate turbulent (eddy) viscosity μ_t .

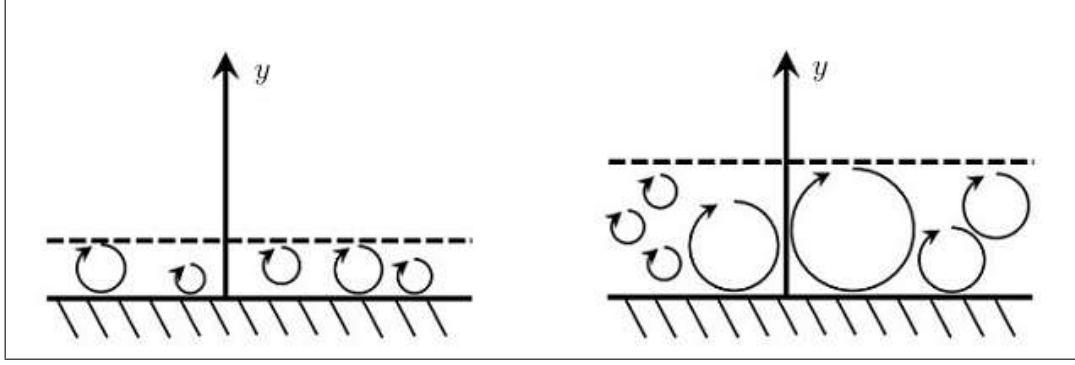


Figure 2.2: Mixing length visualization

2.1.1.1 Mixing length model

Mixing length (l_m) model was developed and used before popular $k - \epsilon$ model to estimate value of turbulent viscosity μ_t [29]. Its definition has close relationship with dissipation rate ϵ , which is presented below.

Mixing length (l_m) represents an indicative size of the turbulent eddies present in the flow. Of course turbulent flow consist the entire spectrum of eddies from microscopic ones to the large ones, so mixing length is just the indicator of flow. Based on equation 2.44, large mixing length indicates presence of large energetic eddies and intense mixing, so the turbulent viscosity is high.

$$\mu_t = \rho k^{0.5} l_m \quad \text{or} \quad \mu_t = \rho l_m^2 \left| \frac{\partial v}{\partial y} \right| \quad (2.44)$$

Equation 2.45 presents Prandtl mixing length hypothesis, which links mixing length with the distance to the nearest wall. That has got a physical meaning, because every eddy is going to be constrained by the presence of wall (Figure 2.2). Furthermore, distance to the nearest wall is well defined and constant for stationary cases.

$$l_m = \kappa y \quad \kappa = 0.41 \quad (2.45)$$

Of course presence of the wall is not the only mechanism affecting eddies size, as viscosity in the viscous sublayer also affects eddies size.

Van Driest proposed an improvement to the Prandtl model by application mixing length correction close to the wall, where viscous sub-layer dampens eddies and reduces their size. This is presented on equation 2.46 and Figure 2.3, where continuous line is deviated from the Prandtl dashed line.

$$l_m = \kappa y \left[1 - \exp \left(-\frac{y^+}{A^+} \right) \right] \quad A^+ = 26.0 \quad (2.46)$$

The improvement to the algebraic equation 2.44 is adding a transport equations for turbulence quantities which takes into account turbulence convection and diffusion through the flow. That is the turbulence kinetic energy k (equation 2.48) and turbulence dissipation rate ϵ . Once transport equations are solved, turbulent viscosity can be calculated based on equation 2.47, which allows to close RANS system of equations.

$$\mu_t = C_\mu \frac{\rho k^2}{\epsilon} \quad (2.47)$$

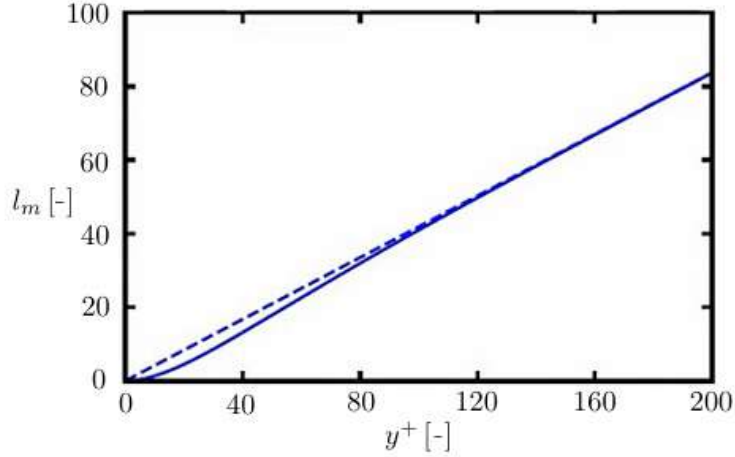


Figure 2.3: Van Driest damping assumption [29]

$$k = 0.5 \left(\overline{v_1'^2} + \overline{v_2'^2} + \overline{v_3'^2} \right) \quad (2.48)$$

Note that equation 2.49 was generated by comparing equations 2.44 and 2.47, so mixing length is directly related to the turbulence dissipation rate ϵ . It means that ϵ is just another transport equation for the mixing length (physical size of eddies).

$$l_m = \frac{C_\mu k^{1.5}}{\epsilon} \quad (2.49)$$

2.1.1.2 Standard $k - \epsilon$ model

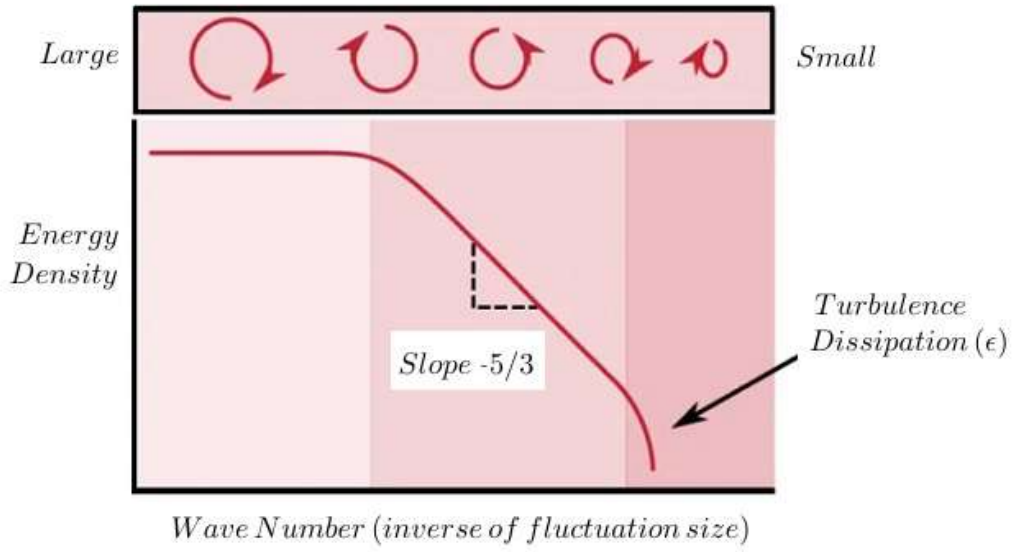
Turbulence dissipation rate ϵ is the rate that turbulent kinetic energy is converted into thermal energy by viscosity [30]. Figure 2.4 presents the energy density which is carried by specific vortices sizes. First zone on the left refers to the large vortices which carries large amount of kinetic energy. Middle zone highlights the rate, at which middle-size vortices loose their kinetic energy. Right zone points at the smallest vortices at which turbulence dissipation occurs.

Turbulence dissipation rate ϵ is theoretically expressed by equation 2.50, which is a product of kinematic viscosity and velocity gradient of turbulent fluctuations. Its unit is $\frac{m^2}{s^3}$. However, this is unknown at the level of RANS model, so transport equation has to be solved to calculate ϵ directly. Note that turbulent dissipation acts as a sink term in the equation for turbulent kinetic energy (equation 2.51), which is the strongest near walls and shear layers.

$$\epsilon = \nu \frac{\partial v_i' \partial v_i'}{\partial x_j \partial x_j} \quad (2.50)$$

Transport equation for the turbulence kinetic energy k and its rate of dissipation are given by the transport equations 2.51 and 2.52 [28]. Once they are solved, turbulence viscosity μ_t can be calculated based on equation 2.47.

$$\frac{\partial}{\partial t}(\rho k) + \frac{\partial}{\partial x_i}(\rho v_i k) = \frac{\partial}{\partial x_j} \left[\left(\mu + \frac{\mu_t}{\sigma_k} \right) \frac{\partial k}{\partial x_j} \right] + G_k + G_b - \rho \epsilon - Y_M + S_k \quad (2.51)$$

Figure 2.4: Turbulence dissipation rate ϵ [30]

Model	σ_k	σ_ϵ	C_1	C_2	C_3
Jones and Launder (1972) [32]	1.0	1.3	1.55	2.0	0.09
Launder and Spalding (1974) [33]	1.0	1.3	1.44	1.92	0.09
Launder and Sharma (1974) [31]	1.0	1.3	1.44	1.92	0.09

Table 2.1: Standard $k - \epsilon$ model constants evolution [29]

$$\frac{\partial}{\partial t}(\rho\epsilon) + \frac{\partial}{\partial x_i}(\rho v_i \epsilon) = \frac{\partial}{\partial x_j} \left[\left(\mu + \frac{\mu_t}{\sigma_\epsilon} \right) \frac{\partial \epsilon}{\partial x_j} \right] + C_{1\epsilon} \frac{\epsilon}{k} (G_k + C_{3\epsilon} G_b) - C_{2\epsilon} \rho \frac{\epsilon^2}{k} + S_\epsilon \quad (2.52)$$

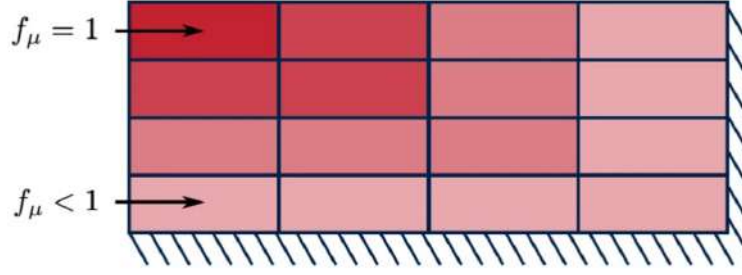
where G_k is the generation of turbulence kinetic energy due to the mean velocity gradients, G_b is the generation of turbulence energy due to the buoyancy, Y_M represents the contribution of the fluctuating dilatation in compressible turbulence to the overall dissipation rate, $C_{1\epsilon}$, $C_{2\epsilon}$ and $C_{3\epsilon}$ are constants, σ_k and σ_ϵ are the turbulent Prandtl numbers for k and ϵ respectively, S_k and S_ϵ are user-defined source terms. Values on constants are taken from [31] (compare with Table 2.1).

Low-Re (Reynolds number) formulation was developed to apply $k - \epsilon$ model in the viscous sub-layer, to obtain similar effect like Van Driest damping assumption for Mixing Length model (equation 2.46). To do that, $k - \epsilon$ coefficients C_1 , C_2 and C_μ are damped with functions f_1 , f_2 and f_μ .

Original damping functions for $k - \epsilon$ model are given by equations 2.53, 2.54 and 2.55.

$$f_1 = 1 \quad (2.53)$$

$$f_2 = 1 - 0.3 \exp(-Re_T^2) \quad (2.54)$$

Figure 2.5: The damping function f_μ [29]

$$f_\mu = \exp \left(\frac{-3.4}{\left(1 + \left(\frac{Re_T}{50}\right)\right)^2} \right) \quad (2.55)$$

Note, that above equations are based on turbulent Reynolds number presented in the equation 2.56.

$$Re_T = \frac{\rho k^2}{\mu \epsilon} \quad (2.56)$$

The physical meaning of the turbulent Reynolds number is the ratio between turbulent forces and viscous forces as presented on equation 2.57. This is an analogy to the classical Reynolds number, which is a ratio between inertia and viscous forces.

$$Re_T = \frac{\text{Turbulent Forces}}{\text{Viscous Forces}} = \frac{\rho k^{0.5} l_m}{\mu} \quad (2.57)$$

Note that the mixing length l_m can be replaced with turbulence dissipation rate ϵ leading to the equations 2.58 and 2.56. When Re_T is small, viscous effects dominates, so the analysed region is close to the wall (viscous sub-layer). When Re_T is high, it implies that turbulent forces dominates, therefore analysed region is further away from the wall.

$$Re_T = \frac{\rho k^{0.5}}{\mu} \left(\frac{k^{1.5}}{\epsilon} \right) \quad (2.58)$$

Damping field function F_μ (equation 2.55) is applied directly into turbulent viscosity according to the equation 2.59 [31].

$$\mu_t = f_\mu C_\mu \frac{\rho k^2}{\epsilon} \quad (2.59)$$

Figure 2.5 presents the f_μ damping function distribution within the flow. This is the visualization of equation 2.59 which applies the strongest μ_t damping in the area of viscous sub-layer.

The damping function f_1 is applied to the energy rate of dissipation transport equation next to G_k which is the generation of turbulence kinetic energy due to the mean velocity gradients (equation 2.60). However Jones and Launder [32] found that it makes no noticeable improvement, so f_1 was left equal to one.

$$\frac{\partial}{\partial t}(\rho \epsilon) + \frac{\partial}{\partial x_j}(\rho v_j \epsilon) = \frac{\partial}{\partial x_j} \left[\left(\mu + \frac{\mu_t}{\sigma_\epsilon} \right) \frac{\partial \epsilon}{\partial x_j} \right] + C_{1\epsilon} \frac{\epsilon}{k} (f_1 G_k + C_{3\epsilon} G_b) - C_{2\epsilon} \rho \frac{\epsilon^2}{k} + S_\epsilon \quad (2.60)$$

The damping function f_2 (equation 2.54) is applied to the dissipation of the turbulent kinetic energy term causing more dissipation near the wall.

$$\frac{\partial}{\partial t}(\rho\epsilon) + \frac{\partial}{\partial x_j}(\rho v_j \epsilon) = \frac{\partial}{\partial x_j} \left[\left(\mu + \frac{\mu_t}{\sigma_\epsilon} \right) \frac{\partial \epsilon}{\partial x_j} \right] + C_{1\epsilon} \frac{\epsilon}{k} (G_k + C_{3\epsilon} G_b) - f_2 C_{2\epsilon} \rho \frac{\epsilon^2}{k} + S_\epsilon \quad (2.61)$$

2.1.1.3 Standard $k - \omega$ model

The $k - \omega$ model was developed in response to the limitations of $k - \epsilon$ model, which was not accurate at predicting boundary layers with adverse pressure gradients. The prediction was even worse when shocks are present [30]. This is specifically important in aerofoils analysis at high angles of attack or diffusing sections internal flow when flow area increases, where $k - \epsilon$ predicts flow separation point incorrectly. In consequence lift and drag coefficients will be significantly incorrect.

Parameter ω is the specific turbulence dissipation rate which unit is 1/s. Based on equation 2.62, both ϵ and ω represents the dissipation of turbulence as they are directly linked with $(C_\mu k)$.

$$\omega = \frac{\epsilon}{C_\mu k} \quad \text{where} \quad C_\mu = 0.09 \quad (2.62)$$

The turbulence kinetic energy k and specific dissipation rate ω are obtained from the following transport equations [28]:

$$\frac{\partial}{\partial t}(\rho k) + \frac{\partial}{\partial x_i}(\rho v_i k) = \frac{\partial}{\partial x_j} \left[\left(\mu + \frac{\mu_t}{\sigma_k} \right) \frac{\partial k}{\partial x_j} \right] + G_k - Y_k + S_k + G_b \quad (2.63)$$

and

$$\frac{\partial}{\partial t}(\rho \omega) + \frac{\partial}{\partial x_i}(\rho v_i \omega) = \frac{\partial}{\partial x_j} \left[\left(\mu + \frac{\mu_t}{\sigma_\omega} \right) \frac{\partial \omega}{\partial x_j} \right] + G_\omega - Y_\omega + S_\omega + G_{\omega b} \quad (2.64)$$

where G_k represents the generation of turbulence kinetic energy due to mean velocity gradients, G_ω represents the generation of ω , Y_k and Y_ω represent the dissipation of k and ω due to turbulence. G_b and $G_{\omega b}$ account for buoyancy. S_k and S_ω are user-defined source terms.

The turbulent viscosity μ_t is computed based on equation 2.65.

$$\mu_t = \alpha^* \frac{\rho k}{\omega} \quad (2.65)$$

Low-Reynolds number correction coefficient α^* damps the turbulent viscosity causing a low-Reynolds number correction given by

$$\alpha^* = \alpha_\infty^* \left(\frac{\alpha_0^* + Re_t/R_k}{1 + Re_t/R_k} \right) \quad (2.66)$$

where

$$Re_t = \frac{\rho k}{\mu \omega} \quad (2.67)$$

$$R_k = 6 \quad (2.68)$$

$$\alpha_0^* = \frac{\beta_i}{3} \quad (2.69)$$

$$\beta_i = 0.072 \quad (2.70)$$

Note that in the high-Reynolds number form of the $K - \omega$ model $\alpha^* = \alpha_\infty^* = 1$ [28].

2.1.1.4 Shear-Stress Transport (SST) $k - \omega$ model

The $k - \omega$ SST model was developed by Menter in 1994 [34] as a response to the limitations of $k - \epsilon$ and $k - \omega$ models [35, 36]. It was needed due to the unreliable $k - \epsilon$ damping functions and $k - \omega$ model sensitivity to the freestream value of ω applied at the inlet [37].

The SST $k - \omega$ model includes all the refinements of the BSL $k - \omega$ model, and in addition it accounts for the transport of the turbulence shear stress in the definition of the turbulent viscosity [28].

The Baseline (BSL) $k - \omega$ model transport equations have the form below.

$$\frac{\partial}{\partial t}(\rho k) + \frac{\partial}{\partial x_i}(\rho v_i k) = \frac{\partial}{\partial x_j} \left[\left(\mu + \frac{\mu_t}{\sigma_k} \right) \frac{\partial k}{\partial x_j} \right] + G_k - Y_k + S_k + G_b \quad (2.71)$$

and

$$\frac{\partial}{\partial t}(\rho \omega) + \frac{\partial}{\partial x_i}(\rho v_i \omega) = \frac{\partial}{\partial x_j} \left[\left(\mu + \frac{\mu_t}{\sigma_\omega} \right) \frac{\partial \omega}{\partial x_j} \right] + G_\omega - Y_\omega + S_\omega + D_\omega + G_{\omega b} \quad (2.72)$$

where G_k represents the production of turbulence kinetic energy and is defined in the same manner as in the standard $k - \omega$ model. G_ω represents the generation of ω , Y_k and Y_ω represent the dissipation of k and ω due to turbulence. G_b and $G_{\omega b}$ account for buoyancy. S_k and S_ω are user-defined source terms. D_ω represents the cross-diffusion term.

Turbulent Prandtl numbers for k and ω are blended according to equation 2.73 and 2.74.

$$\sigma_k = \frac{1}{\frac{F_1}{\sigma_{k,1}} + \frac{1-F_1}{\sigma_{k,2}}} \quad (2.73)$$

$$\sigma_\omega = \frac{1}{\frac{F_1}{\sigma_{\omega,1}} + \frac{1-F_1}{\sigma_{\omega,2}}} \quad (2.74)$$

The blending function F_1 is given by equation 2.75 and is shown schematically at the Figure 2.6 [37].

$$F_1 = \tanh(\phi_1^4) \quad (2.75)$$

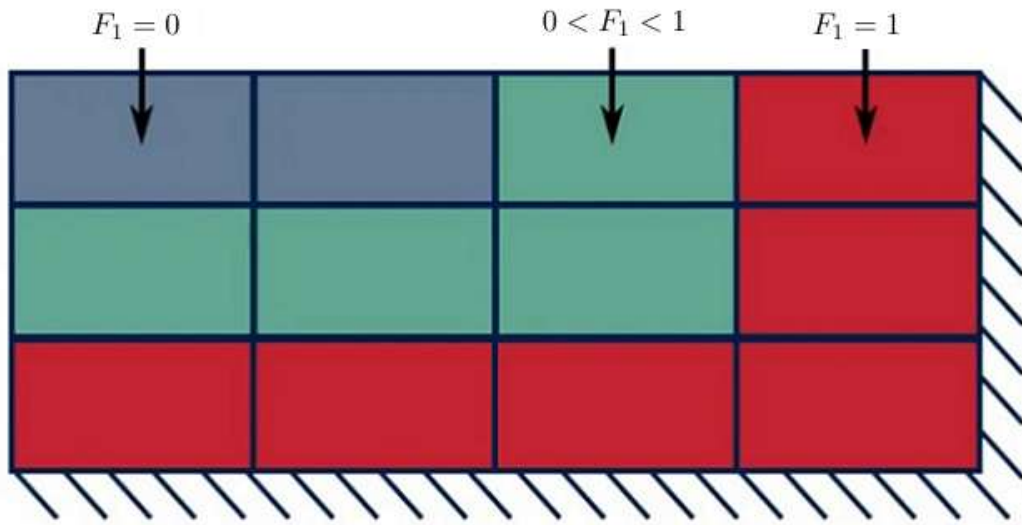
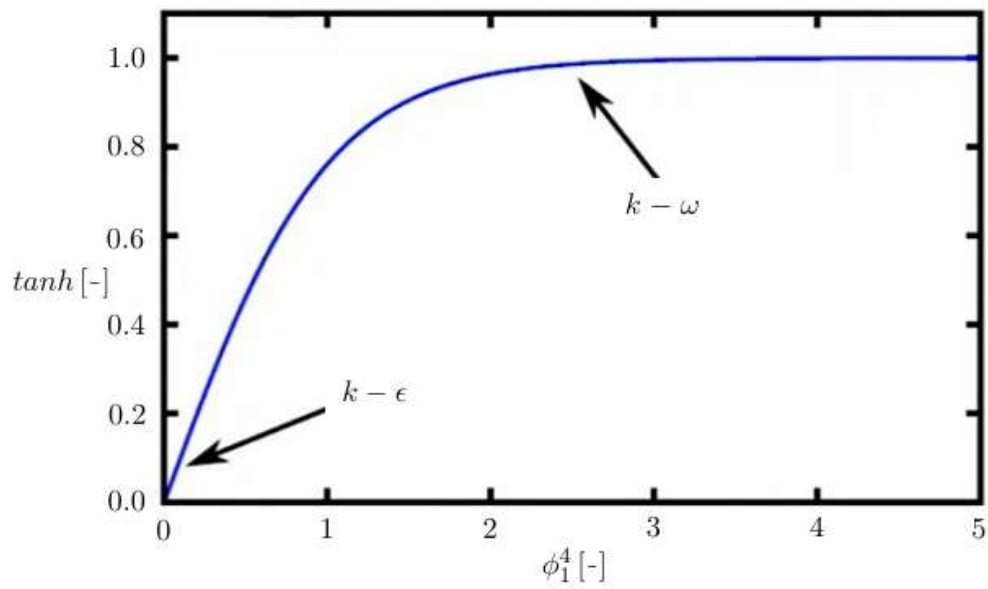
where ϕ_1 is calculated based on equations 2.76 and 2.77. Furthermore, ϕ_1^4 is presented on Figure 2.7, so model $k - \omega$ SST applies $k - \omega$ model next to the wall and $k - \epsilon$ in the freestream area.

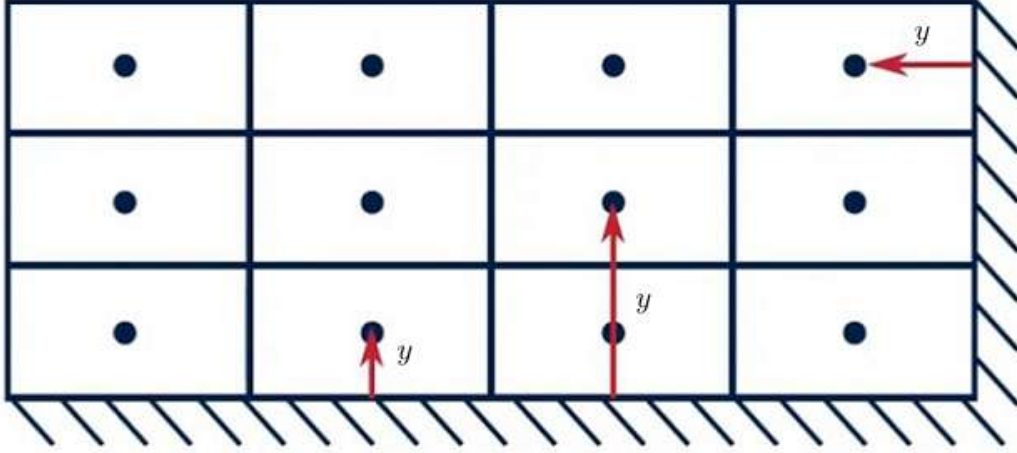
$$\phi_1 = \min \left[\max \left(\frac{\sqrt{k}}{0.09\omega y}, \frac{500\mu}{\rho y^2 \omega} \right), \frac{4\rho k}{\sigma_{\omega,2} D_\omega^+ y^2} \right] \quad (2.76)$$

$$D_\omega^+ = \max \left[2\rho \frac{1}{\sigma_{\omega,2}} \frac{1}{\omega} \frac{\partial k}{\partial x_j} \frac{\partial \omega}{\partial x_j}, 10^{-10} \right] \quad (2.77)$$

where y is the distance to the closest wall (Figure 2.8).

The BSL $k - \omega$ model fails to predict the flow separation from smooth surfaces due to the lack of accounting for the transport of the turbulent shear stress. $K - \omega$ SST model accounts for that by application of an eddy-viscosity limiter to the turbulent viscosity using the equation 2.78.

Figure 2.6: The application of the blending function F_1 [37]Figure 2.7: The graphical representation of ϕ_1^4 function [37]

Figure 2.8: The distance to the nearest wall y [37]

$$\mu_t = \frac{\rho k}{\omega} \frac{1}{\max \left[\frac{1}{\alpha^*}, \frac{SF_2}{\alpha_1 \omega} \right]} \quad (2.78)$$

where S is the strain rate magnitude and α^* is defined in equation 2.66.

The F_2 blending function is given by equation 2.80.

$$F_2 = \tanh(\phi_2^2) \quad (2.79)$$

$$\phi_2 = \max \left[2 \frac{\sqrt{k}}{0.09 \omega y}, \frac{500 \mu}{\rho y^2 \omega} \right] \quad (2.80)$$

where y is the distance to the closest wall (Figure 2.8).

Model constants are as follows: $\sigma_{k,1} = 1.176, \sigma_{\omega,1} = 2.0, \sigma_{k,2} = 1.0, \sigma_{\omega,2} = 1.168, \alpha = 0.31, \beta_{i,1} = 0.075, \beta_{i,2} = 0.0828$. They were found through the thorough comparison between experimental and modelling results.

Note, that if blending function $F_1 = 0$, then $k - \epsilon$ model is applied. In the opposite case ($F_1 = 1$), $k - \omega$ model is used.

$F_1 = 0$, the model is $k - \epsilon$

$F_1 = 1$, the model is $k - \omega$

2.1.2 Model of combustion

Understanding of combustion processes gave people advantage over the natural environment and let to accelerate the development of civilization. Fuel oxidation has a numerous applications within our everyday life. It includes heating, transport, defence systems and electricity generation. Numerical simulation of combustion phenomenon is focused mainly on chemical reactions, but important part of it is a life assessment of combustors. Regarding the flame shape and stability, the key aspect is the reactants mixing intensity which should assure complete combustion. This is closely related to the control of toxic products production, which are strictly controlled due to the environmental impact.

One of the most promising technology to reduce CO_2 emission by CCS (carbon capture and storage) is application of oxy-fuel combustion [38–42]. The advantage of this solution is that generated outlet flow contains predominantly steam and CO_2 , so CO_2 separation can be easily made by condensation of water steam. One of the large scale programmes to develop such technology is covered in Anderson et al. papers [38–41]. They build several demonstrators able to combust natural gas in oxygen with the addition of liquid water. In the first generation rig, exhaust gases propelled modified General Electric J79 turbine at inlet temperature of $760 - 927^\circ C$, which delivered $32MW_e$. Second generation power plant was aimed to increase performance and efficiency by operating intermediate pressure turbine at higher temperature ($1080 - 1260^\circ C$) and pressure. That was based on Siemens SGT900 turbine converted into OFT-900 [40]. It demonstrated the feasibility of the oxy-fuel technology to feed electricity into the U.S. grid. This choice was made taking into account turbine size, flame temperature, pressure condition, cooling system, aerodynamic performance and modification-friendly architecture. Working fluid conversion from the air-based into a steam/ CO_2 mixture is the biggest challenge in turbine redesign. Steam specific heat (c_p) is significantly higher than for air, so the same mass flow carries more power. In the case of OFT-900 turbine, working fluid contains $80 \sim 90\%$ of steam and $10 \sim 15\%$ of CO_2 , resulting in about 60% increase of c_p in comparison to the classical gas turbine. However, this effect is partially offset by the impact of molecular weight, resulting in turbine power growth by about 20% (oxy-fuel vs. air). Third generation of CES power plant was expected to withstand even higher temperature ($1650 - 1760^\circ C$), but there is no much details available in literature for that solution.

This article is a part of the "Negative CO2 Power Plant" project founded by the Norway Grants 2014-2021 via the National Centre for Research and Development in Poland. Based on the advantages of oxy-fuel technology, it was decided to include it into the prototype of the Wet Combustion Chamber (WCC) component [43]. Energy Conversion Department Team has got an experience both in thermodynamic studies of the system performance [44, 45] and in combustion chamber conceptual work [46–48]. However, detailed 3D analysis of combustor covering reaction zones structures and flame dynamics is still missing. Swirling inlet offers numerous advantages over the wide range of work conditions including flame stabilization, easy ignition and reduced flame volume. An efficient way to reduce flame temperature and lower the content of oxygen in the flue gas is adding an CO_2 or water steam into the mixing combustion zone. In order to maintain hot and stable conditions for chain reactions within the flame, certain minimum content of oxidiser needs to be maintained. Liu et al. [49] concluded, that oxidiser supplied through the dome must contain minimum 24% of oxygen at $520^\circ K$ in order to keep stable flame. Kutne et al. [50] studied the characteristics of a swirl-stabilized oxy-methane flames for O_2/CO_2 ratios of $20/80 - 40/60\%$ (equivalence ration of 0.5 to 1.0). They concluded that burner operational limit is minimum 22% of O_2 , because below that value the dilution content is too high leading to the flame extinguishment. Williams et al. [51] performed an extensive studies of syngas and methane combustion characteristics in the presence of oxidiser containing $O_2/CO_2/N_2$.

2.1.2.1 Homogenous mixture approach

Homogenous mixture approach assumes that all components form a new and unique gas, so conservation laws are applicable only once to it. In case of necessity, this model can be extended by the equations of mixture content evolution. That approach offers a great simplification to the model, because it applies average velocity and same temperature to all mixture components. The form of conservation equations in this case is similar to the

single component form, but they slightly differ with the structure of momentum, energy and diffusion fluxes. The homogenous approach can be described as a microstructure containing multiple components, which can be created or destructed by the chemical reactions. Similar simplification is applied to the evolutionary turbulence equations, where mixture is treated as single medium. That property lets to cross-link turbulence with evolutionary equations of new component formation [52].

2.1.2.2 Mass conservation of mixture

The mass conservation law can be written in a form of equation (2.81), where ρ [kg/m³] is a density and \underline{v} [m/s] is a velocity vector of a finite volume [53]

$$\frac{\partial}{\partial t}(\rho) + \text{div}(\rho \underline{v}) = 0. \quad (2.81)$$

The important conclusion from this equation is that density is a basic variable of the numerical model.

In the case of a mixture, the sum of all mass components is equal to unity, according to the equation (2.82)

$$\sum_{k=1}^{NC} Y_k = 1.0 \quad (2.82)$$

where NC is the number of components and Y_k [kg/kg] is the mass concentration of component k . Alternatively, pressure can be used instead of the mixture density. The basic vector of continuous variables is:

$$\mathcal{U} = \{\rho, \rho \underline{v}, \rho e, \rho Y_k\}, \quad (2.83)$$

which contains unknown variables: mixture density ρ [kg/m³], volumetric density of momentum $\rho \underline{v}$ [kg/(m²s)], volumetric density of total energy ρe [kg/(m³J)], volumetric density of component ρY_k [kg/m³].

2.1.2.3 Momentum conservation of mixture

The flux of momentum within a mixture contains thermodynamic pressure p (reversible element) and some dissipative components like flux of viscous strains $\underline{\tau}$ and Reynolds turbulent flux \underline{r} :

$$\underline{t} = -p\underline{I} + \underline{\tau} + \underline{r} + \underline{\tau}^{dif} + \underline{\tau}^{rad} + \underline{\tau}^{trans} = -p\underline{I} + \underline{\tau}^{total}. \quad (2.84)$$

Other components of momentum flux are driven by the diffusion $\underline{\tau}^{dif}$, radiation $\underline{\tau}^{rad}$ and transpiration $\underline{\tau}^{trans}$. By grouping fluxes on convective (first order derivative) and diffusive (second order derivative), evolution of momentum can be written in the following form:

$$\frac{\partial}{\partial t}(\rho \underline{v}) + \text{div}(\rho \underline{v} \otimes \underline{v} + p\underline{I}) = \text{div}(\underline{\tau}^{total}) + \rho \underline{b}, \quad (2.85)$$

or in the Cartesian coordinate system:

$$\frac{\partial}{\partial t}(\rho v_i) + \frac{\partial}{\partial x_j}(\rho v_i v_j + p \delta_{ij}) = \frac{\partial}{\partial x_j}(\tau_{ij}^{total}) + \rho b_i \quad i, j = x, y, z. \quad (2.86)$$

It can be concluded from the above equation of conservation of momentum, that "strain" boundary condition for a flux flowing through the surface normal to the vector \underline{n} can be expressed as

$$\underline{\tau}^* = \underline{t} \underline{n}, \quad (2.87)$$

where $\underline{\tau}^*$ is vector of applied boundary force, which in the specific case can be equal to applied pressure $\underline{\tau}^* = p^* \underline{n}$, where \underline{n} is an unit vector normal to the surface. According to the previous assumption, all components of a mixture have the same velocity \underline{v} and gradients in space, so the tensor of viscous stresses in a mixture can be expressed by the classical Stokes formula:

$$\underline{\tau} = 2\mu \left[\underline{d} - \frac{1}{3} \text{div}(\underline{v}) \underline{I} \right] + \mu' \text{div}(\underline{v}) \underline{I}, \quad (2.88)$$

in which the deformation velocity is given in the form below

$$\underline{d} = \frac{1}{2} (\nabla \otimes \underline{v} + \underline{v} \otimes \nabla) = \frac{1}{2} \left(\frac{\partial v_i}{\partial x_j} + \frac{\partial v_j}{\partial x_i} \right) \hat{e}_i \otimes \hat{e}_j = d_{ij} \hat{e}_i \otimes \hat{e}_j = \underline{d}^T, \quad (2.89)$$

and μ [kg/(m s)] is the dynamic viscosity of a mixture and μ' is a coefficient of second mixture viscosity, which in most cases is equal to zero [54]. In the following considerations, it is assumed that viscous stresses in mixture are the sum of viscous stresses in each component

$$\underline{\tau} = \sum_k^{NC} \underline{\tau}_k, \quad (2.90)$$

which is required in order to apply underneath Wilke equation describing dynamic viscosity of a mixture

$$\mu = \sum_{k=1}^{NC} \frac{X_k \mu_k}{\sum_{k'=1}^{NC} X_k X_{k'} \Phi_{kk'}} = \sum_{k=1}^{NC} \frac{Y_k \mu_k}{W_k \left(\sum_{k'=1}^{NC} \frac{Y_{k'} \Phi_{kk'}}{W_{k'}} \right)} \quad (2.91)$$

where $\mu_k = \mu_k(T)$ is a viscosity of component k , X_k [m³/m³ of mixture] or [mole/mole of mixture] is a volumetric or molar content of component k in the mixture and $\Phi_{kk'}$ is a Wilke matrix given below.

$$\Phi_{kk'} = \frac{1}{8} \left(\frac{1}{\sqrt{1 + \frac{W_k}{W_{k'}}}} \right) \left(1 + \sqrt{\frac{\mu_k}{\mu_{k'}}} \sqrt[4]{\frac{W_{k'}}{W_k}} \right) \quad (2.92)$$

Based on equation (2.92), viscosity of a mixture is a function of temperature T , components mass content Y_k and W_k is a molecular weight of k ingredient. Turbulent flux of the momentum transport in the combustion flow can be influenced by three types of sources:

- turbulence of momentum,
- turbulence of heat,
- turbulence of chemical potentials caused by the combustion of components.

Very often in the literature, turbulence phenomenon is simplified to the turbulence of momentum, induced (much weaker) heat transport (\underline{q}^t) and turbulent diffusion (\underline{J}_k^t). In such a case, it is assumed that velocity fluctuations (\underline{v}') dominates over density (Y_k') and temperature (T') fluctuations. Such simplification is appropriate in the case of two non-burning fluxes characterized with similar constant temperatures. However, more detailed

analysis of combustion-turbulence interaction should better reflect the combustion process impact into the turbulent flux of momentum. The combustion phenomenon impact is crucial, but all models approached so far by the author are based on a cold-flow assumption which simply ignores the presence of combustion within the flow [55–59]. Most common method to close the turbulent Reynolds flux is the Boussinesq relation:

$$r_{ij} = \mu_t \left(\frac{\partial v_i}{\partial x_j} + \frac{\partial v_j}{\partial x_i} - \frac{2}{3} \frac{\partial v_k}{\partial x_k} \delta_{ij} \right) - \frac{2}{3} \rho k \delta_{ij}, \quad (2.93)$$

which is analogous to the formula describing viscous stresses (2.88), where parameter k is a turbulent volumetric viscosity and turbulent viscosity $\mu_t(\underline{x}, t)$ (function of location and time) is classically expressed as

$$\mu_t = C_\mu \rho \frac{k^2}{\epsilon}, \quad (2.94)$$

where $k = \frac{1}{2} \text{tr}(r_{ij})$ is a kinetic energy of turbulence, ϵ is an intensity of its dissipation and C_μ is a constant. Note, that ρ is a density of the entire mixture, so turbulence model cannot be applied separately to each component. Both parameters $k = k(\underline{x}, t)$ and $\epsilon = \epsilon(\underline{x}, t)$ are supposed to model an isotropic and cold turbulence, which sometimes is not sufficient to model heavily anisotropic and hot phenomena occurring during the turbulent combustion process. Sporadically, equation (2.93) is replaced by a non-linear expression, which covers not only the velocity of deformation \underline{d} , but also a spin $\underline{\omega} = \frac{1}{2} (\nabla \otimes \underline{v} - \underline{v} \otimes \nabla)$:

$$\underline{r} = \underline{r} \left(k^2, \epsilon, \underline{d}, \underline{d}^2, \underline{d} \underline{\omega}, \underline{\omega}^2, \underline{d}^2 \underline{\omega}, \underline{d}^3 \right). \quad (2.95)$$

Formula above supports the same evolutionary equations for k and ϵ and allows for non-linear algebraic expression of turbulent stresses named as "non-linear return to isotropy". This name highlights the fact, that models matching definition from equation (2.95) still describe isotropic turbulence, but non-linear version of it.

Transport equations describing $k - \epsilon$ model are:

$$\frac{\partial}{\partial t}(\rho k) + \frac{\partial}{\partial x_j}(\rho v_j k) = \frac{\partial}{\partial x_j} \left[\left(\mu + \frac{\mu_t}{\sigma_k} \right) \frac{\partial k}{\partial x_j} \right] + S_k, \quad (2.96)$$

$$\frac{\partial}{\partial t}(\rho \epsilon) + \frac{\partial}{\partial x_j}(\rho v_j \epsilon) = \frac{\partial}{\partial x_j} \left[\left(\mu + \frac{\mu_t}{\sigma_\epsilon} \right) \frac{\partial \epsilon}{\partial x_j} \right] + S_\epsilon, \quad (2.97)$$

and they have the same structure like other transport equations. Source terms S_k and S_ϵ are dependent from the vector of continuous variables (equation (2.83)) and its gradients in space:

$$S_k = \rho \left(r_{ij} \frac{\partial v_i}{\partial x_j} - \epsilon \right) - \frac{\mu_t}{\rho^2} \frac{\partial \rho}{\partial x_i} \frac{\partial \rho}{\partial x_i}, \quad (2.98)$$

$$S_\epsilon = \rho \frac{\epsilon}{k} \left(C_1 r_{ij} \frac{\partial v_i}{\partial x_j} - C_2 \epsilon \frac{\mu_t}{\rho^2} \frac{\partial \rho}{\partial x_i} \frac{\partial \rho}{\partial x_i} \right). \quad (2.99)$$

Five constant values included in the $k - \epsilon$ are: $\sigma_k = 1.0$, $\sigma_\epsilon = 1.3$, $C_\mu = 0.09$, $C_1 = 1.44$, $C_2 = 1.92$. They are independent from the type of flow (steady, non-steady), type of fluid (compressible, incompressible) and the degree of the combustion and mixing process. The lack of coupling between equations (2.96) and (2.97) with the equations describing mass evolution Y_k along the combustion is a serious disadvantage of the $k - \epsilon$ model. In other words, this model describes the turbulence without the insight into the intense chemical reactions occurring in the analysed volume.

2.1.2.4 Energy conservation of mixture

The conservation equations of total energy (internal and kinetic) of the homogeneous mixture model take into account transient variations of balanced parameter by comparing inlet versus outlet fluxes

$$\begin{aligned} \frac{\partial}{\partial t}(\rho e) + \frac{\partial}{\partial x_j}(\rho e v_j) = \frac{\partial}{\partial x_j}(q_j + q_j^t + t_{ji}v_j + q_j^D + q_j^{rad}) + \\ + \rho r + \rho b_j v_j + \sum_{k=1}^{NC} \rho h_k W_k \dot{\omega}_k, \end{aligned} \quad (2.100)$$

where: $e = \epsilon + v_j^2/2$ is a sum of internal and kinetic energy, q_j and q_j^t is a molecular and turbulent heat flux, $t_{ji}v_j$ - mechanical heat flux, q_j^D and q_j^{rad} are diffusive and radiative heat fluxes of mixture. h_k is a component enthalpy per mass unit (equation (2.101)).

$$h_k = \epsilon_k + \frac{p_k}{\rho_k}. \quad (2.101)$$

Total flux of momentum $t_{ij} = -p\delta_{ij} + \tau_{ij}^\theta$ is split between the elastic reversible part ($p\delta_{ij}$, first order derivative) and mechanical diffusive part. Taking this into account, the mechanical part of momentum flux $-p\delta_{ij}v_i = -pv_i$ should be moved to the left side of equation

$$\frac{\partial}{\partial t}(\rho e) + \frac{\partial}{\partial x_j} \left[\left(e + \frac{p}{\rho} \right) \rho v_j \right] = \frac{\partial}{\partial x_j} (q_j + q_j^t + \tau_{ji}^\theta v_j + q_j^D + q_j^{rad}) + S_e. \quad (2.102)$$

In case of the enthalpy form, expression below is applicable

$$\rho e = \rho h + \rho \frac{v_i^2}{2} - p. \quad (2.103)$$

In the literature, total enthalpy is expressed in the form below

$$h^\theta = h + \frac{v_i^2}{2} = h + \frac{1}{2}(v_i v_i). \quad (2.104)$$

2.1.2.5 Kinetics of reactions

The diffusive-kinetic equation for mass content Y_k of individual (NC-1) components of mixture has a conservative form [60, 61]

$$\frac{\partial}{\partial t}(\rho Y_k) + \text{div}(\rho Y_k \underline{v}) = -\text{div}(\underline{J}_k + \underline{J}_k^t) + \dot{\omega}_k W_k, \quad k = 1, \dots, NC - 1, \quad (2.105)$$

where ρ and \underline{v} are density and average mixture velocity, Y_k is mass content of k^{th} component, \underline{J}_k is the diffusive flux of k^{th} component versus mean velocity \underline{v} and \underline{J}_k^t is a turbulent diffusive flux of k^{th} component.

By knowing the contents of $NC - 1$ components Y_k , the share of last component can be easily calculated from the expression below

$$Y_{NC} = 1 - \sum_{k=1}^{NC-1} Y_k. \quad (2.106)$$

On top of that, average turbulent production of k^{th} component is covered by its source $\dot{\omega}_k [\frac{kg}{m^3s}]$ multiplied by molecular weight of k^{th} component $W_k [\frac{kg}{mol}]$. In case of omitting the turbulent flux of diffusion \underline{J}_k^t , $\dot{\omega}_k [\frac{kg}{m^3s}]$ describes only the molecular source.

Independently from the approach to the description of turbulence flux \underline{J}_k^t presented in equation (2.105), this element requires some kind of closure. Available options can be split into three types:

$$\underline{J}_k^t = \overline{v'Y_k'} = \left\{ \begin{array}{l} \textbf{phenomenological:} \\ \text{four-equations } k - \epsilon - f - g \\ \text{algebraic} \\ \\ \textbf{statistical:} \\ \text{pdf} \\ \text{renormalization group} \\ \\ \textbf{mixed:} \\ \text{LES - Large Eddy Simulation} \\ \text{DNS - Direct Numerical Simulation} \end{array} \right. \quad (2.107)$$

This article is focussed on phenomenological four-equations model $k - \epsilon - f - g$. It assumes, that turbulent flux of momentum (velocity) induces additionally turbulent fluxes of heat and diffusion. In consequence, in the analogy to the phenological closure of \underline{q}^t below equation can be made

$$\overline{v'Y_k'} = -D_k^t \nabla Y_k, \quad (2.108)$$

where D_k^t is a turbulent coefficient of exchange, independent of location and time. It is proportional to the turbulent viscosity of mixture μ_t , similarly like turbulent coefficient of conduction λ_t . The proportionality factor is a turbulent number of Prandtl-Schmidt $PrSt \simeq 0.7$, so

$$D_k^t = \frac{\mu_t}{PrSt}, \quad k = 1 \dots NS - 1. \quad (2.109)$$

The really important fact is that defined coefficient of turbulent diffusion, based on a turbulent viscosity of a mixture μ_t , is equal for all components Y_k . This is a consequence of a fact, that a turbulent viscosity of a mixture is defined for the entire mixture rather than for each component separately. Such definition of D_k is completely dependent on the accuracy of μ_t , which is driven by the application of differential equations to close the $k - \epsilon - f - g$ model, etc.

Frequently used algebraic model of turbulent transport of momentum was invented by Baldwin and Lomax. It does not contain any differential equations, which is a significant advantage in the CFD tasks. Additionally, it is quite accurate in describing the turbulence of the boundary layer, which is crucial in the flows characterized by the high area/volume ratio. In such cases, two-equations differential $k - \epsilon$ model can generate less accurate results if not supported by additional boundary layer correction functions. One of the key limitation in Baldwin-Lomax model is constant turbulent viscosity in regions located far from walls, which is not a point of concern in power generation devices characterized by the high wall area/volume ratio.

Phenological description of \underline{J}_k^t is included in $k - \epsilon - f - g$ model, which describes the impact of turbulent momentum transport $k - \epsilon$ into the combustion and vice-versa, the influence of combustion ($f - g$) into the flow turbulence. This concept was invented by scientists focused on the turbulent momentum transport model, based on the differential two-equations closure containing kinetic energy of turbulence k and its dissipation rate ϵ . This model uses the mixing efficiency f and its mean fluctuation $g = \overline{f'^2} = \overline{f'f'}$.

As a remainder, the complete description of the fuel oxidation level must be given by minimum two dimensionless parameters given below

$$\left\{ \begin{array}{l} f \Leftrightarrow \text{mixing level between fuel and} \\ \text{oxidiser (non-burned and burned)} \\ \\ c \Leftrightarrow \text{stage of combustion advancement} \end{array} \right. \quad (2.110)$$

The degree of mixing is defined as the ratio between the fuel mass (burned and unburned) versus total mass of mixture, so it is independent from the combustion intensity. The oxidation process advancement c can appear only in regions where degree of mixture is above zero. Parameter c is an equivalent of the ratio between combustion products mass versus fuel or oxidizer mass. This factor can vary between zero and one, which means no-combustion and full-combustion respectively

$$c = \frac{\beta - \beta_2}{\beta_1 - \beta_2}, \quad (2.111)$$

where so called Shvaba-Zeldowicz function *beta* is defined as

$$\beta = \beta_{FO} = Y_F - \frac{1}{r}Y_O \quad (2.112)$$

and is referenced to the single-stage chemical reaction

$$\{1 \text{ kg of fuel (F)}\} + \{r \text{ kg of oxidant (O)}\} \rightarrow \{(1 + r) \text{ kg of product (P)}\}. \quad (2.113)$$

In such a case, three possible Shvaba-Zeldowicz parameters

$$\beta_{FO} = Y_F - \frac{Y_O}{r}, \quad (2.114)$$

$$\beta_{FP} = Y_F + \frac{Y_P}{r + 1}, \quad (2.115)$$

$$\beta_{OP} = Y_O + \frac{rY_P}{r + 1} \quad (2.116)$$

are a conservative variables. Factor r is the inverse of stoichiometric factor s . Indexes 0 and 1 refer to streams of oxidizer and fuel respectively.

The transport equation of a mixture factor f and its fluctuation $g = \overline{f'f'}$ can be written based on several simplifications in the reaction description (for instance, assumption of single-stage fast reaction). It should be noted, that equations $k - \epsilon - f - g$ were invented to close turbulent fluxes of momentum $\underline{\tau}$, heat \underline{g}^t and diffusion \underline{J}_k^t , so they have limited impact to the reaction kinetics described by equation (2.105). Transport equations for $f - g$:

$$\frac{\partial}{\partial t}(\rho f) + \frac{\partial}{\partial x_j}(\rho v_j f) = \frac{\partial}{\partial x_j} \left[\left(\mu + \frac{\mu_t}{\sigma_f} \right) \frac{\partial f}{\partial x_j} \right] \quad (2.117)$$

$$\frac{\partial}{\partial t}(\rho g) + \frac{\partial}{\partial x_j}(\rho v_j g) = \frac{\partial}{\partial x_j} \left[\left(\mu + \frac{\mu_t}{\sigma_g} \right) \frac{\partial g}{\partial x_j} \right] + 2 \frac{\mu_t}{\sigma_g} \left(\frac{\partial g}{\partial x_j} \right)^2 - 2 \rho \frac{\epsilon}{k} g \quad (2.118)$$

where: $\sigma_t = \sigma_g \simeq 0.7$, and turbulent viscosity $\mu_t = \rho C_\mu \frac{k^2}{\epsilon}$, $C_\mu = 0.009$. It should be noted, that coupling with transport equations of turbulent momentum is non-direct (through k, ϵ).

Additionally, for a infinitely fast one-step reaction, mass concentrations of fuel and oxidizer are linked with the mixture coefficient f through

$$\text{for } 0 \leq f < f_{st} \quad Y_F = 0, \quad Y_O = Y_{O,0} \frac{f - f_{st}}{f_{st}} \quad (2.119)$$

$$\text{for } f_{st} < f \leq 1 \quad Y_O = 0, \quad Y_F = Y_{O,1} \frac{f - f_{st}}{f_{st}} \quad (2.120)$$

where f_{st} is a stoichiometric value of mixture coefficient, for which $\beta \equiv 0$, which directs to the equation below

$$f_{st} = \frac{Y_{O,1}}{r Y_{F,0} + Y_{O,1}}. \quad (2.121)$$

Assuming $Y^* = \frac{Y_{F,0}}{(1-f_{st})}$, then mass concentration in both cases is equal to

$$f < f_{st} \quad Y_p = (r+1)Y^*f(1-f_{st}) \quad (2.122)$$

$$f > f_{st} \quad Y_p = (r+1)Y^*f_{st}(1-f) \quad (2.123)$$

Missing closure of a phenomenological model $k - \epsilon - f - g$ are direct expressions for fluxes $\underline{r}, \underline{q}^t, \underline{J}_k^t$ in appropriate balance equations. Such closures are not available yet, because model development was directed towards "complex pdf functions". Nevertheless, it sounds reasonable to test fully phenomenological approach deploying four differential equations $k - \epsilon - f - g$ based on the closure type

$$\left\{ \begin{array}{c} \underline{r} \\ \underline{q}^t \\ \underline{J}_k^t \end{array} \right\} = f(k, \epsilon, f, g, \nabla k, \nabla \epsilon, \nabla f, \nabla g, \text{grad } \underline{v}, \text{etc}) \quad (2.124)$$

for instance, for the Reynolds stress tensor

$$\underline{r} = k \underline{I} + \mu_t (\nabla \otimes \underline{v} + \underline{v} \otimes \nabla) + \mu_1 \nabla k \otimes \nabla k + \mu_2 \nabla f \otimes \nabla f, \quad (2.125)$$

in which turbulent viscosities $\mu_t(\epsilon, k), \mu_1(\epsilon, k), \mu_2(f, g)$ are functions of parameters k, ϵ, f, g . In a preferable solution, transport equations k, ϵ, f, g ought to contain explicit coupling between $k - \epsilon$ and $f - g$.

2.1.2.6 Numerical integration of reacting mixture

System of equations describing the thermodynamics of reacting gaseous mixture referenced to the Cartesian coordinate system have the following conservative form in two-dimensional space $x_\alpha = x, y$. In some specific cases it can be extended by the catalytic combustion theory [62].

For the sake of simplicity, the following chapter is based on two-dimensional approach, however it is easily extendable to three dimensions.

- mass conservation equation

$$\frac{\partial}{\partial t}\rho + \frac{\partial}{\partial x_\alpha}(\rho v_\alpha) = 0, \quad (2.126)$$

- momentum conservation equation

$$\frac{\partial}{\partial t}(\rho v_\alpha) + \frac{\partial}{\partial x_\beta}(\rho v_\alpha v_\beta + p\delta_{\alpha\beta}) = \frac{\partial}{\partial x_\beta}(\tau_{\alpha\beta}^\theta) + \rho b_\alpha, \quad (2.127)$$

- energy conservation equation

$$\frac{\partial}{\partial t}(\rho e) + \frac{\partial}{\partial x_\alpha}((\rho e + p)v_\alpha) = \frac{\partial}{\partial x_\alpha}(\tau_{\alpha\beta}^\theta v_\beta + q_\alpha^\theta) + \rho s_e, \quad (2.128)$$

- component balance equation (2.105), $k = 1, \dots, NC - 1$

$$\frac{\partial}{\partial t}(\rho Y_k) + \frac{\partial}{\partial x_\alpha}(\rho Y_k v_\alpha) = \frac{\partial}{\partial x_\alpha}(J_{(k)\alpha}^\theta) + W_k \dot{\omega}_k. \quad (2.129)$$

In the above equations v_α stands for a velocity vector component, which in a vector notation can be expressed as

$$\underline{v} = v_\alpha \hat{e}_\alpha = v_x \hat{e}_x + v_y \hat{e}_y. \quad (2.130)$$

Taking this into account, tensor of total stresses $\underline{\tau}^{total}$ from equation (2.84) can be expressed in index notation as $\tau_{\alpha\beta}^\theta$. It is calculated as a sum of several tensors: molecular viscous stress, Reynolds turbulent stress, diffusive stress, capillary stress etc. Similarly, q_α^θ stands for the components of total energy flux and $J_{(k)\alpha}^\theta$ symbol represents components of diffusion total flux.

The key challenge in the numerical fluid mechanics is a proper representation of equations (2.126) to (2.129). In this paper, separate solution of these equations is named as a classical thermomechanics, whereas solution based on all four equations solved at once is named as numerical fluid mechanics. This is consistent with approach popularized by Charles Hirsch [63]. He proposed the underneath notation, which groups all conservation equations into the single system

$$\frac{\partial}{\partial t} \begin{vmatrix} \rho \\ \rho \underline{v} \\ \rho e \\ \rho Y_k \end{vmatrix} + \text{div} \begin{vmatrix} \rho \underline{v} \\ \rho \underline{v} \otimes \underline{v} + p \underline{I} \\ \rho h \underline{v} \\ \rho Y_k \underline{v} \end{vmatrix} = \text{div} \begin{vmatrix} 0 \\ \underline{\tau}^\theta \\ \underline{\tau}^\theta \underline{v} + \underline{q}^\theta \\ \underline{J}_k^\theta \end{vmatrix} + \begin{vmatrix} 0 \\ \rho \underline{b} \\ \rho s_e \\ W_k \dot{\omega}_k \end{vmatrix}. \quad (2.131)$$

Equation (2.131) is valid for any coordinate system, independently if the model is one, two or three dimensional. It does have an universal structure able to support constitutive equations from a wide range, including: elastic (reversible) fluids, viscous-conductive fluids and fluids described with differential/integral equations of evolution (combustion, phase change, turbulence, etc.).

Above arrangement is complemented with equations of turbulence evolution. For the most simple case of four-equations model of combustion turbulence, equations have the form shown below

$$\frac{\partial}{\partial t} \begin{pmatrix} \rho k \\ \rho \epsilon \\ \rho f \\ \rho g \end{pmatrix} + \text{div} \begin{pmatrix} \rho k \underline{v} \\ \rho \epsilon \underline{v} \\ \rho f \underline{v} \\ \rho g \underline{v} \end{pmatrix} = \text{div} \begin{pmatrix} \underline{J}_k \\ \underline{J}_\epsilon \\ \underline{J}_f \\ \underline{J}_g \end{pmatrix} + \begin{pmatrix} s_k \\ s_\epsilon \\ s_f \\ s_g \end{pmatrix}, \quad (2.132)$$

where diffusive fluxes and sources of $k - \epsilon$ model are consistent with the basic theory. \underline{J}_f with \underline{J}_g equations are presented in equations (2.117) and (2.118).

Underneath vector of conservative variables

$$\mathcal{U} = \begin{pmatrix} \rho \\ \rho v_x \\ \rho v_y \\ \rho e \\ \rho Y_k \\ \vdots \\ \rho Y_{NC-1} \end{pmatrix}, \quad \dim(\mathcal{U}) = (NC - 1) + 4 \quad (2.133)$$

contains $NC + 3$ equations (2.126) - (2.129) which can be presented in the 2D Cartesian coordinate system in the conservative form:

$$\frac{\partial}{\partial t} \mathcal{U} + \frac{\partial}{\partial x} \mathcal{F}_x + \frac{\partial}{\partial y} \mathcal{F}_y = \frac{\partial}{\partial x} \mathcal{F}_x^\nu + \frac{\partial}{\partial y} \mathcal{F}_y^\nu + \mathcal{S}, \quad (2.134)$$

where convective fluxes $\mathcal{F}_\alpha \equiv (\mathcal{F}_x, \mathcal{F}_y)$, $\alpha = x, y$ represent divergences on the left side of equations (2.126) - (2.129).

$$\mathcal{F}_x = \begin{pmatrix} \rho v_x \\ \rho v_x v_y + p \\ \rho v_x v_y \\ \rho h v_x \\ \rho Y_{(1)} v_x \\ \vdots \\ \rho Y_{(NC-1)} v_x \end{pmatrix}, \quad \mathcal{F}_y = \begin{pmatrix} \rho v_y \\ \rho u_x v_y \\ \rho v_y v_y + p \\ \rho h v_y \\ \rho Y_{(1)} v_y \\ \vdots \\ \rho Y_{(NC-1)} v_y \end{pmatrix} \quad (2.135)$$

In the literature, symbol $\mathcal{F}_\alpha \equiv (\mathcal{F}_x, \mathcal{F}_y)$ is often presented as $\mathcal{F}_\alpha \equiv (\mathcal{F}, \mathcal{G})$, but this is not a preferable notation in this article. Taking this into account, equation (2.134) can be rewritten in the shorter form below

$$\frac{\partial}{\partial t} \mathcal{U} + \frac{\partial}{\partial \alpha} \mathcal{F}_\alpha = \frac{\partial}{\partial \alpha} \mathcal{F}_\alpha^\nu + \mathcal{S}, \quad \alpha = x, y \quad (2.136)$$

or in even more compact form

$$\frac{\partial}{\partial t} \mathcal{U} + \text{div}(\mathcal{F}^\theta) = \text{div}(\mathcal{F}^\nu) + \mathcal{S} \quad (2.137)$$

Diffusive fluxes $\mathcal{F}_\alpha^\nu = (\mathcal{F}_x^\nu, \mathcal{F}_y^\nu)$, captured in the form of divergence on the right side of equations (2.126) - (2.129) can be expressed in the detailed form

$$\mathcal{F}_x^\nu = \begin{pmatrix} 0 \\ \tau_{xx}^\theta \\ \tau_{xy}^\theta \\ \tau_{xx}^\theta v_x + \tau_{xy}^\theta v_y + q_x^\theta \\ J_{(1)x}^\theta \\ \vdots \\ J_{(NC-1)x}^t \end{pmatrix}, \quad \mathcal{F}_y^\nu = \begin{pmatrix} 0 \\ \tau_{xy}^\theta \\ \tau_{yy}^\theta \\ \tau_{xy}^\theta v_x + \tau_{yy}^\theta v_y + q_y^\theta \\ J_{(1)y}^\theta \\ \vdots \\ J_{(NC-1)y}^t \end{pmatrix}. \quad (2.138)$$

Sources $\tilde{\mathcal{S}}$ consist two elements

$$\tilde{\mathcal{S}} = \mathcal{S} + \frac{1}{y} \mathcal{S}_a = \begin{pmatrix} 0 \\ \rho b_x \\ \rho b_y \\ \rho e \\ \rho W_{(1)} \dot{\omega}_{(1)} \\ \vdots \\ \rho W_{(NC-1)} \dot{\omega}_{(NC-1)} \end{pmatrix} + \frac{1}{y} \begin{pmatrix} \rho v_y \\ \rho v_x v_y \\ \rho v_y v_y \\ \rho h v_y \\ \rho Y_{(1)} v_y \\ \vdots \\ \rho Y_{(NC-1)} v_y \end{pmatrix}, \quad (2.139)$$

where:

$$\frac{1}{y} = \begin{cases} 0 - \text{2D geometry} \\ -\frac{1}{r} - \text{axial symmetry} \end{cases} \quad (2.140)$$

Some sources denoted by \mathcal{S}_α were added to equations to be compatible with flat and axisymmetric flow (y can be simply replaced by r). It contains also a strategy to proceed in case of diffusive fluxes \mathcal{F}_α^ν , which are added do the source \mathcal{S}_α in a complex way.

The equation system (2.134) can be simplified with the assumption about so called parabolic equations of momentum, which leads to the parabolic-hyperbolic set of equations. This simplification refers to the diffusive elements acting in the direction of main stream. It can be utilized if the x component of velocity is greater than one. That leads to the simplification of equation (2.134) into the following form

$$\frac{\partial}{\partial t} \mathcal{U} + \frac{\partial}{\partial x} \mathcal{F}_x + \frac{\partial}{\partial y} \mathcal{F}_y = \frac{\partial}{\partial y} \mathcal{F}_y^{*\nu} + \mathcal{S}, \quad (2.141)$$

where $\mathcal{F}_y^{*\nu}$ denotes, that derivatives in x direction were omitted. Parabolization of equations triggers other simplifications in the procedure of solution, which can be found in the literature.

2.1.3 Discrete phase modelling

Discrete phase model (DPM) was used to predict behaviour of liquid water droplets injected with high velocity directly into the core of the flame. Application of three water spray nozzles was explicitly modelled as a part of fluid-solid interaction (FSI) model.

2.1.3.1 The Euler-Lagrange approach

Discrete phase model used in the analysis follows the Euler-Lagrange approach [28]. The fluid phase is govern by Navier-Stokes equations, while discrete phase is solved by tracking a large number of droplets using the flow field. It interacts with the fluid phase by exchange of mass, momentum and energy.

2.1.3.2 Particle motion theory

Discrete Phase Model calculates the path of a discrete phase by integrating the force balance acting on a particle. Equation 2.142 written in the Lagrangian reference frame describes balance between particle inertia and external forces acting on it.

$$m_p \frac{dv_p}{dt} = m_p \frac{\underline{v} - \underline{v}_p}{\tau_r} + m_p \frac{\underline{g}(\rho_p - \rho)}{\rho_p} + \underline{F} \quad (2.142)$$

where m_p is the particle mass, \underline{v} is the fluid phase velocity, \underline{v}_p is the particle velocity, ρ is the fluid density, ρ_p is the density of particle, \underline{F} is an additional force, $m_p \frac{\underline{v} - \underline{v}_p}{\tau_r}$ is the drag force, and τ_r is the droplet (particle) relaxation time given by equation 2.143.

$$\tau_r = \frac{\rho_p d_p^2}{18\mu} \frac{24}{C_d Re} \quad (2.143)$$

where μ stands for molecular viscosity of the fluid, C_d is a translational drag coefficient, d_p is a particle diameter and Re is the relative Reynolds number given in equation 2.144.

$$Re \equiv \frac{\rho d_p |\underline{v}_p - \underline{v}|}{\mu} \quad (2.144)$$

Particle rotation is an important component of its movement, because torque balance can change direction of motion significantly. The effect is even stronger for a large particles with significant moments of inertia. To account for that, an ordinary differential equation for particle's angular momentum is solved:

$$I_p \frac{d\omega_p}{dt} = \frac{\rho_f}{2} \left(\frac{d_p}{2} \right)^5 C_\omega |\underline{\Omega}| \underline{\Omega} = \underline{T} \quad (2.145)$$

where I_p is the moment of inertia, ω_p is the particle angular velocity, ρ_f is the fluid density, d_p is the particle diameter, C_ω is the rotational drag coefficient, \underline{T} is the torque applied to a particle in a fluid domain and $\underline{\Omega}$ is a relative particle-fluid angular velocity given by equation 2.146.

$$\underline{\Omega} = \frac{1}{2} \nabla \times \underline{v}_f - \omega_p \quad (2.146)$$

For a spherical particle, the moment of inertia I_p is calculated as below:

$$I_p = \frac{\Pi}{60} \rho_p d_p^5 \quad (2.147)$$

2.1.3.3 Laws for heat and mass exchange

Water droplets (discrete particles) injected into the hot continuous phase go through three interaction steps before completely evaporate. These are: inert heating, droplet vaporization and boiling. Inert heating phase occur before droplet temperature T_p reaches the evaporation temperature T_{vap} , which is just an arbitrary modelling constant without any physical meaning (equation 2.148).

$$T_p < T_{vap} \quad (2.148)$$

At this stage model uses a basic heat balance to relate droplet temperature $T_p(t)$ to the convective heat transfer and the absorption/emission of radiation at the droplet's surface (equation 2.149:

$$m_p c_p \frac{dT_p}{dt} = h A_p (T_\infty - T_p) + \varepsilon_p A_p \sigma (\Theta_R^4 - T_p^4) \quad (2.149)$$

where m_p is a mass of the particle (droplet) $[kg]$, c_p is heat capacity of the particle $[J/kgK]$, A_p is a surface area of the particle (droplet) $[m^2]$, T_∞ is local temperature of the continuous phase $[K]$, h is convective heat transfer coefficient $[W/m^2 K]$, ε_p is particle emissivity $[-]$, σ is Stefan-Boltzmann constant $[5.67 \times 10^{-8} W/m^2 K^4]$, Θ_R is radiation temperature $[K]$.

Second stage of discrete/continuous phase interactions is the droplet evaporation, which is initiated when droplet reaches the evaporation temperature T_{vap} and lasts until it reaches the boiling point T_{bp} , which needs to be taken from the property table.

For the high vaporization rates occurring within the combustion chamber, convection/diffusion controlled model is applied, because the convective flow of the evaporating liquid from the droplet surface is significant. For that case mass transfer was calculated as below:

$$\frac{dm_p}{dt} = -k_c A_p \rho \ln(1 + B_m) \quad (2.150)$$

where m_p is droplet mass $[kg]$, k_c is mass transfer coefficient $[m/s]$, A_p is droplet surface area $[m^2]$, ρ is gas density $[kg/m^3]$, B_m is the Spalding mass number given by equation 2.150:

$$B_m = \frac{Y_{i,s} - Y_{i,\infty}}{1 - Y_{i,s}} \quad (2.151)$$

where $Y_{i,s}$ is vapour mass fraction at the surface, $Y_{i,\infty}$ is vapour mass fraction in the bulk gas.

At the last stage, when droplet (particle) temperature reaches boiling point T_{bp} , remaining mass of droplet evaporates according to equation below:

$$T_p \geq T_{bp} \quad (2.152)$$

It this case, the boiling rate is computed by solving the equation 2.153 [28]:

$$\frac{d(d_p)}{dt} = -\frac{2k_\infty}{\rho_p c_{p,\infty} d_p} \left(2 + 0.46 Re_d^{\frac{1}{2}} \right) \ln \left[1 + \frac{c_{p,\infty} (T_\infty - T_p)}{h_{fg}} \right] \quad (2.153)$$

where $c_{p,\infty}$ is heat capacity of the gas $[J/kg K]$, ρ_p is droplet density $[kg/m^3]$, Re_d is Reynolds number of the continuous phase, k_∞ is thermal conductivity of the gas $[W/m K]$.

2.1.4 Porous Media modelling

The most common approach to model porous media is based on addition of momentum source term to the standard fluid flow equations [64]. As presented on equation 2.154, it contains a viscous loss term proposed by Darcy and an internal loss term on the right.

$$S_i = - \left(\sum_{j=1}^3 D_{ij} \mu v_j + \sum_{j=1}^3 C_{ij} \frac{1}{2} \rho |v| v_j \right) \quad (2.154)$$

where S_i is the source term for the i -th momentum equation, $|v|$ is the magnitude of the velocity and D and C are prescribed matrices. This momentum sink generates pressure drop which is proportional to the fluid velocity in a cell. Computation of forces on porous zones is a function of internal and viscous loss terms, which is shown on equation 2.154.

For the simple homogenous porous media this can be expressed as 2.155. Definition of internal and viscous resistance coefficients determines the properties of the momentum sink and forces.

$$S_i = - \left(\frac{\mu}{\alpha} v_i + C_2 \frac{1}{2} \rho |v| v_i \right) \quad (2.155)$$

where α is the permeability and C_2 is the internal resistance factor.

As an alternative, the source term could be modelled as a power law of the velocity magnitude, which is shown on equation 2.156.

$$S_i = -C_0 |v|^{C_1} = -C_0 |v|^{(C_1-1)} v_i \quad (2.156)$$

where C_0 and C_1 are empirical factors.

In the porous media laminar flow, pressure drop can be taken as proportional to velocity and the constant parameter C_2 can be omitted. By ignoring convective acceleration and diffusion, the porous media model is reduced to Darcy's law:

$$\nabla p = -\frac{\mu}{\alpha} \underline{v} \quad (2.157)$$

The pressure drop in CFD analysis is computed in all three directions within the porous region, which can be expressed with equation 2.158.

$$\begin{cases} \Delta p_x = \sum_{j=1}^3 \frac{\mu}{\alpha_{xj}} v_j \Delta n_x \\ \Delta p_y = \sum_{j=1}^3 \frac{\mu}{\alpha_{yj}} v_j \Delta n_y \\ \Delta p_z = \sum_{j=1}^3 \frac{\mu}{\alpha_{zj}} v_j \Delta n_z \end{cases} \quad (2.158)$$

where $1/\alpha_{ij}$ are the entries in the matrix in equation 2.154, v_j are the velocity components and Δn_i are the thicknesses of the medium in all three directions.

In case of high-flow velocity, the constant C_2 provides a correction for internal flow losses, so it is a loss coefficient per unit length along the flow direction.

For viscous flow, an effective viscosity μ_e is used to take into account the effect of the porous medium on the diffusion term in the momentum equations [64]:

$$\mu_e = \mu_r \mu \quad (2.159)$$

where μ is the fluid viscosity and μ_r is the relative viscosity.

For analyses assuming thermal equilibrium between fluid flow and porous medium, the conduction flux in the solid applies effective conductivity and the transient term. It includes solid thermal inertia according to the equation 2.160.

$$\frac{\partial}{\partial t} (\gamma \rho_f E_f + (1 - \gamma) \rho_s E_s) + \nabla \cdot (\underline{v} (\rho_f E_f + p)) = S_f^h + \nabla \cdot \left[k_{eff} \nabla T - \left(\sum_i h_i J_i \right) + \left(\underline{\tau} \cdot \underline{v} \right) \right] \quad (2.160)$$

where E_f is total fluid energy, E_s is total solid medium energy, ρ_f is fluid density, ρ_s is solid medium density, γ is porosity, k_{eff} is an effective thermal conductivity of the medium, S_f^h is fluid enthalpy source term.

Note, that an effective thermal conductivity K_{eff} is defined as the volume average of the fluid conductivity and the solid conductivity:

$$k_{eff} = \gamma k_f + (1 - \gamma) k_s \quad (2.161)$$

where k_f is a fluid thermal conductivity, K_s is a solid thermal conductivity.

One of the key parameter describing porous media is tortuosity, which describes the geometrical complexity of the porous medium. It is defined as a ratio between the length of the pore and the distance between its beginning and end. An efficient method of tortuosity estimation was proposed by Sobieski [65], which was focused on local velocity maxima rather than all possible streamlines flowing through the porous material.

Porous material characteristic can be obtained with fractal parameters method [66]. This novel approach enables the analysis of porous mineral cross-sections consisting of spherical elements forming a spatial system with varying porosity.

2.2 Numerical modelling – solid domain

Theory presented below assumes that solid material is a continuous medium, so it is modelled at a macroscopic level. In other words, physical properties of a given material are constant regardless of the extracted element size. On the other side, molecular physics says, that matter is made from atoms and molecules positioned at a distance from each other. As a result of that, continuous medium assumption cannot be applied at a microscopic scale. However this dissertation is focused at the macroscopic (engineering) scale, which is acceptable for such phenomena like fluid flow and strength of the combustion chamber structure. Due to the fact, that matter completely fills the space, it can be described by continuous functions and derivatives.

There are two main types of forces which can act on a continuum body: volume and surface forces (Fig. 2.9). Equation 2.162 describes the volume force as a integral through the entire solid. The typical examples of body forces are gravity and magnetic attraction. Specific body forces \underline{b} act at distance for every mass element.

$$\underline{F}_V = \int_V \rho \underline{b}(\underline{x}, t) dV + F_{sup} \quad (2.162)$$

Where:

\underline{F}_V - vector of resulting body force

ρ - density

\underline{b} - vector of body forces per unit mass (function of position and time)

\underline{x} - position vector

t - time

V - volume

F_{sup} - support force acting inside the pore, described by the equation 4.1

Equation 2.163 describes the surface (contact) forces as an integral through the entire exterior. The example of that is the weight on the table or balloon on the string.

$$\underline{F}_S = \int_{\partial V} \underline{t}(\underline{x}, t) dS \quad (2.163)$$

Where:

\underline{F}_S - vector of resulting force

∂V - closed boundary surface

\underline{t} - traction vector of surface forces (function of position and time)

\underline{x} - position vector

t - time

S - surface

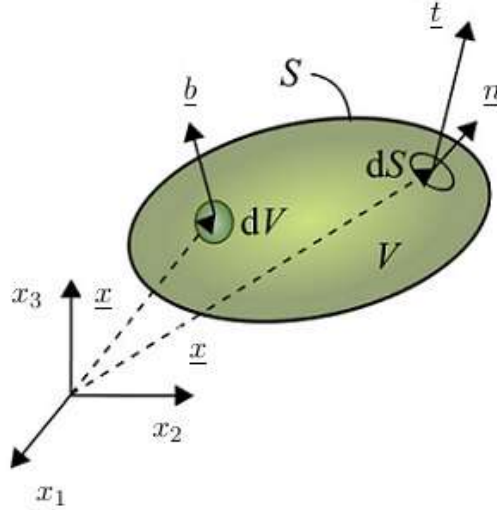


Figure 2.9: Forces acting on a continuum body [67]

The important building blocks of a stress theory are Cauchy's postulates, which are illustrated on Fig. 2.10. They extend the external force concept inside the volume by splitting it on two parts by any plane (flat or curved). Cauchy's first postulate says that the traction vector \underline{t} remains unchanged for all surfaces passing through the point P and having the same normal vector \underline{n} at point P (Eq. 2.164). Traction vector put at any internal point is not affected by the curvature of the section plane.

$$\underline{t} = \underline{t}(P, \underline{n}) \quad (2.164)$$

Cauchy's fundamental lemma says that traction vectors acting at point P on opposite sides of the same surface are equal in magnitude and opposite in the direction (Eq. 2.165). This is an equivalent of third Newton's law which says that action is equal to reaction.

$$\underline{t}(P, \underline{n}) = -\underline{t}(P, -\underline{n}) \quad (2.165)$$

To illustrate the concept of the stress, continuous body is shown on the Figure 2.11 with the point O inside. It is constructed with four surfaces. The biggest one S is positioned at a distance h from the point O and defined by the normal direction \underline{n} . Other three surfaces S_1, S_2 and S_3 are related to the S one by equation 2.166 below.

$$\begin{cases} S_1 = n_1 S \\ S_2 = n_2 S \\ S_3 = n_3 S \end{cases} \quad \text{with } \underline{n} \equiv \{n_1, n_2, n_3\}^T \quad (2.166)$$

Next step of stress tensor derivation is based on the mean value theorem explained below, which can be generalised to any dimension.

Let $f : [a, b] \rightarrow \mathbb{R}$ be a continuous function on the closed interval $[a, b]$ and differentiable

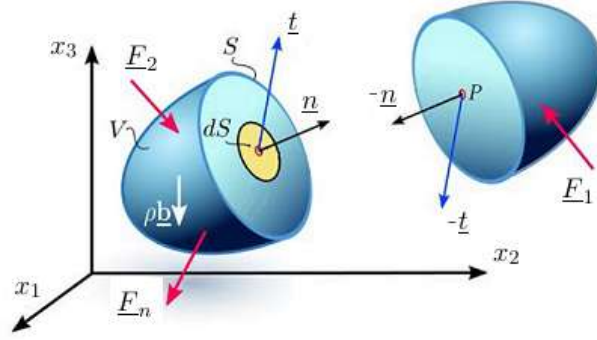


Figure 2.10: Cauchy's postulates [67]

on the open interval (a, b) , where $a < b$ (figure 2.12). Then, there exists some x^* in (a, b) such that [67]:

$$f(x^*) = \frac{1}{\Omega} \int_{\Omega} f(x) d\Omega \quad (2.167)$$

so $f : [a, b] \rightarrow \mathbb{R}$ gets its mean value $f(x^*)$ at the interior of domain Ω . In other words, value x^* is the height of the rectangle having the same area (integral) like coloured area below the curve at figure 2.12.

Mean traction vectors presented on the figure 2.11 are described by the equation 2.168. Taking into account the mean value theorem, mean vectors denoted by "*" have to be positioned within their surfaces (S_1, S_2, S_3, S), which form a closed boundary around the continuous body inside. Consistently with Cauchy's theorem, traction vector depends only on the point of the surface and normal direction.

$$\begin{cases} \underline{t}^* = \underline{t}(\underline{x}_S^*, \underline{n}) \\ -\underline{t}^{(1)*} = \underline{t}(\underline{x}_{S_1}^*, -\hat{e}_1) \\ -\underline{t}^{(2)*} = \underline{t}(\underline{x}_{S_2}^*, -\hat{e}_1) \\ -\underline{t}^{(3)*} = \underline{t}(\underline{x}_{S_3}^*, -\hat{e}_1) \\ \underline{x}_{S_i}^* \in S_i \quad i = 1, 2, 3 \end{cases} \quad (2.168)$$

The surface normal vectors of the planes and axes are

$$\begin{cases} \underline{n}_1 = -\hat{e}_1 \\ \underline{n}_2 = -\hat{e}_2 \\ \underline{n}_3 = -\hat{e}_3 \end{cases} \quad (2.169)$$

Following Cauchy's fundamental lemma:

$$\underline{t}(\underline{x}, -\hat{e}_i) = -\underline{t}(\underline{x}, \hat{e}_i) \quad i \in \{1, 2, 3\} \quad (2.170)$$

Apart from the surface forces presented on the figure 2.11, there are also body forces which act on the given continuous body.

From the second Newton's law, force \underline{f}_i is equal to mass m_i times acceleration \underline{a}_i . This is presented on the equation 2.171.

$$\underline{R} = \sum_i \underline{f}_i = \sum_i m_i \underline{a}_i \quad (2.171)$$

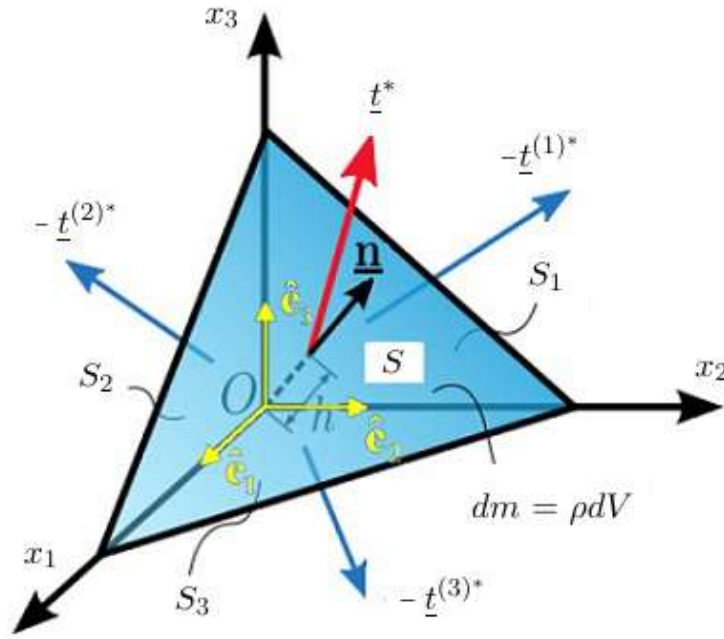


Figure 2.11: Stress tensor derivation [67]

Equations 2.172 and 2.173 are an extension of equation 2.171. They say that the total resultant force causing an acceleration \underline{a} of the continuous body mass (density ρ times volume dV) is an integral of all surface forces ($\int_{\partial V} \underline{t} dS$) and body forces ($\int_V \rho \underline{b} dV$).

$$\int_V \rho \underline{b} dV + \int_{\partial V} \underline{t} dS = \int_V \underline{a} \rho dV = \int_V \underline{a} dm = \int_V \rho \underline{a} dV \quad (2.172)$$

$$\int_V \rho \underline{b} dV + \int_S \underline{t} dS + \int_{S_1} -\underline{t}^{(1)} dS + \int_{S_2} -\underline{t}^{(2)} dS + \int_{S_3} -\underline{t}^{(3)} dS = \int_V \rho \underline{a} dV \quad (2.173)$$

Considering the mean value theorem, equation 2.173 can be transformed into equation 2.174, where symbol "*" denotes mean values.

$$(\rho \underline{b})^* V + \underline{t}^* S - \underline{t}^{(1)*} S_1 - \underline{t}^{(2)*} S_2 - \underline{t}^{(3)*} S_3 = (\rho \underline{a})^* V \quad (2.174)$$

where: S is an area of given face and V is a volume of a given solid element (figure 2.11).

Introducing $S_i = n_i S$ $i \in \{1, 2, 3\}$ (equation 2.166) and tetrahedron volume expression ($V = \frac{1}{3} S h$), equation 2.174 can be transformed to equation 2.175.

$$\frac{1}{3} (\rho \underline{b})^* h S + \underline{t}^* S - \underline{t}^{(1)*} n_1 S - \underline{t}^{(2)*} n_2 S - \underline{t}^{(3)*} n_3 S = \frac{1}{3} (\rho \underline{a})^* h S \quad (2.175)$$

In the case when tetrahedron volume (figure 2.11) shrinks to point O , ($h \rightarrow 0$) keeping same normal vectors, equations 2.176 can be written. The first part describes the transformation of mean tensor vectors $\underline{t}^{(i)*}$ at faces S_i . At the limit these tensors are positioned at point O and aligned with corresponding main axis. Second row describes surface S ,

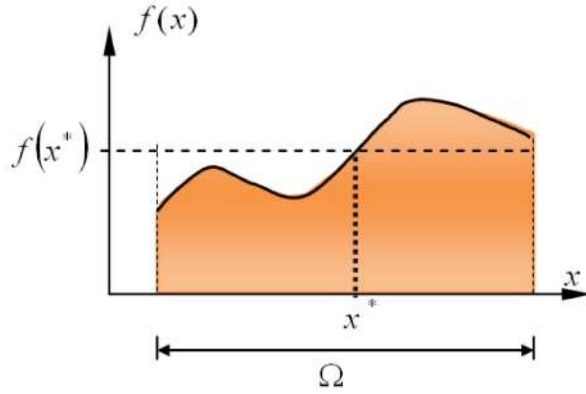


Figure 2.12: Mean value theorem [67]

which mean tensor also moves towards point O at tetrahedron height h approaches zero. Third line is about the volume - the smaller it is, the smaller volume it contains.

$$\begin{cases} \underline{x}_{S_i}^* \rightarrow \underline{x}_O \implies \lim_{h \rightarrow 0} [\underline{t}^{(i)*}(\underline{x}_{S_i}^*, \hat{e}_i)] = \underline{t}^{(i)}(O, \hat{e}_i) & i \in \{1, 2, 3\} \\ \underline{x}_S^* \rightarrow \underline{x}_O \implies \lim_{h \rightarrow 0} [\underline{t}^*(\underline{x}_S^*, \underline{n})] = \underline{t}(O, \underline{n}) \\ \lim_{h \rightarrow 0} (\frac{1}{3}(\rho \underline{b})^* h) = \lim_{h \rightarrow 0} (\frac{1}{3}(\rho \underline{a})^* h) = 0 \end{cases} \quad (2.176)$$

The limit of the expression for the equilibrium of forces becomes [67],

$$\frac{1}{3}(\rho \underline{b})^* h + \underline{t}^* - \underline{t}^{(1)*} n_1 - \underline{t}^{(2)*} n_2 - \underline{t}^{(3)*} n_3 = \frac{1}{3}(\rho \underline{a})^* h \quad (2.177)$$

Which can reduced to equation 2.178, stating that for a very small element size traction vector \underline{t} can be constructed with three adjacent traction vectors aligned with the main coordinate axis.

$$\boxed{\underline{t}(O, \underline{n}) - \underline{t}^{(i)} n_i = 0} \quad (2.178)$$

Equation 2.179 considers the traction vector's Cartesian components presented in the figure 2.13. It is consistent with the previous considerations, but the name of the centre point was changed from O to P . The other naming convention change is that traction vectors $\underline{t}_j^{(i)}$ are renamed and fitted into matrix components σ_{ij} .

$$\begin{cases} \underline{t}^{(i)}(P) = \underline{t}_j^{(i)}(P) \hat{e}_j = \sigma_{ij} \hat{e}_j & i, j \in \{1, 2, 3\} \\ \sigma_{ij}(P) = \underline{t}_j^{(i)}(P) & i, j \in \{1, 2, 3\} \end{cases} \quad (2.179)$$

Equation 2.180 is a modified equation 2.178 written in the form of components.

$$\boxed{\underline{t}(P, \underline{n}) = \underline{t}^{(i)} n_i \implies \begin{cases} \underline{t}_j(P, \underline{n}) = \underline{t}_j^{(i)} n_i = n_i \sigma_{ij} \\ \underline{t}(P, \underline{n}) = \underline{n} \cdot \underline{\sigma}(P) \end{cases}} \quad (2.180)$$

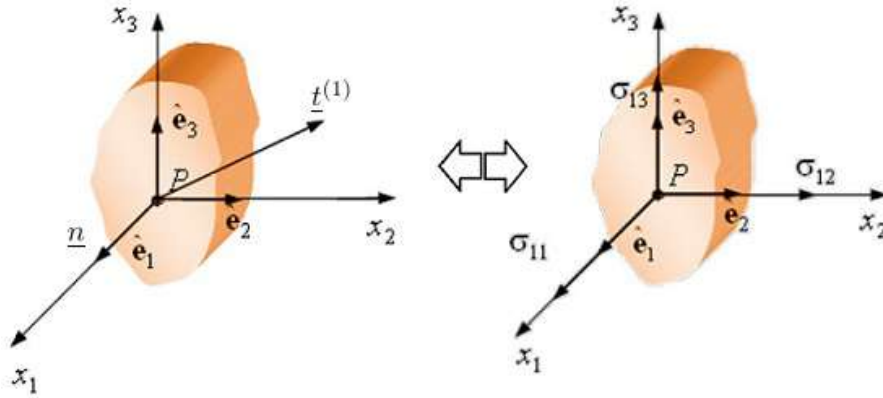


Figure 2.13: Stress tensor components [67]

Equation 2.180 includes Cauchy's Stress Tensor in the form of equation 2.181. It corresponds to the figure 2.14, where individual traction vectors are grouped at the adjacent cube faces. This is a crucial step, as stress tensor components depend only of the point, rather than point and normal direction (as tractions). Of course tensor components varies with the coordinate system change. Nevertheless, this second-order tensor as a physical entity does not change.

$$\underline{\underline{\sigma}} = \sigma_{ij} \hat{e}_i \otimes \hat{e}_j \quad (2.181)$$

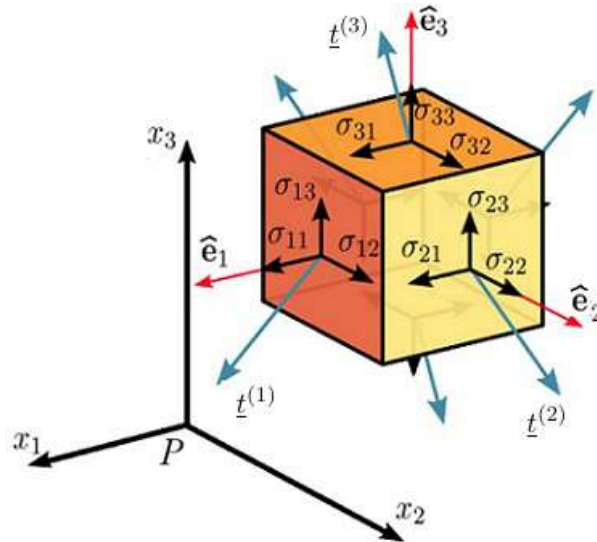


Figure 2.14: Stress tensor [67]

Equation 2.180 is a fundamental building block of the stress theory. In the index and matrix form it can be written as equations 2.182 and 2.183.

$$\begin{cases} t_j = n_j \sigma_{ij} = \sigma_{ji}^T n_i & i, j \in \{1, 2, 3\} \\ [t] = [\underline{\underline{\sigma}}]^T [n] \end{cases} \quad (2.182)$$

$$\begin{bmatrix} t_1 \\ t_2 \\ t_3 \end{bmatrix} = \begin{bmatrix} t_1^{(1)} & t_1^{(2)} & t_1^{(3)} \\ t_2^{(1)} & t_2^{(2)} & t_2^{(3)} \\ t_3^{(1)} & t_3^{(2)} & t_3^{(3)} \end{bmatrix} \begin{bmatrix} n_1 \\ n_2 \\ n_3 \end{bmatrix} = \begin{bmatrix} \sigma_{11} & \sigma_{21} & \sigma_{31} \\ \sigma_{12} & \sigma_{22} & \sigma_{32} \\ \sigma_{13} & \sigma_{23} & \sigma_{33} \end{bmatrix} \begin{bmatrix} n_1 \\ n_2 \\ n_3 \end{bmatrix} \quad (2.183)$$

The expression $\underline{t}(P, \underline{n}) = \underline{n} \cdot \underline{\sigma}(P)$ is consistent with Cauchy's postulates $\underline{t}(P, \underline{n}) = -\underline{t}(P, -\underline{n})$ according to the equation 2.184.

$$\begin{cases} \underline{t}(P, \underline{n}) = \underline{n} \cdot \underline{\sigma} \\ \underline{t}(P, -\underline{n}) = -\underline{n} \cdot \underline{\sigma} \end{cases} \quad (2.184)$$

According to the graphical representation (figure 2.15), the Cauchy stress tensor is constructed from the traction vectors on three coordinate planes passing through point P.

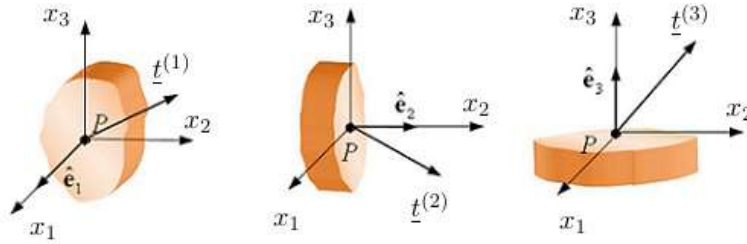


Figure 2.15: Stress tensor structure [67]

$$\underline{\underline{\sigma}} \equiv \begin{bmatrix} \sigma_{11} & \sigma_{12} & \sigma_{13} \\ \sigma_{21} & \sigma_{22} & \sigma_{23} \\ \sigma_{31} & \sigma_{32} & \sigma_{33} \end{bmatrix} \quad (2.185)$$

This tensor contains information on the traction vectors acting on any plane (identified by its normal \underline{n}) which passes through point P. Each row of it is represented as a separate graph of figure 2.15.

Each component σ_{ij} is characterised by its sub-indices:

- Index i designates the coordinate plane on which the component acts.
- Index j identifies the coordinate direction in which the component acts.

2.2.1 Model of the isotropic elasticity

Isotropic elasticity in materials occurs when its physical properties at any point are invariant to any rotation of coordinates [68]. It occurs when constituents of the material of a solid member are distributed sufficiently randomly. Additionally, material is homogenous if all its properties are invariant under a translation. Taking it into account, homogenous material at the uniform temperature is nonhomogenous at a non-uniform temperature, which affects elastic constants [69]. According to Hooke's law, in the area of elastic deformation, axial strain ε_{11} is proportional to the applied force f_{11} at the same direction (equation 2.186). Of course this is the most basic case, when isotropic string is loaded uniaxially below the yield strength of the material. Examples of strain-stress curves shown on figure 2.16 cover all stages of specimen test result. Hook's law is applicable to the initial straight part of graph, until the yield strength point (permanent plastic deformation).

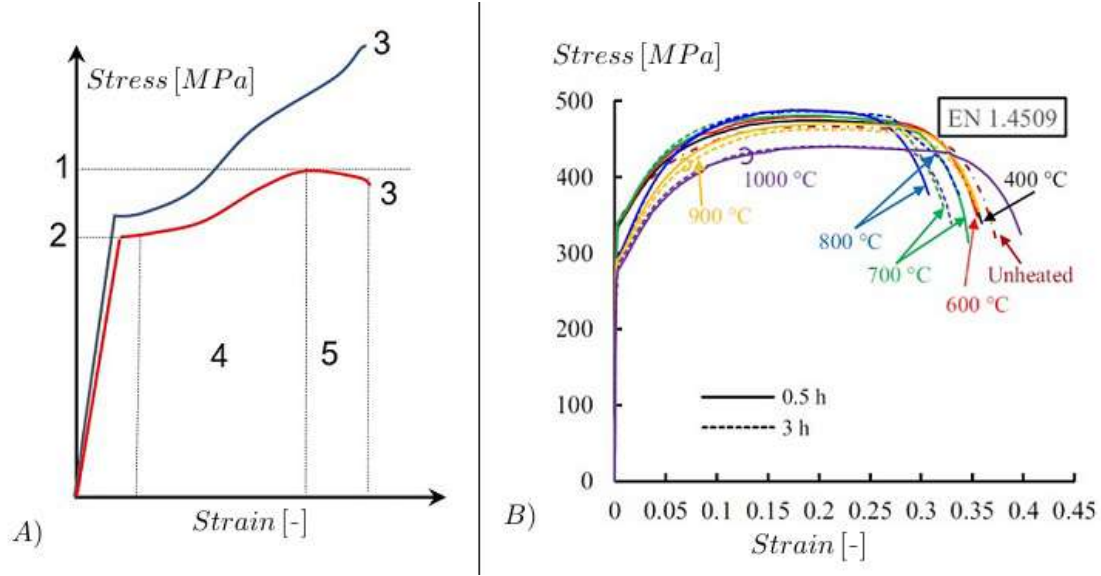


Figure 2.16: Stress-strain curve, A) general, B) actual [70]

where: 1- ultimate strength, 2- yield strength point, 3- rupture, 4-strain hardening region, 5- necking region, A- engineering stress (assuming no necking), B- actual stress (necking included).

$$f_{11} = k\varepsilon_{11} \quad (2.186)$$

Although the original Hooke's experiment was done using uniaxial load, this concept can be successfully applied to the complex 3D geometries. To obtain that, 3D generalised Hooke's law equivalent for continuous media can be written as follows:

$$\underline{\underline{\sigma}} = \underline{\underline{c}} \underline{\underline{\varepsilon}} \quad (2.187)$$

where: $\underline{\underline{\sigma}}$ is a second-order stress tensor, $\underline{\underline{\varepsilon}}$ is a second-order strain tensor, $\underline{\underline{c}}$ is a fourth-order stiffness tensor. Both second-order tensors are presented in matrix form in the equation 2.188.

$$\underline{\underline{\sigma}} = \begin{bmatrix} \sigma_{11} & \sigma_{12} & \sigma_{13} \\ \sigma_{21} & \sigma_{22} & \sigma_{23} \\ \sigma_{31} & \sigma_{32} & \sigma_{33} \end{bmatrix}; \quad \underline{\underline{\varepsilon}} = \begin{bmatrix} \varepsilon_{11} & \varepsilon_{12} & \varepsilon_{13} \\ \varepsilon_{21} & \varepsilon_{22} & \varepsilon_{23} \\ \varepsilon_{31} & \varepsilon_{32} & \varepsilon_{33} \end{bmatrix} \quad (2.188)$$

Stiffness tensor is a mapping between nine stress components σ_{ij} and nine strain components ε_{kl} , so it is represented by a matrix of $3 \times 3 \times 3 \times 3 = 81$ real numbers c_{ijkl} , which can be written in index notation as:

$$\sigma_{ij} = \sum_{k=1}^3 \sum_{l=1}^3 c_{ijkl} \varepsilon_{kl} \quad i, j, k, l \in \{1, 2, 3\} \quad (2.189)$$

Due to the fact, that isotropic materials are characterised with the uniform properties in the entire volume, physical equations are independent from the coordinate system. Since the trace of any tensor is independent of coordinate system, the most complete

coordinate-free decomposition contains the sum of a volumetric and traceless deviatoric (shear) strain tensor [71]. Equation 2.190 shows this in the index notation.

$$\varepsilon_{ij} = \left(\frac{1}{3} \varepsilon_{kk} \delta_{ij} \right) + \left(\varepsilon_{ij} - \frac{1}{3} \varepsilon_{kk} \delta_{ij} \right) \quad (2.190)$$

The generalised Hooke's law for isotropic materials can be expressed as a combination of these two tensors in a form of equation 2.191.

$$\sigma_{ij} = 3K \left(\frac{1}{3} \varepsilon_{kk} \delta_{ij} \right) + 2G \left(\varepsilon_{ij} - \frac{1}{3} \varepsilon_{kk} \delta_{ij} \right) \quad (2.191)$$

where K is a bulk modulus and G is a shear modulus.

In the matrix form, Hooke's law for isotropic materials can be written in the Voigt notation as

$$\begin{bmatrix} \varepsilon_{11} \\ \varepsilon_{22} \\ \varepsilon_{33} \\ 2\varepsilon_{23} \\ 2\varepsilon_{13} \\ 2\varepsilon_{12} \end{bmatrix} = \begin{bmatrix} \varepsilon_{11} \\ \varepsilon_{22} \\ \varepsilon_{33} \\ \gamma_{23} \\ \gamma_{13} \\ \gamma_{12} \end{bmatrix} = \frac{1}{E} \begin{bmatrix} 1 & -\nu & -\nu & 0 & 0 & 0 \\ -\nu & 1 & -\nu & 0 & 0 & 0 \\ -\nu & -\nu & 1 & 0 & 0 & 0 \\ 0 & 0 & 0 & 2+2\nu & 0 & 0 \\ 0 & 0 & 0 & 0 & 2+2\nu & 0 \\ 0 & 0 & 0 & 0 & 0 & 2+2\nu \end{bmatrix} \begin{bmatrix} \sigma_{11} \\ \sigma_{22} \\ \sigma_{33} \\ \sigma_{23} \\ \sigma_{13} \\ \sigma_{12} \end{bmatrix} \quad (2.192)$$

where $\gamma_{ij} = 2\varepsilon_{ij}$ is an engineering shear strain.

The invert relation between stress and strain can be expressed with equation 2.193.

$$\begin{bmatrix} \sigma_{11} \\ \sigma_{22} \\ \sigma_{33} \\ \sigma_{23} \\ \sigma_{13} \\ \sigma_{12} \end{bmatrix} = \frac{E}{(1+\nu)(1-2\nu)} \begin{bmatrix} 1-\nu & \nu & \nu & 0 & 0 & 0 \\ \nu & 1-\nu & \nu & 0 & 0 & 0 \\ \nu & \nu & 1-\nu & 0 & 0 & 0 \\ 0 & 0 & 0 & \frac{1-2\nu}{2} & 0 & 0 \\ 0 & 0 & 0 & 0 & \frac{1-2\nu}{2} & 0 \\ 0 & 0 & 0 & 0 & 0 & \frac{1-2\nu}{2} \end{bmatrix} \begin{bmatrix} \varepsilon_{11} \\ \varepsilon_{22} \\ \varepsilon_{33} \\ 2\varepsilon_{23} \\ 2\varepsilon_{13} \\ 2\varepsilon_{12} \end{bmatrix} \quad (2.193)$$

Alternatively, equation 2.193 can be expressed using *Lamé* constants λ and μ .

$$\begin{bmatrix} \sigma_{11} \\ \sigma_{22} \\ \sigma_{33} \\ \sigma_{23} \\ \sigma_{13} \\ \sigma_{12} \end{bmatrix} = \begin{bmatrix} 2\mu + \lambda & \lambda & \lambda & 0 & 0 & 0 \\ \lambda & 2\mu + \lambda & \lambda & 0 & 0 & 0 \\ \lambda & \lambda & 2\mu + \lambda & 0 & 0 & 0 \\ 0 & 0 & 0 & \mu & 0 & 0 \\ 0 & 0 & 0 & 0 & \mu & 0 \\ 0 & 0 & 0 & 0 & 0 & \mu \end{bmatrix} \begin{bmatrix} \varepsilon_{11} \\ \varepsilon_{22} \\ \varepsilon_{33} \\ 2\varepsilon_{23} \\ 2\varepsilon_{13} \\ 2\varepsilon_{12} \end{bmatrix} \quad (2.194)$$

In vector notation it becomes

$$\begin{bmatrix} \sigma_{11} & \sigma_{12} & \sigma_{13} \\ \sigma_{12} & \sigma_{22} & \sigma_{23} \\ \sigma_{13} & \sigma_{23} & \sigma_{33} \end{bmatrix} = 2\mu \begin{bmatrix} \varepsilon_{11} & \varepsilon_{12} & \varepsilon_{13} \\ \varepsilon_{12} & \varepsilon_{22} & \varepsilon_{23} \\ \varepsilon_{13} & \varepsilon_{23} & \varepsilon_{33} \end{bmatrix} + \lambda \underline{\underline{I}} (\varepsilon_{11} + \varepsilon_{22} + \varepsilon_{33}) \quad (2.195)$$

2.2.2 General model of the anisotropic materials

Anisotropic materials mathematical model is much more complicated than the isotropic one. In the most general case anisotropic model contains 81 factors which linearly link every combination of stress and strain components (3D generalised Hooke's law). Equation 2.196 visualises that case, which is a matrix form of equation 2.187.

$$\begin{bmatrix} \sigma_{11} & \sigma_{12} & \sigma_{13} \\ \sigma_{21} & \sigma_{22} & \sigma_{23} \\ \sigma_{31} & \sigma_{32} & \sigma_{33} \end{bmatrix} = \begin{bmatrix} c_{1111} & c_{1112} & c_{1113} & c_{1211} & c_{1212} & c_{1213} & c_{1311} & c_{1312} & c_{1313} \\ c_{1121} & c_{1122} & c_{1123} & c_{1221} & c_{1222} & c_{1223} & c_{1321} & c_{1322} & c_{1323} \\ c_{1131} & c_{1132} & c_{1133} & c_{1231} & c_{1232} & c_{1233} & c_{1331} & c_{1332} & c_{1333} \\ c_{2111} & c_{2112} & c_{2113} & c_{2211} & c_{2212} & c_{2213} & c_{2311} & c_{2312} & c_{2313} \\ c_{2121} & c_{2122} & c_{2123} & c_{2221} & c_{2222} & c_{2223} & c_{2321} & c_{2322} & c_{2323} \\ c_{2131} & c_{2132} & c_{2133} & c_{2231} & c_{2232} & c_{2233} & c_{2331} & c_{2332} & c_{2333} \\ c_{3111} & c_{3112} & c_{3113} & c_{3211} & c_{3212} & c_{3213} & c_{3311} & c_{3312} & c_{3313} \\ c_{3121} & c_{3122} & c_{3123} & c_{3221} & c_{3222} & c_{3223} & c_{3321} & c_{3322} & c_{3323} \\ c_{3131} & c_{3132} & c_{3133} & c_{3231} & c_{3232} & c_{3233} & c_{3331} & c_{3332} & c_{3333} \end{bmatrix} \begin{bmatrix} \varepsilon_{11} & \varepsilon_{12} & \varepsilon_{13} \\ \varepsilon_{21} & \varepsilon_{22} & \varepsilon_{23} \\ \varepsilon_{31} & \varepsilon_{32} & \varepsilon_{33} \end{bmatrix} \quad (2.196)$$

Taking into account that stress ($\underline{\underline{\sigma}}$) and strain ($\underline{\underline{\varepsilon}}$) tensors are symmetric, only 21 c_{ijkl} coefficients are unique. This can be presented in the compact form using Voigt notation below

$$\begin{bmatrix} \sigma_{11} \\ \sigma_{22} \\ \sigma_{33} \\ \sigma_{12} \\ \sigma_{13} \\ \sigma_{23} \end{bmatrix} = \begin{bmatrix} C_{11} & C_{12} & C_{13} & C_{14} & C_{15} & C_{16} \\ C_{21} & C_{22} & C_{23} & C_{24} & C_{25} & C_{26} \\ C_{31} & C_{32} & C_{33} & C_{34} & C_{35} & C_{36} \\ C_{41} & C_{42} & C_{43} & C_{44} & C_{45} & C_{46} \\ C_{51} & C_{52} & C_{53} & C_{54} & C_{55} & C_{56} \\ C_{61} & C_{62} & C_{63} & C_{64} & C_{65} & C_{66} \end{bmatrix} \begin{bmatrix} \varepsilon_{11} \\ \varepsilon_{22} \\ \varepsilon_{33} \\ \varepsilon_{12} \\ \varepsilon_{13} \\ \varepsilon_{23} \end{bmatrix} \quad (2.197)$$

or in the index notation as

$$\sigma_i = C_{ij} \varepsilon_j \quad (2.198)$$

2.2.3 Classical laminate theory

Classical laminated-plate theory (CLT) was developed in 1960's mainly for military purposes [72]. It is much more complex than the mechanics of isotropic materials, but basic elements of it are similar, including plane stress, plane strain and generalised 3D anisotropic elasticity. Shells and plates are characterised by the specific shape, where one dimension is much smaller than other two. CLT describes the behaviour of plates from two perspectives. The first one (elastic response) is the prediction of deformation, which occurs under the certain load state. The second one tries to answer the question about the failure load and character. From the elastic constants point of view, isotropic materials can be described by just two independent numbers: Young Modulus E and Poisson Ratio ν . These values can be taken from the specimen test results equipped in strain gauges. For fully anisotropic materials this is much more complex, because as many as 21 elastic constants has to be figured out to fully describe such body. To reduce such a difficult multidimensional problem, following chapters are focused on the orthoptic assumption, which reduces number of unknown elastic constants to four: E_{11} (stiffness in 11 direction), E_{22} (stiffness in 22 direction), G_{12} (Shear Modulus in 12 direction) and ν_{12} (Poisson's Ratio in 12 direction). In terms of failure mechanisms, composites are

even more complicated than the isotropic metals. The most common structure contains a bunch of fibers embedded in the matrix material (Figure 1.3). Such a structure exhibits multiple failure modes such as matrix yielding, matrix cracking, delamination (in case of multiple orthotropic layers), fiber cracking and fiber/matrix interface failure. All of these modes interact with each other uniquely under certain load state. That makes it very difficult to predict when given failure occurs and in which mode. Figure 2.17 presents the most common composites failure modes on the logarithmic scale. At the lowest scale (micron level), the constituent is a single fiber, which itself is made from the isotropic material. Due to the restraints in the manufacturing process, it can contain scratches or cracks at the external surface or inside. Further up on the scale, there is a single ply matrix cracking. Initially, (under the certain load) it appears in the matrix between the fibers and propagates along the weakest path until the ply boundary. At this point it is extremely difficult to continue the growth inside the adjacent ply positioned at the different angle. This is the point when a crack stops or redirects between plies if the applied load is large enough. Severe delamination state is shown on the third picture. The last photo contains the failure occurred at the centimetre level, where wrinkling failure appeared as a result of a compression test.

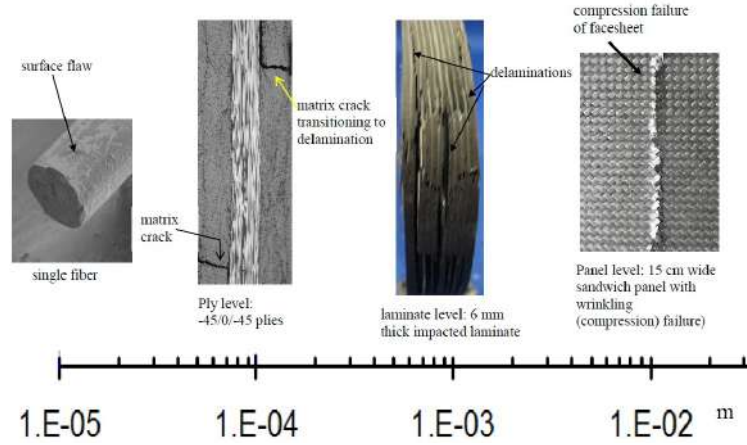


Figure 2.17: Failure in composites [72]

From the analysis point of view, it is important to understand assumptions and simplifications of the applied method. In the general case it is impossible to model directly given material in a perfect way including its structure at the molecular level with all the random anomalies inside. Instead, a row of assumptions has to be made in order to simplify the problem at the practical level. In the presented case, the basic building block of the method is a composite layer (ply), which makes it impossible to directly model physical phenomena at the more-detailed level. The key simplification assumption is that analysed laminate is an orthotropic material, which has two planes of symmetry. Figure 2.18 visualises the difference between assumption and reality. During the manufacturing process fibers are always randomly distributed within a ply, which is never a perfect symmetry. Nevertheless, this level of inconsistency is acceptable to manage the complexity of the problem.

Figure 2.19 presents the stack of plies of different orientations [72]. It is characterised by three main directions x_1 , x_2 , x_3 , two normal forces N_{11} , N_{22} and three moments M_{11} , M_{22} , M_{12} which leads to the deformation. According to the assumptions made for single ply, forces and moments in x_3 direction are assumed to be negligible. The question to

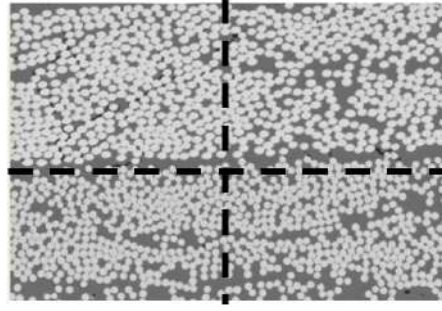


Figure 2.18: Orthotropic assumption [72]

answer is about the properties of the entire stack by knowing properties of a single ply.

Equation 2.199 presents the constitutive relations between six stresses and strains. For a single orthotropic ply, several stiffness parameters E become conveniently zero. The 3×3 portion at the left upper corner describes dependency between normal stresses and strains, whereas diagonal portion links shear stresses with strains.

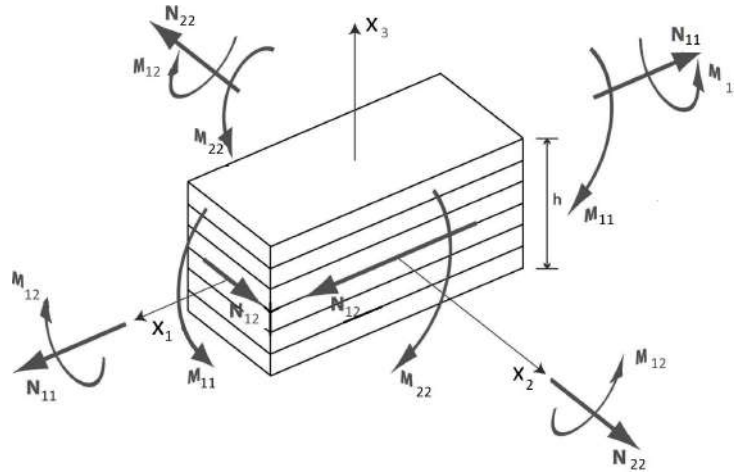


Figure 2.19: Laminae (stack plies) structure (positive sign convention) [72]

Constitutive relations for a single ply are shown in the equation 2.199.

$$\begin{bmatrix} \sigma_{11} \\ \sigma_{22} \\ \sigma_{33} \\ \sigma_{23} \\ \sigma_{13} \\ \sigma_{12} \end{bmatrix} = \begin{bmatrix} E_{11} & E_{12} & E_{13} & 0 & 0 & 0 \\ E_{21} & E_{22} & E_{23} & 0 & 0 & 0 \\ E_{31} & E_{32} & E_{33} & 0 & 0 & 0 \\ 0 & 0 & 0 & E_{44} & 0 & 0 \\ 0 & 0 & 0 & 0 & E_{55} & 0 \\ 0 & 0 & 0 & 0 & 0 & E_{66} \end{bmatrix} \begin{bmatrix} \varepsilon_{11} \\ \varepsilon_{22} \\ \varepsilon_{33} \\ \varepsilon_{23} \\ \varepsilon_{13} \\ \varepsilon_{12} \end{bmatrix} \quad (2.199)$$

Very important assumption behind the single ply modelling is that stresses and strains across the thickness are equal zero. If laminate is thin enough, equation 2.199 could be reduced to the form represented by equations 2.200, which determines ply stresses in terms of strains.

$$\begin{cases} \sigma_{11} = \left(E_{11} - \frac{E_{13}^2}{E_{33}}\right) \varepsilon_{11} + \left(E_{12} - \frac{E_{13}E_{23}}{E_{33}}\right) \varepsilon_{22} = Q_{11}\varepsilon_{11} + Q_{12}\varepsilon_{22} \\ \sigma_{22} = \left(E_{12} - \frac{E_{13}E_{23}}{E_{33}}\right) \varepsilon_{11} + \left(E_{22} - \frac{E_{23}^2}{E_{33}}\right) \varepsilon_{22} = Q_{12}\varepsilon_{11} + Q_{22}\varepsilon_{22} \\ \sigma_{12} = E_{66}\varepsilon_{12} \end{cases} \quad (2.200)$$

In a matrix form, equations 2.200 can be expressed as equation 2.201.

$$\begin{bmatrix} \sigma_{11} \\ \sigma_{22} \\ \sigma_{12} \end{bmatrix} = \begin{bmatrix} Q_{11} & Q_{12} & 0 \\ Q_{21} & Q_{22} & 0 \\ 0 & 0 & Q_{66} \end{bmatrix} \begin{bmatrix} \varepsilon_{11} \\ \varepsilon_{22} \\ \varepsilon_{12} \end{bmatrix} \quad (2.201)$$

Elastic constants can be obtained from the tests presented on figure 2.20. Test A) loads specimen along the fibers direction, so the relation between stress and strain is named as E_L and Poisson's ratio is ν_{LT} . Case B) is similar to case A) but load is applied in a transverse direction with respect to fibers, so stiffness factor is named E_T and Poisson's ratio is ν_{TL} . Case C) shows complicated shear stress test which result links shear stress and strain with constant parameter G_{LT} . Note, that ν_{LT} and ν_{TL} are dependent values according to the expression $\nu_{LT}E_T = \nu_{TL}E_L$.

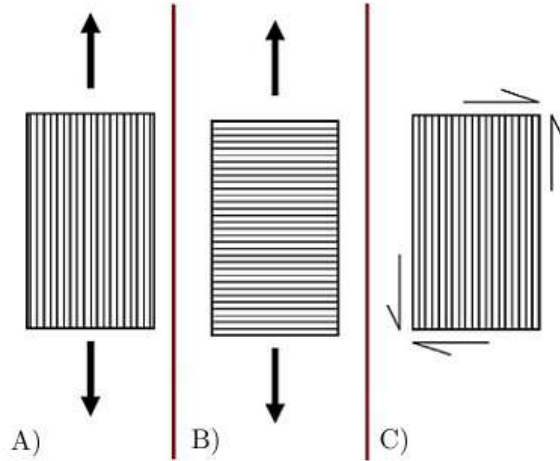


Figure 2.20: Single ply tests A) longitudinal, B) transverse, C) shear [72]

Equations 2.202 show how to calculate the stiffness quantities Q based on the test results.

Equation 2.203 shows the coordinate systems transformation presented on figure 2.21. In the case when coordinate system is not aligned with the fiber direction, it is very convenient to realign in by the rotation by angle θ .

$$\begin{cases} Q_{11} = \frac{E_L}{1-\nu_{LT}\nu_{TL}} \\ Q_{22} = \frac{E_T}{1-\nu_{LT}\nu_{TL}} \\ Q_{12} = \frac{\nu_{TL}E_L}{1-\nu_{LT}\nu_{TL}} \\ Q_{66} = G_{LT} \end{cases} \quad (2.202)$$

$$\begin{bmatrix} \sigma'_{11} \\ \sigma'_{22} \\ \sigma'_{12} \end{bmatrix} = \begin{bmatrix} \cos^2\theta & \sin^2\theta & 2\sin\theta\cos\theta \\ \sin^2\theta & \cos^2\theta & -2\sin\theta\cos\theta \\ -\sin\theta\cos\theta & \sin\theta\cos\theta & (\cos^2\theta - \sin^2\theta) \end{bmatrix} \begin{bmatrix} \sigma_{11} \\ \sigma_{22} \\ \sigma_{12} \end{bmatrix} \quad (2.203)$$

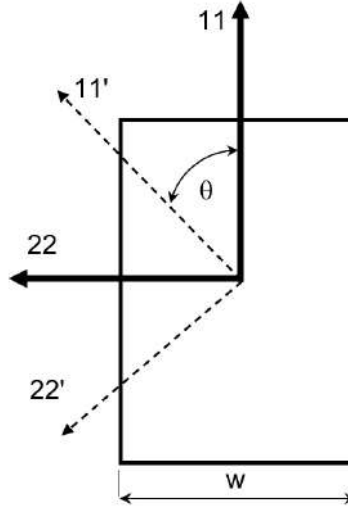


Figure 2.21: Coordinate system rotation

Stiffness transformation matrix is presented on equation 2.204 where every rotated component Q' is a function of initial value Q .

$$\begin{bmatrix} Q_{11}' \\ Q_{22}' \\ Q_{12}' \\ Q_{66}' \\ Q_{16}' \\ Q_{26}' \end{bmatrix} = \begin{bmatrix} m^4 & n^4 & 2m^2n^2 & 4m^2n^2 & 0 & 0 \\ n^4 & m^4 & 2m^2n^2 & 4m^2n^2 & 0 & 0 \\ m^2n^2 & m^2n^2 & m^4 + n^4 & -4m^2n^2 & 0 & 0 \\ m^2n^2 & m^2n^2 & -2m^2n^2 & (m^2 - n^2)^2 & 0 & 0 \\ m^3n & -mn^3 & mn^3 - m^3n & 2(mn^3 - m^3n) & 0 & 0 \\ mn^3 & -m^3n & m^3n - mn^3 & 2(m^3n - mn^3) & 0 & 0 \end{bmatrix} \begin{bmatrix} Q_{11} \\ Q_{22} \\ Q_{12} \\ Q_{66} \\ Q_{16} \\ Q_{26} \end{bmatrix} \quad (2.204)$$

where: $m = \cos\theta$ and $n = \sin\theta$.

In the case when coordinate system is not aligned with the fibers in a ply, Q_{16} and Q_{26} are non-zero (equation 2.205). This is also visualized on the figure 2.22, where none of the axes (11 and 22) is aligned with the fiber direction.

$$\begin{bmatrix} \sigma_{11} \\ \sigma_{22} \\ \sigma_{12} \end{bmatrix} = \begin{bmatrix} Q_{11} & Q_{12} & Q_{16} \\ Q_{21} & Q_{22} & Q_{26} \\ Q_{16} & Q_{26} & Q_{66} \end{bmatrix} \begin{bmatrix} \varepsilon_{11} \\ \varepsilon_{22} \\ \varepsilon_{12} \end{bmatrix} \quad (2.205)$$

In most cases a single ply is just the basic building block of the laminate made of multiple plies (figure 2.23). As a result of that, few key questions need to be answered regarding the transformation method from the single to multiple layers. Equations 2.206 contain a set of assumptions, which link single ply with the laminate. It refers to the laminate equivalent stiffness $(EA)_{lam}$ as the sum of the individual values of plies $(EA)_{ply\ i}$. On the other hand, individual stiffness of each ply $(EA)_{ply\ i}$ is rewritten in the laminate convention, where Q is just another name of E , t is a individual ply thickness and w is the laminate (ply) width.

$$\begin{cases} (EA)_{ply\ i} = (Q_{ij})_{ply\ i} A_{ply\ i} = (Q_{ij})_{ply\ i} t^{(i)} w \\ (EA)_{lam} = \sum_{i=1}^n (EA)_{ply\ i} \end{cases} \quad (2.206)$$

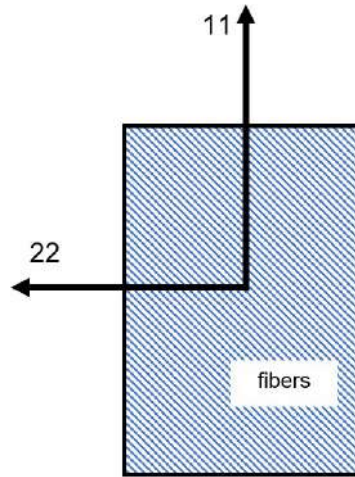


Figure 2.22: 2D stresses for non-aligned coordinate system to fibers

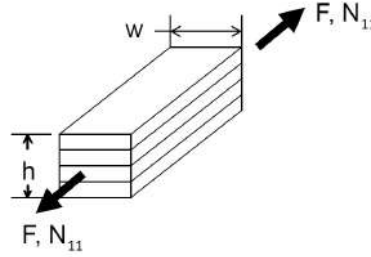


Figure 2.23: Uniaxial tension case [72]

where: $t^{(i)}$ and w is the ply thickness and width respectively.

Equations 2.207 define stress resultants which are the forces and moments divided by the unit of width. All of them are presented graphically on the figure 2.19 with the positive sign convention. This is a convenient approach, because is independent from the laminate width and takes into account stress variation through the entire laminate height.

$$\left\{ \begin{array}{l} N_{11} = \int_{-\frac{h}{2}}^{\frac{h}{2}} \sigma_{11} dx_3 \\ N_{22} = \int_{-\frac{h}{2}}^{\frac{h}{2}} \sigma_{22} dx_3 \\ N_{12} = \int_{-\frac{h}{2}}^{\frac{h}{2}} \sigma_{12} dx_3 \\ M_{11} = \int_{-\frac{h}{2}}^{\frac{h}{2}} \sigma_{11} x_3 dx_3 \\ M_{22} = \int_{-\frac{h}{2}}^{\frac{h}{2}} \sigma_{22} x_3 dx_3 \\ M_{12} = \int_{-\frac{h}{2}}^{\frac{h}{2}} \sigma_{12} x_3 dx_3 \end{array} \right. \quad (2.207)$$

Equations 2.208 describe an example of a specific case of uniaxial tension, where σ_o is an average applied stress. The purpose of them is to visualize the application of forces and moments per unit width.

$$\begin{cases} \sigma_o = \frac{F}{wh} \\ \sigma_o = \frac{1}{h} \int_{-\frac{h}{2}}^{\frac{h}{2}} \sigma_{11} dx_3 \\ \sigma_o = \frac{N_{11}}{h} \end{cases} \quad (2.208)$$

In the case of membrane (in-plane) behaviour, it is assumed that no bending load (symmetric layup) is applied and mid-plane loads ε_{11o} , ε_{22o} and ε_{12o} are applicable through the entire thickness. As an example, the integration of σ_{11} from equation 2.205 will result with equation 2.209.

$$\int_{-\frac{h}{2}}^{\frac{h}{2}} \sigma_{11} dx_3 = \int_{-\frac{h}{2}}^{\frac{h}{2}} Q_{11} \varepsilon_{11o} dx_3 + \int_{-\frac{h}{2}}^{\frac{h}{2}} Q_{12} \varepsilon_{22o} dx_3 + \int_{-\frac{h}{2}}^{\frac{h}{2}} Q_{16} \varepsilon_{12o} dx_3 \quad (2.209)$$

Taking into account the definition of N_x from equation 2.207, the integral 2.209 transforms into equation 2.210.

$$\begin{aligned} N_{11} &= \left[\int_{-\frac{h}{2}}^{\frac{h}{2}} Q_{11} dx_3 \right] \varepsilon_{11o} + \left[\int_{-\frac{h}{2}}^{\frac{h}{2}} Q_{12} dx_3 \right] \varepsilon_{22o} + \left[\int_{-\frac{h}{2}}^{\frac{h}{2}} Q_{16} dx_3 \right] \varepsilon_{12o} = \\ &= A_{11} \varepsilon_{11o} + A_{12} \varepsilon_{22o} + A_{16} \varepsilon_{12o} \end{aligned} \quad (2.210)$$

Similar transformation can be done for the rest of equation 2.205, which will change to the form below.

$$\begin{bmatrix} N_{11} \\ N_{22} \\ N_{12} \end{bmatrix} = \begin{bmatrix} A_{11} & A_{12} & A_{16} \\ A_{21} & A_{22} & A_{26} \\ A_{16} & A_{26} & A_{66} \end{bmatrix} \begin{bmatrix} \varepsilon_{11} \\ \varepsilon_{22} \\ \varepsilon_{12} \end{bmatrix} \quad (2.211)$$

where A_{ij} is given as

$$A_{ij} = \int_{-\frac{h}{2}}^{\frac{h}{2}} Q_{ij} dx_3 \quad (2.212)$$

Due to the fact, that Q_{ij} is constant within each ply, equation 2.212 can be written in a form of a summation 2.213, where $(z_k - z_{k-1})$ is the thickness of k^{th} ply.

$$A_{ij} = \sum_{k=1}^N (Q_{ij})^{(k)} (z_k - z_{k-1}) \quad (2.213)$$

In the general case, out-of-plane laminate behaviour contains bending and stretching (compressing). To model that, it is required to model strains variations through the ply thickness. For simplicity, further considerations assume linear strains distribution (equation 2.214), where κ_{11} , κ_{22} and κ_{12} , are laminate curvatures.

$$\begin{cases} \varepsilon_{11} = \varepsilon_{11o} - \frac{\partial^2 w}{\partial x_1^2} x_3 = \varepsilon_{11o} + z \kappa_{11} \\ \varepsilon_{22} = \varepsilon_{22o} - \frac{\partial^2 w}{\partial x_2^2} x_3 = \varepsilon_{22o} + z \kappa_{22} \\ \varepsilon_{12} = \varepsilon_{12o} - 2 \frac{\partial^2 w}{\partial x_1 \partial x_2} x_3 = \varepsilon_{12o} + z \kappa_{12} \end{cases} \quad (2.214)$$

In the case of pure bending, strains in the mid-plane are equal to zero ($\varepsilon_{11o} = \varepsilon_{22o} = \varepsilon_{12o} = 0$). Equation 2.205 is still valid, but strain needs to be replaced with its linear dependence. The integration of first equation through the thickness after the multiplication by x_3 gives equation 2.215.

$$\int_{-\frac{h}{2}}^{\frac{h}{2}} x_3 \sigma_{11} dx_3 = \int_{-\frac{h}{2}}^{\frac{h}{2}} Q_{11} x_3 \left(-x_3 \frac{\partial^2 w}{\partial x_1^2} \right) dx_3 \quad (2.215)$$

Using the definition of M_x given in equation 2.216

$$M_{11} = - \int_{-\frac{h}{2}}^{\frac{h}{2}} Q_{11} x_3^2 \frac{\partial^2 w}{\partial x_1^2} dx_3 - \int_{-\frac{h}{2}}^{\frac{h}{2}} Q_{12} x_3^2 \frac{\partial^2 w}{\partial x_2^2} dx_3 - \int_{-\frac{h}{2}}^{\frac{h}{2}} 2Q_{16} x_3^2 \frac{\partial^2 w}{\partial x_1 \partial x_2} dx_3 \quad (2.216)$$

Pure bending moment can be described by equation 2.217. It takes into account that curvatures like $-\frac{\partial^2 w}{\partial x^2}$ are constant and can be taken before the integral sign.

$$M_{11} = \kappa_{11} \int_{-\frac{h}{2}}^{\frac{h}{2}} Q_{11} x_3^2 dx_3 + \kappa_{22} \int_{-\frac{h}{2}}^{\frac{h}{2}} Q_{12} x_3^2 dx_3 + \kappa_{12} \int_{-\frac{h}{2}}^{\frac{h}{2}} Q_{16} x_3^2 dx_3 \quad (2.217)$$

or, since Q_{ij} is constant for each ply, equation 2.217 turns into equation 2.218.

$$\begin{aligned} M_{11} = \kappa_{11} \sum_{k=1}^N (Q_{11})^{(k)} \frac{(x_{3(k)})^3 - (x_{3(k-1)})^3}{3} + \kappa_{22} \sum_{k=1}^N (Q_{12})^{(k)} \frac{(x_{3(k)})^3 - (x_{3(k-1)})^3}{3} + \\ + \kappa_{12} \sum_{k=1}^N (Q_{16})^{(k)} \frac{(x_{3(k)})^3 - (x_{3(k-1)})^3}{3} = \kappa_x D_{11} + \kappa_{22} D_{12} + \kappa_{12} D_{16} \end{aligned} \quad (2.218)$$

By repeating steps from equation 2.218 for remaining two equations from 2.205, general matrix form below can be written.

$$\begin{bmatrix} M_{11} \\ M_{22} \\ M_{12} \end{bmatrix} = \begin{bmatrix} D_{11} & D_{12} & D_{16} \\ D_{21} & D_{22} & D_{26} \\ D_{16} & D_{26} & D_{66} \end{bmatrix} \begin{bmatrix} \kappa_{11} \\ \kappa_{22} \\ \kappa_{12} \end{bmatrix} \quad (2.219)$$

Bending with stretching case is also possible to occur with the composites, as in-plane loads can interact with bending and torsional moments. Implementing equation 2.214 into 2.205 results with formula below.

$$\sigma_{11} = Q_{11}(\varepsilon_{11o} + x_3 \kappa_{11}) + Q_{12}(\varepsilon_{22o} + x_3 \kappa_{22}) + Q_{16}(\varepsilon_{12o} + x_3 \kappa_{12}) \quad (2.220)$$

By integrating it with respect to x_3 and application of equation 2.207 the underneath form can be obtained.

$$N_{11} = A_{11} \varepsilon_{11o} + \int_{-\frac{h}{2}}^{\frac{h}{2}} Q_{11} x_3 dx_3 \kappa_{11} + A_{12} \varepsilon_{22o} + \int_{-\frac{h}{2}}^{\frac{h}{2}} Q_{12} x_3 dx_3 \kappa_{22} + A_{16} \varepsilon_{12o} + A_{12} \varepsilon_{22o} + \int_{-\frac{h}{2}}^{\frac{h}{2}} Q_{16} x_3 dx_3 \kappa_{12} \quad (2.221)$$

Taking into account, that the thickness of each ply is known and constant, equation 2.221 can be turned into 2.222 (B matrix).

$$\begin{aligned}
N_{11} &= A_{11}\varepsilon_{11o} + A_{12}\varepsilon_{22o} + A_{16}\varepsilon_{12o} + \kappa_{11} \sum_{k=1}^N Q_{11}^{(k)} \left[\frac{(x_3)^2 - (x_{k-1})^2}{2} \right] + \\
&+ \kappa_{22} \sum_{k=1}^N Q_{12}^{(k)} \left[\frac{(x_3)^2 - (x_{k-1})^2}{2} \right] + \kappa_{12} \sum_{k=1}^N Q_{16}^{(k)} \left[\frac{(x_3)^2 - (x_{k-1})^2}{2} \right] = \\
&= \kappa_{11}B_{11} + \kappa_{22}B_{12} + \kappa_{12}B_{16}
\end{aligned} \tag{2.222}$$

The general form of relating forces/moments with mid-plane strains/curvatures is shown in equations 2.223. Part *A* is for the in-plane case, part *D* is for pure bending and part *B* describes complex interactions between bending/twisting moments with stretching ([72]). Note that for symmetric laminates matrix *B* is zero and for balanced laminates $A_{16} = A_{26} = 0$.

$$\begin{bmatrix} N_{11} \\ N_{22} \\ N_{12} \\ M_{11} \\ M_{22} \\ M_{12} \end{bmatrix} = \begin{bmatrix} A_{11} & A_{12} & A_{16} & B_{11} & B_{12} & B_{16} \\ A_{12} & A_{22} & A_{26} & B_{12} & B_{22} & B_{26} \\ A_{16} & A_{26} & A_{66} & B_{16} & B_{26} & B_{66} \\ B_{11} & B_{12} & B_{16} & D_{11} & D_{12} & D_{16} \\ B_{12} & B_{22} & B_{26} & D_{12} & D_{22} & D_{26} \\ B_{16} & B_{26} & B_{66} & D_{16} & D_{26} & D_{66} \end{bmatrix} \begin{bmatrix} \varepsilon_{11o} \\ \varepsilon_{22o} \\ \varepsilon_{12o} \\ \kappa_{11} \\ \kappa_{22} \\ \kappa_{12} \end{bmatrix} \tag{2.223}$$

Inverted stress-strain relations are much more convenient, because most often specimen test programmes apply load, so strains and curvatures need to be calculated. Matrix 2.224 is an inverted version of 2.223.

$$\begin{bmatrix} \varepsilon_{11o} \\ \varepsilon_{22o} \\ \varepsilon_{12o} \\ \kappa_{11} \\ \kappa_{22} \\ \kappa_{12} \end{bmatrix} = \begin{bmatrix} \alpha_{11} & \alpha_{12} & \alpha_{16} & \beta_{11} & \beta_{12} & \beta_{16} \\ \alpha_{12} & \alpha_{22} & \alpha_{26} & \beta_{12} & \beta_{22} & \beta_{26} \\ \alpha_{16} & \alpha_{26} & \alpha_{66} & \beta_{16} & \beta_{26} & \beta_{66} \\ \beta_{11} & \beta_{12} & \beta_{16} & \delta_{11} & \delta_{12} & \delta_{16} \\ \beta_{12} & \beta_{22} & \beta_{26} & \delta_{12} & \delta_{22} & \delta_{26} \\ \beta_{16} & \beta_{26} & \beta_{66} & \delta_{16} & \delta_{26} & \delta_{66} \end{bmatrix} \begin{bmatrix} N_{11} \\ N_{22} \\ N_{12} \\ M_{11} \\ M_{22} \\ M_{12} \end{bmatrix} \tag{2.224}$$

where:

$$[\alpha] = [A]^{-1} + [A]^{-1}[B] \left[[D] - [B][A]^{-1}[B] \right]^{-1} [B][A]^{-1}$$

$$[\beta] = -[A][B] \left[[D] - [B][A]^{-1}[B] \right]^{-1}$$

$$[\delta] = \left[[D] - [B][A]^{-1}[B] \right]^{-1}$$

For a symmetric laminate, inverted relations are less complex than for the non-symmetric case (matrix 2.224). Note, that α was replaced by a and δ was replaced by d .

$$\begin{bmatrix} \varepsilon_{11o} \\ \varepsilon_{22o} \\ \varepsilon_{12o} \\ \kappa_{11} \\ \kappa_{22} \\ \kappa_{12} \end{bmatrix} = \begin{bmatrix} a_{11} & a_{12} & a_{16} & 0 & 0 & 0 \\ a_{12} & a_{22} & a_{26} & 0 & 0 & 0 \\ a_{16} & a_{26} & a_{66} & 0 & 0 & 0 \\ 0 & 0 & 0 & d_{11} & d_{12} & d_{16} \\ 0 & 0 & 0 & d_{12} & d_{22} & d_{26} \\ 0 & 0 & 0 & d_{16} & d_{26} & d_{66} \end{bmatrix} \begin{bmatrix} N_{11} \\ N_{22} \\ N_{12} \\ M_{11} \\ M_{22} \\ M_{12} \end{bmatrix} \tag{2.225}$$

Elastic constants for a symmetric laminate shown on figure 2.23 are Young Modulus E (figure 2.24) and Poisson's ratio ν . However mid-plane strain ε_{11o} is not necessary equal to the one measured by the strain gauge at the surface.

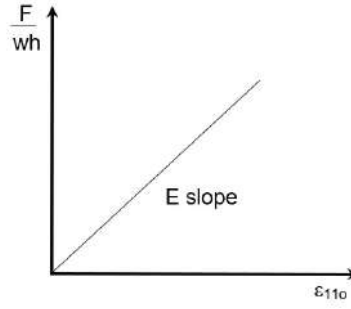


Figure 2.24: Laminate Young Modulus definition

For a symmetric laminate under uniaxial tension ($N_{22} = N_{12} = 0$) equation 2.223 is reduced to the form below.

$$\begin{cases} N_{11} = A_{11}\varepsilon_{11o} + A_{12}\varepsilon_{22o} \\ 0 = A_{12}\varepsilon_{11o} + A_{22}\varepsilon_{22o} \end{cases} \quad (2.226)$$

Which can be turned into the N_{11} formula below.

$$N_{11} = \left(A_{11} - \frac{A_{12}^2}{A_{22}} \right) \varepsilon_{11o} \quad (2.227)$$

Taking into account relationship between N_x and σ_o , mean mid-plane strain can be calculated according to equation 2.228.

$$\sigma_o = \frac{F}{wh} = \frac{1}{h} \left[\frac{A_{11}A_{22} - A_{12}^2}{A_{22}} \right] \varepsilon_{11o} \quad (2.228)$$

By applying formula for inverted a matrix,

$$a_{11} = \frac{A_{22}}{A_{11}A_{22} - A_{12}^2} \quad (2.229)$$

equation 2.230 can be obtained and transformed into equation 2.231.

$$\sigma_o = \frac{1}{ha_{11}} \varepsilon_{11o} \quad (2.230)$$

$$E_{1m} = \frac{1}{ha_{11}} \quad (2.231)$$

where m states for membrane (in-plane) strains.

Equations 2.232 contain formulas for elastic constants calculations based on a and b matrix components. E stands for elastic modulus, G is shear modulus and ν is a Poisson's ration. From the index perspective, column m stands for membrane (in-plane strains) and column b stands for a pure bending case.

$$\begin{cases} E_{1m} = \frac{1}{ha_{11}}; & E_{1b} = \frac{12}{h^3d_{11}} \\ E_{2m} = \frac{1}{ha_{22}}; & E_{2b} = \frac{12}{h^3d_{22}} \\ G_{12m} = \frac{1}{ha_{66}}; & G_{12b} = \frac{12}{h^3d_{66}} \\ \nu_{12m} = -\frac{a_{12}}{a_{11}}; & \nu_{12b} = -\frac{d_{12}}{d_{11}} \\ \nu_{21m} = -\frac{a_{12}}{a_{22}}; & \nu_{21b} = -\frac{d_{12}}{d_{22}} \end{cases} \quad (2.232)$$

The Inverse Classical Laminate Theory (ICLT) is a method to mathematically convert any composite material into the equivalent unidirectional layer composite [17]. Examples of these are shown on the Figure 2.25.

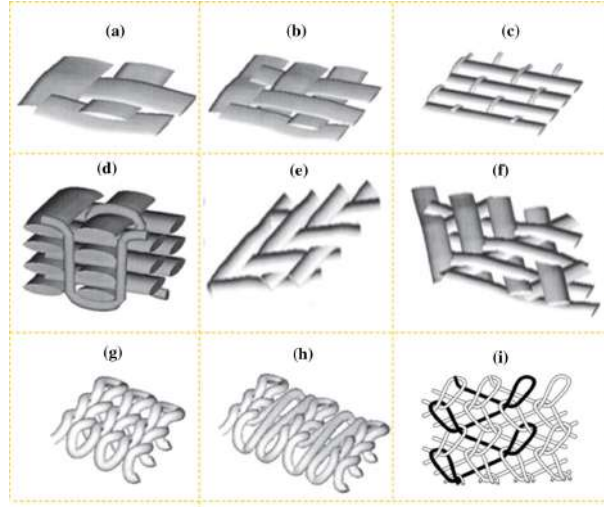


Figure 2.25: Textile fabrics structure: 2D woven fabric (a– c), 3D woven fabric (d), braided woven structured fabric (e and f), knitted fabric (g and h) and warp knitted fabric. [73]

2.2.4 Ply failure behaviour

In the simplified case, a single ply can fail at least in 5 different modes (Figure 2.26). First one is a tension along the fibers' direction, where in the case of porous matrix, most of the load is carried by the fibers. Second case is a tensile force in the transverse direction to fibers, where most of the load is carried by the matrix. That is much more weaker direction than along fibers. Third case is a compression along fibers, which are not straight in the real composite. That leads to the kinking and buckling (shear load). Fourth case is compression across fibers, which leads to the matrix-driven failure. Fifth one is a shear load, which cause matrix failure triggered fibers' cracking. After describing single ply failure, the next step is to try generalize that theory to the laminate. This is one of the best approaches, but needs to be used with caution and supported by experimental results.

Due to the fact, that basic failure modes can interact with each other, there is a necessity of introducing a failure criteria. Alternative, microscopic approach can be started at the constituent level, but is is very hard to translate it to the ply level [72]. One of the reason is that fibers have no equal strength, non-uniform distribution and are weakened by a random defects (scratches or cracks) generated at the manufacturing level. As a result of these factors, a single random fibre is going to fail first. In such a case, surrounding matrix will carry additional portion of load with the shear stress to the adjacent fibers. If the load is strong enough, initialized crack could grow through adjacent fibers.

Figure 2.27 presents complex situation occurring within the compressed ceramic matrix composite. At the micro-level (picture B), single fibers tend to wave in-phase, out-of-phase or randomly. At the bundle level (picture A), fibers tend to kink and crack in the most deflected regions. As a result of that, matrix between fibres crack and loses its load-carrying capability. This is much more complex failure mode in comparison to the

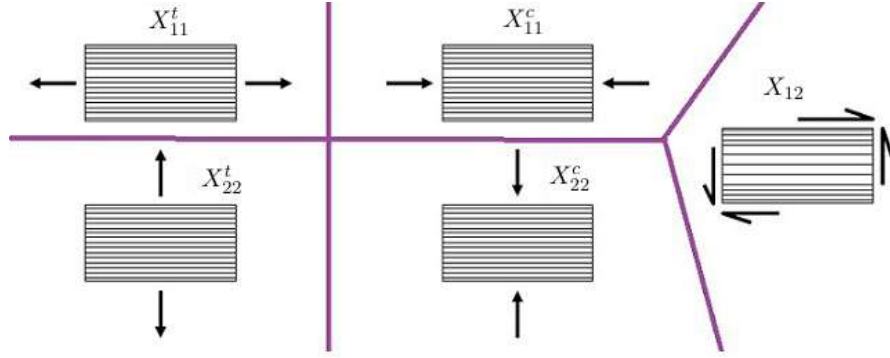


Figure 2.26: Single ply basic load cases [72]

isotropic metals.

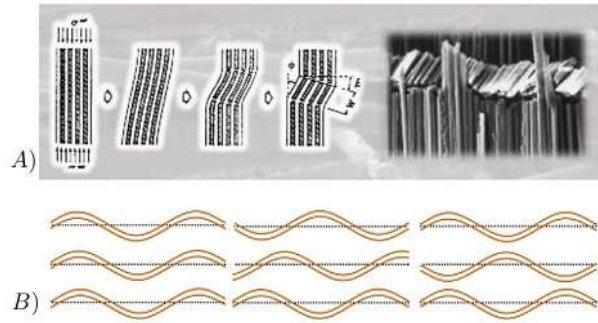


Figure 2.27: Compression laminate response [72]

Figure 2.26 presents five most common strength properties, which are used in popular failure criteria. They are itemised below:

- X^t - tensile strength along fibers
- X^c - compressive strength along fibers
- Y^t - tensile strength across fibers
- Y^c - compressive strength across fibers
- S - shear strength

In general, failure criteria are based on the phenomenological properties, omitting very complex and random processes inside. In other words, they treat matrix composite as a continuous material (ply) with no differentiation between fiber and matrix phases. For that reason, none of them is generic and applicable to all composite all the time.

Burzyński et al. [74] developed the elastic constitutive law for the resultant statically and kinematically exact, non-linear, 6-parameter shell theory. Presented formulae contain explicitly two material parameters of Cosserat continuum, which is the micropolar modulus and the characteristic micromolar length. Chróścielewski et al. [75] established theoretical values of two correction factors for the respective transverse shear stress resultants and stress couples within the general, dynamically and kinematically exact 6-field theory of

elastic shells. They found that these values do not depend on the shell material symmetry, geometry of the base surface, the shell thickness or any kind of dynamic/kinematic constraints.

Composite damage detection can be done using non-destructive methods such as wave propagation analysis [76]. Other popular and well established methods are: ultrasonic inspection, acoustography, low frequency methods, radiographic inspection, shearography, acoustic emission and acousto-ultrasonics [77].

2.2.5 Composite failure criteria

Composite failure criteria are the subject of continuous development for decades [78]. Nevertheless there are still many challenges to overcome, as a result of very complicated failure modes possible to develop inside composite materials under multiaxial external load. Due to the limited understanding of failure physics at the single ply level, behaviour of the multilayered structure is even more of a challenge [79]. As a support of theoretical considerations, engineers performed multiple experiments to obtain comprehensive data of failure mechanisms character, speed and direction [80].

Hundreds of composite failure criteria developed over the years worldwide can be grouped according to the list below.

- **Scale.** Microscopic criteria are much less useful than macroscopic ones. According to the results of WWFE (World-Wide Failure Exercise) event, top five most popular criteria are based on macroscopic observations. They were developed by Puck [81, 82], Tsai [83], Zinoviev [84, 85], Bogetti [86, 87], and Cuntze [88, 89].
- **Input.** In the general case, failure criteria can be divided as strain-based and stress-based. The most common one from the first category is the maximum-strain criterion [83, 90]. Most popular stress based criteria are Puck [81, 82], Tsai-Hill [91], Hashin [92], LaRC [93, 94] and Hoffmann [95].
- **Mode prediction.** Basic criterion predicts only occurrence of failure, so they are blind to the mode (which is a fair assumption for most engineering applications). They are presented as a mathematical curve/surface in the stress/strain space [78]. A mode-dependent criterion contain equations able to model particular failure mode. Most common examples are Puck [81, 82], Hashin [92], LaRC [93, 94], Sun [80] and Hashin-Rotem [96].

A general formulation of failure criteria has been first proposed by Goldenblat and Kopnov [97]. According to this article, the general equation of criterion can be written in index notation as:

$$(F_i \sigma_i)^\alpha + (F_{ij} \sigma_i \sigma_j)^\beta + (F_{ijk} \sigma_i \sigma_j \sigma_k)^\gamma + \dots = 1 \quad (2.233)$$

The coefficients F_i, F_{ij}, F_{ijk} are calculated from uniaxial and biaxial failure stresses and the parameters α, β, γ are selected to yield a good correlation with experimental data [98]. These criteria can be classified as polynomial.

2.2.6 Maximum stress criterion

The most commonly used failure criterion is the maximum stress criterion presented in equation 2.234. It says that for a single type of load, composite will fail when stress exceeds the strength value obtained from the experiment. This criterion is quite accurate,

but is applicable only for a single type of load, which rarely occurs in the engineering construction. Any type of load interaction is not accounted for.

$$\begin{cases} \sigma_{11} < X_{11}^t & \text{or} & X_{11}^c \\ \sigma_{22} < X_{22}^t & \text{or} & X_{22}^c \\ |\sigma_{12}| < X_{12} \end{cases} \quad (2.234)$$

2.2.7 Maximum strain criterion

Maximum strain criterion presented on equation 2.235 has got an analogical structure to the maximum stress criterion. In detail, composite is going to fail, if one of the five basic cases presented on Figure 2.26 exceeds allowable strain.

$$\begin{cases} \varepsilon_{11} < \varepsilon_{X11}^t & \text{or} & \varepsilon_{X11}^c \\ \varepsilon_{22} < \varepsilon_{X22}^t & \text{or} & \varepsilon_{X22}^c \\ |\varepsilon_{12}| < \varepsilon_{X12} \end{cases} \quad (2.235)$$

2.2.8 Tsai-Wu failure criterion

Tsai-Wu failure criterion (equation 2.236) is a form of generalisation of Tsai-Hill criterion. It takes into account the strength difference between tensile and compression load in composite, which is denoted with index t or c respectively. X denotes the direction of applied load, which can be along fibers 11, transverse to them 22 or shear 12. σ stands for applied stress in the chosen ply direction. Similarly to Tsai-Hill criteria, failure occurs when left side of the equation is equal or greater than 1 (applied stresses are greater than strength). Note, that for the isotropic material, Tsai-Wu and Tsai-Hill criteria take a form of Huber-Mises-Hencky yield criterion, which does not mean they are better than other criterion due to that fact [72]. Both of them capture failure through the regular mathematician formulas, which in fact do not describe the failure process at the microstructural level. This is the reason, why they have numerous critics.

$$\begin{aligned} & \frac{\sigma_{11}^2}{X_{11}^t X_{11}^c} + \frac{\sigma_{22}^2}{X_{22}^t X_{22}^c} - \sqrt{\frac{1}{X_{11}^t X_{11}^c} \frac{1}{X_{22}^t X_{22}^c}} \sigma_{11} \sigma_{22} + \\ & + \left(\frac{1}{X_{11}^t} - \frac{1}{X_{11}^c} \right) \sigma_{11} + \left(\frac{1}{X_{22}^t} - \frac{1}{X_{22}^c} \right) \sigma_{22} + \frac{\sigma_{12}^2}{X_{12}^2} \geq 1 \end{aligned} \quad (2.236)$$

An index notation of general 3D case is shown on equation 2.237

$$F_i \sigma_i + F_{ij} \sigma_i \sigma_j + F_{ijk} \sigma_i \sigma_j \sigma_k \geq 1 \quad (2.237)$$

where $i, j, k = 1, \dots, 6$ for a 3D case [99]. The parameters F_i, F_{ij} and F_{ijk} represent material strengths of the lamina principal directions. Due to the fact, that parameters F_{ijk} are difficult to obtain and have minor impact to the final result, they are often neglected, leading to the quadratic equation below:

$$F_i \sigma_i + F_{ij} \sigma_i \sigma_j \geq 1 \quad (2.238)$$

where σ_i are components of the stress tensor. All the coefficients F_i and F_{ij} are evaluated by simple traction, compression and shear stress, except F_{12} which must be obtained by biaxial stress. Taking into account that shear stress is sign independent, all

terms containing it to the first power vanish: $F_4 = F_5 = F_6 = 0$ [99]. Then, the explicit form of the general Tsai-Wu expression is shown below.

$$F_1\sigma_1 + F_2\sigma_2 + F_3\sigma_3 + 2F_{12}\sigma_1\sigma_2 + 2F_{13}\sigma_1\sigma_3 + 2F_{23}\sigma_2\sigma_3 + F_{11}\sigma_1^2 + F_{22}\sigma_2^2 + F_{33}\sigma_3^2 + F_{44}\sigma_4^2 + F_{55}\sigma_5^2 + F_{66}\sigma_6^2 \geq 1 \quad (2.239)$$

where factors F are defined as: [99]

$$\left\{ \begin{array}{l} F_1 = \frac{1}{X_{11}^t - X_{11}^c} \\ F_2 = \frac{1}{X_{22}^t - X_{22}^c} \\ F_3 = \frac{1}{X_{33}^t - X_{33}^c} \\ F_{12} = -\frac{1}{2\sqrt{X_{11}^t X_{11}^c X_{22}^t X_{22}^c}} \\ F_{13} = -\frac{1}{2\sqrt{X_{11}^t X_{11}^c X_{33}^t X_{33}^c}} \\ F_{23} = -\frac{1}{2\sqrt{X_{22}^t X_{22}^c X_{33}^t X_{33}^c}} \\ F_{11} = \frac{1}{X_{11}^t X_{11}^c} \\ F_{22} = \frac{1}{X_{22}^t X_{22}^c} \\ F_{33} = \frac{1}{X_{33}^t X_{33}^c} \\ F_{44} = \frac{1}{X_{23}^2} \\ F_{55} = \frac{1}{X_{13}^2} \\ F_{66} = \frac{1}{X_{12}^2} \end{array} \right. \quad (2.240)$$

Tsai-Wu criterion belongs to the oldest failure criteria of composites [100]. Although it does not distinguish the failure mode, it is applicable with no limitations to various composites, i.e. uni- or bidirectionally as well as disperse reinforced composites.

2.2.9 Tsai-Hill failure criterion

Maximum stress or strain criterion do not take into account interaction of loads. For example, cracked matrix due to the tensile load can still carry some shear load by friction. In the general case various types of loads can magnify the damaging effect or reduce it. Tsai-Hill failure criterion shown on equation 2.241 is one of the earliest attempts to capture that interaction. It was created by Steven Tsai by a modification of Hill's yield theory developed for anisotropic metals. σ stands for applied stresses in the given ply directions and X is a strength in the chosen directions. According to it, failure in the composite occurs when left side of the equation is equal or higher than 1 (applied stresses are greater than strength). 2D version of it is shown below.

$$\frac{\sigma_{11}^2}{X_{11}^2} - \frac{\sigma_{11}\sigma_{22}}{X_{11}^2} + \frac{\sigma_{22}^2}{X_{22}^2} + \frac{\sigma_{12}^2}{X_{12}^2} \geq 1 \quad (2.241)$$

where: X_{11} and X_{22} are tensile or compressive stresses accordingly.

In the general 3D case and the form of equation 2.238, Tsai-Hill criterion can be presented as a series of F parameters below:

$$\left\{ \begin{array}{l} F_1 = F_2 = F_3 = 0 \\ F_{12} = -\frac{1}{2} \left(\frac{1}{X_{11}^2} + \frac{1}{X_{22}^2} - \frac{1}{X_{33}^2} \right) \\ F_{13} = -\frac{1}{2} \left(\frac{1}{X_{33}^2} + \frac{1}{X_{11}^2} - \frac{1}{X_{22}^2} \right) \\ F_{23} = -\frac{1}{2} \left(\frac{1}{X_{22}^2} + \frac{1}{X_{33}^2} - \frac{1}{X_{11}^2} \right) \\ F_{11} = \frac{1}{X_{11}^2} \\ F_{22} = \frac{1}{X_{22}^2} \\ F_{33} = \frac{1}{X_{33}^2} \\ F_{44} = \frac{1}{X_{23}^2} \\ F_{55} = \frac{1}{X_{13}^2} \\ F_{66} = \frac{1}{X_{12}^2} \end{array} \right. \quad (2.242)$$

2.2.10 Hoffman failure criterion

Hoffman's criterion is applicable for an orthotropic lamina with unequal strengths in the compressive and tensile load. Its elements compare loads and strengths in an unique configuration, which apart from the σ_{11} *vs* σ_{22} is very similar to the Tsai-Wu criterion shown on equation 2.235. Its 2D version can be presented in a form of equation 2.243 [101].

$$\frac{\sigma_{11}^2}{X_{11}^t X_{11}^c} + \frac{\sigma_{11} \sigma_{22}}{X_{11}^t X_{11}^c} + \frac{\sigma_{22}^2}{X_{22}^t X_{22}^c} + \left(\frac{1}{X_{11}^t} + \frac{1}{X_{11}^c} \right) \sigma_{11} + \left(\frac{1}{X_{22}^t} + \frac{1}{X_{22}^c} \right) \sigma_{22} + \frac{\sigma_{12}^2}{X_{12}^2} \geq 1 \quad (2.243)$$

In the general form consistent with the equation 2.239, Hoffman's F parameters can be written as below [99].

$$\left\{ \begin{array}{l} F_1 = \frac{1}{X_{11}^t - X_{11}^c} \\ F_2 = \frac{1}{X_{22}^t - X_{22}^c} \\ F_3 = \frac{1}{X_{33}^t - X_{33}^c} \\ F_{12} = -\frac{1}{2} \left(\frac{1}{X_{11}^t X_{11}^c} + \frac{1}{X_{22}^t X_{22}^c} - \frac{1}{X_{33}^t X_{33}^c} \right) \\ F_{13} = -\frac{1}{2} \left(\frac{1}{X_{33}^t X_{33}^c} + \frac{1}{X_{11}^t X_{11}^c} - \frac{1}{X_{22}^t X_{22}^c} \right) \\ F_{23} = -\frac{1}{2} \left(\frac{1}{X_{22}^t X_{22}^c} + \frac{1}{X_{33}^t X_{33}^c} - \frac{1}{X_{11}^t X_{11}^c} \right) \\ F_{11} = \frac{1}{X_{11}^t X_{11}^c} \\ F_{22} = \frac{1}{X_{22}^t X_{22}^c} \\ F_{33} = \frac{1}{X_{33}^t X_{33}^c} \\ F_{44} = \frac{1}{X_{23}^2} \\ F_{55} = \frac{1}{X_{13}^2} \\ F_{66} = \frac{1}{X_{12}^2} \end{array} \right. \quad (2.244)$$

2.2.11 Hashin strain criterion

Hashin has developed for transversally isotropic unidirectional laminates a quadratic polynomial criterion which takes into account physical considerations [98]. His method

presents a semi-empirical approach, to address the problem of different failure modes between two phases of a composite material. Hashin defines four modes by which the composite could fail and considers the stress state under which each would occur, resulting in a piecewise failure surface [102]. Four failure modes taken into account are:

- Tensile fiber failure mode

$$\left(\frac{\sigma_{11}}{X_{11}^t}\right)^2 + \left(\frac{\sigma_{12}}{X_{12}}\right)^2 = 1; \quad \sigma_{11} > 0 \quad (2.245)$$

- Compressive fiber failure mode

$$\sigma_{11} = -X_{11}^c; \quad \sigma_{11} > 0 \quad (2.246)$$

- Tensile matrix failure mode

$$\left(\frac{\sigma_{22}}{X_{22}^t}\right)^2 + \left(\frac{\sigma_{12}}{X_{12}}\right)^2 = 1; \quad \sigma_{22} > 0 \quad (2.247)$$

- Compressive matrix failure mode

$$\left(\frac{\sigma_{22}}{X_{12}}\right)^2 + \left(\left(\frac{X_{22}^c}{2X_{12}}\right)^2 - 1\right) \frac{\sigma_{22}}{X_{22}^c} + \left(\frac{\sigma_{12}}{X_{12}}\right)^2 = 1; \quad \sigma_{22} < 0 \quad (2.248)$$

In this criterion, some approximations were applied to approximate constant parameters requiring otherwise difficult and expensive biaxial tests. The assessment of fiber failures is more straightforward than for matrix, because at least failure plane can be identified. Figure 2.28 presents fiber and matrix failure planes positions. Fiber failure plane is expected to be opened across the smallest possible fiber cross-section, whereas matrix failure plane most likely will follow path between fibers.

2.2.12 Puck failure criterion

The Puck failure criterion [103] is accepted as one of the most successful methods, because its accuracy was proven during the World-Wide Failure Exercise [104] which accessed 13 different failure theories in 125 cases. Puck's approach distinguishes between fiber and matrix failure and cope very well with with accessing ultimate strength of multidirectional composite laminates [102]. Five failure type is taken into account is listed in equations 2.249 to 2.253. Fiber failure is spilt into tension/compression case, whereas matrix failure is divided in to modes A, B and C, which depends on the ration between transverse (σ_{22}) and shear (σ_{12}) stress. Furthermore Puck's theory considers degradation model and distinguishes between initial and final failure. Consistently with previous chapters, ε^t and ε_c represent ultimate strain in tension and compression at the direction of fibers (11) and transverse to fibers (22). γ_{12} is the shear strain, which is assumed to be zero in unidirectional laminate tests. The parameter ν_{f12} is the Poisson's ratio in fibers and m_{of} is a mean stress magnification factor for fibers in the transverse direction and assumed as 1 for the unidirectional laminates tests [102]. The parameter $p_{\perp\parallel}^{(-)}$ is the slope of the σ_{11} and σ_{12} failure curve when $\sigma_{11} \leq 0$, $p_{\perp\parallel}^{(+)}$ is the slope of the σ_{11} and σ_{12} failure curve when $\sigma_{11} > 0$ and $p_{\perp\perp}^{(-)}$ is the slope of the σ_{11} and σ_{12} failure curve when $\sigma_{11} \leq 0$. The parameter $|\sigma_{11D}|$ is a stress value for linear degradation. Examples of Puck's criteria application are available in [105, 106].

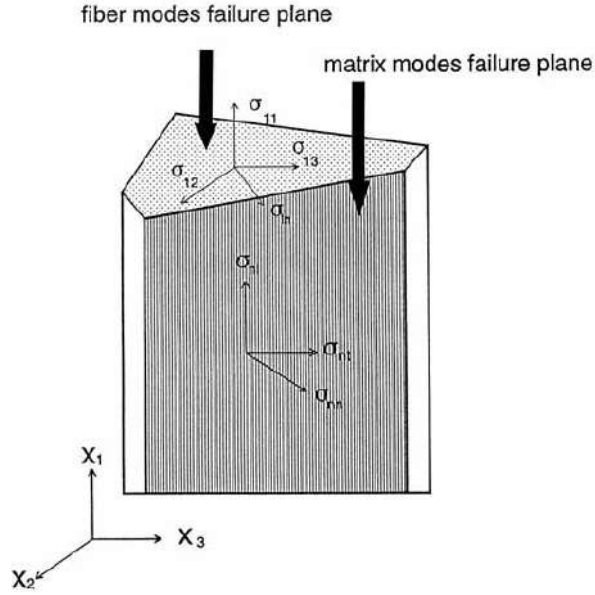


Figure 2.28: Failure modes and the corresponding failure planes of Hashin criterion [98]

- Tensile fiber failure mode

$$\frac{1}{\varepsilon_{11}^t} \left(\varepsilon_{11} + \frac{\nu_{f12}}{E_{f11}} m_{\sigma f} \sigma_{22} \right) = 1 \quad (2.249)$$

- Compressive fiber failure mode

$$\frac{1}{\varepsilon_{11}^c} \left| \left(\varepsilon_{11} + \frac{\nu_{f12}}{E_{f11}} m_{\sigma f} \sigma_{22} \right) \right| = 1 - (10\gamma_{12})^2 \quad (2.250)$$

- Matrix failure mode A

$$\sqrt{\left(\frac{\sigma_{12}}{X_{12}} \right)^2 + \left(1 - p_{\perp\parallel}^{(+)} \frac{X_{22}^t}{X_{12}} \right)^2 \left(\frac{\sigma_{22}}{X_{22}^t} \right)^2} + p_{\perp\parallel}^{(+)} \frac{\sigma_{22}}{X_{12}} = 1 - \left| \frac{\sigma_{11}}{\sigma_{11D}} \right| \quad (2.251)$$

- Matrix failure mode B

$$\frac{1}{X_{12}} \left(\sqrt{\sigma_{12}^2 + \left(p_{\perp\parallel}^{(-)} \sigma_{22} \right)^2} + p_{\perp\parallel}^{(-)} \sigma_{22} \right) = 1 - \left| \frac{\sigma_{11}}{\sigma_{11D}} \right| \quad (2.252)$$

- Matrix failure mode C

$$\left(\left(\frac{\sigma_{12}}{2 \left(1 + p_{\perp\perp}^{(-)} \right) X_{12}} \right)^2 + \left(\frac{\sigma_{22}}{X_{22}^c} \right)^2 \right) \frac{X_{22}^c}{-\sigma_{22}} = 1 - \left| \frac{\sigma_{11}}{\sigma_{11D}} \right| \quad (2.253)$$

2.2.13 Specific numerical model for the WHIPOX

WHIPOX (Wound Highly Porous OXide Ceramic) is a CMC (Ceramic Matrix Composite) material which is going to be used as a WCC (wet Combustion Chamber) liner.

As shown in Figure 1.5A, it is made from the fibers embedded in the ceramic matrix. The advantage of this solution is that porous matrix is loosely bonded to fibers, so in the case of matrix crack initiation, crack do not propagate inside fibers.

Table 2.2 contains elastic properties of WHIPOX. E is Young modulus, G is shear modulus and ν is Poisson's ratio.

E_{11} [GPa]	125
E_{22}, E_{33} [GPa]	101.72
G_{12} [GPa]	43.9
G_{13}, G_{23} [GPa]	42.92
ν_{12} [-]	0.144
ν_{13}, ν_{23} [-]	0.193
density [g/m^3]	2.8
coef. of thermal expansion (600°C) [$10^{-6}/K$]	7.5
thermal cond. (20°C) [W/mK]	3.10
thermal cond. (1000°C) [W/mK]	1.55
specific heat (20°C) [J/gK]	1.02
specific heat (600°C) [J/gK]	1.22
specific heat (1400°C) [J/gK]	1.31

Table 2.2: Elastic properties of WHIPOX

Equation 2.254 presents reduced form of Tsai-Wu failure criterion, where factors F are based on the experimental results. The only exception is factor F_{66} which is difficult to measure, so it was estimated based on the other factors and specimen strength.

$$F_1\sigma_{11} + F_2\sigma_{22} + F_{11}\sigma_{11}^2 + F_{22}\sigma_{22}^2 + F_{66}\sigma_{12}^2 = 1 \quad (2.254)$$

Table 2.3 contains WHIPOX strength factors obtained from the experimental results available in the literature [17]. All of them will be applied at the analysis part of this doctoral dissertation.

X_{11}^t	289 MPa
X_{22}^t, X_{33}^t	75 MPa
X_{11}^c	-375 MPa
X_{22}^c, X_{33}^c	-175 MPa
X_{12}, X_{13}, X_{23}	75 MPa

Table 2.3: Strength properties of WHIPOX [17]

2.2.14 Methods' application

2.2.14.1 ANSYS ACP approach

Ceramics matrix materials modelling methods are the subject of intensive and expensive research programmes across the aviation industry. One of the leaders in this field is GE Aviation, which successfully apply CMC materials for many years in the gas turbines [107]. At the initial stage, CMC components were applied in the less critical power plant

turbines. Millions of operating hours in the safe ground environment let the GE to acquire a significant amount of service data, including CMC resistance to transient phases, impact, extreme pressure and temperature. Another key advantage is a significant mass reduction in comparison to any alloy used in the aerospace engine. Of course most of that commercially acquired data is a valuable asset, so companies are rather reluctant to share it in the public domain. However, owners of numerical analysis software and scientists are keen to share research data [108]. The leading software available both commercially and scientifically is Ansys Composite PrepProp (ACP) [109] able to predict stiffness and strength (failure) of CMC materials. In the most common cases, it is able to define composite laminate layer by layer using material properties for the orthotropic material. As a result, nine different elastic constants have to be defined according to the list below.

- E_1 - Young's modulus in direction x_1
- E_2 - Young's modulus in direction x_2
- E_3 - Young's modulus in direction x_3
- ν_{12} - Poisson's ratio in direction x_{12}
- ν_{23} - Poisson's ratio in direction x_{23}
- ν_{13} - Poisson's ratio in direction x_{13}
- G_{12} - shear modulus in direction x_{12}
- G_{23} - shear modulus in direction x_{23}
- G_{13} - shear modulus in direction x_{13}

Figure 2.29 presents the mechanical property notation. Young modulus along longitudinal, transverse and thickness direction, Poisson's ratio in three load directions and shear modulus in three pairs of surfaces. Note black dots which symbolizing cross sections of fibers, which in CMC materials are five times thinner than a human hair [107].

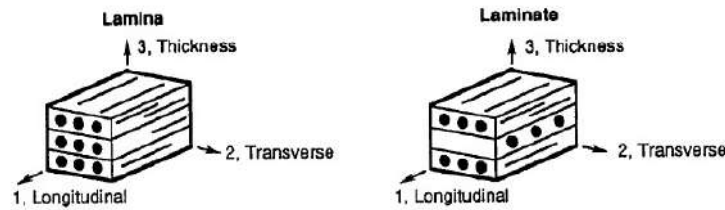


Figure 2.29: Mechanical property directions [110]

Obtaining the whole list of properties is an expensive and difficult process, so full set of this data is rarely available in the public domain. Table 2.4 contains a full set of orthotropic elastic constants of SiC/SiC composite at temperature 1204 °C.

Figure 2.30 presents basic Ansys Workbench workflow containing three blocks. The first one on the left is the Ansys Composite Preprocessor (ACP) which allows to define composite structure input to further analyses. Second step is the thermal analysis, which let to figure out internal composite temperature based on the boundary conditions and material conduction data. Third block is a structural analysis, which applies thermal and

Property	Without voids	With 2.7% voids		Experiment
		Lower bound	Upper bound	
E_x, E_y	246.57	204.37	246.15	233.74 ± 19.51
E_z	200.64	190.58	200.37	60.47 ± 0.69
G_{xy}	86.60	82.88	86.53	84.12
G_{xz}, G_{yz}	84.67	81.22	84.60	---
ν_{xy}	0.144	0.166	0.144	---
ν_{xz}, ν_{yz}	0.193	0.186	0.193	---

Table 2.4: Mechanical property directions (GPa)[111]



Figure 2.30: Basic Ansys thermo-mechanical workflow

structural load into the composite structure. As a result, elastic stresses are obtained as a material response.

The most efficient method to explain ACP environment is to present a basic example of cylindrical composite. The most efficient approach starts with the thin geometry and extrudes it based on the ply properties, as shown on Figure 2.31. That method let to control position of inter-laminate layers and significantly improves computational mesh. A tree of key input parameters is shown on the left. Note that the input order is precisely chosen, so it needs to be filled from the top to the bottom.

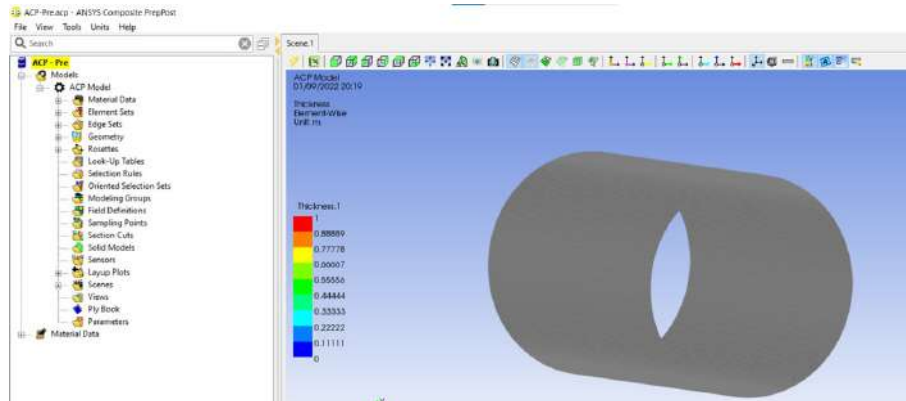


Figure 2.31: Shell geometry input - example

Figure 2.32 presents an example of stackup structure, which is characterised by the set of layers at different orientation. Each ply is built from the fibers positioned at an angle against main direction. Several model preparation steps below are designed to define it.

In the very first step of model setup, materials data is required for a given composite.

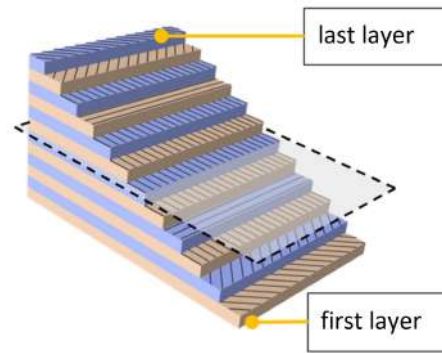


Figure 2.32: Random stack of plies [112]

Figure 2.33 A) visualizes orthotropic material input summarised in table 2.4 versus the position angle. This data is valid for a single ply, where all fibers are positioned in the same direction. In Ansys ACP this is referenced as a fixed thickness Fabric. Next level down is a stackup definition, which is built from multiple fabrics rotated against each other. Figure 2.33 B) presents ten plies at angles plus/minus 10 degrees versus main axis, so thickness can be easily calculated as a multiplication of fabrics layers.

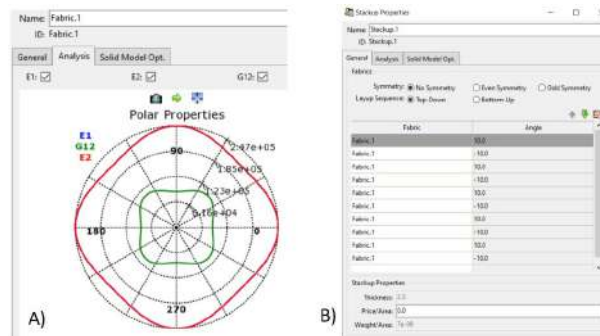


Figure 2.33: A) Fabric and B) Stackup (material data) input

The following key step is the definition of "rosette", which is a coordinate system fixed to the geometry. "Oriented selection set" (Figure 2.34 A)) input controls fiber position with respect to the rosette (geometry) and the direction of the thickness (applicable only to the shell geometries). This needs to be consistent with the manufacturing winding process. "Modelling ply" (Figure 2.34 B)) is similar to the stackup, but is a higher level function based on the previously defined stackups. Thanks to it, in the more general case, sandwich composite structures can be obtained.

Figure 2.35 summarises all modelling steps followed before. In the case of CMC cylinder, single stackup definition is just right, but for the demonstration purpose two this stackups were combined into single ply. Fiber position pattern is also repeatable, so one rosette was applied. At this stage, for the control purpose, thickness scale is presented as a colour on the shell geometry. This is particularly important for a variable multilayer composites and must be equal to a fiber thickness multiplied by the layers/plies number.

Figure 2.36 A) visualizes the rosette, which has to be well defined based on the geometry. Blue arrow directs material thickness, red arrow is a reference for the fabric angle and green is a transverse direction. For a control purpose, green dotted lines visualize

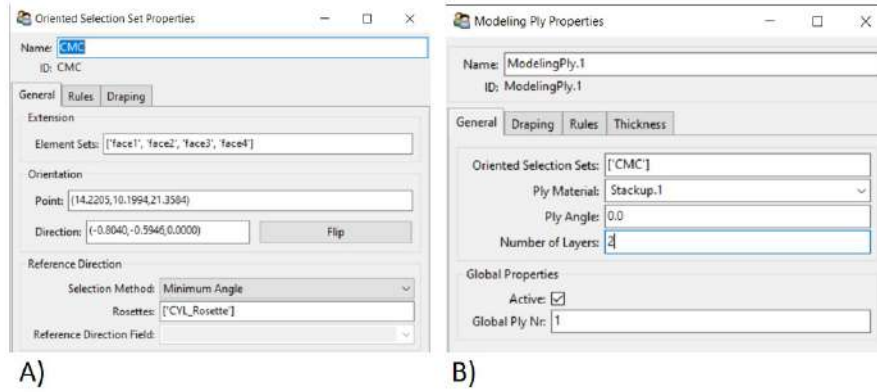


Figure 2.34: A)Oriented set and B)Modeling ply input

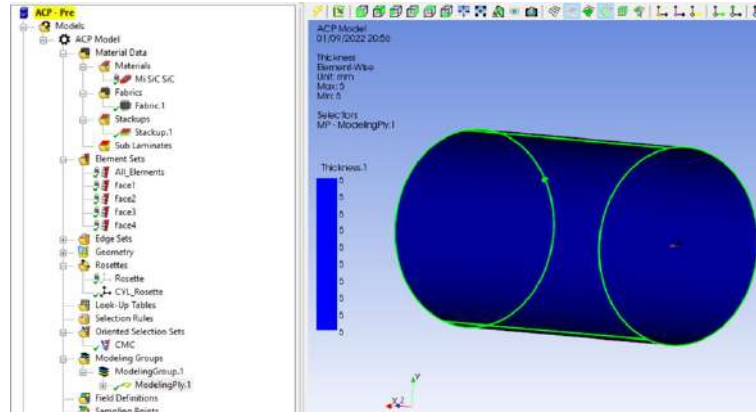


Figure 2.35: Model details

the reference direction across the entire liner. For a more complex shapes than cylinder, reference lines can be quite complex, so their paths have to be carefully checked against the design intend.

Figure 2.37 presents the final step of the Ansys ACP laminate definition. Once all required composite parameters are applied, update function in Ansys ACP triggers 3D geometry generation. There are several advantages from that approach. The first one is that generated mesh is fully structural and element surfaces are coplanar with the interlaminar interfaces. That feature is important, as material properties varies across the thickness and convenient at the results post-processing stage, where each fabric can be separated and described.

2.2.14.2 Recent research advances

Ceramics matrix composite materials are subject to intensive research projects, funded by companies offering advanced gas turbine solutions on land, sea and air. The reason being is that this technology exceeds other known materials in the field of temperature resistance and durability [113–116]. Due to the fact that CMC materials can vary significantly between components, analysis methods need to support various winding angles, shapes and multiple symmetry axis [117–121]. Efficient and affordable manufacturing

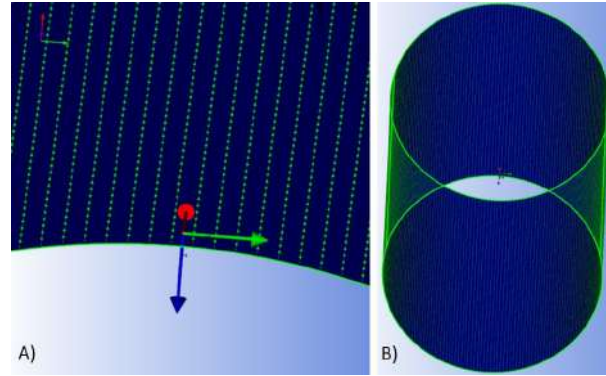


Figure 2.36: Rosette (reference) direction A)Detail and B)Global

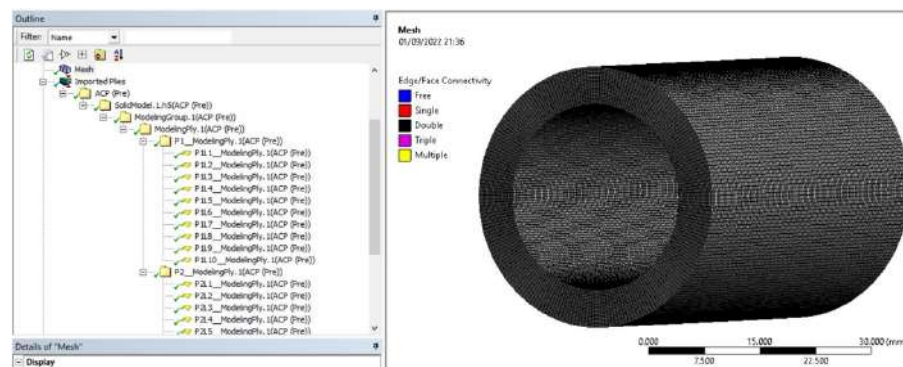


Figure 2.37: 3D mesh

techniques are desirable, because they can help to align fiber directions along principal stresses.

CMC materials are a state-of-art technology, which combines two brittle ceramic components into a non-brittle structure. This behaviour was proved during a numerous tests, which are very difficult to model due to their complex anisotropic in-plane mechanical behaviour. Especially difficult phenomena occurs at the boundary between fibers and matrix, where weak bounding forces form a sort of a fuse against the rapid brittle fracture. Advanced modelling methods supporting effective algorithms are based on the material homogenization assumptions as Classical Laminate Theory (CLT) and Representative Volume Unit (RVU) able to estimate elastic properties [122–125], progressive damage [126, 127] and maximum allowable loading [128, 129]. The fatigue strength prediction for variable winding angle and density of CMC material selection is investigated in [130–134]. Common simplification used in other types of composites like reinforced polymers is assumption of individual unidirectional (UD) layers. However, this is not the case in CMC materials, where non-typical unhindered shrinkage of matrix (transverse to the fibers) occurs at the manufacturing stage [17]. As a consequence of that, basic unidirectional (UD) material assumption cannot be applied to model CMC materials.

To address aforementioned limitations, specific modifications to the UD approach need to be applied. An equivalent UD-layer technique consist an advanced solutions, able to better predict the response of wounded CMC internal structure. Available studies in this topic [135, 136] evaluate equivalent UD-layers properties using an inverse approach of CTL

able to determine wounded CMC properties as a function of fiber orientation and matrix microstructure.

Physical failure criterion are validated against the experimental behaviour of composites. One of the most successful hypothesis was proposed by Puck [128], which combines two independent criteria - fiber failure (FF) and inter-fiber (matrix/interface) failure (IFF). Another criterion was developed by Cuntze [137] who proposed five independent failure modes based on the stress invariants. The limitation of these criterion is that they do not work properly in a case of the zero normal stress at the fracture surface. In such a case an additional inclination parameters are required, which are difficult to obtain for CMC materials (e.g. [138]). On the other hand, non-physical failure criterion are more flexible and easier to use for discussed CMC materials. The most popular one in the Tsai-Wu criterion [129] which is based on quadratic failure conditions considering interactions between strain and stress tensor elements. Usage of polynomial tensor is convenient, as result can be graphically expressed as a failure surface. In addition to the aforementioned models, many more were developed to predict the failure of fiber-reinforced composites [139–142].

Koch et al. [143] performed an experimental analysis and modelling of CMC materials, which split into two groups: weak interface CMC (WI-CMC) and weak matrix CMC (WM-CMC). The reason being is that fibre-matrix de-bonding is a key ability to stop the instant brittle failure. They concluded, that for WI-CMC materials, where matrix is stiff and strong and interfacial properties become dominant, micromechanical based models can be applied to explain fracture toughness. In the case of WM-CMC materials, the weak (porous) matrix toughness has to be evaluated based on the macromechanical tests, which takes into account statistical properties of highly random structured matrix. Such approach can be applied to the complex loading conditions, shapes and internal structures. Figure 2.38 presents results based on Hill failure criterion. It proves very well consistency between experiment and finite element (FE) model.

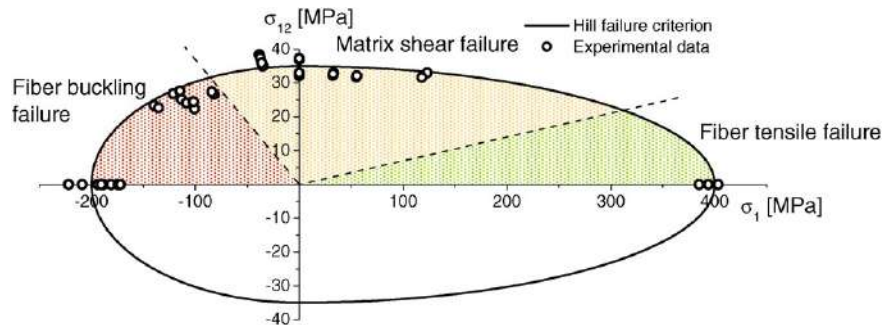


Figure 2.38: Summary of measured strength values and failure modes depending on fiber orientations and loading direction [143]

Volkman et al. [144] made a single-edge notch bend (SENB) test of three oxide/oxide matrix composites to research the dependency between mechanical performance and heat treatment. All of them were based on the Nextel 610 fibres [14]. They found that strength and stiffness decreased rapidly between 1000 °C and 1200 °C after 50 hours of high-temperature exposure. The formal fracture toughness was calculated on the basis of the maximum force according to Munz and Fett [145]. Hou et al. [146] run a fatigue life prediction experiment of needled matrix composite presented schematically of Figure 2.39.

They proposed a stress-life (S-N) curve based on constant amplitude test and combined

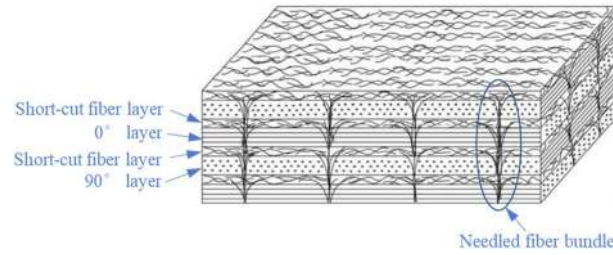


Figure 2.39: Schematic diagram of microstructure of needled composite [146]

it with the variable amplitude tests results. Both results were combined using rainflow counting method and the Goodman line. They concluded, that the loading normalization can effectively establish the general relationship between loading parameter and life. Fang et al. [147] investigated a residual strength model of needled CMC material. According to the test results, residual tensile strength grows in the initial stage and drops as test progresses. On that basis, a brand new model was developed by incorporating wear-in and wear-out mechanisms. The difference between them is that wear-in enhance the strength, while wear-out reduces the load capacity. Figure 2.40 presents micro damage mechanisms for loading along and in traverse direction to the fibre position. Left photo visualizes the matrix crack bridging with fibers, whereas right photo shows matrix spalling.

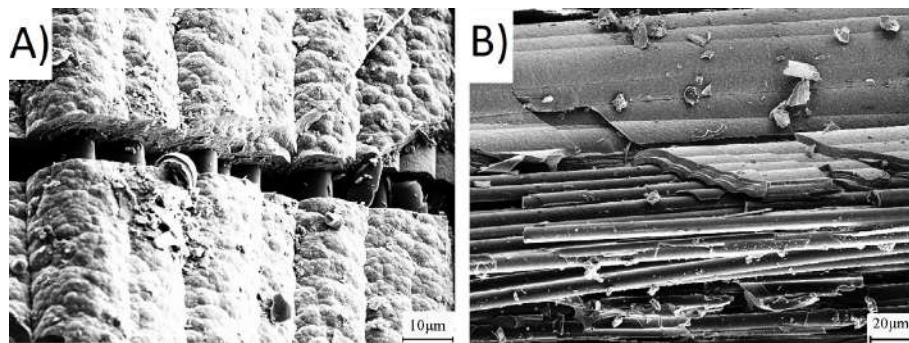


Figure 2.40: Micro-damages after fatigue loading A) 0°layer, B) 90°layer [147]

Yu et al. [148] developed new experimental method to test behaviour of ceramic matrix mini-composites. Key challenges they faced were proper material preparation, specimen design gripping method, loading regime, strain measurement and transverse tensile stress calculation. The stress-strain characteristics were strongly non-linear, but elastic modulus was positively correlated to the matrix volume fraction. One of the key findings was that strain field uniformity has a strong correlation with the damage level, which occurs across the fibers. The other aspect taken into account was the impact of the microstructure into the elastic modulus. Hou et al. [149] investigated fatigue life prediction method for a needled CMC specimen with a central hole. In the very first step, the macroscopic elastic constants and stress concentration factor were calculated using finite element method. In the following step, the fatigue notch factors were obtained for the corresponding stress levels. Based on this approach, a fatigue life prediction method was proposed for a central-hole specimen made from needled C/SiC composite. As an input, it requires a smooth-specimen SN (stress-life) curve and a stress concentration factor. Figure 2.41 presents broken specimens used for the lifing method correlation and validation.



Figure 2.41: Failed fatigue specimens with central hole, A) $D=10\text{mm}$, B) $D=14\text{mm}$ [149]

Apart from the tensile/compression load experiments made with CMC materials, other states of load and structures are a subject of scientific considerations. Shi et al. [150] determined a bending properties for continuous fiber reinforced C/C-SiC sandwich structure with a grid core. The effective bending and shear stiffness (deflection) at the mid-span of the sandwich were determined and compared across three methods: experiment, FE simulation and analytical. Proposed methods appeared as a suitable and versatile tools for further product development. Zhang et al. [151] modelled a fatigue failure of CMC at elevated temperature, by applying a multi-scale validation to their results. Multiple micro-damage models were developed to describe the evolution processes of matrix cracking, interface wear and fiber fracture under the applied load. In the macro scale, SN curve was derived from the fatigue test. At the microscale level, several measurements were taken as percentage of fracture fibers, interfacial shear stress and matrix crack density. Comparison showed, that both macro and microscale experimental results were close enough to the predicted values. CMC materials can also be manufactured in the woven pattern.

Yang et al. [152] investigated mechanical behaviour of woven CMC under non-uniform stress and strain loads. It is much more simple pattern than wounded structure, so explicit meso-scale model can be applied. Figure 2.42 presents applied modelling steps, which are possible to do in the modern FEM commercial software. The sequence of steps covers extraction of basic repeatable geometry (micro-scale model), grouping it into fiber tow and meso-scale model. Their study focuses on the inhomogeneous stress and strain fields and compares predicted results with experiment. It became apparent, that strain and stress concentrations appear at the location of tow cross-overs, because of the local bending and stretching.

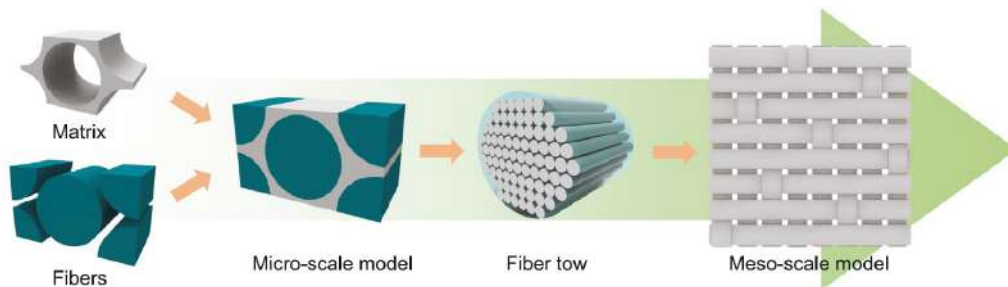


Figure 2.42: The basic principle of the multiscale model [152]

Xiang et al. [153] performed micromechanical analysis of CMC material using a hierarchical quadrature element method. It takes into account three typical stages occurring during the failure process: interface perfectly bonded, interface debonding and fiber failure (Figure 2.43).

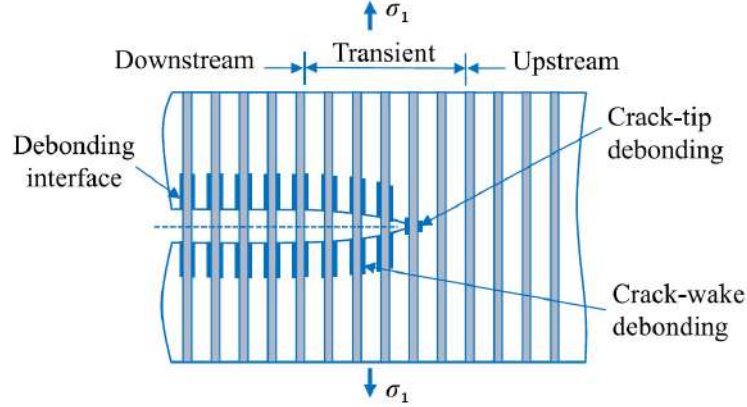


Figure 2.43: Schematic representation of a CMC matrix crack [153]

Li [154] went even deeper into the CMC microstructure, focusing on the CMC crack opening/closing stress identification based on the hysteresis. This is a very important topic from the durability and reliability of CMC components applied in the extremely hot conditions. Based on the matrix cracking and interference slip damage mechanisms, the micro-mechanical hysteresis loop models were developed considering variable matrix cracking density and interface slip rate (Figure 2.44.)

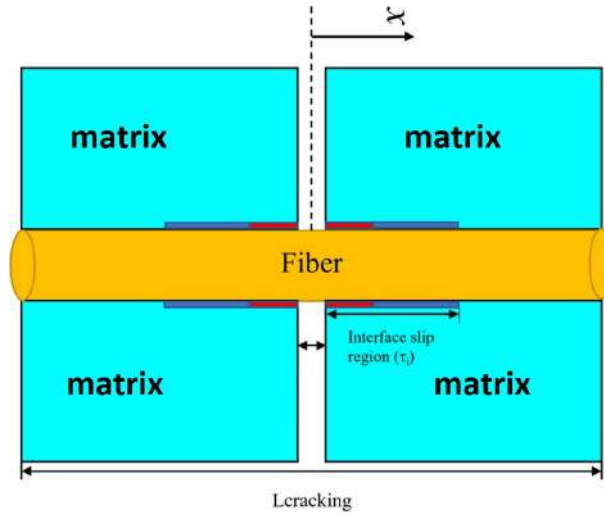


Figure 2.44: Schematic of unit cell with fiber and matrix of damaged CMC [154]

CMC self-healing process [155] helps to seal created matrix cracks reducing the ability of oxygen to penetrate and oxidise exposed fibres. Such CMCs contain layers or reactive matrix which passively seals cracks due to the oxidation, helping with significant fibers life extension. Bellezza et al. [156] proposed a 2D image-based multiphysics model for lifetime evaluation and failure of self-healing ceramics matrix mini-composite under a

tensile load. They proposed partial differential equations for the oxygen and other species transport responsible for the matrix healing process, concerning integration time and boundary conditions. As a result, a slow crack growth model explicitly dependent on the environmental parameters was calibrated and integrated numerically for a general use. Lv et al. [157] investigated the strength of $SiC_f/\beta - Yb_2Si_2O_7$ fiber/matrix interface for different requirements in SiC_f/SiC CMC material. Figure 2.45 summarises result of the experiment, where weak interfaces sintered at 1200 °C exhibited crack deflection (top photos). This is the desired case, as fibers do not follow brittle matrix failure. On the other side, strong bonding (bottom photos) could be a optimum solution for the higher end of operational temperature, as it is much more plastic (weak) with the temperature growth.

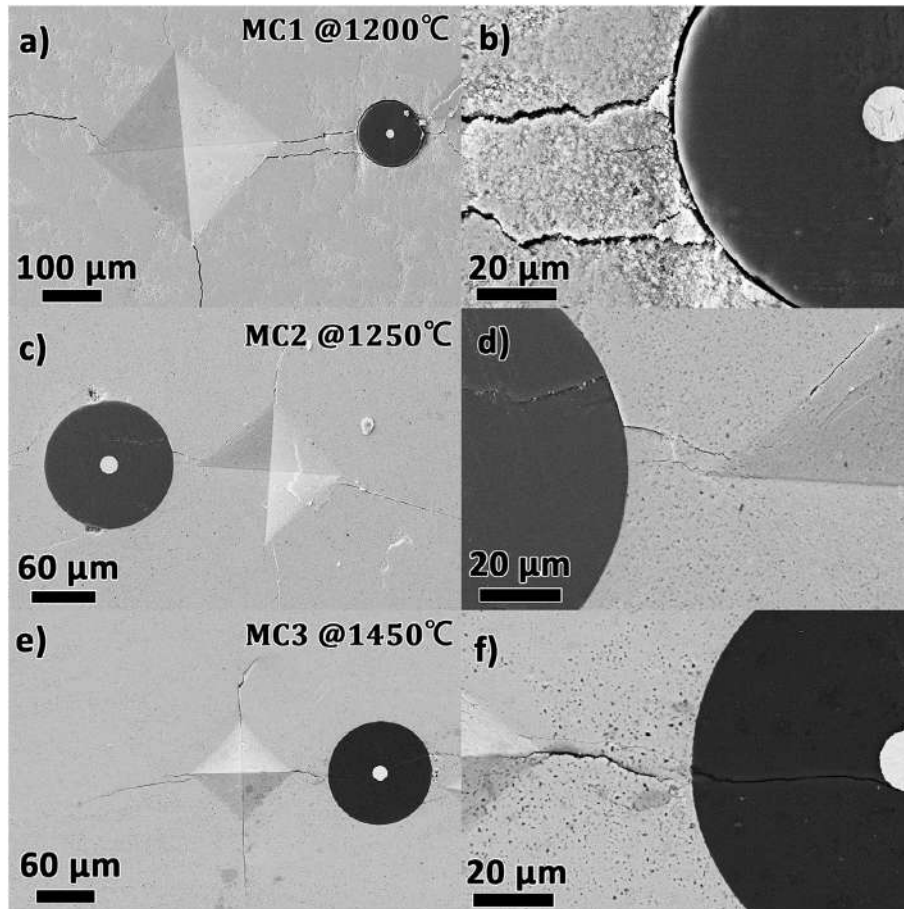


Figure 2.45: Crack-interface interaction in model composites, a) and b) illustrates the crack deflection around the fiber, c) and d) shown the moderate crack deflection, e) and f) crack penetration through the interface [157]

Hackemann et al. [158] investigated creep properties of alumina-based all-oxide CMC made of Nextel 610 fibers [14]. Results revealed, that processing conditions has got a significant effect to creep rates, so they cannot be applied to the different sintering temperatures, matrix systems or grain sizes. They concluded, that elastic constants of the 1D material have to be modified due to the anisotropic matrix damage during the sintering process for the 0 °and 90 °CMCs if planned to be used within the laminate theory. Volkmann et al. [6] have studied similar set of creep tests based on Nextel 610 fibers

at the temperature up to 1200 °C. They found, that creep tests in the fiber dominated orientation revealed approximately 10-50 times shorter primary creep zone compared to the off-axis (45°) direction. This results is consistent with the common sense, that in the on-axis orientation most of the load is carried by fibers rather than matrix.

Zhao et al. [159] studied CMC material oxidation with application of damage-induced short-circuit diffusion model. They proposed a chemo-thermo-mechanical coupled constitutive model for CMCs operating in the oxidizing environment. For the matrix, initiation and propagation of micro-cracks is covered by the constitutive model and oxidation is modelled as a damage factor driven by the actual physical processes. For fibers, the oxidation reaction is taken into account. Additionally to developed models, the corresponding finite element analysis procedure is developed based on the Galerkin method and Newton-Raphson iteration scheme. Another attempt of two-way coupling of stress, diffusion and oxidation in the heterogeneous CMC microstructures was made by Schichtel and Chattopadhyay [160]. They proposed a multiphysics methodology and corresponding numerical scheme to capture complex interactions between stress, oxygen diffusion, oxidation and matrix cracking in CMC at the microstructural level. The model is derived from the governing equations for force equilibrium and conservation of oxygen/carbon mass which are coupled using reaction terms, solubilities, oxygen diffusivities and matrix damage. The model is demonstrated to predict creep-like strain with stresses oxidation tests and able to capture differences between reaction-limited and diffusion-limited temperature regimes. Ramachandran et al. [161] investigated experimental and mathematical modelling of CMAS (calcium-magnesium aluminosilicate) coated oxide/oxide CMCs. This type of corrosion is particularly severe in the gas turbine blades, where CMC materials are expected to operate after technology achieves mature level. The studies revealed that coated blades can gain as much as 6% additional mass due to the formation of $\alpha - Al_2O_3$ at 1000 °C. As a result, indentation fracture toughness of the oxide/oxide CMC dropped by 12% after 10 hours.

2.3 Numerical modelling - fluid-solid interaction

Fluid-solid interaction (FSI) approach describes coupled motions of solids and fluids, so it is a cornerstone in many modern engineering applications [162–164]. From the mathematical point of view FSI couples two systems of partial differential equations [165]. FSI non-linearities occur in solid materials, flows (Navier-Stokes equations) and moving interfaces. Some practical examples of interactions between fluid and solid can be found in articles [166, 167].

Classic numerical description of motion in Computational Solid Dynamics (CSD) employs Lagrangian algorithms. That could be applied, because small deformation of solid can be followed by mesh without causing large finite elements deformation. On the other hand, Computational Fluid Dynamics (CFD) models employ Eulerian algorithms, where mesh integration points do not follow moving particles of the flow. That behaviour can handle large distortion easily, but at the expense of precise interface definition and the resolution of flow details [168]. ALE modelling can be used in various applications like blood flow medical diagnostics [169], thermo-corrosive fatigue modelling within a gas turbine [170] or material deformation response next to the cavitation bubble collapse [171].

Arbitrary Lagrangian-Eulerian (ALE) combines advantages of Lagrangian and Eulerian approach [172]. It enables three computational options: pure Lagrangian, pure Eulerian and hybrid one which can be moved in some arbitral way providing additional flexibility and accuracy [173]. That ability is the essence of the Arbitrary Lagrangian-Eulerian formulation [174].

Figure 2.46 presents material (R_X), spatial (R_x) and referential (R_χ) domains in motion. Material domain contains particles X , the spatial domain is composed of spatial points x and the referential domain identifies the coordinates of mesh reference points χ .

From thermal-FSI perspective, proper calculation of heat transfer coefficient (HTC) is a key advantage over separate CFD/CSD analyses. According to the calculation methods review [175], analytical methods are based on the Newton Law, lumped thermal capacity assumption, 1D unsteady heat conduction equation for a semi-infinite wall, the fin model, energy conservation and the analogy between heat and mass transfer. The common issues associated with proper HTC determination are linked with lack of thermal sensors access to the analysed surfaces. On the other hand, boundary conditions required for CFD model setup are not always available. In such a case an inverse methods are applicable, as they can figure out CFD boundary conditions based on the measurements performed at a certain distance from the wall. An example of such approach is available in [176].

2.3.1 Description of the ALE kinematics

The motion of material particles \underline{X} to spatial points \underline{x} is achieved by introducing a mapping φ presented of equations 2.255 and 2.256 [173]:

$$\varphi : R_{\underline{X}} \times [t_0, t] \rightarrow R_{\underline{x}} \times [t_0, t] \quad (2.255)$$

$$(\underline{X}, t) \rightarrow \varphi(\underline{X}, t) = (\underline{x}, t) \quad (2.256)$$

which links \underline{X} and \underline{x} in time by the motion law below:

$$\underline{x} = \underline{x}(\underline{X}, t) \quad (2.257)$$

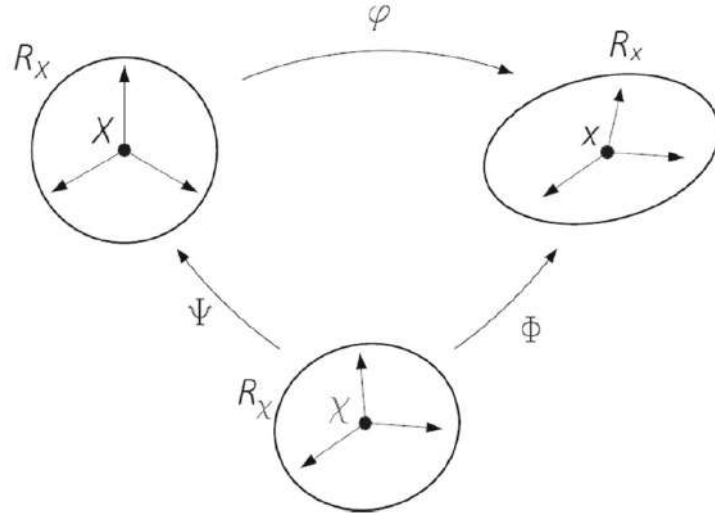


Figure 2.46: Material, spatial and referential domains in motion [173]

Such formulation defines spatial coordinates \underline{x} as a function of its initial position \underline{X} and elapsed time of motion t . A matrix representation of the φ gradient is shown on the equation 2.258.

$$\frac{\partial \varphi}{\partial (\underline{X}, t)} = \begin{pmatrix} \frac{\partial \underline{x}}{\partial \underline{X}} & \underline{v} \\ \underline{0}^T & 1 \end{pmatrix} \quad (2.258)$$

where $\underline{0}^T$ is a null row-vector and the material velocity \underline{v} is represented by equation below:

$$\underline{v}(\underline{X}, t) = \left. \frac{\partial \underline{x}}{\partial t} \right|_{\underline{X}} \quad (2.259)$$

where $|_{\underline{X}}$ denotes that material coordinates \underline{X} are fixed.

The referential domain R_X shown on figure 2.46 is defined to store the definition of reference (non-deformed) mesh. It is mapped by parameters Ψ and Φ into material and spatial domain respectively. The particle motion φ can be expressed as $\varphi = \Phi \circ \Psi^{-1}$, which interlinks all three definitions.

The mapping from the referential domain to the spatial domain is defined as Φ , which is the motion of the mesh in the spatial domain represented by equations 2.260 and 2.261.

$$\Phi : R_{\underline{X}} \times [t_o, t] \rightarrow R_{\underline{x}} \times [t_o, t] \quad (2.260)$$

$$(\underline{\chi}, t) \rightarrow \Phi(\underline{\chi}, t) = (\underline{x}, t) \quad (2.261)$$

where gradient Φ equals [173]:

$$\frac{\partial \Phi}{\partial (\underline{\chi}, t)} = \begin{pmatrix} \frac{\partial \underline{x}}{\partial \underline{\chi}} & \underline{w} \\ \underline{0}^T & 1 \end{pmatrix} \quad (2.262)$$

where mesh velocity \underline{w} is given based on the relation below:

$$\underline{w}(\underline{\chi}, t) = \left. \frac{\partial \underline{x}}{\partial t} \right|_{\underline{\chi}} \quad (2.263)$$

Figure 2.46 present material particles position \underline{X} as a product of Ψ transformation, however its inversion is more convenient to use in the following considerations:

$$\Psi^{-1} : R_{\underline{X}} \times [t_0, t] \rightarrow R_{\underline{\chi}} \times [t_0, t] \quad (2.264)$$

$$(\underline{X}, t) \rightarrow \Psi^{-1}(\underline{X}, t) = (\underline{\chi}, t) \quad (2.265)$$

where the gradient of Ψ^{-1} equals to:

$$\frac{\partial \Psi^{-1}}{\partial (\underline{X}, t)} = \begin{pmatrix} \frac{\partial \underline{\chi}}{\partial \underline{X}} & \underline{v} \\ \underline{0}^T & 1 \end{pmatrix} \quad (2.266)$$

where the velocity \underline{u} can be presented in the following form:

$$\underline{u}(\underline{X}, t) = \left. \frac{\partial \underline{x}}{\partial t} \right|_{\underline{X}} \quad (2.267)$$

Equation 2.268 was created by differentiation of $\varphi = \Phi \circ \Psi^{-1}$, so it presents relations between all three velocities.

$$\frac{\partial \varphi}{\partial (\underline{X}, t)}(\underline{X}, t) = \frac{\partial \Phi}{\partial (\underline{\chi}, t)}(\Psi^{-1}(\underline{X}, t)) \frac{\partial \Psi^{-1}}{\partial (\underline{X}, t)}(\underline{X}, t) = \frac{\partial \Phi}{\partial (\underline{\chi}, t)}(\underline{\chi}, t) \frac{\partial \Psi^{-1}}{\partial (\underline{X}, t)}(\underline{X}, t) \quad (2.268)$$

which can be presented in the matrix form below:

$$\begin{pmatrix} \frac{\partial \underline{x}}{\partial \underline{X}} & \underline{v} \\ \underline{0}^T & 1 \end{pmatrix} = \begin{pmatrix} \frac{\partial \underline{x}}{\partial \underline{\chi}} & \underline{w} \\ \underline{0}^T & 1 \end{pmatrix} \begin{pmatrix} \frac{\partial \underline{\chi}}{\partial \underline{X}} & \underline{v} \\ \underline{0}^T & 1 \end{pmatrix} \quad (2.269)$$

which leads to the equation below,

$$\underline{v} = \underline{w} + \frac{\partial \underline{x}}{\partial \underline{\chi}} \cdot \underline{v} \quad (2.270)$$

which can be expressed as a convective velocity \underline{c} , which is the relative velocity between the material and the mesh.

$$\underline{c} = \underline{v} - \underline{w} = \frac{\partial \underline{x}}{\partial \underline{\chi}} \cdot \underline{u} \quad (2.271)$$

Convective velocity \underline{c} is the particle velocity relative to the mesh as seen from the spatial domain $R_{\underline{x}}$.

2.3.2 Time derivatives in the ALE formulation

Material, spatial and differential time derivatives relations are crucial to write conservation laws for momentum, mass and energy in ALE approach. For that reason, scalar physical quantities are described by the symbolic forms: $f(\underline{X}, t)$, $f(\underline{x}, t)$ and $f(\underline{\chi}, t)$ in the material, spatial and referential domain respectively.

The spatial description $f(\underline{x}, t)$ can be mapped into material description $f(\underline{X}, t)$ using equation 2.272:

$$f(\underline{X}, t) = f(\varphi(\underline{X}, t), t) \quad \text{or} \quad f(\underline{X}, t) = f(\underline{x}, t) \circ \varphi(\underline{X}, t) \quad (2.272)$$

The gradient of the mapping expression above is presented on equation 2.273:

$$\frac{\partial f}{\partial(\underline{X}, t)}(\underline{X}, t) = \frac{\partial f}{\partial(\underline{x}, t)}(\underline{x}, t) \frac{\partial \varphi}{\partial(\underline{X}, t)}(\underline{X}, t) \quad (2.273)$$

which can be expressed in the matrix form below:

$$\left(\frac{\partial f}{\partial \underline{X}} \frac{\partial f}{\partial t} \right) = \left(\frac{\partial f}{\partial \underline{x}} \frac{\partial f}{\partial t} \right) \begin{pmatrix} \frac{\partial \underline{x}}{\partial \underline{X}} & \underline{v} \\ \underline{0}^T & 1 \end{pmatrix} \quad (2.274)$$

and converted by block multiplication to equations 2.275 and 2.275.

$$\frac{\partial f}{\partial \underline{X}} = \frac{\partial f}{\partial \underline{x}} \frac{\partial \underline{x}}{\partial \underline{X}} \quad (2.275)$$

$$\left. \frac{\partial f}{\partial t} \right|_{\underline{X}} = \left. \frac{\partial f}{\partial t} \right|_{\underline{x}} + \frac{\partial f}{\partial \underline{x}} \cdot \underline{v} \quad (2.276)$$

Equation 2.276 relates the material and spatial time derivatives, which can be expressed as equation 2.277.

$$\frac{df}{dt} = \frac{\partial f}{\partial t} + \text{div}(f \underline{v}) \quad (2.277)$$

Note that the referential time derivative is included in the relation between spatial and material time derivative.

Based on the figure 2.46, scalar transformation from the referential form $f(\underline{\chi}, t)$ to the material description $f(\underline{X}, t)$ can be written as below:

$$f(\underline{X}, t) = f(\underline{\chi}, t) \circ \Psi^{-1} \quad (2.278)$$

which gradient can be expressed as below:

$$\frac{\partial f}{\partial(\underline{X}, t)}(\underline{X}, t) = \frac{\partial f}{\partial(\underline{\chi}, t)}(\underline{\chi}, t) \frac{\partial \Psi^{-1}}{\partial(\underline{X}, t)}(\underline{X}, t) \quad (2.279)$$

which can be rewritten in the matrix form:

$$\left(\frac{\partial f}{\partial \underline{X}} \frac{\partial f}{\partial t} \right) = \left(\frac{\partial f}{\partial \underline{\chi}} \frac{\partial f}{\partial t} \right) \begin{pmatrix} \frac{\partial \underline{\chi}}{\partial \underline{X}} & \underline{u} \\ \underline{0}^T & 1 \end{pmatrix} \quad (2.280)$$

after block multiplications of equations 2.281 and 2.282.

$$\frac{\partial f}{\partial \underline{X}} = \frac{\partial f}{\partial \underline{\chi}} \frac{\partial \underline{\chi}}{\partial \underline{X}} \quad (2.281)$$

$$\left. \frac{\partial f}{\partial t} \right|_{\underline{X}} = \left. \frac{\partial f}{\partial t} \right|_{\underline{\chi}} + \frac{\partial f}{\partial \underline{\chi}} \cdot \underline{u} \quad (2.282)$$

Equation 2.282 evaluates the gradient of considered quantity in the referential domain. Its solution is more numerically demanding than for the spatial domain case, so equation 2.282 was converted into spatial form 2.283.

$$\left. \frac{\partial f}{\partial t} \right|_{\underline{X}} = \left. \frac{\partial f}{\partial t} \right|_{\underline{\chi}} + \frac{\partial f}{\partial \underline{x}} \cdot \underline{c} \quad \text{or} \quad \left. \frac{\partial f}{\partial t} \right|_{\underline{X}} = \left. \frac{\partial f}{\partial t} \right|_{\underline{\chi}} + \text{div}(f\underline{c}) \quad (2.283)$$

This formula contains key ALE relations between spatial gradients and material/spatial time derivatives. The time derivative of analysed quantity for a chosen element \underline{X} is its local derivative if the reference coordinate χ is fixed. Additionally a convective term \underline{c} takes into account the relative velocity between the material and reference system.

2.3.3 The ALE form of balance equations

The set of mass, momentum and energy balance equations are presented below. Equations 2.284 contain Euler-based ALE description [173]:

$$\frac{\partial}{\partial t} \begin{pmatrix} \rho \\ \rho \underline{v} \\ \rho e \end{pmatrix} + \text{div} \begin{pmatrix} \rho \underline{v} \\ \rho \underline{v} \otimes \underline{v} \\ \rho e \underline{v} \end{pmatrix} = \text{div} \begin{pmatrix} 0 \\ \underline{t} \\ \underline{t} \underline{v} + \underline{q} \end{pmatrix} + \begin{pmatrix} 0 \\ \rho \underline{b} \\ \rho \underline{b} \underline{v} \end{pmatrix} \quad (2.284)$$

where ρ is the density of the continuum particle, \underline{v} is their velocity, e is the total energy given by equation: $e = c_v T + \frac{1}{2} \underline{v}^2$, c_v is a specific heat at constant volume, T is the temperature, \underline{t} is the Cauchy stress flux, $\underline{q} = \lambda \cdot T \lambda$ is the molecular heat flux defined by Fourier law (λ is the thermal conductivity coefficient), \underline{b} is the earth acceleration. The Cauchy stress flux can be split into a diffusive and elastic part:

$$\underline{t} = \underline{P} + \underline{\tau}^c \quad (2.285)$$

where \underline{P} is an elastic momentum reversible flux and $\underline{\tau}^c$ is a total diffusive irreversible momentum flux.

The elastic part \underline{P} is the spherical pressure tensor, which in the case of fluids cannot transmit the elastic shear stress. For solids, \underline{P} is a full elastic stress tensor, which is shown on equation 2.286.

$$\underline{P} = \begin{cases} -p \underline{I} = -p \delta_{ij} \underline{e}_i \otimes \underline{e}_j & - \text{fluid} \\ \underline{\sigma} = \sigma_{ij} \underline{e}_i \otimes \underline{e}_j & - \text{solid} \end{cases} \quad (2.286)$$

where p is a pressure, which elastic momentum flux is directed towards the centre of the particle.

The total diffusive momentum flux is defined in the form below:

$$\underline{\tau}^c = \underline{\tau} + \underline{R} + \underline{D} + \dots \quad (2.287)$$

where $\underline{\tau}$ is a viscous momentum flux, \underline{R} is a turbulent momentum flux, \underline{D} is a diffusion flux, "... " denotes other possible fluxes like transpirational momentum flux.

The viscous momentum flux $\underline{\tau}$ can be written in the equation below:

$$\underline{\tau} = -\frac{2}{3} \mu I_d \underline{I} + 2\mu \underline{d} \quad (2.288)$$

where μ is the molecular viscosity, $I_d = \text{tr} \underline{d}$ is the first invariant of the strain rate, $\underline{d} = \frac{1}{2} (\underline{v} \otimes \nabla + \nabla \otimes \underline{v})$ is the strain rate tensor.

The turbulent momentum flux \underline{R} also known as turbulent Reynolds stress can be given in a form analogical to the Newtonian fluid model below:

$$\underline{R} = -\frac{2}{3}\mu I_d \underline{I} + 2\mu_t \underline{d} \quad (2.289)$$

where μ_t is the turbulent viscosity coefficient.

Based on the previous sections it is necessary to replace the velocity \underline{v} with the relative velocity \underline{c} in the convective part of the balance equation to obtain the ALE formulation of the balance [168]. In such a case, a set of ALE balance equations can be written in the form below:

$$\frac{\partial}{\partial t} \begin{pmatrix} \rho \\ \rho \underline{v} \\ \rho e \end{pmatrix} + \text{div} \begin{pmatrix} \rho \underline{c} \\ \rho \underline{v} \otimes \underline{c} \\ \rho e \underline{c} \end{pmatrix} = \text{div} \begin{pmatrix} 0 \\ \underline{t} \\ \underline{t} \underline{v} + \underline{q} \end{pmatrix} + \begin{pmatrix} 0 \\ \rho \underline{b} \\ \rho \underline{b} \underline{v} \end{pmatrix} \quad (2.290)$$

or in the direct form taking into account the relative velocity between the material and the mesh (equation 2.291).

$$\frac{\partial}{\partial t} \begin{pmatrix} \rho \\ \rho \underline{v} \\ \rho e \end{pmatrix} + \text{div} \begin{pmatrix} \rho (\underline{v} - \underline{w}) \\ \rho \underline{v} \otimes (\underline{v} - \underline{w}) \\ \rho e (\underline{v} - \underline{w}) \end{pmatrix} = \text{div} \begin{pmatrix} 0 \\ \underline{t} \\ \underline{t} \underline{v} + \underline{q} \end{pmatrix} + \begin{pmatrix} 0 \\ \rho \underline{b} \\ \rho \underline{b} \underline{v} \end{pmatrix} \quad (2.291)$$

Chapter 3

Method Validation

Every numerical model is a simplification of the real component, which is far too complicated to be modelled perfectly. The main assumption behind employed numerical models is that domains are made from the continuous substances, which ignores existence of crystals, molecules or atoms at the micro level. For that reason, material properties used for the solid domains are statistically meaningful, assuming average numbers of defects at the crystallographic level. However, it is acknowledged in the background, that general population of components contains stronger and weaker items. This is driven by some level of randomness in the manufacturing process expressed as random microstructure defects. From the CFD point of view, same assumption is made regarding continuous medium. However, the largest source of model uncertainty is driven by the complex flow structures, which are simplified using RANS model. For the aforementioned reasons, numerical Thermal FSI models need to be validated at some stage against the experimental results. In the case, when no experimental results are available, method should be validated based on similar, but no identical analysis. This can be improved at the later stage of the design process, when prototype is build and tested.

3.1 Method validation based on C3X vane

Analysed Wet Combustion Chamber is designed to provide efficient cooling system for oxy-combustion process, which for methane exceeds 3050°K [177]. At the initial stage of design, where experimental results are not available, it is justified to validate numerical results against other experiments, which experiences similar conditions. For that reason, it was decided to use the example of C3X turbine vane [178] at condition code 4321-158, where inlet temperature was equal 808°K . Obtained results were summarised and published by M. Froissart and T. Ochrymiuk publication [179].

Figure 3.1 presents cross section of NASA C3X aerofoil with ten internal cooling channels. One of the main unknowns was the inlet temperature of water at each passage, as only average inlet/outlet temperature was reported for each hole. For that reason very precise studies were done at the very fine structural mesh prepared in the ICEM software. Based on that and literature review it was proved that constant 293.15°K was used during the experiment.

Figure 3.2 shows an experimental setup containing turbulence augmentation rods (station 1), total pressure and total temperature racks (station 2), inlet static pressure taps (station 3), laser Doppler anemometry measurement volume (station 4), a cascade of three internally cooled straight vanes (station 5) and exit static pressure taps (station 6).

Figure 3.3 captures key boundary conditions applied to the thermal-FSI model. Hot

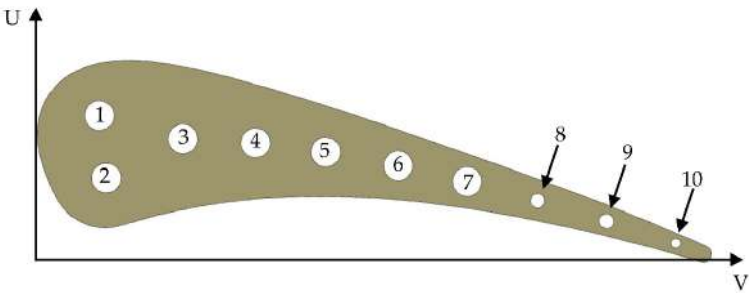


Figure 3.1: C3X section with cooling holes

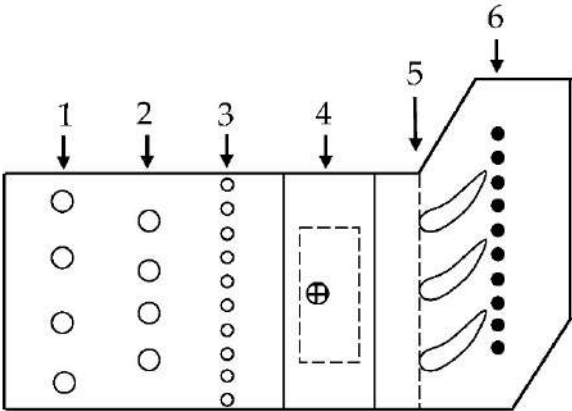


Figure 3.2: C3X test facility

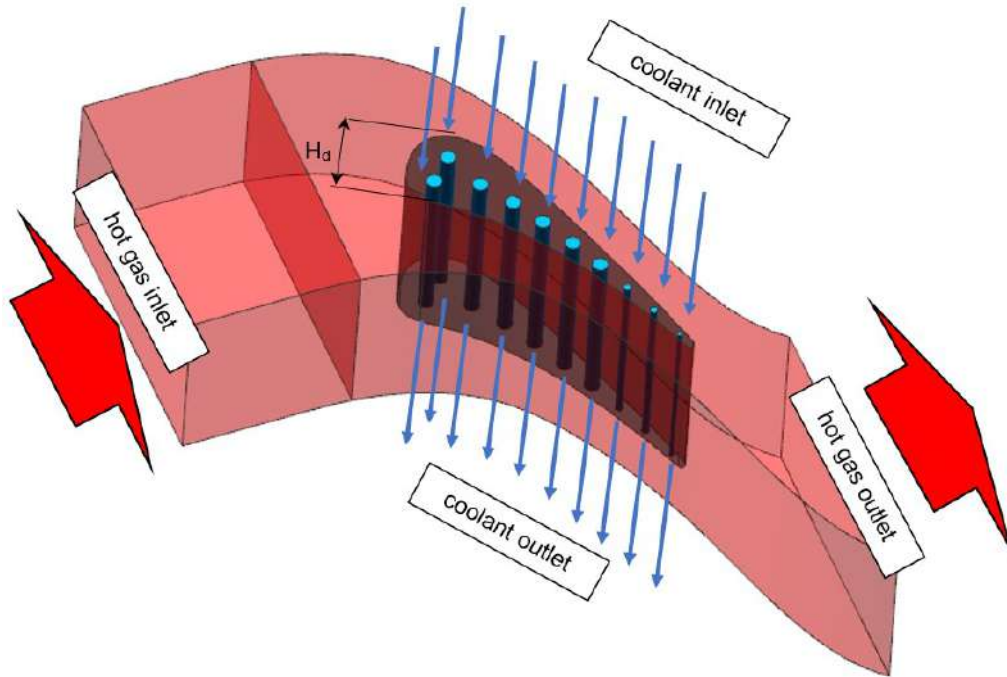


Figure 3.3: C3X FSI model

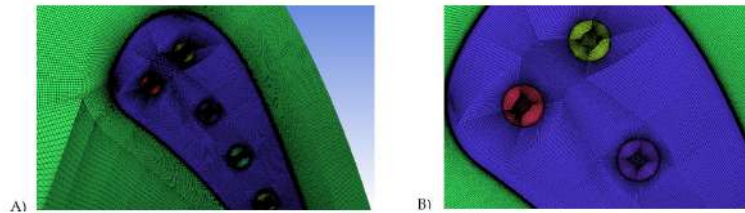


Figure 3.4: C3X mesh refinement around leading edge, A) half view, B) front view

gas is uniformly supplied at the inlet to make sure that there is enough distance before the leading edge to properly capture flow structure. Curved cyclic surfaces were specially optimised to keep uniform distance from the aerodynamic profile - note that only the middle blade from the cascade was experimentally tested and numerically modelled. Uniform inlet coolant temperature was applied at the mass flow rate taken from the test report.

Analysed C3X blade is a straight geometry, so high quality hexagonal mesh was build in ICEM and presented on Figure 3.4. To obtain that effect, geometry was split into blocks following edged and surfaces. Special attention was paid to the inflation layer around the profile to capture pressure and heat transfer coefficient precisely.

Figure 3.5 is focused at passage 1 cooling hole, which was fitted into block and meshed using o-grid function to avoid low quality elements at the circumference. Note that consistent and uniform mesh layers were applied at the fluid/solid interface helping with solution convergence (node-to-node interface).

An important part of C3X vane study was to cross-compare most popular turbulence models available in the commercial CFD codes. Graph shown on Figure 3.6 presents temperature distribution at the aerofoil midspan starting and finishing at the trailing

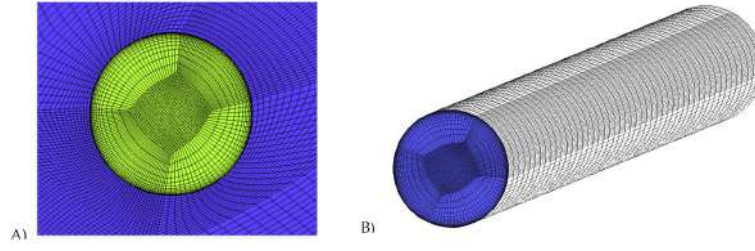


Figure 3.5: C3X mesh refinement of the first cooling hole, A)inlet view, B) interface view

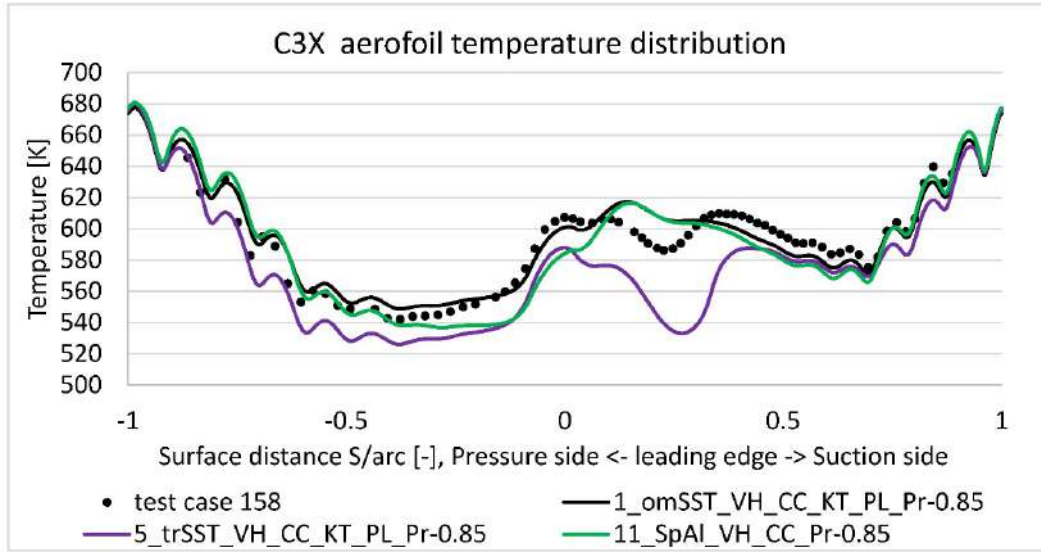


Figure 3.6: Predicted vane external surface temperature at midspan versus experimental results (measurement uncertainty is $\pm 11^\circ K$)

edge. Central part ($X=0$) is a leading edge where local high temperature occurs due to the hot gas impingement. On the other side, trailing edge is even hotter, because there is a large heated area with little cooling holes inside unable to sink high heat flux.

Black dots mark measurements obtained from thermocouples installed along the vane's midspan. Continuous lines is a result obtained from the CFD code for $k-\omega$ SST model (black line), transition SST (purple line) and Spalart-Allmaras (green line). Comparison shows that $k-\omega$ SST prediction is the closest to the measurement, so it was decided to use it in the wet combustion chamber analysis. From the shape perspective *Transistion SST* model better predicts temperature drop (distribution) around position 0.25, however $40^\circ K$ underestimation makes it worse than $k-\omega$ SST. It can be said, that Spalart-Allmaras model gives a fair temperature prediction taking into account that it is a much simpler (1 equation) model than other two.

Figure 3.7 compares an absolute pressure prediction around an aerofoil at the midspan position. Black dots mark measurement points while continuous line is in fact eleven lines positioned on top of each other. Nine of these lines were generated using different variants of $k-\omega$ SST model, one was drawn using *Transistion SST* model and one with *Spalart-Allmaras* model. The obvious conclusion from this graph is that 1-equation (*Spalart-Allmaras*), 2-equations ($k-\omega$ SST) and 4-equations (*Transistion SST*) models

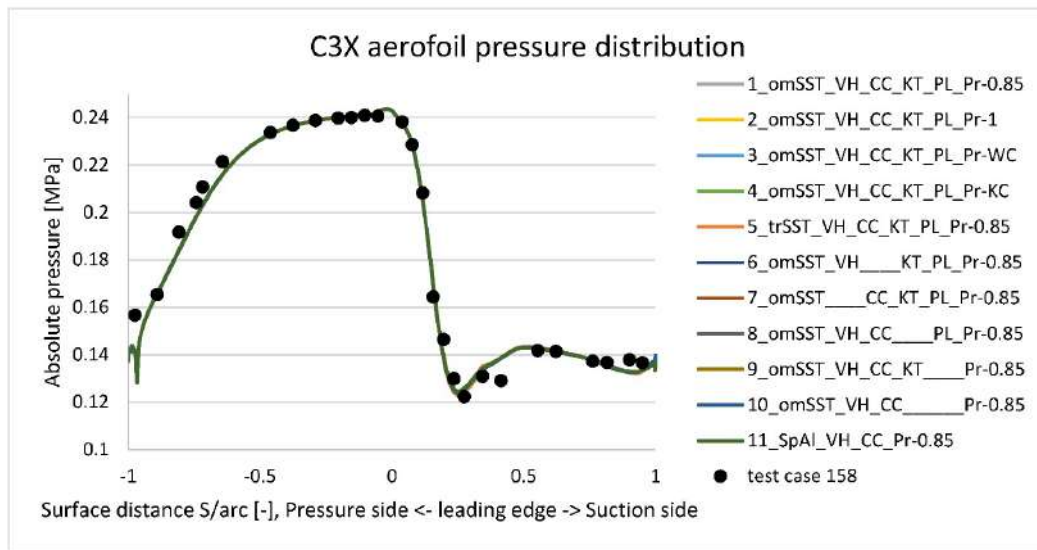


Figure 3.7: Predicted vane external absolute pressure at midspan versus experimental results (measurement uncertainty is $\pm 700 Pa$)

give equivalent pressure prediction.

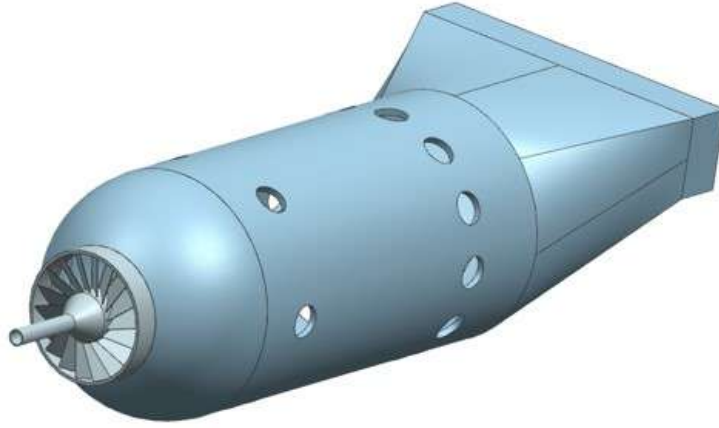


Figure 3.8: Tay combustion chamber geometry

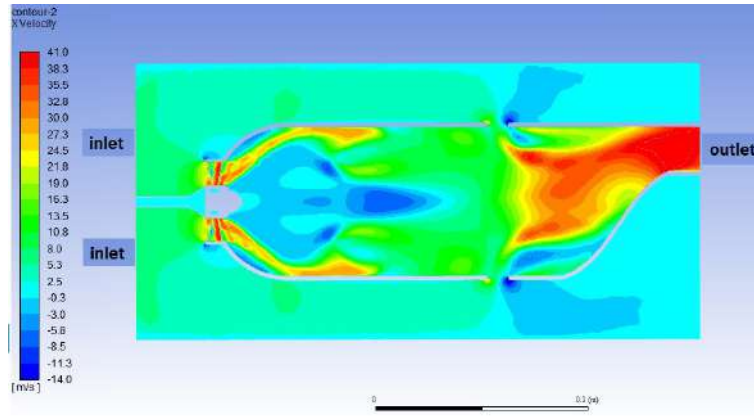


Figure 3.9: Tay combustion chamber BC - side sectional view

3.2 Method validation based on Tay combustor

Due to the complexity and uncertainty built into any CFD model, some level of validation is required in order to support obtained results [180]. Tay combustor presented on Figure 3.8 was chosen for this purpose, because extensive experimental data is publicly available for that design [181]. In addition, this combustor was used in multiple industrial applications, so its usefulness was proved in service. This design contains ten fuel holes, liner, swirler, six mixing holes and twelve dilution holes.

This model is a proper experimental case to qualitatively investigate the phenomena occurring when converting existing classical combustion chamber into the wet combustion chamber (WCC) concept. Such preliminary and simplified 3D model (cold air flow) allows to estimate further proceedings related to the design of WCC proposed in the nCO2PP (Negative CO_2 Power Plant) project. Figure 3.9 presents a cross-section of the 3D fluid domain taken for the analysis. Circular inlet supplies 0.085 kg/s of air at temperature 300°K . Atmospheric absolute pressure (101325 Pa) was applied at the rectangular outlet.

Figure 3.10 presents the axial velocity distribution across the horizontal cross-section going through the main axis. High velocity at the swirler is caused by the fact, that

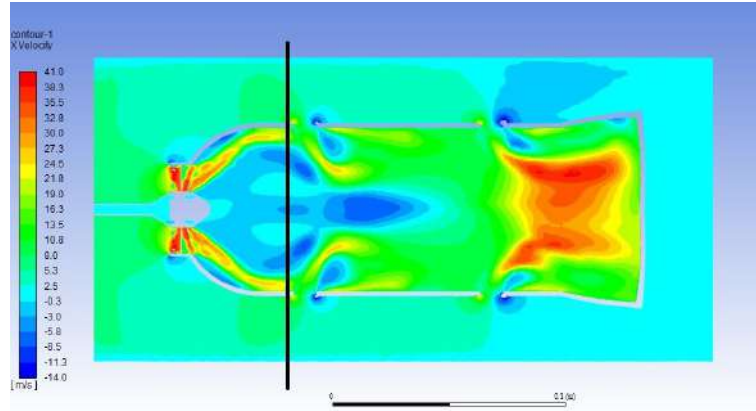


Figure 3.10: Tay combustion chamber velocity plot - top sectional view

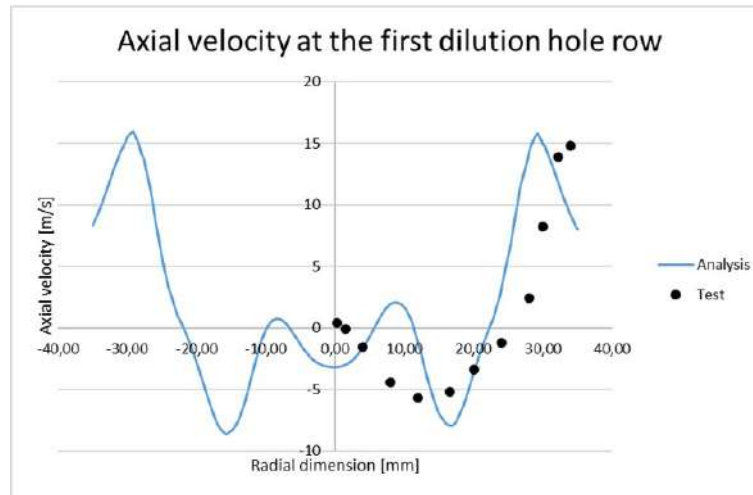


Figure 3.11: Comparison between analysis and experiment - axial velocity

air is squeezed inside the neck between external and internal chambers. Swirl velocity component induces centrifugal force which pushes air molecules towards the liner, which is represented as the red path along the wall. At the position of mixing holes, front air impinges into the mixing radial streams, which causes a complex 3D vortex generation. This interaction enhances mixing efficiency inside the combustion chamber. At the other end, outlet high-velocity spot is driven by the gradual reduction of the flow area. Black vertical line positioned next to the mixing holes marks cross-section used to generate graphs on Figures 3.11 and 3.12.

Graph presented on Figure 3.11 presents axial velocity distribution at the section highlighted on Figure 3.9. Black dots mark experimental results from the literature [182] whereas continuous line was generated by the CFD cold flow analysis. Based on this validation chart, it can be concluded, that analysis result is sufficiently close to the experiment. Minor discrepancies occur in the boundary zone and in the centre. According to the analysis, peak axial velocity is positioned at a distance from the wall, which suggests slightly thicker boundary zone than in the experiment. At the other end, central velocity is under-predicted slightly, which is fine for a such complex velocity field.

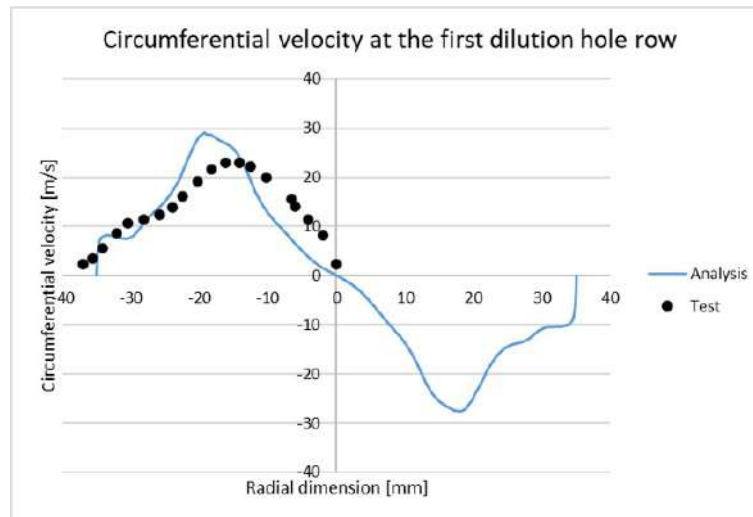


Figure 3.12: Comparison between analysis and experiment - circumferential velocity

Even better data agreement was achieved for the circumferential velocity graph on Figure 3.12, where velocity discrepancy does not exceed few meters per second.

Chapter 4

Wet Combustion Chamber Models

4.1 Geometry

4.1.1 Actual assembly

Figure 4.1 presents the cross section of wet combustion chamber with additional elements such as applied materials, fluid flows and type of support. Most of its geometry is cyclic symmetrical at the angle 120 degrees. From the fluids point of view, concentric channels A supply cooling water used in the transpiration cooling through both segments of liner number 1. For the nominal case, each porous segment is supplied with 6 g/s of liquid water at the room temperature. The adjacent holes A' are used only for regulation system - in some transient conditions they are going to reverse some stream of water supplied by channels A. Channel B supplies water cooling of the burner, where B' is the outlet of that flow. Channel C supplies methane through the swirler 19 and channel D delivers oxygen through the reverse swirler. Channel E supplies liquid water directly into the flame zone using spray nozzle. Channel F is the central zone, where combustion and water evaporation occur.

The liner is marked as number 1 and positioned in the centre. It is made of two porous ceramic matrix composites (WHIPOX) and mounted to the casing using orange elements (2, 4 and 12) made with copper CW021A. This choice was made based on the very good thermal conduction properties helping with more effective cooling of the hottest zone. Domain 3 provides efficient cooling of the burner through the ribbed cylindrical surface. Elements 3, 5-11, 15 and 18 are made from Steel X5CrNi18-10/1.4301/AISI304. The interface between elements 15 and 9 is a contact able to compensate thermal expansion difference between hot core and cold casing. On the diagram it is marked as red dashed lines. Springs 13 are important to assure axial load at multiple seals between cylindrical domains. The exception seals are marked with red circles, as they are pre-tensioned with bolts. Elements 14, 16 and 17 are made from the high-temperature resistant steel 1.4843. Symbolic support system is shown at the bottom edge, where front is fixed and rear one is able to roll axially and compensate thermal expansion at elevated temperatures.

Figure 4.2 shows a simplified single section of WHIPOX liner. Its length is 60mm, inner diameter is 25mm and wall thickness is 5mm. In the figure above it has additional grooves at the outer edges to fit seals able to protect flame zone against water leaks. These grooves were omitted consistently in all analyses, as they introduce significant model complication (layered composite material)

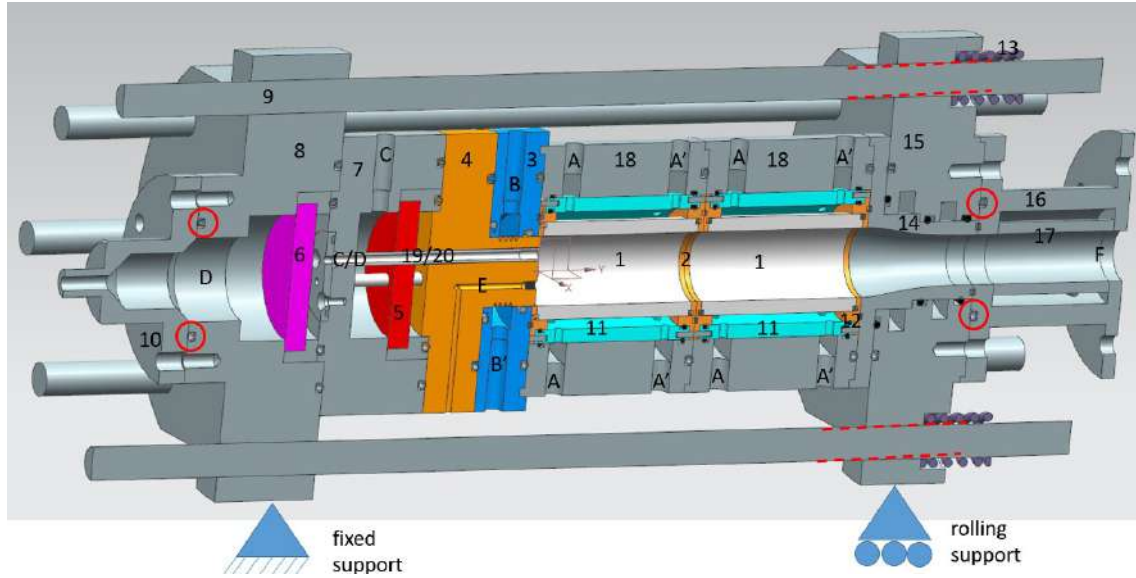


Figure 4.1: WCC cross-section

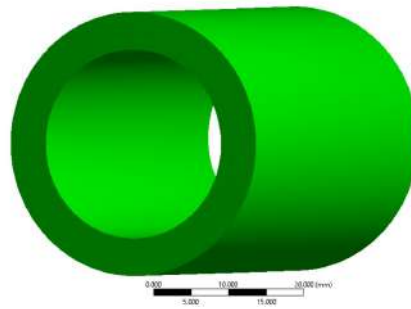


Figure 4.2: Single liner simplified geometry

4.1.2 Simplified assembly

Figure 4.1 presents fully featured geometry with such details like sealing, springs and bolted joints. Although this is helpful to understand the assembly and interactions between elements, this is not practical to cover everything at once in the finite element model. For example such detail like sealing requires an enormous number of elements and very detailed description of the contact face. Similarly springs are computational demanding due to the large amount of highly deflected elements. Bolted joints at the front and at the rear of the assembly are modelled as a bonded contact to avoid unnecessary complications with thread modelling. It was decided that these joints are far enough from the porous liner, so they can be simplified. Figure 4.3 presents defeatured assembly with frictionless contacts between adjacent components. The most significant assumption is removal of seals and filling sealing grooves with solid metal. That simplification has a negligible effect on stresses and is convenient for future CFD analysis.

Figure 4.4 presents workflow taken for analysis of an assembly model. Block B contains geometry of the isotropic elements of assembly made from steel and copper. Blocks F and H define geometry of front and rear liner, which is created in a form of thin cylinder. Ansys

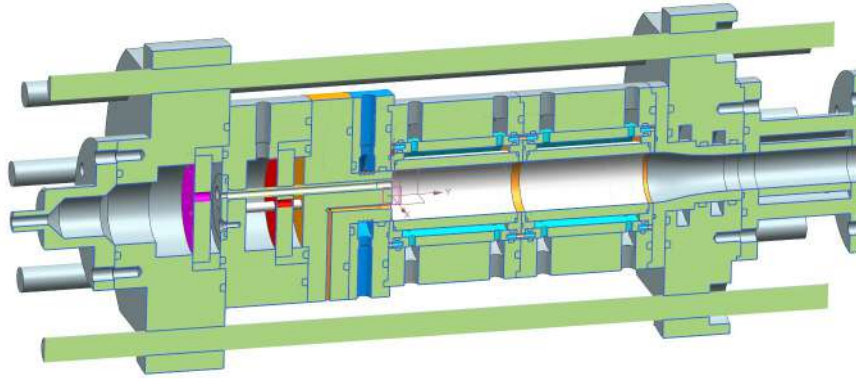


Figure 4.3: Geometry simplifications

Composite Preprocessor (ACP) requires 2D sheet model in order to create mesh consistent with defined plies. Blocks G and I support ACP able to define composite liner sector (front and rear) with detailed ply definition (Figure 4.5). Block D combines isotropic assembly with two orthotropic composite liners, creates interfaces and executes steady state thermal analysis. Result from it is supplied directly into the block E representing steady-state structural analysis. Block A contains material database of steel, copper and WHIPOX. It is feed into blocks C,G,I to maintain material database consistency between assembly components.

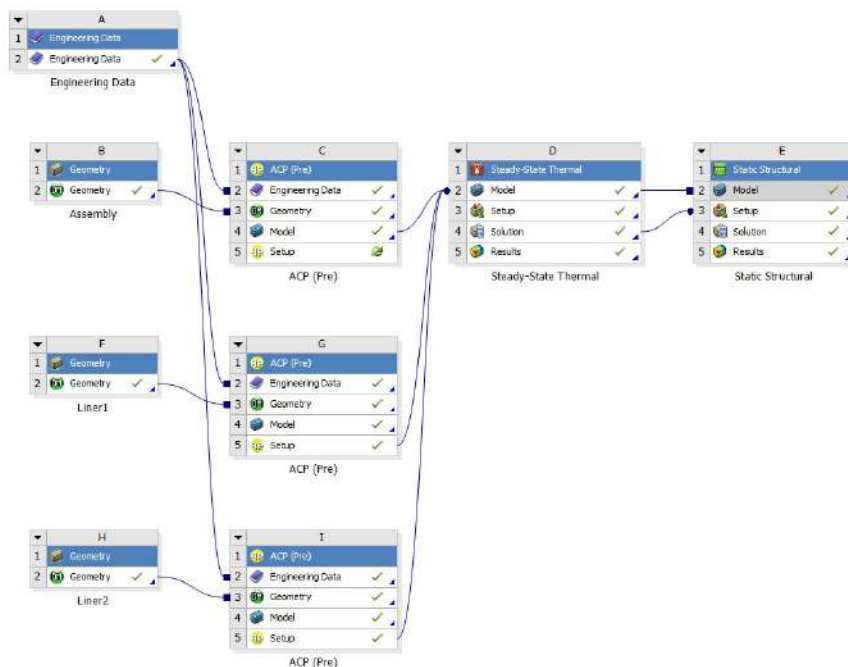


Figure 4.4: Analysis workflow

4.1.3 Liner

Figure 4.5 presents mesh taken for the detailed strength analysis of porous ceramic matrix composite liner. This is a crucial part of assessment, because WHIPOX is a relatively new material, which can be characterized by the orthotropic elastic constants. Its failure modes are very complicated, because of the interaction between porous matrix and thousands fibers inside. Presented mesh was created in ACP software (figure 2.30) designed to preprocess composite analysis. As a result of that, to improve the accuracy, the thickness of each mesh layer is consistent with the width of a ply. Such mesh consists of 529788 nodes and 500320 structural hexagonal elements.

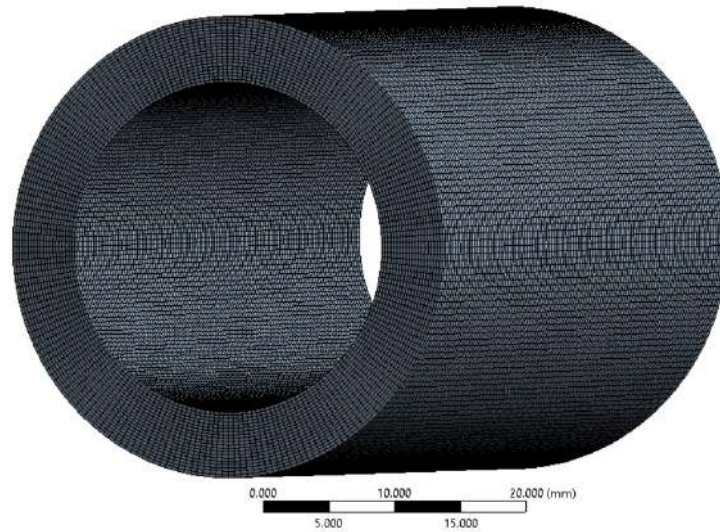


Figure 4.5: Mesh used for isolated liner analysis

Figure 4.6 presents three plies out of twenty modelled - top one, middle one and bottom one. Each of them has thickness of 0.25mm, which altogether gives 5mm total thickness (20 plies applied). As mentioned before, each ply is modelled as a layer of hexagonal elements.

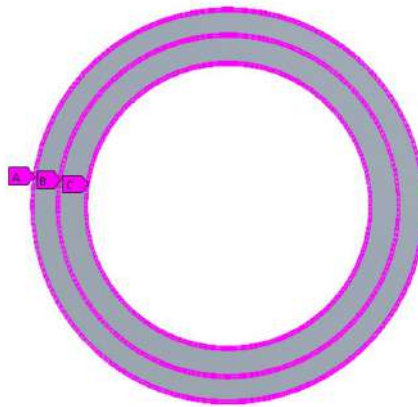


Figure 4.6: View at the top (A), middle (B) and bottom (C) plies



Figure 4.7: Full CFD combustion domain

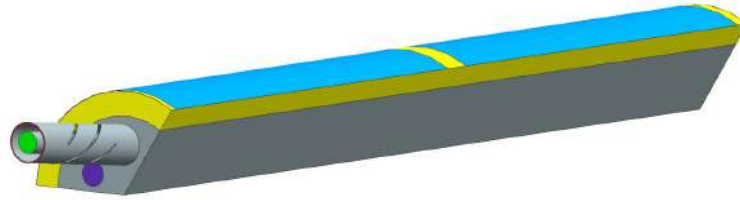


Figure 4.8: CFD combustion domain sector

4.1.4 Computational Fluid Dynamics Model

Computational Fluid Dynamics (CFD) model was build during the process of creating advanced Thermal-FSI model. That step was crucial, because it let to significantly reduce time required for tuning analysis settings. That iterative process was build from multiple steps, starting from cold uniform flow towards advanced CFD model containing combustion and water evaporation.

Figure 4.7 presents full CFD domain containing explicit oxygen and fuel swirlers, which are designed to enhance mixing intensity by the opposite spin. Additionally, there are positioned at the angle to the main axis which additionally promotes mixing intensity and complete combustion. There are also three circles at the cap, which are located at the water spray nozzle positions.

Figure 4.8 takes cyclic symmetry advantage of the design. 120 degrees model reduces geometry by 66% while taking into account all key aspects of flow. Red ring at the left marks gas fuel inlet which is swirled in the counter-clockwise direction. Green surface inside in an oxygen inlet which is swirled in the clockwise direction. Purple dot is the water spray nozzle inlet, where water droplets are injected directly into the core of the flame. Light blue surfaces is the inlet of water at the surface of the porous CMC liner. After multiple attempts of liquid water injection it was found that analysis is unstable and struggles to converge. To improve numerical stability, water vapour was injected instead of liquid phase. However, that approach required to separate yellow domain and define it as a latent heat sink.

4.1.5 Fluid-Solid Interaction Model

Fluid-Solid Interaction (FSI) model presented on figure 4.9 contains both solid and fluid domains, so thermal interaction between them is captured at the same time. To improve stability and convergence, consistent mesh was created at the every interface. Mesh size was set to 23 millions nodes to maintain the balance between results accuracy

and model size/computational time. To achieve that, certain domains with low impact to temperatures and stresses were suppressed. Based on physics understanding, it was assumed that fluid domains supplying methane and oxygen have secondary impact to temperature distribution inside heavily cooled copper cap. A significant number of node count reduction was achieved by suppressing CFD swirlers domains, which otherwise have to be very fine due to the narrow highly curved oxygen/fuel channels. Instead of this, oxygen/fuel streams are supplied from flat surface with appropriate inlet angles taking into account each swirler pitch and position.

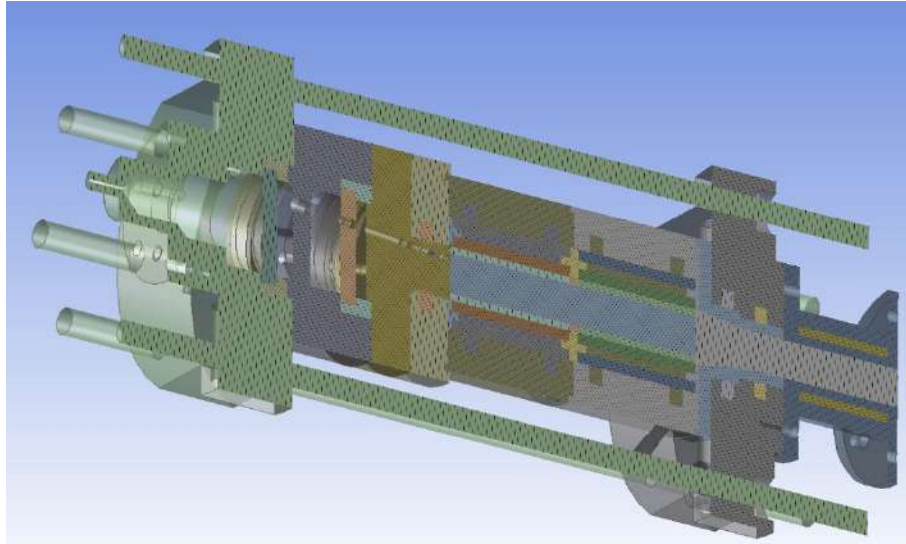


Figure 4.9: Fluid/solid domains taken for FSI model

4.2 Boundary conditions

4.2.1 Static liner

Figure 4.10 presents analysed liner in a form of wireframe. As a preparation for the boundary condition application, surface of the cylinder was split horizontally and vertically on four symmetric pieces. Support boundary conditions were applied on three vertexes in a way to restrain all six degrees of freedom. An attention was paid to avoid over-constraining, so liner can freely expand and contract in all direction without introducing reaction forces. Point A on figure 4.10 is a fixed support applied in a point, so that point movement is restrained in all directions (X, Y, Z). Displacement B supports structure in two directions (X and Y) leaving Z direction unsupported. Thanks to that, liner can freely expand and contract thermally without any reaction force. Based on these two points, only five degrees of freedom are restrained, so liner still can rotate around axis AB. To support the last degree of freedom, point C was restrained in the Y direction.

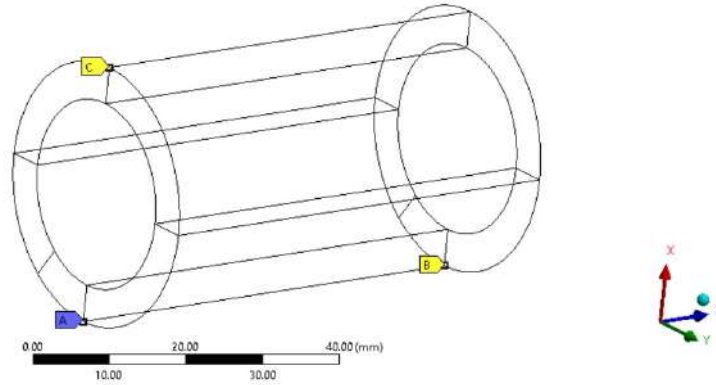


Figure 4.10: Support boundary condition

Figure 4.11 shows pressure boundary conditions applied to the liner. This selection is based on the physics interpretation. Internal pressure B is fixed at an absolute pressure of 1MPa. This is treated as unchanged, because combustion chamber control system maintains it by regulating fuel and oxygen inlet pressure. External pressure A is a function of flow resistance inside the porous material of liner. It should be high enough to ensure proper liquid mass flow required for a transpiration cooling. This pressure can change over time due to the matrix condition change such as local blockage of internal crack propagation. As a result of that, sensitivity study will be performed to assess safe operational conditions.

Figure 4.12 presents thermal boundary conditions applied on both sides of porous liner. The precise assessment of these temperatures will be performed using global fluid-solid interaction model, however due to the level of complexity involved, the results uncertainty level will be significant. This is due to the fact, that three complicated physical processes happen simultaneously: combustion, water evaporation and porous media flow. For the purpose of the sensitivity studies, external temperature was fixed at 100 °C. This can physically happen, as water boiling temperature at pressure 1MPa is equal to 183 °C and grows with the pressure rise. In fact what really matters mechanically is the thermal gradient across the wall, so outer surface temperature variance has a secondary impact. Internal temperature in the sensitivity study is going to vary between 150 and 350 °C with step of 50 °C. That range is very likely to capture possible conditions variations within

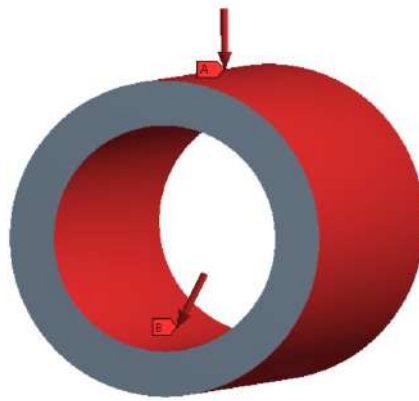


Figure 4.11: Pressure boundary condition

the planned running range.

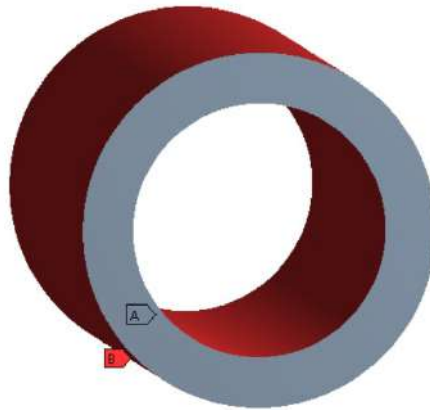


Figure 4.12: Temperature boundary condition

4.2.2 Transient liner

A series of transient liner analyses were made in order to capture stress overshoot driven by the temporary local thermal gradients. To capture most likely scenarios, eight acceleration rates were analysed from 1 to 15 seconds. All of them were restrained consistently to the static case (Figure 4.10) and have pressure/temperature uniformly applied at the internal and external surfaces. Figure 4.13 presents single case where external temperature is kept constant at 20°C and internal temperature grows linearly from 20 to 200 °C. Similar linear approach was taken for the pressure load, where initial 0.1 MPa pressure grows to 1MPa internally and 1.7MPa externally. Pressure drop across the wall was chosen at the most likely level, but steady-state analysis revealed that this parameter has a secondary effect on the stress level inside ceramic composite liner.

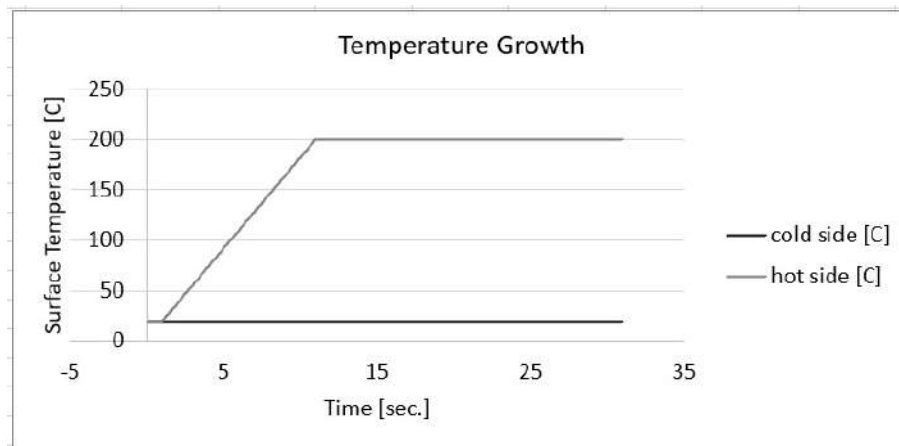


Figure 4.13: Temperature growth assumption (10sec. case)

4.2.3 Static assembly – solid

Figure 4.14 presents analysed assembly model, which is restrained by two bulky rings on both sides. Eight equally spaced rods provide a support for rear ring, which is expected to move rearwards under the thermal expansion. Each ring contains two pairs of flat surfaces designed to match support fixtures. Front lower pair is restrained in three points to support all six degrees of freedom. Front upper part is restrained in single point in axial and circumferential directions. Rear lower pair is supported in one point in radial and circumferential direction. Rear upper pair is supported circumferentially in a single point. That arrangement was carefully chosen to model rear support as closely as possible without unrealistic over-constraints. Figure 4.14 presents analysed assembly model, which is axially compressed with eight uniformly distributed springs. This is crucial to maintain proper sealing capability between adjacent elements which are made from different materials and are subject to strong thermal gradients. Axial load of the set of springs is equal to 800N, which was modelled as eight pairs of forces acting axially in the opposite directions.

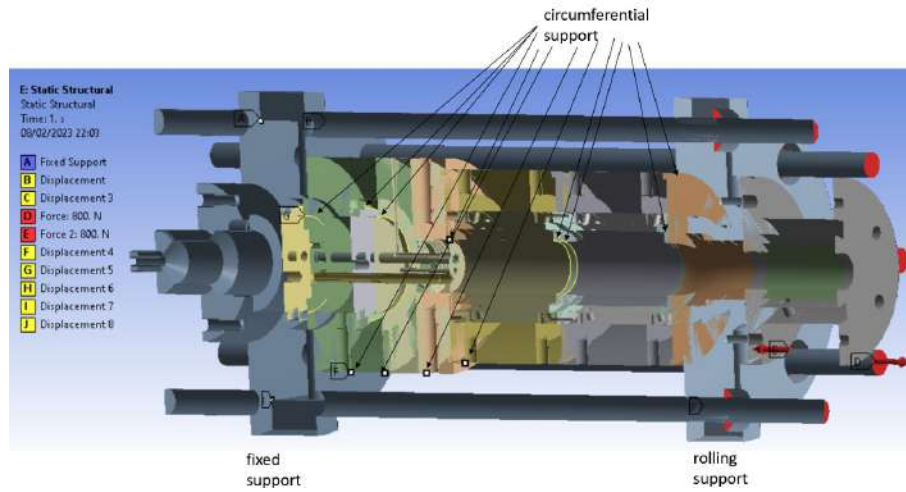


Figure 4.14: Assembly support

Assembly cross-section at Figure 4.15 presents contact surfaces between adjacent metal components. Proper contact modelling is crucial to capture interaction between elements made from different materials and loaded with temperature gradients and external loads. Especially important region is located around flame zone, where thermal gradients are the highest.

Figure 4.16 highlights key set of contacts, which are defined between copper rings and ceramic matrix composite liners. This approach required special attention, as it combines isotropic with orthotropic elements, which were defined and meshed in another composite pre-processor (ACP) software. Supporting rings were made from copper, as it has very high thermal conductivity coefficient helping with efficient cooling.

All elements have interpolated temperature from the simplified thermal analysis. Figure 4.17 highlights a set of surfaces, which are cooled by the liquid water. Looking from left to right, second and third channel supply cooling water inside the combustion chamber through the porous ceramic liner. All highlighted surfaces have thermal boundary condition applied equal to 80 °C. This value is higher than water inlet temperature (20 °C), but lower than the water boiling temperature at the pressure 10.5 bar (183 °C).

Frictionless contacts were applied between non-bolted adjacent elements to reduce com-

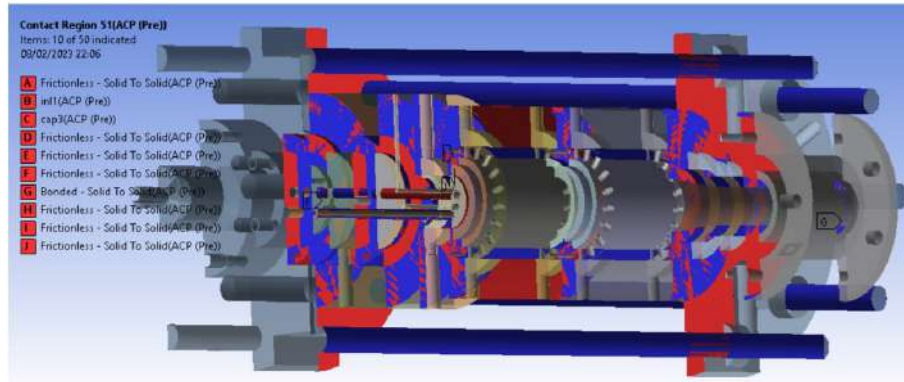


Figure 4.15: Contact surfaces between metal elements

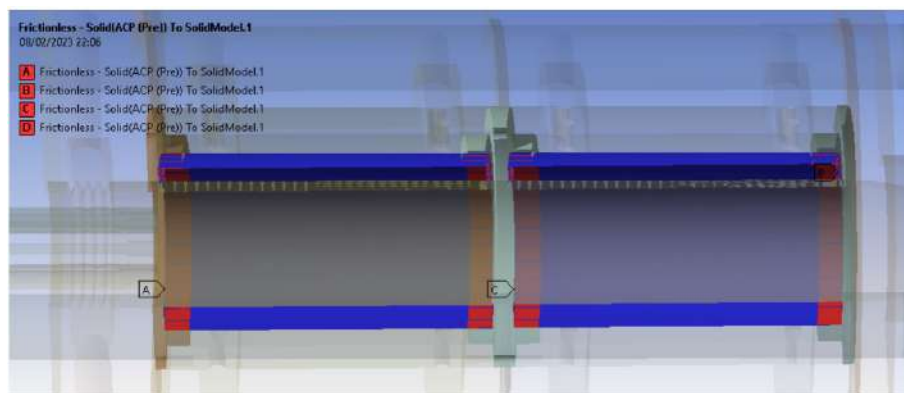


Figure 4.16: Contact surfaces between liners and supporting copper rings

putational time and complexity. However, to provide efficient constraints, that approach was complemented with the circumferential displacement for every cylindrical component. Otherwise mechanical model will not be sufficiently restrained due to the possibility of cylindrical elements spin.

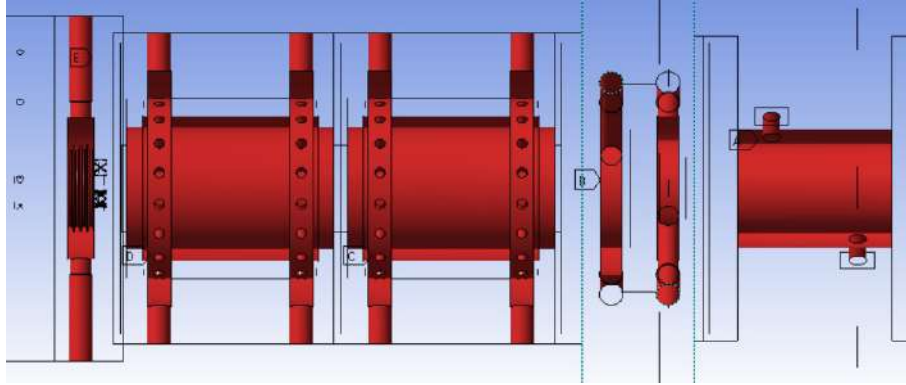


Figure 4.17: Cooling system

4.2.4 Transient assembly – solid

Transient analysis of wet combustion chamber assembly is a particularly complex task, so only the worst case scenario was taken into consideration. From the peak stress perspective, one-second acceleration from cold to hot condition for the 175°C thermal gradient ($255^{\circ}\text{C}/80^{\circ}\text{C}$) is considered. At this stage of analysis no CFD assessment was done, so combustion is modelled as an uniform temperature at the heated and cooled surfaces. All other boundary conditions like contact definition and mechanical support are consistent with steady-case model described in the previous Chapter.

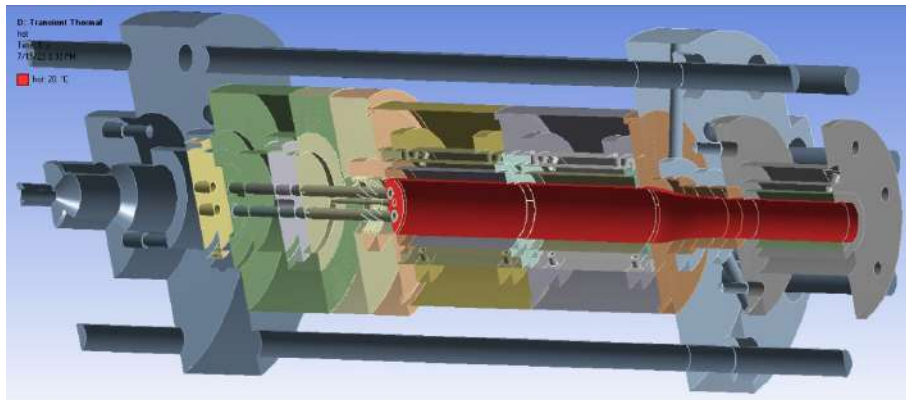


Figure 4.18: Heated surfaces

In the initial condition (first second of analysis), all domains presented on Figure 4.18 have ambient temperature equal 20°C . This period is a starting point for the next second of analysis, where full scale flame is formed. During this phase all surfaces highlighted on Figure 4.18 are rapidly hot (255°C) whereas all surfaces presented on Figure 4.19 getting to the temperature of 80°C .

Wet Combustion Chamber, but for simplicity fuel/oxygen supply system was suppressed and replaced by the implicit definition at the later stage. Cell D consists Fluid-Solid Interaction analysis, as fluid and solid domains are coupled together in a form of single hybrid mesh. Cells F and I contain front and rear liners, as they need to be preprocessed as composite materials in contrast to isotropic components from cell B. Cells G and J are preprocessors of front/rear liners, where plies structure such as fibers angle is defined. Cell H preprocessor is required to capture contacts between structural elements, which was not modelled in similar cell C. Cell E is a static structural analysis of the entire assembly, which imports temperature distribution from the Fluid-Solid Interaction cell D.

Figure 4.21 presents 3D thermal FSI model containing both solid and fluid domains. This approach has a significant advantage over non-combined fluid and solid models, because thermal conduction between hot and cold zones is a function of temperature.

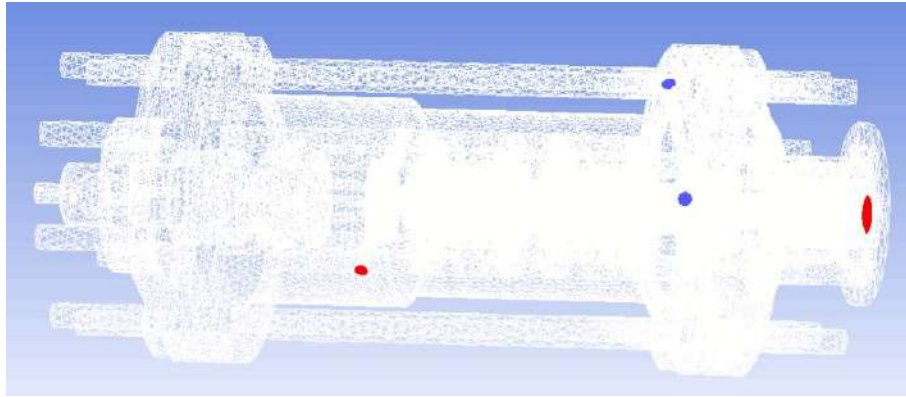


Figure 4.21: Fluid-Solid Interaction model

Key elements of built thermal fluid-solid interaction model are:

- $\kappa - \omega SST$ model of turbulent flow
- Volumetric Species Transport method to predict local mass fraction of each species within the wet combustion chamber
- Eddy-Dissipation method method to model turbulence-chemistry interaction
- GRI-Mech 3.0 chemistry mechanism model
- Discrete Phase Model (DPM) model to evaporate discrete water droplets

Figure 4.22 shows geometry detail of Fluid-Solid Interaction model. The entire structure is supported on two rings, which have displacement boundary conditions applied. To avoid over-constraining, geometry is supported on three points at the front and along the line at the rear. Point A is a fixed support, so translation degrees of freedom are taken by it. Points B and C support all three rotational degrees of freedom without unnecessary over-constraining. Line D supports five degrees of freedom, as axial displacement is crucial to compensate thermal expansion (otherwise structure could be damaged by excessive thermally-driven axial stresses). All contacts are applied as frictionless to improve solution stability and reduce computational time. The disadvantage of such approach is that cylindrical components have unsupported one degree of freedom, so circumferential displacement was applied to each of them (displacements E,F,G on Figure 4.22).

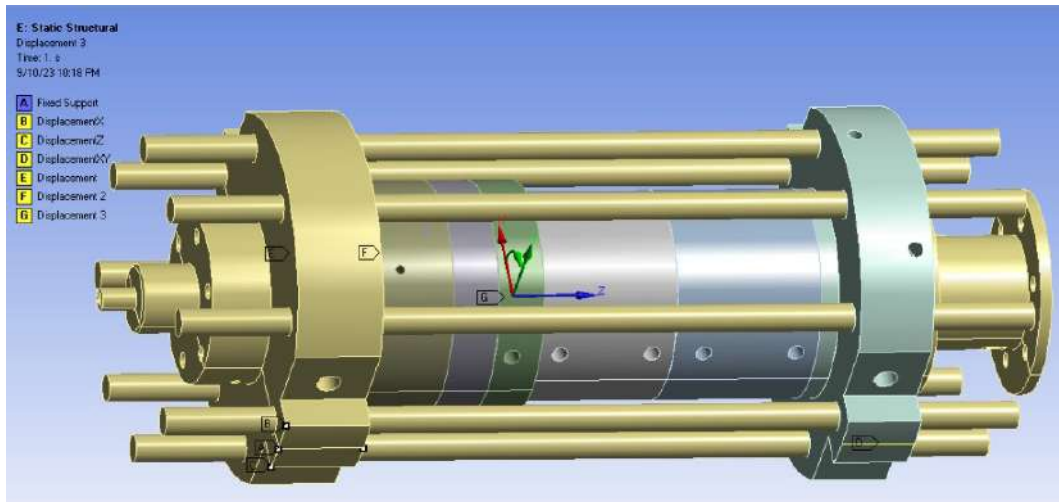


Figure 4.22: Fluid-Solid Interaction model support

Due to numerical problems with liquid water evaporation modelling at the liners' porous surface, it was decided to supply water vapour instead. Figure 4.23 presents three types of domains: liner (grey), vapour mass source/energy sink (blue) and hot gas path (red and blue). Special attention needs to be paid to blue cylindrical domains, which supplies water vapour at required mass flow - 9g/s at the front and 3g/s at the rear. That split was figured out during an iterative process assessing liners' surface temperature. Note, that mass source was applied uniformly at the entire volume of blue domains, which is a fair assumption that in the real chamber water will evaporate at a few millimetre distance from the wall. To satisfy energy conservation law, blue domains are also a uniform heat sink at the rate equivalent to water latent heat, which assumes that transpiration water evaporates uniformly in the entire volume of blue domains.

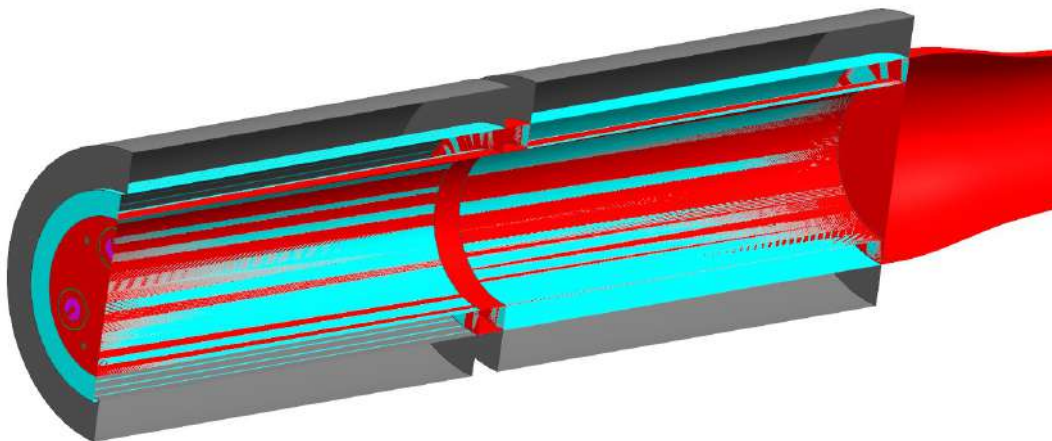


Figure 4.23: Water vapour heat sink/ mass source domains

Figure 4.24 corresponds to Figure 4.23, but is focused at the Wet Combustion Chamber inlet pattern. Apart from the colour code used for domains, front surface of hot gas path is split between regions according to supplied medium. Central pink area of each swirler

is an inlet of oxygen (4.8g/s total), green ring is an inlet of methane (1.2g/s total) and brown circle aside is a water spray nozzle ejection (2g/s total).

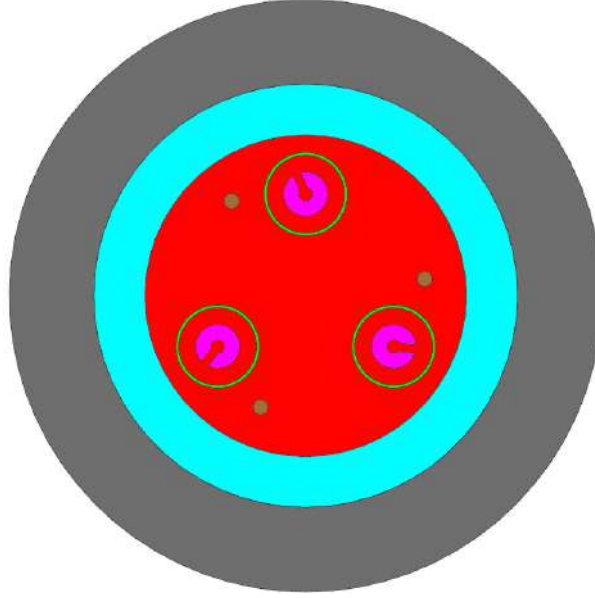


Figure 4.24: Cap inlet pattern

4.2.6 Wet liner transient model

Wet liner mathematical model is a crucial element of this doctoral dissertation, as dry porous medium behaves differently to the wet one. The reason behind is the pore's support force acting between fluid and wall, which in the general case is described by the equation 4.1 below.

$$\underline{F}_{sup} = F_{sup} \underline{n} = - \left(F_{cru} - F_{cru} E_{\mu} \frac{dV_p}{dt} \right) \underline{n} \quad (4.1)$$

where: \underline{F}_{sup} is a pore support hydrostatic force, F_{cru} is a crushing force, V_p is a pore volume, E_{μ} is a fluid function, t is a time, \underline{n} is an unit vector normal to the pore surface.

Hydrostatic support force \underline{F}_{sup} acts at the normal direction to the pore's surface \underline{n} and can be carried by the pressure increase within the trapped incompressible fluid. In the extreme case, when impact crushing force is applied, constant pore volume filled with incompressible fluid carries all the hydrostatic load between walls ($\underline{F}_{sup} = -\underline{F}_{cru}$).

Porous material crushing support force impact needs to be supplemented by the pore geometry, which in general case has a candy shape, i.e. narrow inlet and outlet with a cavity between (Figure 4.25). If the pore is filled with the gas, material properties do not change substantially with the speed of applied external load. This is a consequence of a fact that gas has low viscosity and is compressible. Completely different situation occurs when pores are filled with water, which during rapid strains can carry hydrostatic load between walls, as it has no enough time to flow away and is non-compressible. Viscous force is a function of dynamic viscosity, wetted area and velocity gradient. Rapid deformation does not affect viscosity and the impact to the wetted area is minimal. The main variable is water velocity gradient, which has transient plugging effect leading to water trap inside the pore.

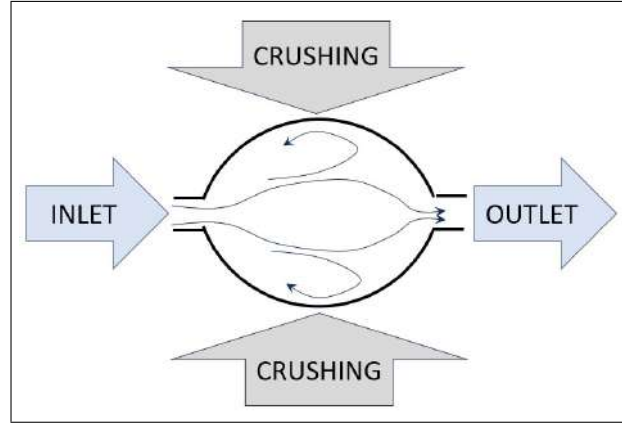


Figure 4.25: Pore crushing diagram

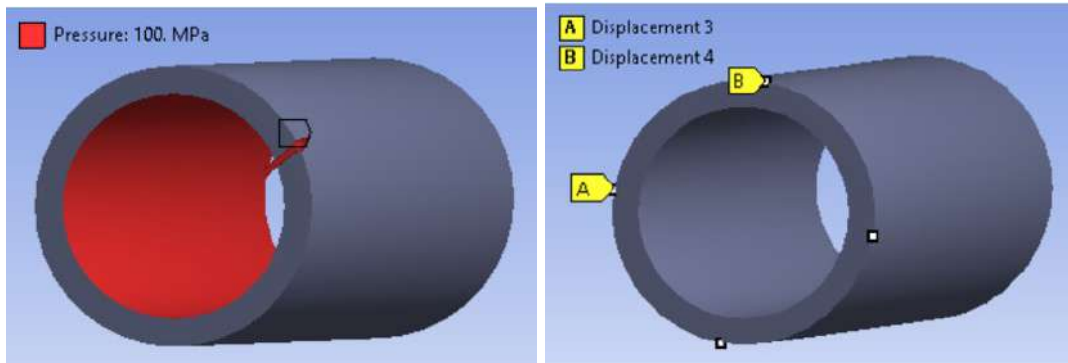


Figure 4.26: Pressure and support boundary conditions

Figure 4.26 presents geometry taken for the analysed case together with the load and support applied. Cylindrical shape and material properties were chosen to be consistent with liner made from porous ceramic matrix composite material. For clarity, internal uniform pressure was applied at the 100 MPa level. This is not consistent with combustion chamber liner, where thermal load dominates pressure. Nevertheless, it was decided that pressure load is a better choice due to its simplicity. Figure 4.26 presents support system, which was designed to constrain position of the main axis, to let free radial expansion in all directions. To obtain that, all four displacement points restrain all directions apart from the radial one.

Figure 4.27 presents concentric position of orthotropic properties of WHIPOX CMC material and reference coordinate system. For simplicity, theta angle of fibers was chosen at zero degrees, so Composite Preprocessor (ACP) was not required at this stage. For obvious reasons, cylindrical coordinate system was chosen, where axis X is radial position, axis Y is circumferential direction and axis Z is aligned with main axis of symmetry.

Direct application of wet porous zone support force F_{cru} is not yet available in the commercial CFD codes, due to the high level of complexity. As a consequence, in the presented thesis non-direct support force implementation was employed in the clear and robust manner. That method is based on the fact, that support force F_{cru} is driven by incompressible fluid pressure inside the pore, which stiffens Young and shear modules of the orthotropic material. That effect was introduced to the numerical model by time-evolution of aforementioned modules, which is controlled by model constants listed in

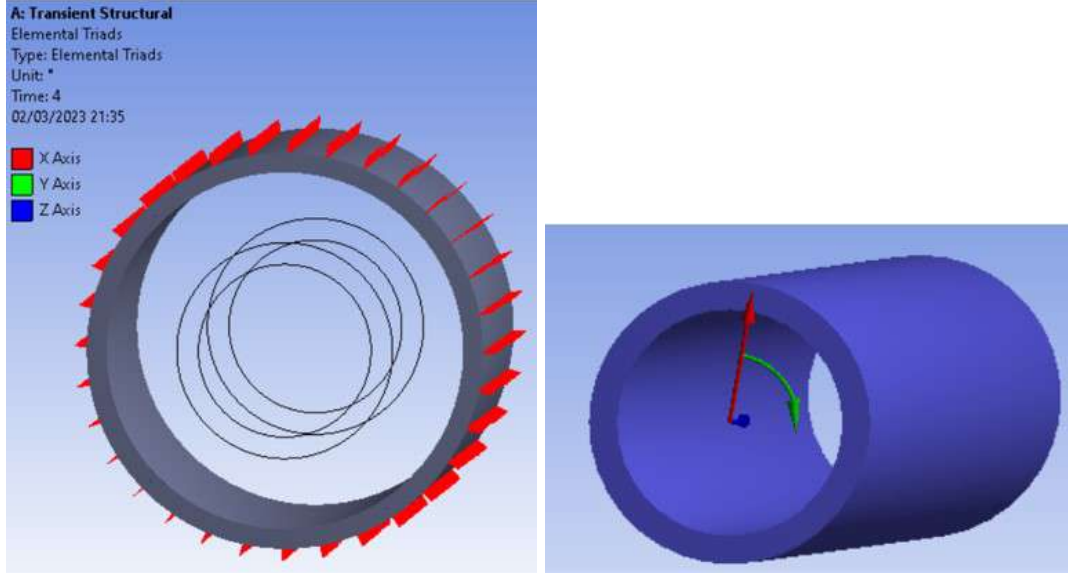


Figure 4.27: Material properties orientation

Table 4.1. They were calibrated based on the series of analyses performed for the same porous material. That approach have led to the generation of the model, which is easily applicable to the CSD analysis as an APDL procedure, which implementation does not extend the solution time.

Process of variable Young and Shear Modulus selection is based on dry CMC liner analysis results presented on Figure 4.28. This graph shows transient hoop stress distribution at the surface of the hot liner, which was heated from 20°C to 200°C within the one second (compare with Figure 5.18). Based on this data, five periods of constant stress gradient were selected, where gradients were as follows: -95.77MPa/sec, 25.26MPa/sec, 5.68MPa/sec, 0.81MPa/sec, 0MPa/sec. During the next step, scaling factors were obtained by multiplication of absolute gradients' values by 0.01044 on heated surface and 0.00522 on cooled surface. These baseline factors were tailored to generate maximum Young/Shear modulus factors on 1.0 and 0.5 on hot and cold surface respectively. These factors have a very complex physical meaning when applied into porous CMC liner, so their precise values have to be obtained during a testing programme. For the following four gradient periods, baseline scaling factors are scaled down based on the hoop stress gradient. Based on the physics interpretation, it was decided to not scale Poisson's factors due to their insensitivity to the wet liner condition.

Equation 4.2 presents hoop stress (σ_h) evolution over the time and is consistent with Figure 4.28. It is based on the dry porous media.

$$\sigma_h = -99.216 \cdot (t - 0.7)^{-1.567} - 20 \quad (4.2)$$

Equations 4.3 and 4.4 govern wet Young modulus (\underline{E}_w) and shear modulus (\underline{G}_w). They are expressed as a function modifying dry modules \underline{E}_d and \underline{G}_d based on "dry" hoop stress time derivative $\partial\sigma_h/\partial t$ and scaling factor ζ . Note that for the orthotropic material three elastic modules are applicable which varies based on the direction.

$$\underline{E}_w(t) = \underline{E}_d \left(1 + \frac{\partial\sigma_h}{\partial t} \zeta \right) \quad (4.3)$$

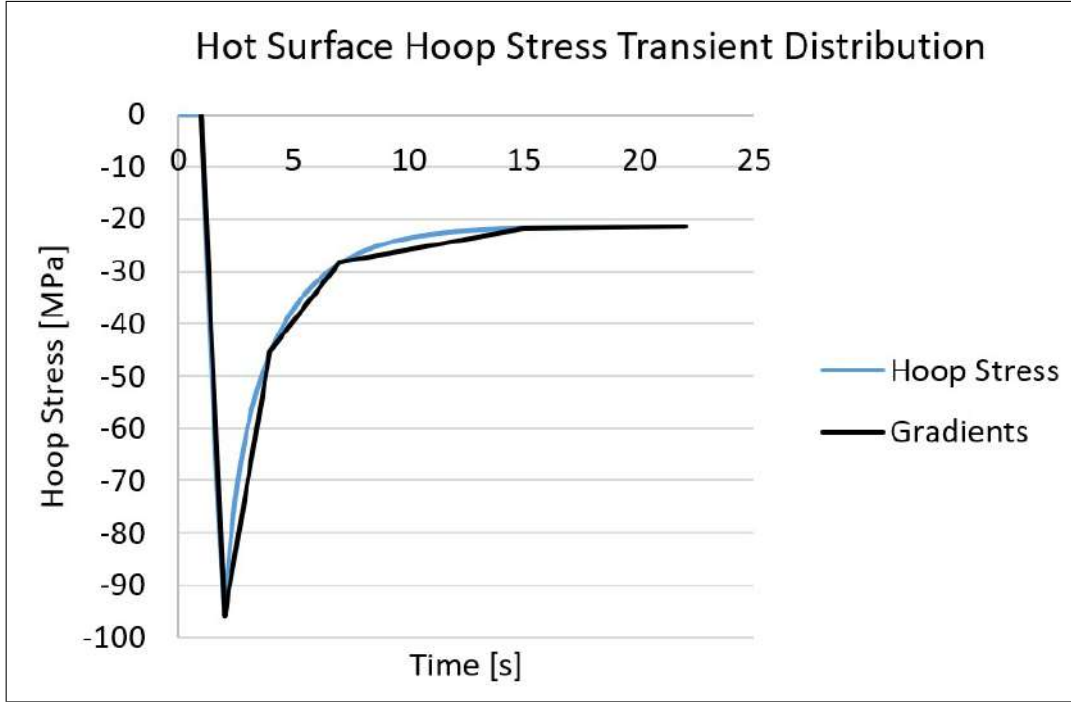


Figure 4.28: Variable Young/Shear Modulus selection

$$\underline{G}_w(t) = \underline{G}_d \left(1 + \frac{\partial \sigma_h}{\partial t} \zeta \right) \quad (4.4)$$

where ζ scaling factor was interpolated linearly across the liner's wall based on the equation 4.5

$$\zeta = \begin{cases} 0.012614 & \text{for hot surface} \\ 0.006307 & \text{for cold surface} \end{cases} \quad (4.5)$$

and "dry" hoop stress time derivative $\partial \sigma_h / \partial t$ is given by the equation 4.6.

$$\frac{\partial \sigma_h}{\partial t} = -99.216 \cdot (-1.567) \cdot (t - 0.7)^{-2.567} \quad (4.6)$$

Table 4.1 presents wet CMC liner analysis profile, which was defined to capture variable Young/Shear Modulus impact to liner's stress. To obtain that, time increments and modulus factors were matched to the analysis results presented on Figure 4.28. In the Ansys Mechanical environment, variable material properties were defined as a APDL code presented on Figure 4.29. Note that this is an alternative method to modify elastic modules, so it is not based on the equations 4.2 to 4.6.

Figure 4.29 presents a block of Ansys Parametric Design Language (APDL) commands which were used to manage material properties over the analysis time. Function "TB" activates a data table for material properties, according to the pattern "TB, Lab, MATID, NTEMP, NPTS, TBOPT". In this code, "Lab" is the material model, "MATID" is material reference identification number, "NTEMP" is the number of temperatures for which data is provided, "NPTS" is number of data points to be specified at a given temperature, "TBOPT" is elasticity options input. In the provided code, "ELASTIC" means that elasticity specification is supplied, first "1" means that first material is modified, second

Time [sec.]	0 to 1	1 to 2	2 to 4	4 to 7	7 to 15	15 to 22
Pressure [MPa]	0	0 to 100	100	100	100	100
Inner Side Modulus Factor [-]	1.000	1.500	1.132	1.030	1.004	1.000
Outer Side Modulus Factor [-]	1.000	2.000	1.264	1.059	1.008	1.000

Table 4.1: Wet CMC liner analysis profile

"1" means that data for a one temperature is provided, "9" means that nine parameters are provided for each time point. "OELN" means that orthotropic option was chosen with major Poisson's ratio (EX,EY,EZ,GXY,GYZ,GXZ,PRXY,PRYZ,PRXZ), where E is Young modulus at directions X Y Z, G is shear modulus at directions XY YZ XZ, PR is Poisson's ratio at directions XY YZ and XZ. "TBEO,FDCS,1" sets coordinate system to the user-predefined one, which in the example is cylindrical coordinate system presented in Figure 4.27.

Below the APDL header, a series of data inputs are presented for time points defined as "TBFIELD,TIME,X": 0sec, 1sec, 2sec, 4 sec, 7 sec, 15sec and 22sec. Each time step has got two sets of data: "TBFIELD,XCOR,40" and "TBFIELD,XCOR,50", which stand for internal (40mm) and external (50mm) surface radial position. This is very important to differentiate transient effect between heated and cooled surfaces, as stress and strain time distribution varies between them. Figure 5.18A presents hoop stress at hot surface which drops rapidly to -95.77MPa (1sec acceleration period) and stabilizes after 20 seconds at 22 MPa level. That particular graph was used to read stress gradients between key time points, which helped to find material properties at analysed transient time points. Note that variation at cold surface (radius = 50mm) is half the magnitude in comparison to hot surface (radius = 40mm), because internal surface is subject to sudden heating from ambient to combustion condition temperature.

```

TB,ELASTIC,1,1,9,OELN
  TBEO,FDCS,1

  TBFIELD,TIME,0
  TBFIELD,XCOR,40
  TBDATA,1,1.25e5,1.02e5,1.02e5,0.43e5,0.43e5,0.43e5,0.144,0.193,0.193
  TBFIELD,XCOR,50
  TBDATA,1,1.25e5,1.02e5,1.02e5,0.43e5,0.43e5,0.43e5,0.144,0.193,0.193

  TBFIELD,TIME,1
  TBFIELD,XCOR,40
  TBDATA,1,1.25e5,1.02e5,1.02e5,0.43e5,0.43e5,0.43e5,0.144,0.193,0.193
  TBFIELD,XCOR,50
  TBDATA,1,1.25e5,1.02e5,1.02e5,0.43e5,0.43e5,0.43e5,0.144,0.193,0.193

  TBFIELD,TIME,2
  TBFIELD,XCOR,40
  TBDATA,1,2.5e5,2.04e5,2.04e5,0.86e5,0.86e5,0.84e5,0.144,0.193,0.193
  TBFIELD,XCOR,50
  TBDATA,1,1.88e5,1.53e5,1.53e5,0.65e5,0.65e5,0.64e5,0.144,0.193,0.193

  TBFIELD,TIME,4
  TBFIELD,XCOR,40
  TBDATA,1,1.58e5,1.29e5,1.29e5,0.54e5,0.54e5,0.54e5,0.144,0.193,0.193
  TBFIELD,XCOR,50
  TBDATA,1,1.41e5,1.15e5,1.15e5,0.49e5,0.49e5,0.48e5,0.144,0.193,0.193

  TBFIELD,TIME,7
  TBFIELD,XCOR,40
  TBDATA,1,1.32e5,1.08e5,1.08e5,0.45e5,0.46e5,0.46e5,0.144,0.193,0.193
  TBFIELD,XCOR,50
  TBDATA,1,1.29e5,1.05e5,1.05e5,0.44e5,0.44e5,0.44e5,0.144,0.193,0.193

  TBFIELD,TIME,15
  TBFIELD,XCOR,40
  TBDATA,1,1.26e5,1.03e5,1.03e5,0.43e5,0.43e5,0.43e5,0.144,0.193,0.193
  TBFIELD,XCOR,50
  TBDATA,1,1.26e5,1.02e5,1.02e5,0.43e5,0.43e5,0.43e5,0.144,0.193,0.193

  TBFIELD,TIME,22
  TBFIELD,XCOR,40
  TBDATA,1,1.25e5,1.02e5,1.02e5,0.43e5,0.43e5,0.43e5,0.144,0.193,0.193
  TBFIELD,XCOR,50
  TBDATA,1,1.25e5,1.02e5,1.02e5,0.43e5,0.43e5,0.43e5,0.144,0.193,0.193

```

Figure 4.29: APDL command used to modify porous medium mechanical properties

Chapter 5

Results

5.1 Liner - validation case

The key enabler of the Wet Combustion Chamber concept is liner made from WHIPOX, which is a porous Ceramic Matrix Composite (CMC) material described on section 1.3. It is resistant to very high temperatures as a ceramic, but does not break in a brittle way due to the matrix/fibre interaction. Its porous structure prevents matrix cracks from fiber penetration and enables transpiration cooling. One of the key parameters taken to FEM analysis is material thermal expansion, so it was experimentally found at the Institute of Fluid-Flow Machinery in Gdansk, Polish Academy of Sciences. Based on results presented on Figure 5.2, thermal expansion coefficient applied to FEM model predicts very well experimental results marked with a continuous line. Thermal expansion module was split into two ranges - below temperature of 100 °C it is equal to 1.84E-6, whereas above it is equal to 8.88E-6. This is of course only a simplification, which interpolates non-linear thermal expansion coefficient of ceramics made from 85% of Al_2O_3 and 15% of SiO_2 [183].

Figure 5.2 presents experimental setup used to measure liner thermal expansion. Red line at the right side is the strain gauge, which measured axial expansion of liner at the distance of 10mm. A complementary microscope photos were taken and shown on Figure 5.3. The left one uses 1mm linear scale, whereas the right one is magnified ten times. Both photos show structure of fibers embedded in the porous ceramic matrix. At the given example theta angle between fibers is 75 °, in which case liner has got increased

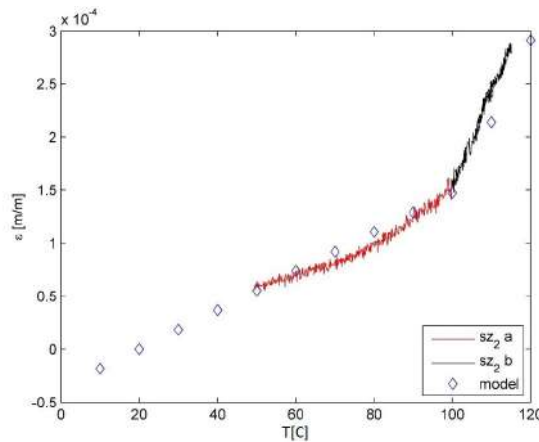


Figure 5.1: Liner thermal expansion measurement (*theta* 75°)

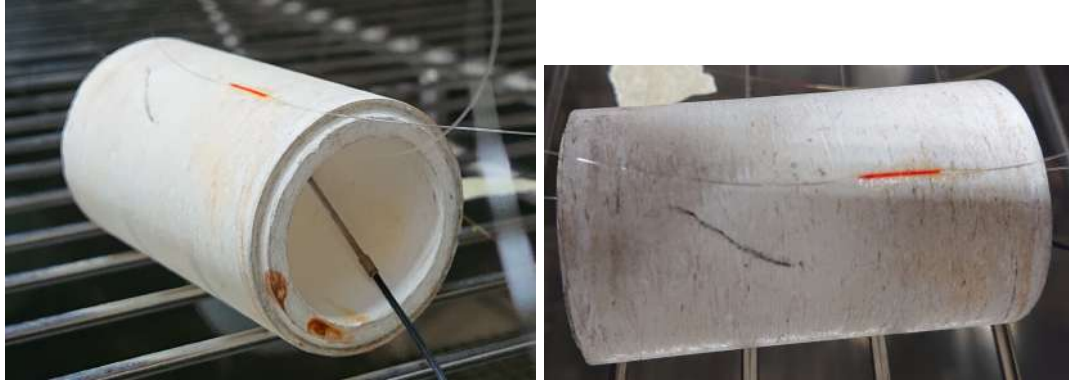


Figure 5.2: Liner thermal expansion measurement setup*

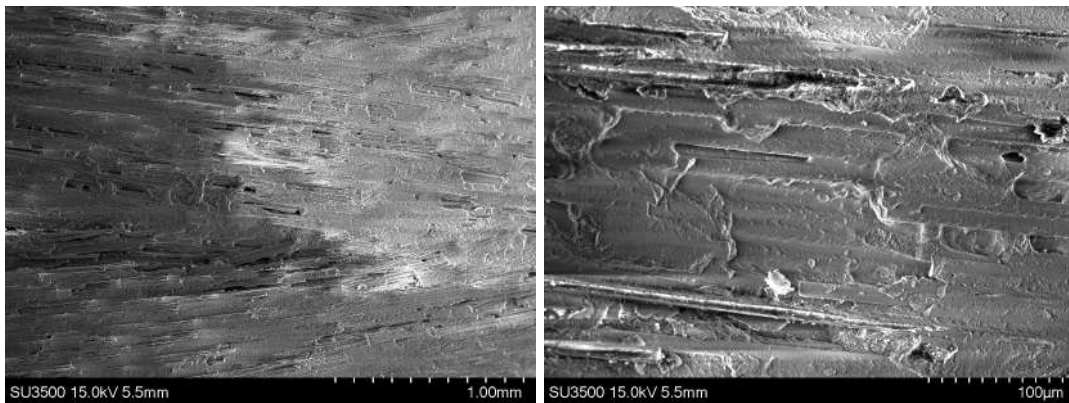


Figure 5.3: Liner microstructure*

strength in the hoop direction. On top of that, matrix porosity can easily be recognised in a form of empty gaps between fibers.

* Photos courtesy of D.Sc. Ph.D. Eng. Magdalena Mieloszyk, Associate Professor of IFFM PAS

5.2 Liner results – static

Figure 5.4 shows a temperature distribution through the wall, where value outside is 100 °C and inside is 250 °C. For the performed sensitivity studies, the highest thermal gradient is 250 °C (100 °C externally to 350 °C internally). Other thermal gradients look similar to this plot - the only difference is the maximum value at the top of the scale. Such temperature distribution is a simplification, as the actual component is made from the porous medium filled with liquid water. For that reason, the internal temperature is not expected to exceed boiling point by much (which is 183 °C in 1MPa pressure). In the extreme case outside temperature can be as low as 20°, so the highest theoretical gradient should not exceed 163 °C.

Figure 5.5 presents theta angle definition of two adjacent plies. Due to the difficulties with explicit modelling of actual WHIPOX wounded pattern, Shi et al. [17] created a CSD model based on the equivalent unidirectional (UD) layers. For presented combustion chamber analysis, theta angle varies from zero to 90°. Note that liner is made from 20

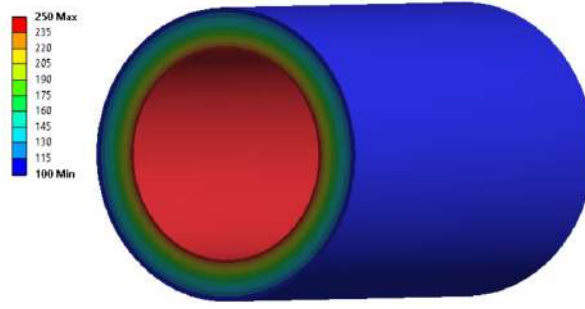


Figure 5.4: Liner temperature distribution for the lowest gradient case [°C]

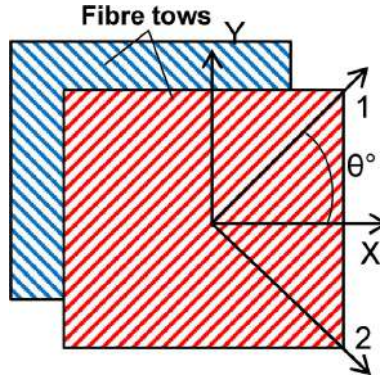
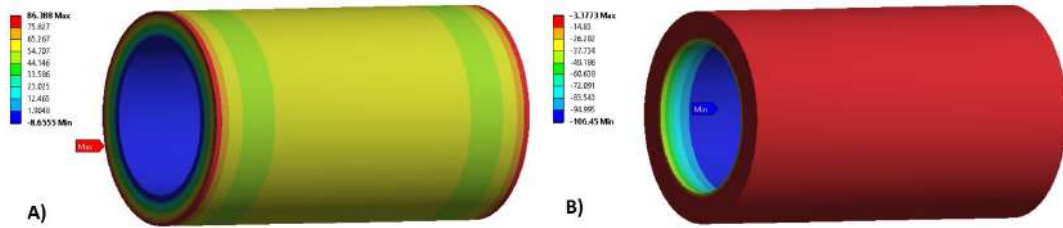


Figure 5.5: Theta angle definition [17]

plies, so 45° means 10 pairs of -45° and $+45^\circ$.

Figure 5.6 presents first and third principal stress plot for a thermal gradient 150°C , pressure difference 3 MPa and fiber angle $\pm 75^\circ$. Based on the physical interpretation, there is a strong thermal fight between the hot core and cold exterior (wall thickness is only 5mm). Hot interior tries to expand axially, circumferentially and radially leading to the tensile load outside. From the other side, cold exterior expands less in all three directions adding compression into the hottest surface. Figure 5.6 A) contains plot of first principal stress, which reveals that more of liner's body is loaded in tension, with peak value at the edges - the most flexible cold region. Figure 5.6 B) reveals, that very low third principal stress (below 90 MPa) occurs at the relatively thin region containing few internal plies. The internal/external surface area ratio causes slight load imbalance, because cold region is bigger (stronger) than hot region.

Figure 5.6: First principal stress plot [MPa] (A) and third principal stress plot [MPa] (B) (ext. press. 3MPa, temp. gradient 150°C , theta $\pm 75^\circ$)

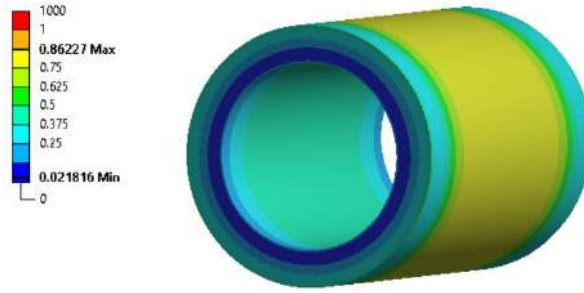


Figure 5.7: Inverse Reserve Factor for Tsai-Wu failure criteria [-]

Figure 5.7 presents the Tsai-Wu failure criterion in the form of Inverse Reserve Factor (IRF). As long as it is lower than one, analysed structure is fine. Based on a given example, it is equal to 0.86, so there is still some safety margin before failure is triggered. Yellow zone marking IRF above 0.75 is quite vast, suggesting that failure can occur at most of cooled surface. Taking into account that it does not extend into hot gas path, some delamination process is expected to take place leading to the complex failure mode triggered by wall thinning and transpiration cooling unbalance.

Graph on figure 5.8A) presents the highest value of first principal stress and as a function of thermal gradient across the wall - as presented on figure 5.6A) this value occurs at the cold external surface, which is stretched by the hot interior. This full factorial sensitivity study result was generated for 35 models without the pressure difference across the liner (1 MPa on both sides). Of course in such condition cooling water will not be delivered through the porous liner inside the flame zone, but this is a good extreme reference case to compare other analysed pressure differences. There are two input parameters which varies, so presented graph can be easily converted into 3D plane graph, where third axis contains CMC winding angle. For the purpose of clear visualization, each angle (line) was coloured with different colour. The top one was obtained for angle $\pm 90^\circ$, so all fibers are consistently directed in the hoop direction leading to the alignment of the highest Young modulus E_{11} with the first principal stress. Taking into account that thermal expansion coefficient is equal in all directions (matrix and fibers made from same material AL_2O_3), same strain in hoop direction will result in the highest stress in comparison to other directions. Second line was drew for fibers winding angle $\pm 75^\circ$, which resulted in modest drop in the max. first principal stress. This is most noticeable at the higher temperature gradients, because thermal strains in hoop direction are no longer aligned with fibers. Angle of $\pm 75^\circ$ with respect to main axis results of $\pm 15^\circ$ with reference to the circumferential direction. That angle causes reduction of Young modulus in hoop direction, as more load is carried by more flexible matrix. This effect is even more noticeable for $\pm 60^\circ$ curve, which is positioned in the middle of the analysed angular range. Note that curve $\pm 45^\circ$ is close to $\pm 0^\circ$, which collapsed to $\pm 15^\circ$ and $\pm 30^\circ$. The interpretation of this is that all three lowest curves carry thermal load through matrix and fibers at the similar ratio. For example, at $/pm\ 45^\circ$ hoop load tries to open or close angle between fibers leading to the situation, where matrix between them is stretched or compressed. Further reduction of theta angle leads do the growth of the angle against hoop direction, so nearly all hoop load is carried by the matrix. Regarding the axial component of stress, it is less significant than the hoop one, because liner can freely expand axially. Certainly there will be some axial shear interlaminar load between plies due to the thermal gradient and radial load due to the thickness change of adjacent plies. However, both directional loads has a secondary impact

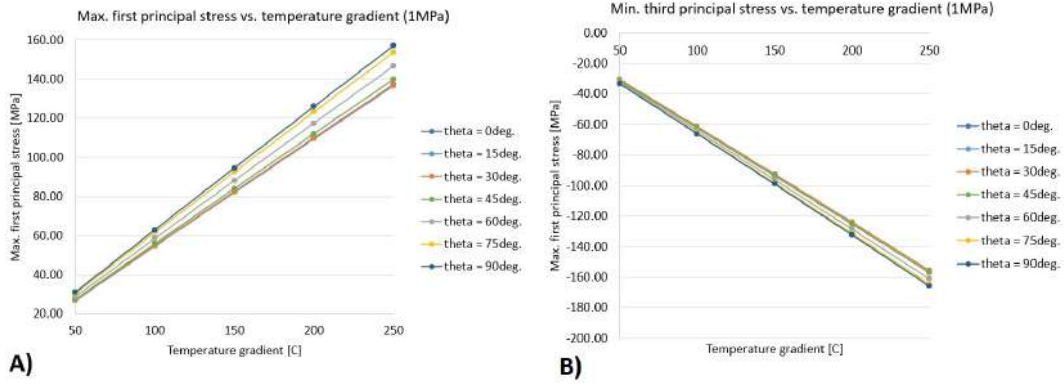


Figure 5.8: Max. first principal stress (A) and min. third principal stress (B) vs. temperature gradient (ext. press. 1MPa)

in comparison to the hoop direction. The reason being is that liner can grow freely in axial and radial direction, unlikely to hoop direction, where growth is restrained by the circular shape.

Based on the results from figure 5.8A) it can be said, that the highest first principal stress grows linearly with temperature gradient growth. This value is even more significant, because in the 3D axisymmetric model it occurs at the entire circumference. The other interesting conclusion is that change at low angles (0° to 30°) makes marginal impact to the highest sigma 1 stress. The reason behind this is the degree of alignment between fibers and circumferential direction of stress, which is dominant. Based on table 2.2, Young modulus along the fibre E_{11} is about 20% higher than across fibres, so higher stress is expected for the same strain.

Graph on figure 5.8B) presents the lowest value of third principal stress and as a function of thermal gradient across the wall. As presented on figure 5.6B) this value occurs at the hot internal surface, which is compressed by the cooled exterior. This graph is a "mirror" representation of figure 5.8A), which if focused at the same component, but on the cold side. All theta curves are close to straight line and the order is same, but reversed. This picture has an excellent physical meaning, because more tensile load on the cold side corresponds to more compression load on the hot side. Note, that both graphs compare stresses in the peak location, so there is no information about the average stress on surrounding elements. However, gaps between corresponding curves are influenced by the size of peak stress area. For instance, graph of figure 5.8A) is characterised by wider gaps between curves, because peak stress is very localised at both edges of the liner. In contrast to that, lines on figure 5.8B) are much closer to each other, because there is a large internal area at the similar stress to peak value. This can be seen clearly on the figure 5.6.

Graph on figure 5.9A) is similar to figure 5.8A), apart from the external pressure which was increased to 3MPa. For the constant internal pressure at 1MPa, this case analyses 2MPa gradient across the wall. The physical meaning of that difference is the necessity to pump liquid water through the liner made from porous medium. Pressure is nothing more than the force distributed uniformly at the entire area at the direction normal to the surface. For that reason, external pressure tries to uniformly compress analysed CMC liner, creating compressive stress component in the hoop direction. The highest-thermal-gradient points on figure 5.9A) uniformly dropped by about 10MPa, which helps to reduce load carried by the CMC material. That reduction occurs at the cold (external) surface,

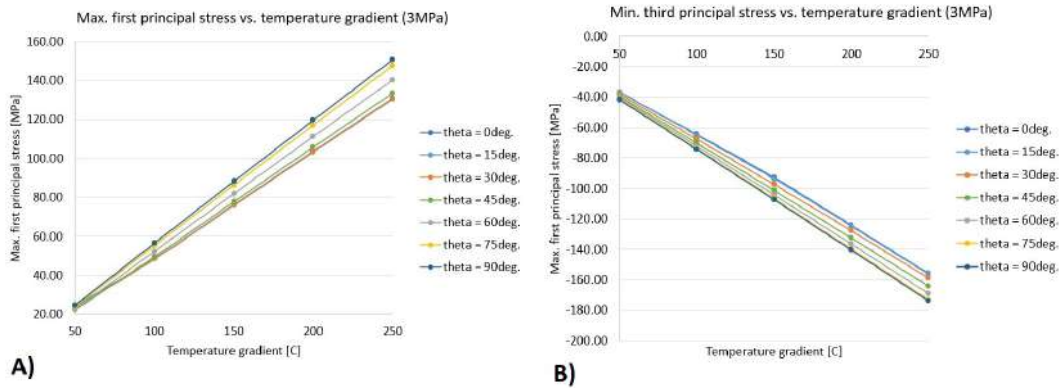


Figure 5.9: Max. first principal stress (A) and min. third principal stress (B) vs. temperature gradient (ext. press. 3MPa)

because of the tensile thermal load induced by the hot interior. Of course pressure induced compression affects entire liner, including thermally compressed internal surface. However, analysed CMC material has got higher strength in compression than tensile, so external tensile load reduction has more benefit than compression increase on the internal gas-washed surface. 2MPa pressure drop is a relatively high value in comparison to the design intent, so 10MPa stress benefit presented here will be lower in the experimental setting of 0.7 MPa pressure drop.

Results presented on figure 5.9A) show that first principal stress dropped consistently for all points. Note that average expected stress drop should be similar in any θ and any thermal gradient, because pressure has to be balanced by the liner internal forces. However, presented results show peak stress value for the entire domain, so not-equal stress drop is a result of non-uniform stress distribution within CMC liner. Peak minimum third principal stress at figure 5.9B) is taken from the same component but at the hot surface, which is compressed by cold exterior. In general, the more tensile load on one side, the more compression load on other side is required to compensate it. Both graphs on figure 5.9 are consistent from that point of view, because same order of curves is maintained (although reversed). The main difference references to the gaps between θ lines, because third principal stress graph can be characterised by more equal steps. Interestingly, $\theta \pm 15^\circ$ collapses with $\theta 0^\circ$ similarly to $\theta \pm 75^\circ$ and $\pm 90^\circ$. Collinear curves happen, when matrix/fiber load is split at the same ratio.

Graph on figure 5.10A) is similar to figure 5.9A), apart from the external pressure which was increased to 6MPa (5MPa pressure drop across the liner). That value is unlikely to be reached in the designed installation, but it can be used as a substantiation to the pressure growth limit. Resultant 5MPa pressure gradient reduced σ_1 peak stress even further up to 140 MPa (250°C thermal gradient). As explained before, the higher pressure difference, the lower hoop stresses in the liner. Yellow line marks case of $\pm 75^\circ$ which is claimed as the optimum winding angle, as higher values are difficult to obtain during the manufacturing process. Due to the very high crushing pressure, it is important to pay attention at the lowest minimum σ_3 stress, which is shown on figure 5.10B). Regarding the trend, third principal stress (σ_3) drops linearly with temperature gradient for all analyses θ angles, which is consistent with lower pressure-drop cases analysed before. Worth mentioning, that stress inversion occurred at cold surface for first principal stress (σ_1) at 100°C does not exist on the σ_3 hot side. The reason being is that load on hot side is much more uniformly distributed than on the cold side.

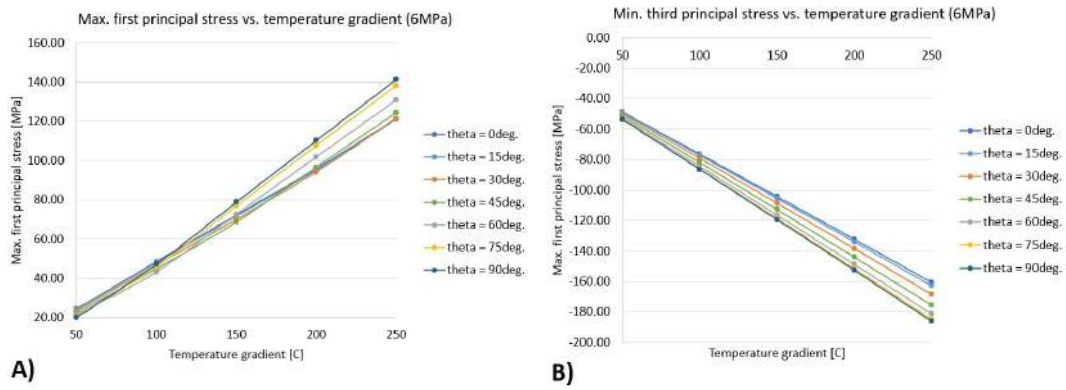


Figure 5.10: Max. first principal stress (A) and min. third principal stress (B) vs. temperature gradient (ext. press. 6MPa)

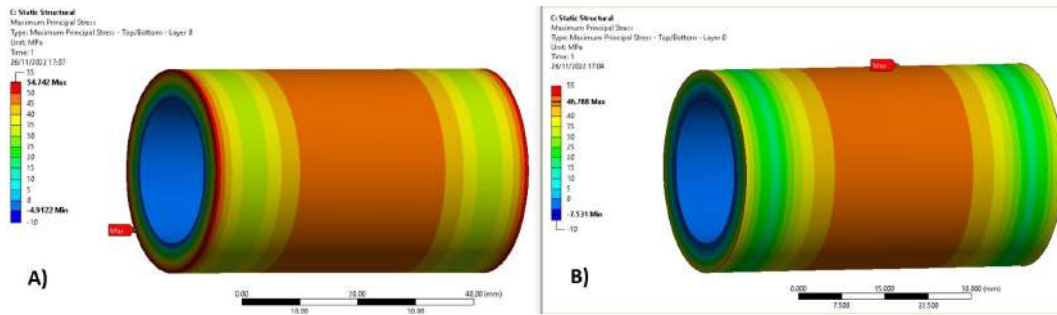


Figure 5.11: Max. first principal stress (temp. gradient 100°C, theta angle 30°), A) 1MPa, B) 6MPa

From the WHIPOX point of view, compressive strength is 30% higher than tensile one (table 2.3), so failure risk is significantly reduced at the compressed hotter side.

Graph on figure 5.10A) is significantly different to these generated for lower pressures, because theta curves intersect with each other. This is especially apparent at the temperature gradient equal to 100°C, where line $\pm 30^\circ$ moved from the bottom position for no-pressure-difference case (figure 5.8A)) near the top. This discrepancy is explained on the figure 5.11, where peak stress point changed location from the edge into the middle zone. For most of the cases, maximum first principal stress occurs at the edge (figure 5.11A). This area is stretched by hot interior in all three directions, but it is supported by adjacent material only from one side. This boundary condition leads to the extensive stress there in most from analysed 105 cases. However, for some unique combination of pressure, thermal gradient and fibre winding angle, stress at the liner's edge can be reduced below the middle zone. This is the case on figure 5.11B), where very high external pressure is able to reduce load at the edge by supporting it in the radial direction.

Graph on figure 5.12 shows Inverse Reserve Factor of a Tsai-Wu failure criterion. It is directly based on results presented on figure 5.8, equation 2.236 and strength factors from table 2.3. When factor's value is equal or higher than one, failure is expected according to the Tsai-Wu criterion. For the robustness reason, designer should maintain some level of safety margin below one, as every structure deteriorates along the time losing its strength. In this case it will be gradual matrix cracking transforming more load into fibers. The other reason of safety margin necessity is the manufacturing variability, which

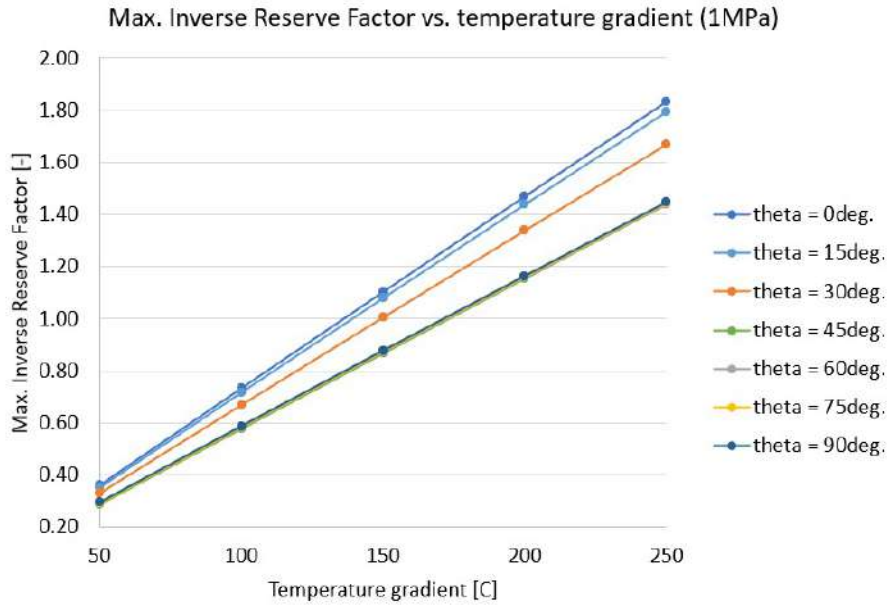


Figure 5.12: Max. Inverse Reserve Factor vs. temperature gradient (ext. press. 1MPa)

can vary between suppliers and batches. However, for the purpose of a prototype design, safety margin could be neglected. A set of results from figure 5.12 was obtained for the worst case of no-pressure-drop across the liner. As explained before, this is a non-realistic condition as transpiration cooling would stop under these circumstances. Nevertheless, lack of external force acting in opposite direction to the thermal load is an unrealistically extreme case, helpful to capture design space boundaries. The worst Inverse Reserve Factor equal to 1.81 occurs for the theta angle zero and temperature gradient 250 °C. This happened due to the fact, that all fibers are aligned with main axis, so they are unable to carry any circumferential load normal to them. As a consequence of this, load is carried by the weak porous matrix leading to the significant strength drop. Note that there is a noticeable threshold between ± 30 and ± 45 theta angle, as all points above that value collapse into single curve. The reason of that behaviour is the balance between individual Tsai-Wu components (equation 2.236), which captures if load is carried by strong fibers or weak porous matrix. According to figure 5.12 all lines between ± 45 and ± 90 are equally good, however extreme angles should be avoided due to the neighbourhood of strength threshold (± 45) or manufacturing difficulties (± 90). For that reason, theta angle equal to ± 75 is deemed as optimal.

Graph on figure 5.13 presents maximum Tsai-Wu Inverse Reserve Factor for a pressure difference equal to 2MPa (3MP outside and 1 MPa inside). In comparison to most conservative pressure case from figure 5.12, theta $\pm 90^\circ$ is nearly unchanged due to fibers' alignment with circumferential direction, which is additionally compression-loaded by the external pressure. Opposite to that, other curves are shifted downwards due to the reduction in the highest first principal stress. Again, curves with theta angle below $\pm 45^\circ$ behave differently than the rest of angles due to their fibers' misalignment with hoop direction (most hoop load is carried by the matrix). It can be said, that each of them dropped by the Inverse Reserve Factor of 0.075, which for low thermal gradients moved them below theta $\pm 90^\circ$ point. In contrast to that, curve $\pm 45^\circ$ dropped below unchanged curve

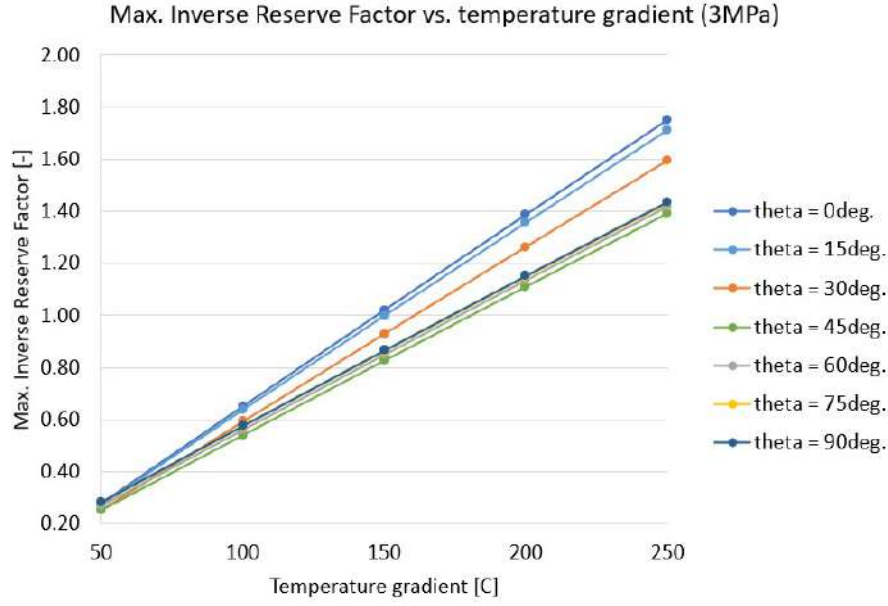


Figure 5.13: Max. Inverse Reserve Factor vs. temperature gradient (ext. press. 3MPa)

$\pm 90^\circ$ marginally, because only small fraction of load is carried by matrix, which is sensitive to pressure change. Last two curves $\pm 60^\circ$ and $\pm 75^\circ$ have dropped marginally below the strongest case $\pm 90^\circ$, but from the manufacturing process perspective, $\pm 75^\circ$ case is deemed as the optimal one.

Graph on figure 5.14 presents maximum Tsai-Wu Inverse Reserve Factor for a pressure difference equal to 5MPa (6MP outside and 1 MPa inside). As mentioned before, this is an extreme pressure case not planned to be tested at the current stage of experiment. However, the purpose of analysing it is a robustness assessment, which is supposed to answer the question about liner's behaviour in random transient or failure situations. Graph on figure 5.14 is similar to other two analysed cases at and above thermal gradient of 150°C . As for the lower pressure difference case, curve $\pm 90^\circ$ stays in the same position due to its alignment with stress-dominating hoop direction. Curves below $\pm 45^\circ$ drop by about 0.15 inverse reserve factor. The threshold between $\pm 45^\circ$ and $\pm 30^\circ$ is still significant, so $\pm 45^\circ$ is not the optimum angle due to its lack of robustness. Two remaining angles of $\pm 60^\circ$ and $\pm 75^\circ$ are close to each other, so consequently angle $\pm 75^\circ$ is deemed as a optimum one. Graph on figure 5.14 is significantly different to other pressure cases at the thermal gradient of 100°C , because curves changed the order. This effect is clearly stronger for smaller-than 45° theta angle, which slightly increases their safety margin. Nevertheless, due to the fact that this local effect happens only for a specific set of parameters, it is not deemed as robust, so design decision should not take it into account. The explanation of this effect is shown on figure 5.11, where the weakest point relocates from the edge to the middle of external surface.

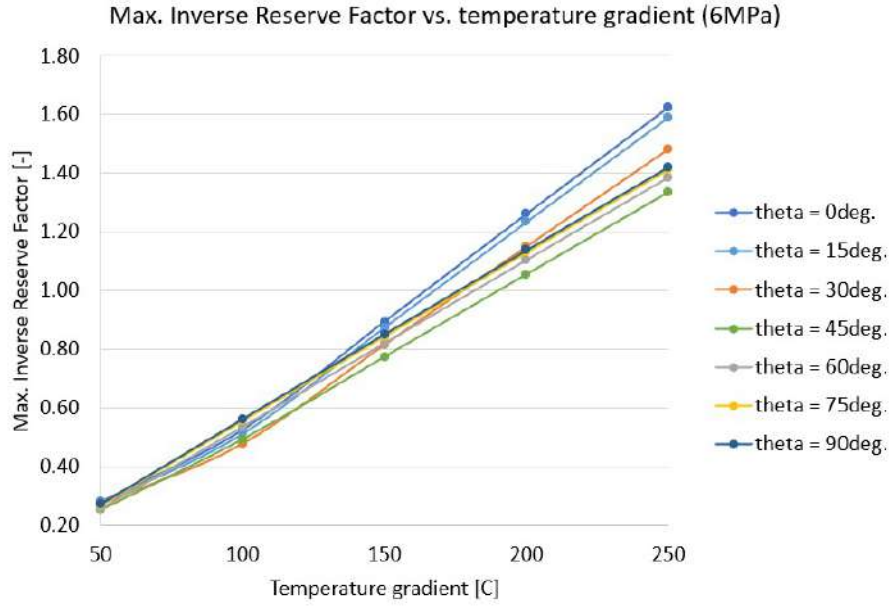


Figure 5.14: Max. Inverse Reserve Factor vs. temperature gradient (ext. press. 6MPa)

5.3 Liner cooled acceleration – transient

Transient analysis is an important element of the design process, as during the acceleration/deceleration temporary thermal gradients can induce much higher stress than in the steady state. This is particularly important in the power system peak load, when generators are required to cover the power demand as quickly as possible. The other example is the aircraft engine, which needs to be designed to withstand very rapid acceleration at take off flight phase.

Figure 5.15 presents porous liner which is going to be analysed mechanically for different acceleration speeds. At the beginning of the process, entire domain has an uniform ambient temperature (20°C) and atmospheric pressure (0.1MPa) around, so thermal gradient in any location is equal zero. In such conditions, no stress is present inside. After the ignition, in the very first moment, hot flame touches cold and wet liner's surface leading to the local temperature growth. At that time, thin layer of hot surface cannot expand, because is restrained by the thick cold solid body. This leads to the very high compressive stress in the hoop direction, which is steadily released as deeper parts of liner gets hotter. Figure 5.15B highlights point on hot surface, which will be used as a probe location "B" in post-processing. In contrast to that, figure 5.15A points cold location "A", which is going to be stretched as internal surface gets hotter. At the end of the acceleration (steady-state conditions), internal surface temperature is 200°C at pressure 1MPa (flame zone), whereas external surface temperature is 20°C at pressure 1.7MPa (water pump zone). For every analysed case, linear temperature and pressure interpolation is assumed between initial (cold) and final (hot) conditions.

Figure 5.16B presents first principal stress time plots at the hot surface (Figure 5.15B). Each colour marks the stress evolution obtained for different acceleration time - from the shortest 1sec. to the longest 15sec. However, to capture stress redistribution correctly, each analysis has got a 1sec. cold "introduction" phase and 20sec. hot "stabilisation" phase. It can be said, that regardless of the acceleration time, stress overshoot does not

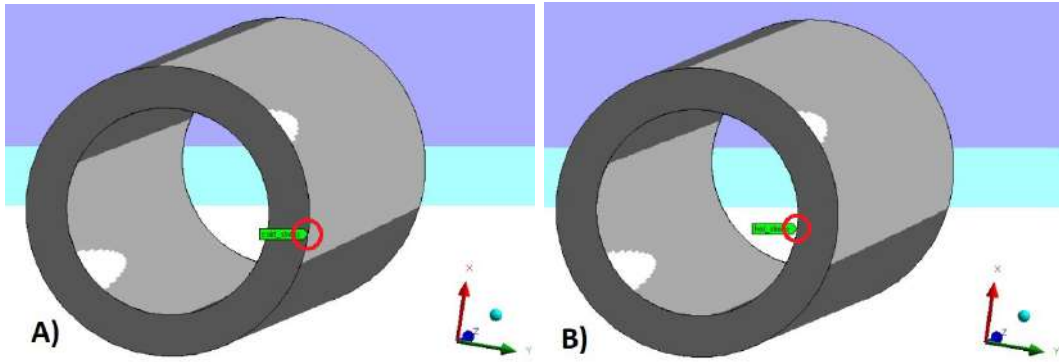


Figure 5.15: Locations of stress probe (A) cold surface (B) hot surface

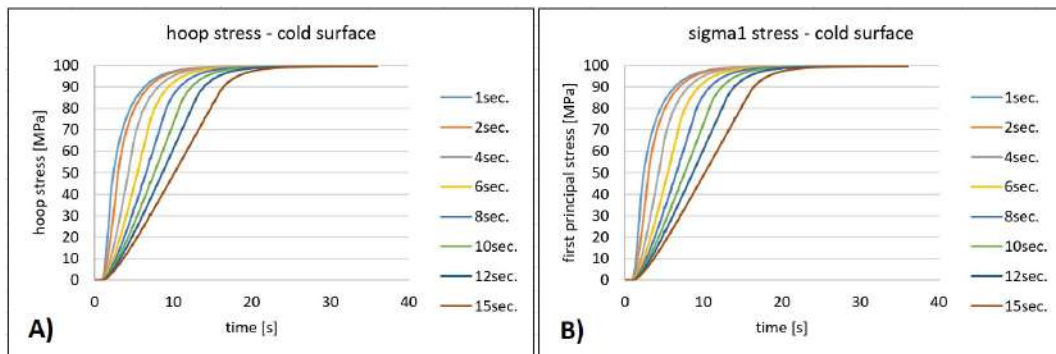


Figure 5.16: Cold surface stress time plot (A) hoop direction (B) first principal

appear, so cold surface life is not affected by the transient effects. First principal stress is an important parameter affecting life of analysed component, but for the full picture of occurring physics, it is important to look at stresses in three main directions, which for cylinder are: hoop, radial and axial. Comparison between figure 5.16B and 5.16A shows clearly, that first principal stress (sigma 1) is dominated by hoop direction.

Figure 5.17 presents transient axial and radial stress distribution at the liner's cold surface. As expected, both values are relatively small in comparison to hoop direction - this is consistent with similar graphs shown on figure 5.16. Axial stress is very small, because liner is free to expand axially. Complex shape of intersecting lines is driven by hot surface and end surface interaction. Radial stress is equally small, because most of the thermal fight between hot interior and cold exterior is carried by hoop stress. Its sign is negative, because hot interior presses cold exterior.

Figure 5.18A illustrates hoop stress time plot at hot surface for various acceleration times. For an extreme case of 1 second, stress overshoot is equal to 4.5, which is a significant value. On the other side, acceleration time of 15 seconds results in 1.6 transient overshoot factor. This is summarised in figure 5.19. Obtained transient overshoot factors have a proper physical interpretation, because they are driven by the temporary thermal gradients occurring during the rapid change of boundary conditions. In the analysed liner, flame rapidly heats internal surface of ceramic liner, so for a short period of time hot fibers are adjacent to cold fibers. This gradient is gradually flattened due to the thermal conductivity of ceramic (which is very low). Comparison between figure 5.18A and 5.18B reveals, that third principal stress is dominated by hoop direction.

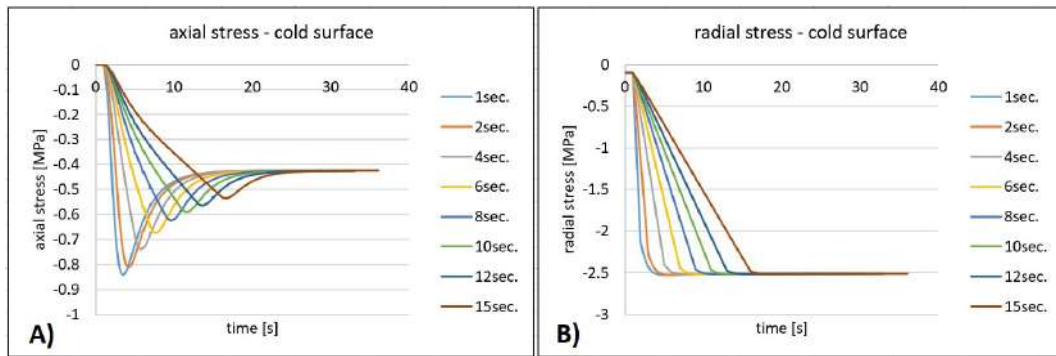


Figure 5.17: Cold surface stress time plot (A) axial direction (B) radial direction

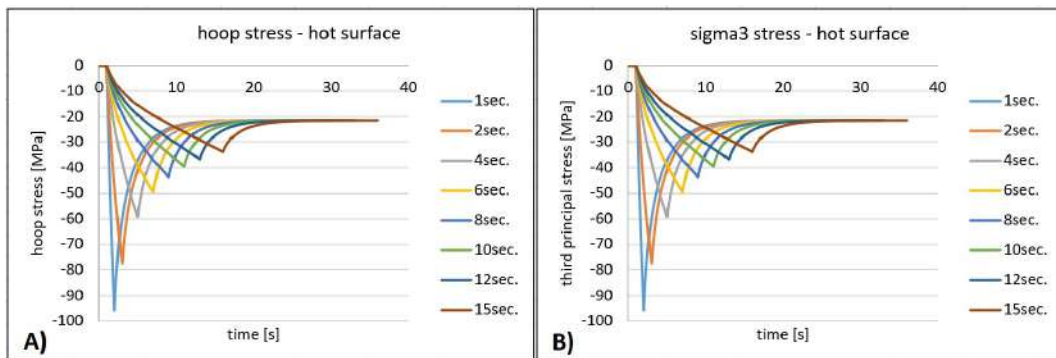


Figure 5.18: Hot surface stress time plot (A) hoop direction (B) third principal

acc. time [s]	peak stress [MPa]	stress overshoot [-]
1	-95.8	4.5
2	-77.5	3.6
4	-59.1	2.8
6	-49.5	2.3
8	-43.5	2.0
10	-39.5	1.8
12	-36.7	1.7
15	-33.7	1.6

Figure 5.19: Third Principal Stress overshoot (hot surface)

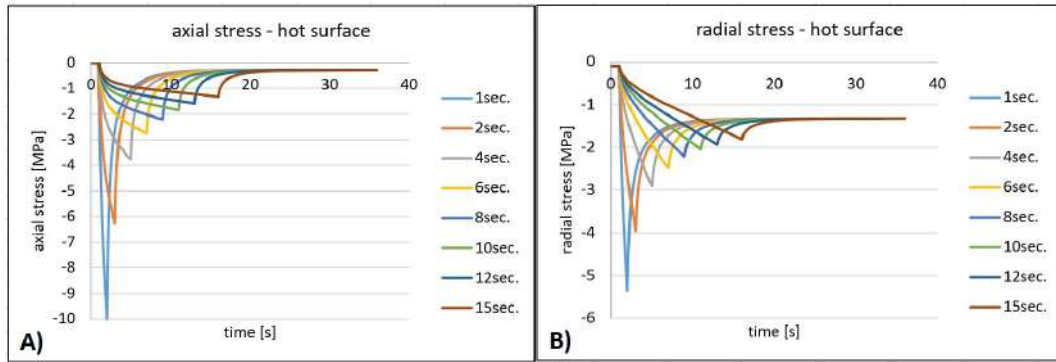


Figure 5.20: Hot surface stress time plot (A) axial direction (B) radial direction

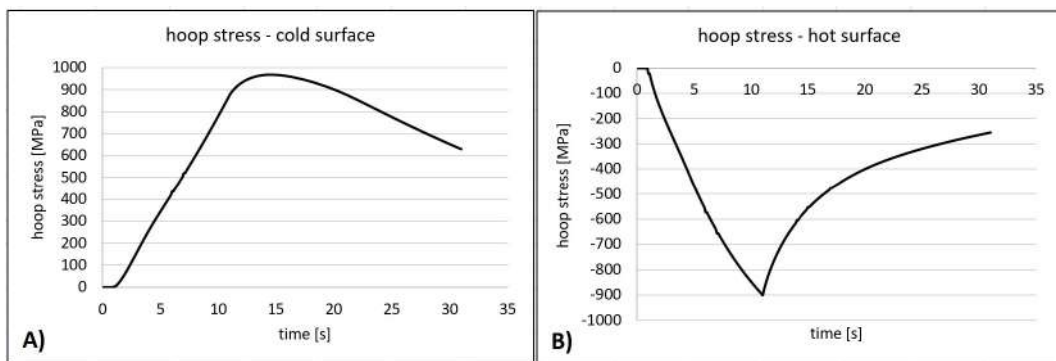


Figure 5.21: Hoop stress time plot (A) cold surface (B) hot surface

Figures 5.20A and 5.20B show stress time plots for the hot surface of the liner. Both of them are similar to the hoop direction (figure 5.20A), apart from the peak value which is several times lower. Radial stress is so low, because thermal fight in this direction is restrained by hoop growth. Regarding axial direction stress, it is relatively low due to the fact that liner can freely expand axially and radially. The intersection between lines and transient overshoot are driven by the same factors like hoop stress - local temporary very high thermal gradient between hot surface and cold adjacent fibers.

5.4 Liner non-cooled acceleration – transient

Figure 5.21 presents hoop stress time plots for cooling failure case at locations from figure 5.15. Its assumptions are: acceleration time is 10 seconds, constant cold surface pressure equal to 0.1 MPa, hot surface pressure growth from 0.1 MPa to 1 MPa, hot surface temperature growth from 20 to 3000 °C, initial temperature is 20 °C.

Figure 5.21A presents cold surface stress growth up to 967 MPa, which is far beyond WHIPOX strength (Table 2.3). Although only first 31 seconds were analysed, it is expected that stress is going to reach zero when thermal gradient finally disappears. Note that peak stress occurs at 14.4 seconds, which is a little bit later than full load is applied (11th second). This delay is driven by the low WHIPOX's thermal conductivity. Similar situation is observed at the hot surface - compressive hoop stress gradually drops to -900 MPa during the acceleration phase and levels up to zero as thermal gradient dissipates.

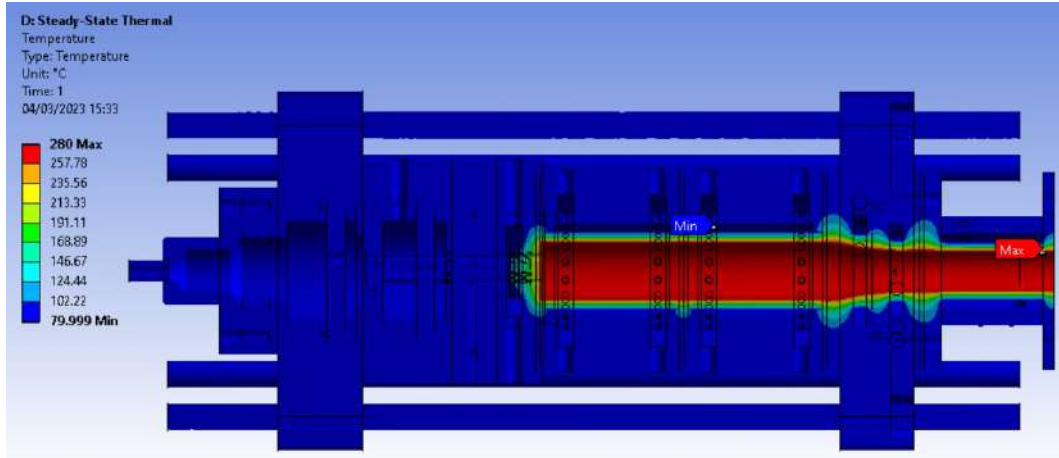


Figure 5.22: Temperature distribution of an assembly

Such scenario of a failed-cooling acceleration is of course a simplification, as it does not take into account hot gas penetration of porous liner, which will augment the heat distribution rate inside it. Nevertheless, non-cooled acceleration is going to cause almost instant liner failure due to the very high radial thermal gradient followed by temperature decomposition.

5.5 Solid assembly - static

Figure 5.22 presents steady-state temperature distribution at the cross section of wet combustion chamber assembly. At this stage of analysis, temperature boundary conditions were applied, because no CFD assessment was carried out. Surfaces having contact with coolant are fixed at 80 °C, whereas hot gas path temperature is equal to 230 °C (as a parameter, this value varies from 155 to 280 °C). Under such assumptions, hot gas path encounters significant radial thermal gradient, because flame and coolant streams are very close to each other. More detailed thermal map is planned to be obtained with 3D CFD analysis at the later stage, but it is not expected that refined values will deviate from presented assumptions by a significant amount.

Figure 5.23 presents a total deformation plot for a steady-state thermal gradient shown on Figure 5.22. Lower front region is close to zero, because assembly is restrained there in all six degrees of freedom. Front upper part deformation is about 0.05mm, which is dominated by radial growth of the front ring. Lower part of the rear ring is deformed mainly in axial direction, as it is restrained radially and circumferentially. The upper part of rear ring is restrained circumferentially only, so it deflects the most. From the sealing point of view, the largest axial gaps occur on both sides of the rear liner. That is driven by the significant radial thermal gradient and differences in the thermal expansion coefficients across this gradient. Figure 5.23 reveals that rear ring leans down resulting in non-uniform gap width and bending of restraining rods. The main reason behind this is the L-shaped cross-section, which is very sensitive to the radial thermal gradient.

Figure 5.24 presents worst principal stress plot, which is consistent with deformation shown on Figure 5.23. The highest stress point (725 MPa) occurs at the edge of a flange, because this region supports bending moment deflecting the rear ring. Regarding the direct thermal gradient impact, surface of the rear water passage experiences 322 MPa.

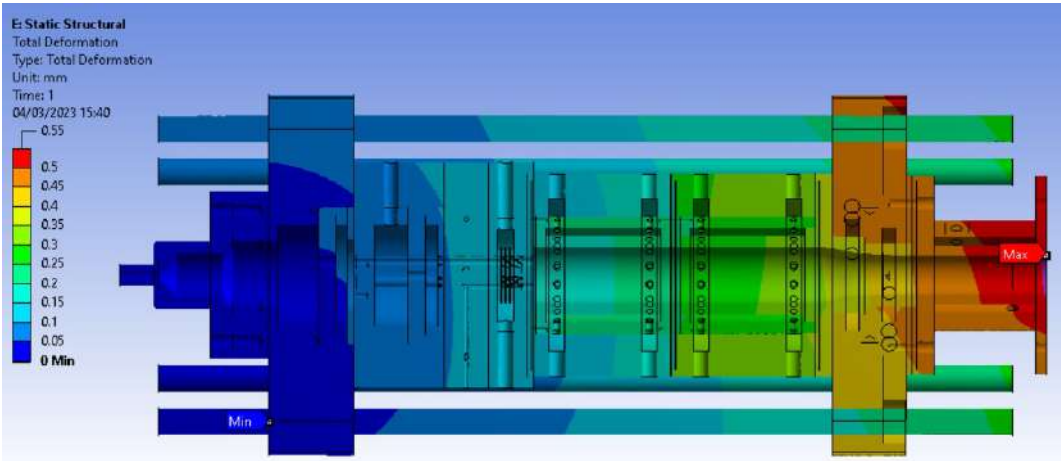


Figure 5.23: Total deformation of an assembly (thermal gradient 80-280 °C)

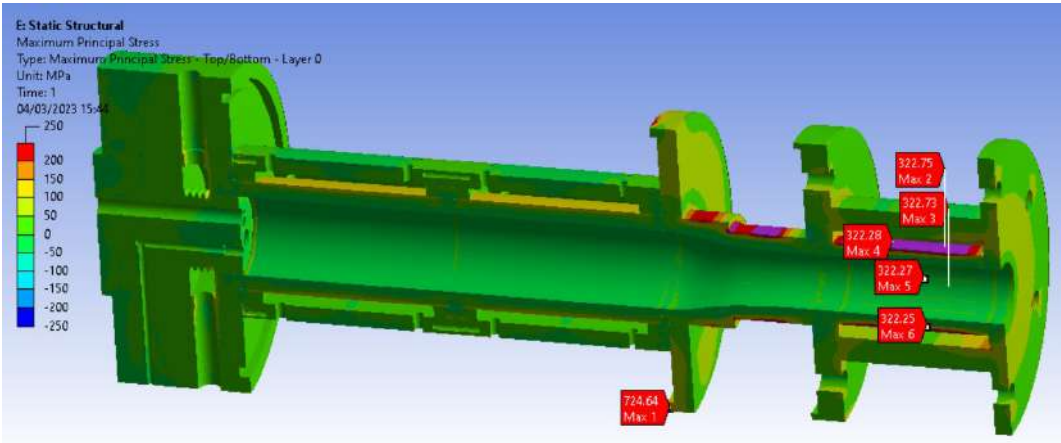


Figure 5.24: Worst principal stress of assembly [MPa] (thermal gradient 80-280 °C)

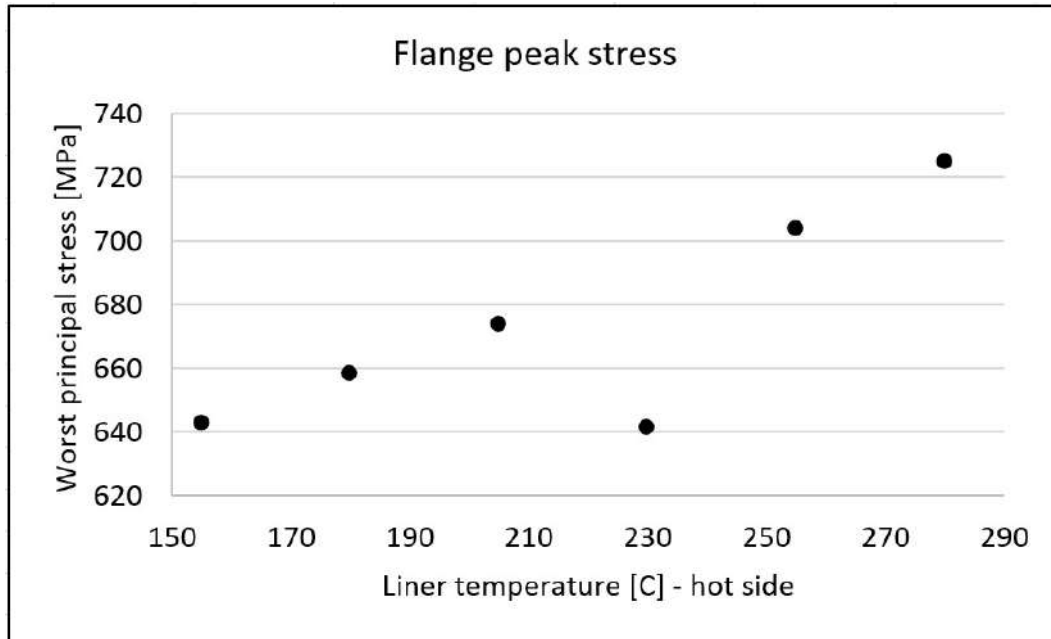


Figure 5.25: Peak worst principal stress on the flange [MPa]

Graph on figure 5.25 summarises flange peak stress as a function of cross-wall thermal gradient. It reveals, that five out of six points follow linear trend. The exception is point at thermal gradient equal to 230 °C, which is about 50 MPa lower than expected. The reason behind this is non-linear interaction between multiple contact regions.

Figure 5.26 presents worst principal stress distribution at the surface of the ceramic matrix composite liners. They are loaded mainly due to the radial thermal gradient, so cooled external surface is stretched while heated internal surface is compressed. The axial load variation occurs due to the fact, that liners' edges are supported by sealed T-shaped copper rings. That makes a difference of about 20 MPa between middle and the edge of the liner.

Figure 5.27 shows the variation of peak stress on the liner versus hot-wall temperature. Although points are not perfectly aligned, their positions can be very well described by the linear function.

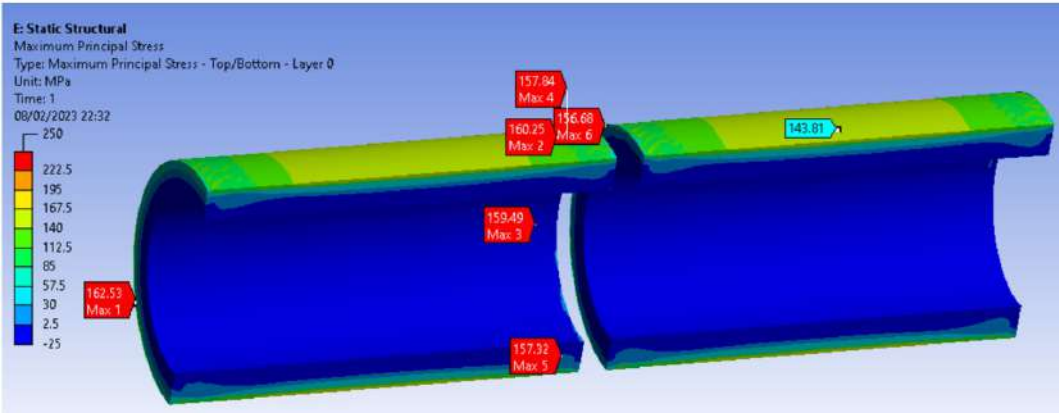


Figure 5.26: Worst principal stress of liner in assembly (thermal gradient 80-280 °C)

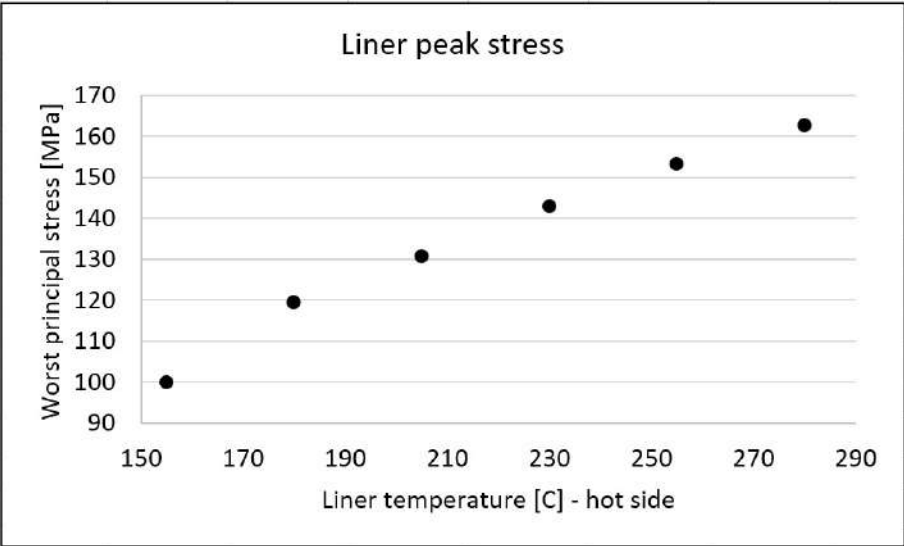


Figure 5.27: Worst principal stress of liner in assembly

5.6 Solid assembly - transient

Wet combustion chamber is a structure which is loaded by a very high transient thermal gradients. This effect is the strongest next to the rapidly heated surfaces, which at the very beginning are much hotter than the rest of the solid material. For that reason rapidly heated surface cannot expand freely, as it is restrained by the bulky interior of the component. This effect is stronger for insulators like ceramics, because low thermal conductivity increases the time required to conduct heat from hotter fibers outside to cooler inside. In the analysed Wet Combustion Chamber (WCC) elements most exposed to transient stress overshoot are ceramic liners, as at the thickness of few millimetres extremely hot flames are separated from cold liquid water. Described effect is partially eased by the fact, that porous liners enable transpiration cooling which delivers protective film at the liner surface. Transient stress overshoot is also significant at the other metal regions trapped between cold liquid water and hot gas. However, in this case thermal conductivity factor is much higher than in ceramic. There are other reasons why stress transient effects are noticeable. They include such factors like variable heat transient coefficient, differences in thermal expansion of adjacent elements, possible transient leakages between distorted parts, thermal fight and effects from external structural fixtures.

Transient thermo-mechanic analysis was run to complement steady state results. Due to the requirement of full combustion chamber assembly analysis, mesh density was reduced in comparison to the steady-state model. The main objective of that step was confirming transient behaviour and finding stress overshoot factors. Steady-state stress results obtained for solid assembly highlighted regions most prompted for cracking. As expected, most of the highly loaded points appeared at the steel outlet section, where non-porous cylinder experiences very high thermal gradient across the wall. However, less loaded ceramic liners are less elastic than steel, so some thermal deterioration could appear there.

Instead of running multiple transient analysis for several acceleration periods, it was decided to run single transient analysis for the worst case scenario. The faster acceleration rate, the higher transient stress overshoot is expected, so one-second acceleration time was taken for analysis. At the beginning of analysis (at time 0 to 1 sec.) the whole assembly was kept at the ambient temperature to numerically stabilize model. Acceleration phase was modelled between the first and second second, which means that thermal gradient across liner increased from zero to 175 °C within one second. Note that transient phase duration is estimated at about 20 seconds, which is required to stabilize temperature in every single assembly component. Figure 5.28 presents temperature distribution after 21 second of mission, which is assumed to be a steady-state condition.

Figure 5.29 presents first principal stress plot at the maximum loaded time point, i.e. between second and third second. To improve clarity, only components affected by high thermal gradient are displayed. Six maximum loaded points are positioned in the area of supporting ring. At this step, maximum load ("Max 1") location is the bolt hole. This location is not a surprise, as it has very high stress concentration factor (K_t) and is situated axially between ceramic and steel sectors on the hot gas path. Other five points have similar stresses, but it was decided to take point "Max 3" for further analysis due to its low stress concentration factor. Note that it is located just in the middle of steel cylinder, which is not a subject of transpiration cooling. Figure 5.30 presents first principal stress distribution over the time for points "Max 1" and "Max 3" marked at Figure 5.29. Stress overshoot factor is defined as the steady-state stress at 21sec divided by maximum stress. As expected low-stress-concentration (K_t) point "Max 3" has lower

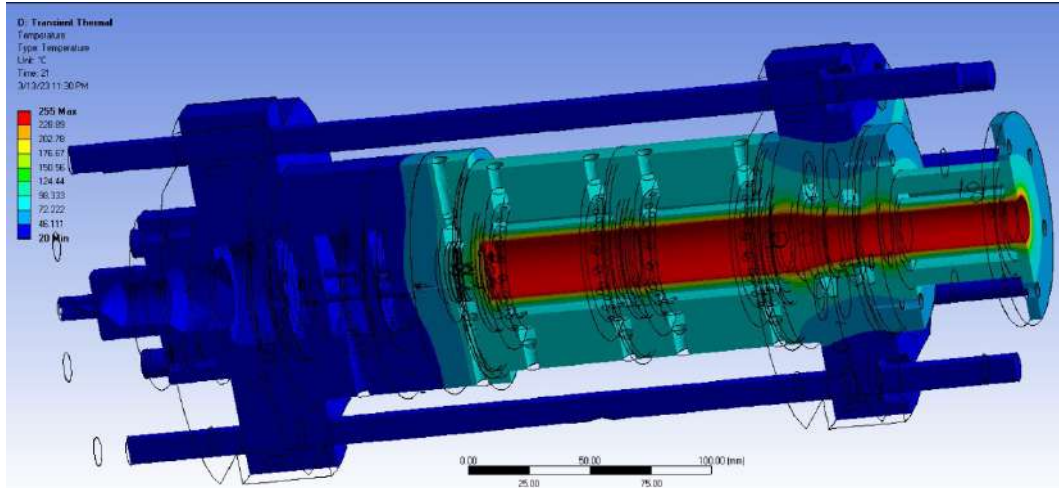


Figure 5.28: Temperature distribution after 21 seconds (1sec acceleration)

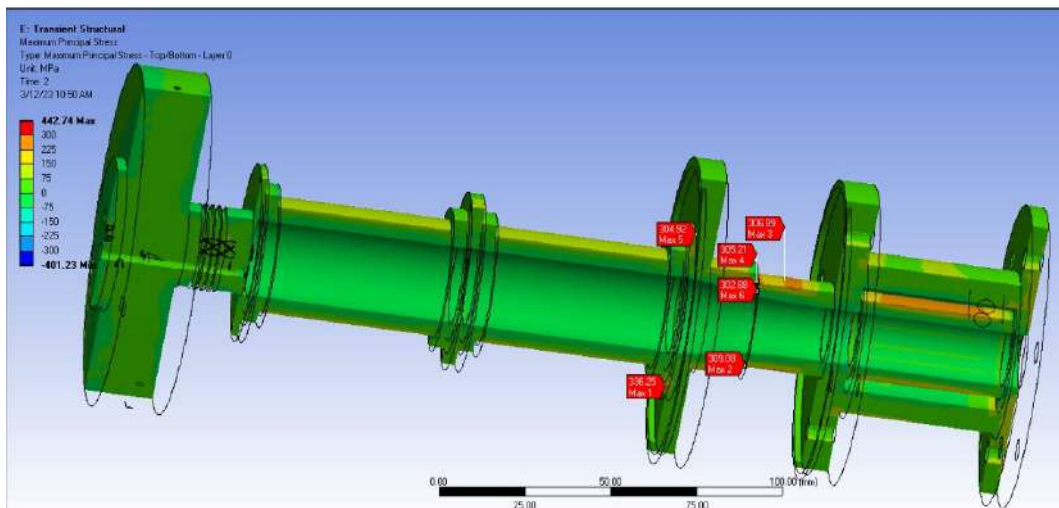


Figure 5.29: Sigma 1 Stress distribution at 2sec time step

stress overshoot factor (equal to 1.13 (345MPa/306MPa)) than high Kt point "Max 1" (equal to 3.26 (358MPa/110MPa)). Note that "Point 1" is located inside the flange, which is loaded in a very complex way both mechanically and thermally. On one side it is heated directly by the hot gas, on other side it is cooled by conduction from adjacent structural elements. It is also compressed and bended by main cooling passages as it carries deflection to the rear rings causing its movement on rolling support.

Figure 5.31 highlights five most loaded points on the hot gas path. Third principal stress was chosen for this comparison, because hot surfaces are continuously under the compressive load applied by the colder adjacent components. Note that all points are grouped into two regions - one next to the swirlers and the second one at the necking section. For that reason one point from each region was taken for further analysis: "Min 1" and "Min 5". Figure 5.32 presents stress distribution over the acceleration phase. Unlikely to Figure 5.30, peak values are exactly at the end of acceleration time. Additionally, stress overshoot factors are moderate and equal to 1.53 (-765 MPa/-500MPa) for point "Min 1"

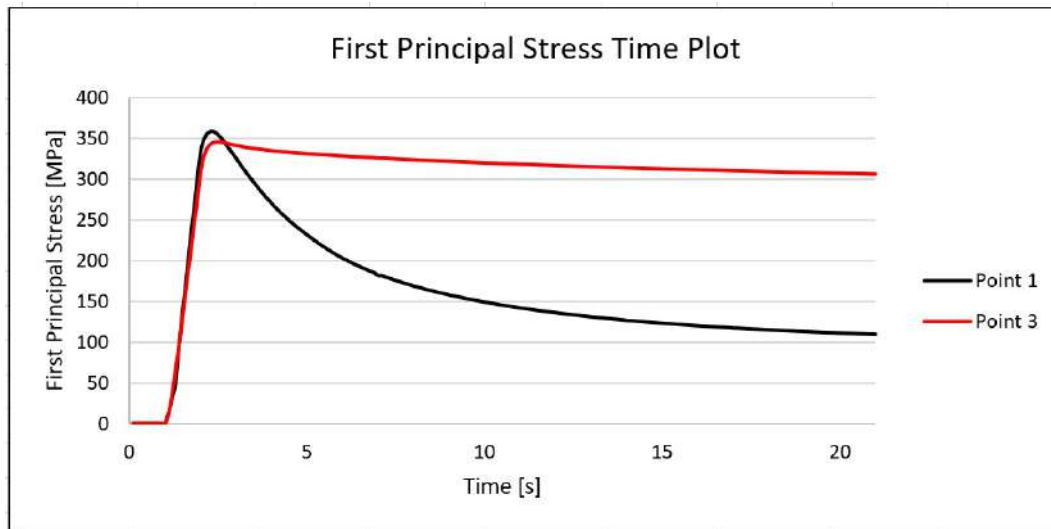


Figure 5.30: Sigma 1 Stress distribution at 2sec time step

and 1.21 (-631 MPa/ -522 MPa) for point "Min 5". In the general case compressive stresses are safer than tensile, because cracks opened by them may be arrested if stresses relaxation occurs. "Point 1" is located at the edge of cap, so there is a moderate stress concentration factor (K_t) there. Additionally, cap is formed from a bulky component, so there is some lag before conduction heats up the entire mass. That effect was taken into account at the initial phase of design, so copper was chosen as a material with very high heat conductivity coefficient.

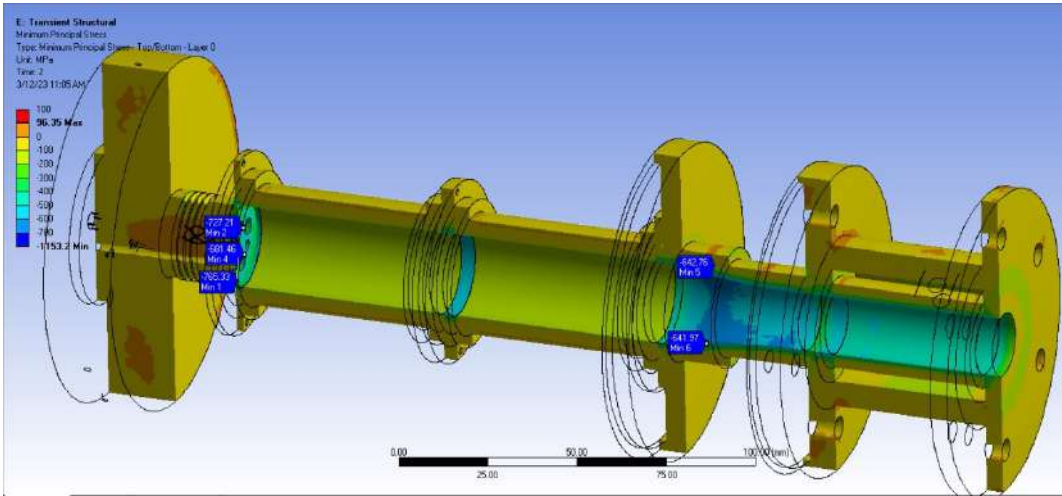


Figure 5.31: Sigma 3 Stress distribution at 2sec time step

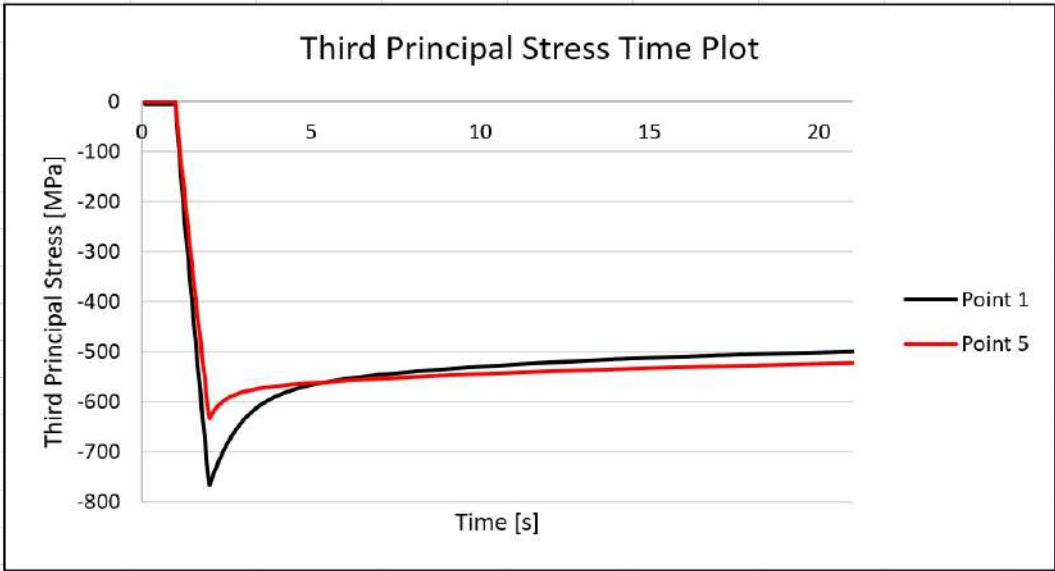


Figure 5.32: Sigma 3 Stress distribution at 2sec time step

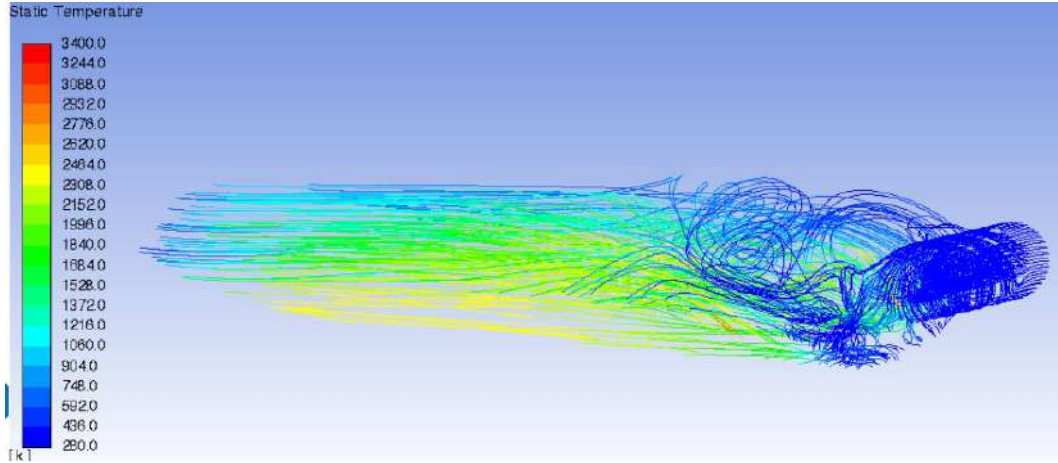


Figure 5.33: Methane/oxygen streamlines for 2g/s + 12 g/s case

5.7 CFD Analysis

Figure 5.33 presents temperature of wet combustion chamber streamlines, which were obtained with CFD analysis and published by M. Froissart and T. Ochrymiuk [184]. That particular result was obtained with 2g/s spray water injection and 12g/s of transpiration water inlet mass flow. This 120deg cycle symmetric model was build and analysed during the preparation phase to create WCC assembly FSI model. Streamlines of methane and oxygen inlet at the right are twisted thanks to the explicitly modelled swirlers. That required a very refined mesh, which was feasible due to the geometry scope reduction (cyclic symmetry and lack of solid domains). This analysis confirmed inlet flow structure which was obtained at the earlier stage with the 2D CFD model, predicting large recirculation zone at the cap edge. Under these assumptions, some parts of flame core exceeds temperature of 3000K.

Figure 5.34 presents temperature prediction which is consistent with Figure 5.33. Surface temperature distribution reveals three hot spots separated with thin cold strips. This is driven by the fact that three swirlers are separated by three liquid water spray nozzles. That pattern is uniformed at the outlet, which suggests that combustor is long enough to provide flat traverse at the outlet.

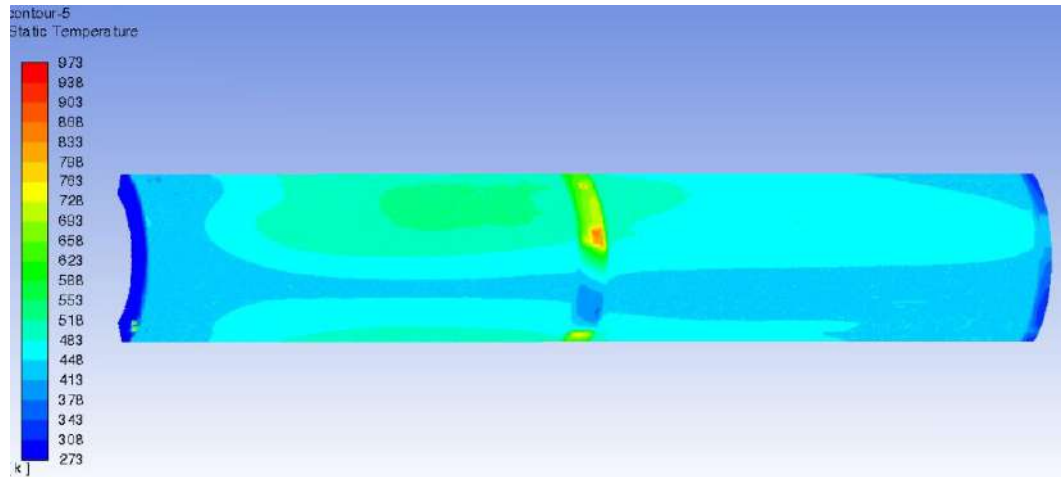


Figure 5.34: Liner temperature distribution obtained with CFD analysis

5.8 Fluid-Solid Interaction

Analysed Fluid-Solid Interaction model contains 23 millions nodes which are split between solid and fluid domains. Although solid and cooling CFD domains are relatively straightforward to model, hot gas path contains mixture of three substances, combustion process and water droplet evaporation. Furthermore, presented Fluid-Solid Interaction model captures instantly heat exchange between fluid and solid and adjusts solid properties accordingly. That helps to tune solid parameters which are temperature dependent like thermal conductivity and thermal expansion. Figure 5.35 presents flowlines representing oxygen and methane flow starting from swirlers and finishing at the outlet. They are coloured according to the temperature, which grows rapidly due to the combustion process modelling using GRI-Mech 3.0 method. Inlet region contains swirling angles, which are imposed to enhance mixing intensity between oxygen and fuel to improve combustion completeness. This graph reveals that along the cap circumference the toroidal vortex is formed helping with cap thermal protection. Cold streamlines along the liner are driven by the water evaporation and absorbed latent heat.

Figure 5.36 presents water droplets tracks, as they are ejected by spray nozzle and gradually evaporate after the contact with hot flame. At the pressure equal to 10.5 bars, water boiling temperature is equal to 455°K, which is reflected at the scale. The key conclusion from that ejection is that pressure fluctuation accompanying boiling droplets significantly improves mixing intensity leading to more complete combustion at the Wet Combustion Chamber outlet.

Plot on Figure 5.37 reveals that core flame temperature is around 2986°K and the average outlet temperature is equal to 1150°K. As a matter of results validation, both temperatures were checked against baseline 0D calculations, which gave 3053.8°K [177] and 1177°K respectively. That level of results discrepancy is deemed as acceptable, so results are considered as validated. Additional observation can be related to the empty spaces at the inlet, which mark non-modelled CFD domains supplying oxygen and methane to the swirlers.

Temperature distribution at liners' surfaces are shown on Figure 5.38, where swirlers are on the right side. Front liner looks cooler than the rear one, because it supplies three time more cooling water than the rear one (9g/s vs. 3g/s). The reason behind

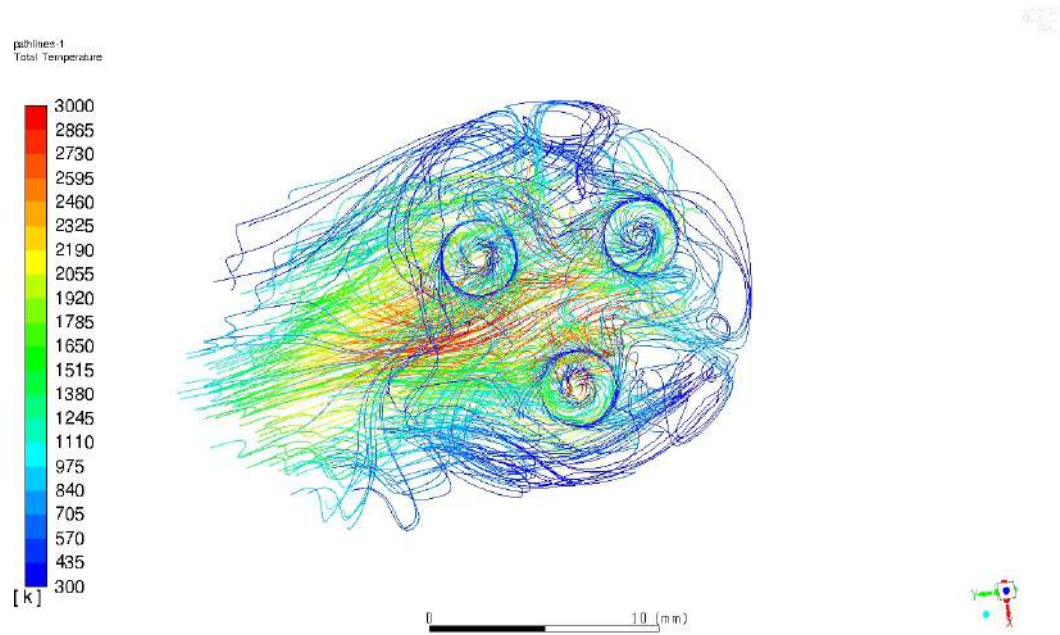


Figure 5.35: Streamline plot from oxygen/methane inlets

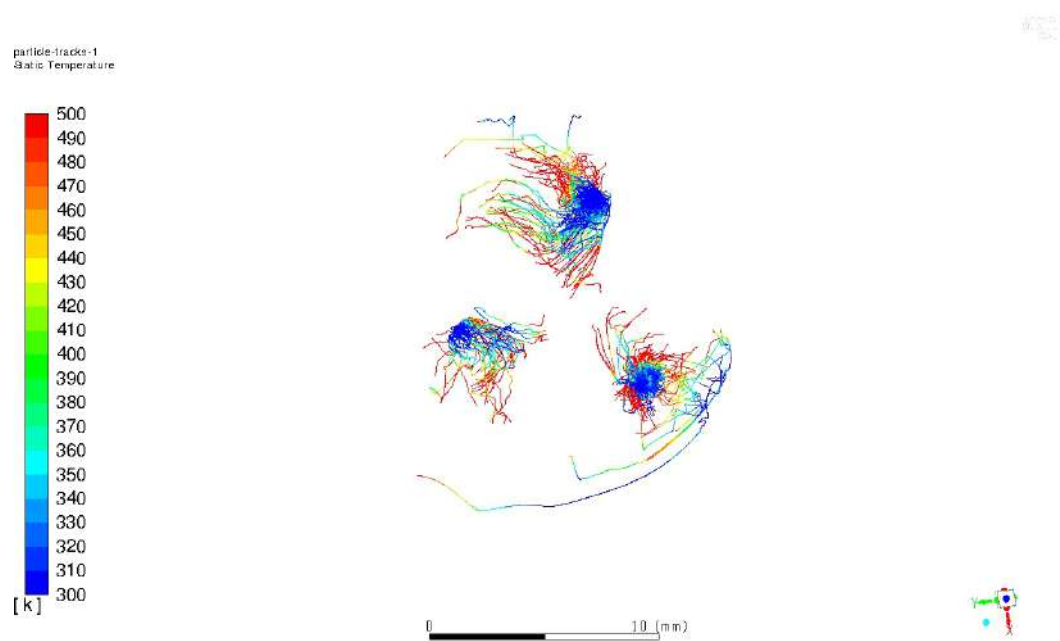


Figure 5.36: Water spray inlet (Discrete Phase Model)

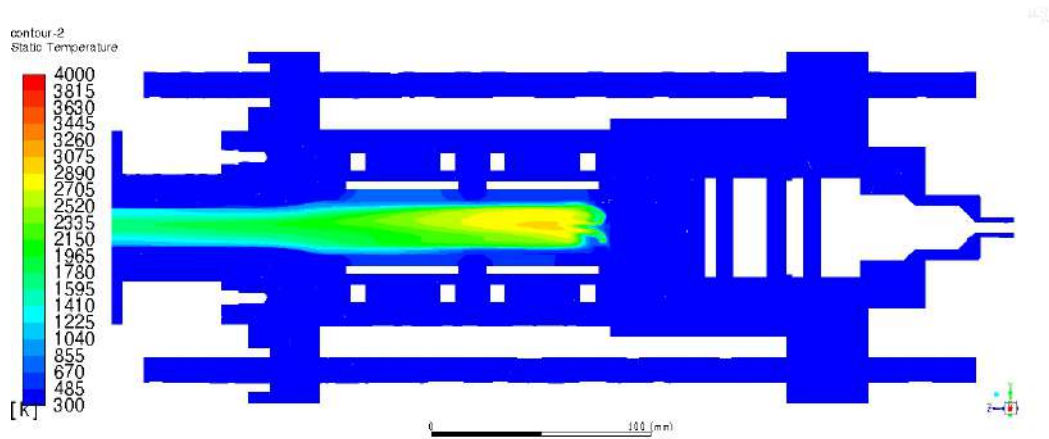


Figure 5.37: Temperature plot inside combustion chamber [K]

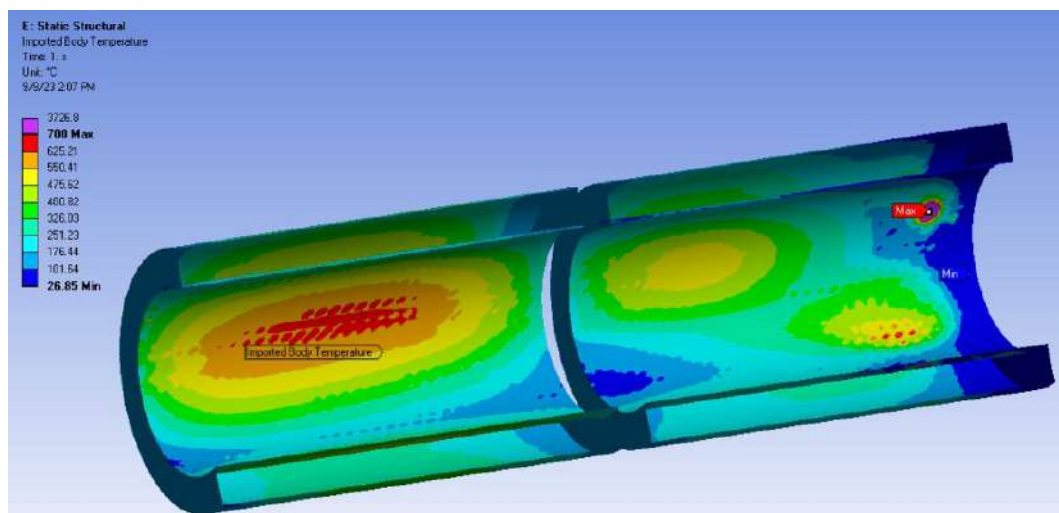


Figure 5.38: Temperature distribution in liners [C]

this is associated with the flame formation zone, where rapid pressure growth has got higher ability to brake transpiration cooling film from the porous liner. Special attention should be paid to the maximum temperature spot equal to 3727°K , which is the peak temperature of the flame's core. This high value occurring at the very limited area looks like numerical error associated with toroidal vertex modelling difficulties. In comparison, other two hotspots on the front liner look more credible, so stresses in their areas will be taken for conclusions.

Figure 5.39 shows first principal stress (Sigma 1) for the entire assembly. Maximum stressed point occurs just at the combustor inlet, where the core of flame is pushed towards the liner and transpiration cooling has limited efficiency by the close proximity of the cap. However, such a high stress (723 MPa) is a result of extremely high temperature above 3700°K , which is caused by a numerical error. This stressed region is shown also on Figure 5.40, where maximum and minimum Sigma 1 stress occur in the same region. It can be concluded, that maximum Sigma 1 stress is about 200 MPa and appear at the liner edge.

Third principal stress (Sigma 3) distribution is presented on Figure 5.41. Due to

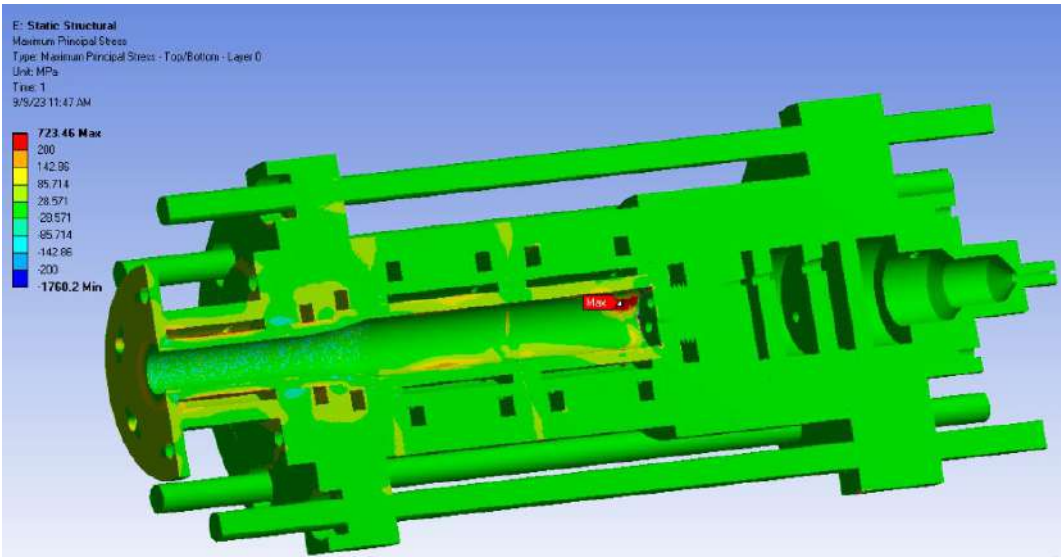


Figure 5.39: First principal stress plot for entire assembly [MPa]

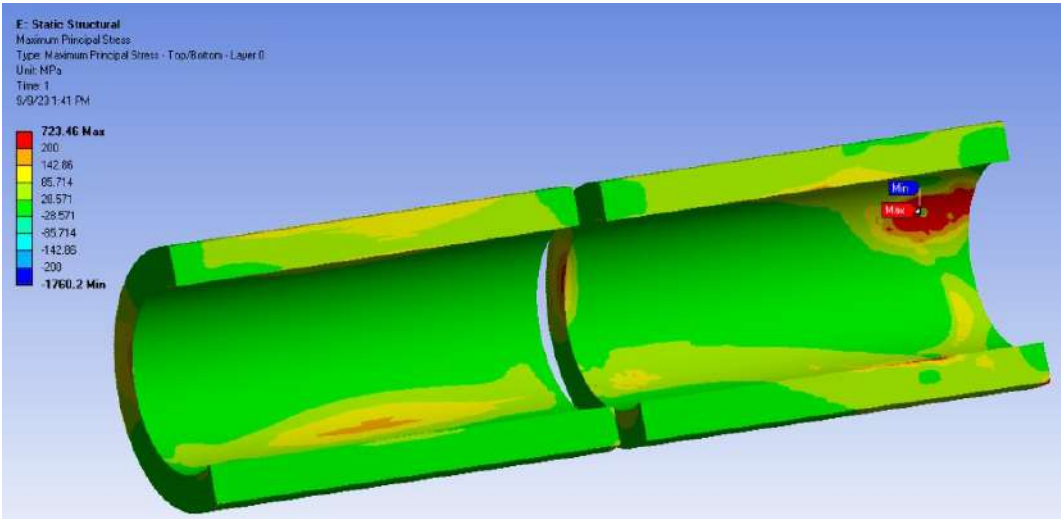


Figure 5.40: First principal stress plot for liners[MPa]

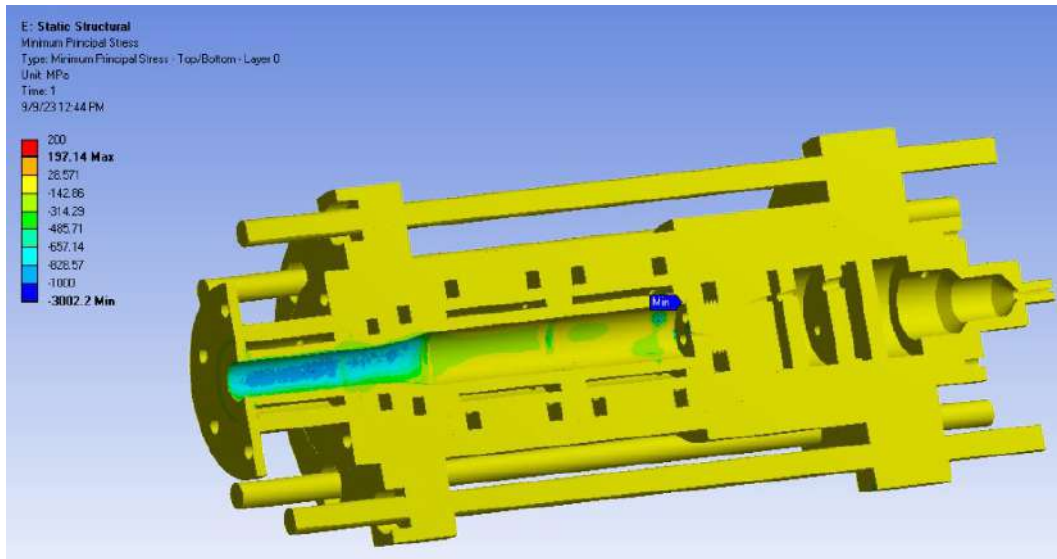


Figure 5.41: Third principal stress plot for entire assembly [MPa]

the thermal gradient across the hot gas path, hot surfaces are restrained from thermal expansion, so high hoop compressive stress can be observed. As stated before, very high stress next to the extreme hot spot is driven by the numerical error, therefore should be ignored. Important conclusion is that actively cooled liners made from WHIPOX are much less stressed than the non-cooled steel combustor outlet passage. In a very localised case minimum elastic Sigma 3 stress can drop up to -1000 MPa, which in the real structure will be a subject of plastic deformation or even could crack after certain amount of hot/cold cycles. Figure 5.42 is focused on Ceramic Matrix Composite (CMC) liner with minimum Sigma 3 stress around -300 MPa. As expected, these negative stress patches follow hotspots revealed on Figure 5.38.

Although Wet Combustion Chamber temperature and stress distribution is an important data about the mechanical load, it needs to be compared against the failure criteria to assess if structure is able to withstand it or not. Figure 5.43 presents Tsai-Wu inverse reserve factor, which was calculated based on equation 2.236. Each region with reserve factor higher than one is expected to crack, although additional considerations need to be made to interpret this data. At first, large red region at the front is driven by the numerical error in CFD temperature calculation, so it is expected to be no-worse than other front-liner hotspots. The other factor not taken into account is the behaviour of porous material affecting transpiration cooling. In the case of liner's wall thickness reduction, water could more easily penetrate it improving local cooling effectiveness. However, non-uniform resistance will lead to non-uniform cooling effectiveness across the liner. Through-wall crack would splash a stream of liquid water inside the flame zone, which will very likely leave some areas without an effective cooling system.

Fluid-Solid Interaction model is a very efficient tool in predicting complex interactions between flow, combustion, evaporation and deformation. However, every model has got some simplifications, leading to unavoidable discrepancies. Taking into account that analysed Wet Combustion Chamber is a prototype, Tsai-Wu failure criterion exceeding two in some areas is an acceptable level of risk.

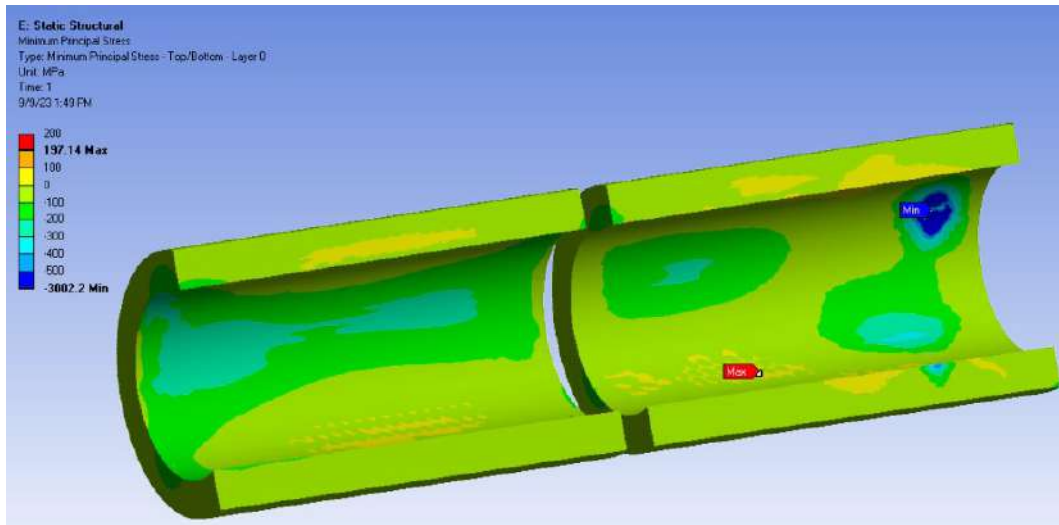


Figure 5.42: Third principal stress plot for liners [MPa]

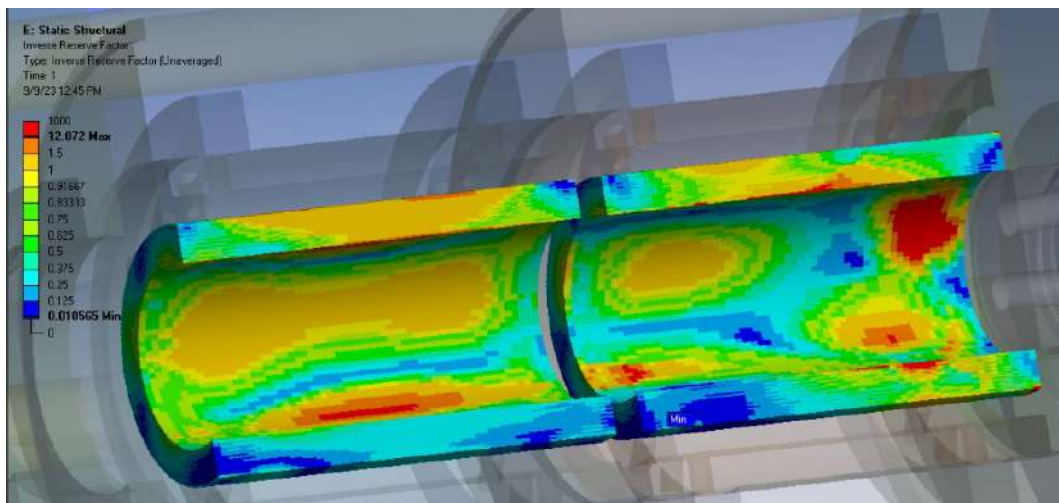


Figure 5.43: Tsai-Wu inverse reserve factor [-]

5.9 Fluid-Solid Interaction model advantage over CFD

Fluid-Solid Interaction model is able to capture relationships between thermo-mechanical loading parameters and changes in composite structure of liner in wet combustion chamber. This is done in CFD domains by taking into account the occurrence of such complex phenomena as the droplets evaporation and combustion. Due to the numerical instability during the application of transpiration model on top of combustion and evaporation, it was decided to model transpiration process implicitly by application of latent heat sink domain which emulates the existence of evaporation at the liner's surface proximity. As a result of the conjunction of CFD and CSD (Computational Solid Dynamics) domains in one FSI model with consistent and continuous mesh, heat fluxes were calculated instantly within solid and fluid domains at the same time. Such approach reduced significantly thermal prediction uncertainty inside porous CMC liner improving the damage evolution calculation in it.

Comparison between CFD (Figure 5.34) and FSI (Figure 5.38) thermal prediction reveals, that CFD temperature is optimistic by about 300°C. Additionally, FSI thermal map predicts much more complex thermal map which better predicts flame behaviour due to the proper heat transfer coefficients applied. Note that the large hot spot on Figure 5.38 follows the pattern of fibers in the composite material, which is simply impossible to capture in the pure CFD model ignoring such details.

5.10 Wet liner transient model

Transient CSD model of wet Ceramic Matrix Composite liner is proposed to capture change of mechanical properties due to the rapid load variation. In the case of slow pore deformation, water inside it have enough time to flow out, so no change in mechanical properties is expected. Situation looks different when pores full of water are squeezed faster than liquid penetration time. In that case trapped incompressible water is able to carry hydrostatic load between pore walls. Similar situation occurs during the tensile load, as trapped water cannot expand to adapt to larger pore volume.

Figure 5.44 presents hoop stress plot of the WHIPOX cylinder loaded with 100 MPa internally, which is much higher than 10MPa condition inside the wet combustion chamber. Additionally, variable orthotropic and time dependent CMC material properties were applied across the wall, which is well described in Chapter 4.2.6.

Figure 5.45 shows hoop stress time plot in the inner and outer side of the cylinder from Figure 5.44. Note that on the inner side there is a 12% stress overshoot, with peak value equal to 505MPa dropping to 450MPa at the end (steady state). This behaviour is a result of variable Young/Shear Moduli, which grows twice at the inner side between the first and the second second. Opposite behaviour can be noticed at the outer side of the cylinder, where stress growth is shallower between second and ten seconds. This is driven by the fact, that at the second second Young and Shear Moduli are increased by 50% at the outer side in comparison to 100% increase on the inner side (more load is carried through the inner side).

This particular example is a test case of the new method to capture the impact of rapid loading change of wet porous CMC liner. Its results are not applicable to the Wet Combustion Chamber due to non-representative boundary conditions. Due to the fact, that test case analyses WHIPOX theta angle equal to 0°, this method is not directly applicable to the 75° composite winding angle.

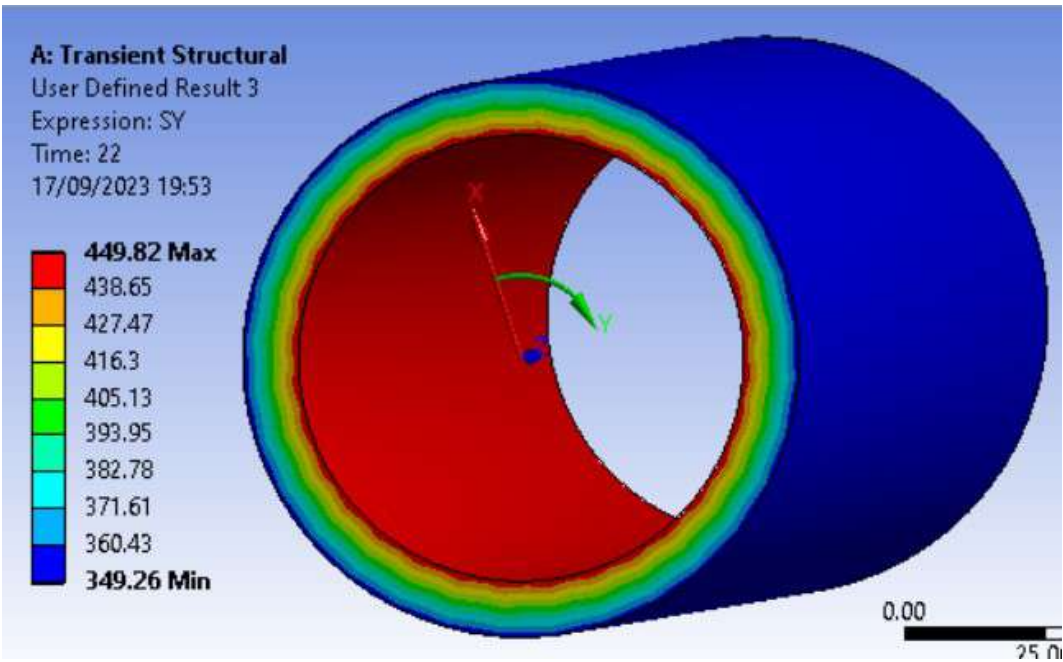


Figure 5.44: Hoop stress in wet cylinder [MPa]

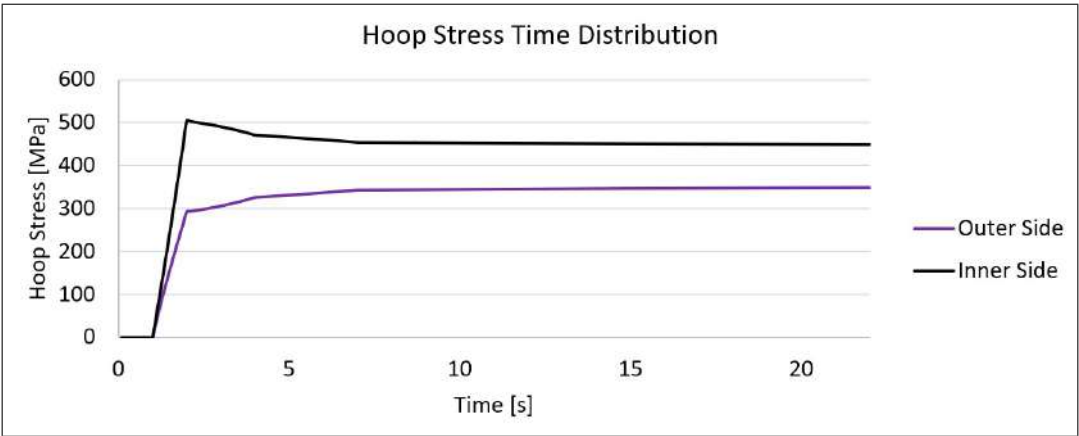


Figure 5.45: Hoop stress time plot in wet cylinder [MPa]

Chapter 6

Summary

6.1 General conclusions

Thermal FSI (Fluid-Solid Interaction) method was successfully applied and extended to describe relationships between thermo-mechanical loading parameters and changes in composite structure of combustion liner. Proposed extensions improved the control of water droplets evaporation rate and took into account mechanical properties variation between dry and wet CMC (Ceramic Matrix Composite) material.

Thermal FSI model combines fluid and solid domains in one single assembly to apply CFD and CSD simulations simultaneously. That approach enables precise calculations of heat transfer between solid and fluid in every iteration of numerical analysis. The first experiment used for validation study was based on C3X NASA vane, which was washed externally by hot air and actively cooled through the ten internal vertical passages. Based on the analysis cases performed in this thesis, it was found that $k-\omega SST$ turbulence model generates the best thermal prediction, which was compared against the experimental data. However, midspan aerofoil pressure distribution was well predicted by all viscous models including Spalart-Allmaras and Transition SST.

Application of GRI-Mech 3.0 combustion model was proved as a powerful method to predict complex chemical reactions occurring inside the oxy-combustion flame. Intense mixing of methane with oxygen was achieved by application of three swirlers, which were explicitly included within the 3D Thermal FSI model. Due to the coupling of combustion process with DPM (Discrete Particle Modelling) model, it was found that rapidly boiled water droplets create local pressure oscillation which significantly improves mixing intensity within the flame. Although DPM model was successfully applied to the water droplet evaporation phenomena, it was created to support boiling of liquid fuel droplets. For that reason, its mathematical formula assumes that once evaporation has started (liquid fuel ignition) it never stops because droplet combustion supplies enough energy to continue the process until the entire liquid phase is evaporated. In contrast to that, water droplet sinks latent heat from the continuous phase, so process should stop when not enough energy is available around it. This is the scenario for which DPM model was not prepared, as it drops continuous phase temperature below the ambient level by sinking all available energy by the droplet which never stops evaporating. To address that limitation, an ADPL (Ansys Parametric Design Language) code was developed to stop droplet evaporation below the certain temperature of continuous phase.

Another limitation of the Ansys Fluent software is that the porous zone modelling is incompatible with combustion and evaporation models. When all three methods are applied at the same time, the mass conservation law is not met leading to the numerical

convergence issue. To address this limitation, porous zone water flow was modelled as a vapour mass source and a latent heat sink inside the cylindrical CFD domain adjacent to the liners. The thickness of this domain was chosen to cover the hot gas path region, where water evaporation is expected.

CSD modelling of the liner made of Ceramic Matrix Composite required special effort, as geometry was reproduced in ACP (Ansys Composite Prep) software as a stack of twenty plies. Each ply was meshed with one layer of hexagonal elements and its mechanical properties were defined by direction of fibres (theta angle). To maintain WHIPOX wounded structure, unidirectional layers have alternately defined layer as plus or minus theta angle. That definition was successfully used inside the Thermal FSI model, which enabled calculation of liner's durability with Tsai-Wu criterion. Note, that orthotropic CMC material definition was used, which required values of three Young modules, three Shear modules and three Poisson ratios.

An important extension of Thermal FSI method was proposed in this thesis, as wet porous CMC material properties varies when rapid external load is applied, such as impact or vibration. When the load application is too quick, non-compressive fluid has not enough time to outflow from the pore, so it carries hydrostatic load between pores' wall. That modification was numerically applied in a form of variable Young modules, which increase as a function of stress time derivative.

Presented Thermal FSI analysis contains an assembly of multiple solid components made from steel, copper and ceramic matrix composite. It was found that thermo-mechanical contact between them assures proper heat flow and displacements prediction, which is as a result of various temperature gradients and thermal expansion coefficients. Due to the high complexity of mechanical interactions between components, frictionless contacts were applied, which helped with numerical solution stability and convergence.

6.2 Detailed conclusions

The scope of presented thesis contains multiple CFD and CSD results, which were regularly presented and discussed during nCO2PP Project meetings. Based on them, nCO2PP Project Team have made some key design decisions, which resulted with prototype wet combustion chamber (WCC) presented on Figure 6.1.

The key design decision about the length of the WCC was made based on the 3D CFD analysis, which was able to model mixing intensity, cooling efficiency, combustion completeness, exit velocity and outlet temperature profile. Reaction completeness is a crucial parameter from the efficiency and pollution point of view. Certainly non-burned and partially burned fuel (carbon monoxide) is a loss from the economical point of view, but it also contaminates exhaust fumes leading to complications with carbon dioxide capture and storage technology. On top of that, combustor needs to provide uniform mixture at the outlet, with minimal temperature gradients. The reason behind is the necessity of turbine components protection, which otherwise could be burned or even melted by hot gas in the central flow. As a result, it was decided that the minimum combustor length should be equal to 120mm. The extension of this is always beneficial, as it will increase particle residence time inside the combustor.

An efficient combustion chamber ought to provide turbulent flow structure, to promote complete burning process. To provide that, many geometrical parameters were explored at the design optimisation stage. This included number of swirlers, swirl angle injection of methane and oxygen and relative location of inlet channels. It was concluded, that the more inlets, the better mixing process due to the interaction between them. Another

important parameter was the inlet lean angle towards the main axis, as it promotes collision between streams. Taking into account analysis results, it was decided to employ three inlets with clockwise oxygen swirler and counter-clockwise methane swirler. An optimum swirler angle is 45° , because at that condition flow has significant axial and circumferential velocity components.

Wet combustion chamber cooling system is built from three spray nozzles at the cap and two CMC liners. Spray nozzle optimisation considered such parameters like water mass flow, droplet sizes and axial velocity. It was found that the optimum case is 0.66g/s water flow through the single nozzle, with droplet diameter of 1e-6m and axial droplet velocity of 100m/s. If droplet is injected too slowly, it is very likely to be trapped inside toroidal vertex next to the cap and form a non-stable cold zone next to the flame. The water flow supplied through the porous liner was fixed at 12 g/s, as at this flow an efficient heat protection zone is formed next to the liner and outlet temperature is matched to the turbine requirements.



Figure 6.1: Wet combustion chamber prototype*

* Photo courtesy of D.Sc. Ph.D. Eng. Ryszard Szwaba, Associate Professor of IFFM PAS

Structural optimisation of wet combustion chamber was done simultaneously with flow study. The key aspect of CMC liner durability is its circumferential strength. The reason behind is that thermal gradient across the wall creates hoop thermal fight, so cold fibres are stretched and hot are squeezed. Due to the orthotropic structure of cylindrical CMC component, it is stronger along the fibres and weaker across them. That was well reflected in the analysis results, so theta angle of 75° was chosen for a prototype build. Non-linear thermal expansion coefficient is one of the key parameters of CMC stress and durability analysis. For that reason it was measured in the laboratory and directly applied into Thermal FSI analysis presented in this thesis.

The estimated pressure drop to pump required water mass flow across porous CMC liner is less than 0.1MPa, however it was decided to apply conservative value to CSD analysis of 1MPa. That case would capture all porosity variations expected at the later

stage of prototype testing programme. Under such assumptions, maximum allowable thermal gradient across liner is 150 °C, as for this case Tsai-Wu Inverse Reserve Factor of equal one (durability limit). The higher external pressure the more hoop compressive load is added to the load. The comparison analyses were made for 3MPa and 6MPa, which resulted in maximum allowable thermal gradient of 165°C and 180°C respectively.

Static CSD analysis of combustion chamber assembly revealed regions which are particularly sensitive to high stress load during the steady state of load. These are features at the rear flanges, which experience high stress concentration and high thermal gradient. These features are expected to relax under the plastic deformation. Another group of high stressed features is located at the outlet cooling channel, where steel cylinder is employed instead of ceramic liner. Due to the fact, that its structure is non-porous, it is cooled only by heat conduction from the hot towards cold surface. For that reason high thermal gradient of 200 °C causes stress above 300 MPa. Based on the fact, that steel thermal expansion coefficient is linear, stress grows proportionally to the thermal gradient.

Transient CSD analysis was made on the assumption, that acceleration time takes only 1 second, so thermal gradient across CMC liner grew from zero to 175°C. For the current cooling system, it was found that temperature stabilization time is equal to 21 seconds, as after this period stresses are nearly constant. Transient analysis is important to find stress overshoot factors driven by temporary high thermal gradients. The highest tensile stress transient factor occurs at a rear flange and is equal to 3.26 (358MPa/306MPa). On the other side, compressive transient factors are twice lower with value 1.53 (-765MPa/-500MPa) near to the swirlers.

Thermal FSI analysis was built using the workflow able to combine nine elements into one structure. Its geometrical structure was divided on three elements, as composite liners had to be preprocessed separately to isotropic components. Note that all geometry needs to go through ACP preprocessor for a compatibility reasons. It applies equally to orthotropic CMC components and isotropic ones.

6.3 Research hypothesis

The research hypothesis is formulated as follows: "It is possible to describe relationships between thermo-mechanical parameters and changes in composite structure of highly loaded components of gas turbines such as combustion liner. This will take into account the occurrence of such complex phenomena as the transpiration of the coolant through the micropores of the ceramics and evaporation at the inner wall of the combustion chamber. It is also possible to predict the process of damage evolution of ceramic matrix composite (component durability) with known load parameters. Description of such physical mechanisms and phenomenon is necessary to control deterioration effects".

The task formulated in this thesis is original and forms an important step in the design process improvement. The research hypothesis was confirmed using the Thermal FSI method, which enables heat transfer modelling between fluid and solid within one model operating on consistent mesh at interfaces. As a consequence, boundary layer temperature variation influences solid temperature and vice versa. The other element of the research hypothesis confirmation was application of GRI-Mech 3.0 combustion model and DPM (Discrete Phase Modelling) model, which links droplet evaporation (discrete phase) with continuous phase. From the solid side, it was crucial to model composite structure of liner, as it enabled application of Tsai-Wu failure criterion at the later stage.

Presented Thermal FSI approach is of a greater importance when modelling actively cooled components such as combustion chamber, where solid wall is washed simultaneously

with cold and hot flow. On top of that, it was proved that consistent mesh at fluid/solid interferences improves considerably analysis convergence, so it should be always used instead of coarse and non-consistent mesh.

Especially important step in the model build was determination of thermal expansion coefficient of CMC (Ceramic Matrix Composite) material in an experimental way. This is a key parameter enabling the proper prediction of thermal stresses, which dominates in structures heavily heated and cooled at the same time. Due to the complex internal structure of CMC liner, measured thermal expansion coefficient is non-linear. It is caused by the fact, that heat it conducted better along the fibres than through the porous matrix. Additionally, weak contact between fibres and matrix can be easily broken, which adds additional non-linearity into thermal expansion behaviour.

The final result of Thermal FSI analysis is the distribution of Tsai-Wu inverse reserve factor within the domain of CMC liner. Region located at the proximity of flame has Tsai-Wu inverse reserve factor exceeding one. It means that some regions of liner are expected to be cracked, which does not disqualifies the experiment. It should be noted, that presented results refer to the prototype, so project assumptions will be verified at the later stage of the design process. Combustion chamber analysis at the highly loaded conditions is a key requirement from the thermodynamic and economic point of view.

Detailed description of Thermal FSI model geometry, boundary conditions and results was supplemented by deep and wide study of mathematical models. From the CFD (Computational Fluid Dynamics) side this is the turbulence, combustion, water evaporation and porous medium model. From the CSD (Computational Solid Dynamics) side this is the elastic model of isotropic and orthotropic materials (composite). Thermal FSI method integrates CFD and CSD analyses into one numerical model.

It should be highlighted, that CMC material was developed by research institutions as a response to the necessity of having material able to withstand high temperatures like monolithic ceramic, but non-brittle at the same time. CMC material is employed mainly in aerospace and space industry, but it can be found in other sectors as well. Due to the fact that CMC manufacturing methods is a modern technology developed by only few companies worldwide, the experimental data is not easily accessible in the public domain. WHIPOX is a commercial name of CMC material developed by the German Institute of Aviation. Its porous structure was designed to reduce brittleness in the extremely high temperatures, so available publications ignore WHIPOX behaviour in the wet condition. The key innovative element of presented research is the WHIPOX ability to enable transpiration cooling of liners. This application is present in the literature, but it is much less common than mixing enhancement and flame stability methods. Another important subject widely explored in the literature are active cooling systems based on the cooling films application.

6.4 Research objectives

Presented research can be well summarised by answering three key scientific questions formulated at the thesis preparation stage.

The first question is: "What is the effect of high temperature on the structure and mechanical properties of the combustion chamber liner made of ceramic material?"

WHIPOX material in an example of ceramic matrix composite which is build from Nextel 720 fibres and a porous matrix, both made predominantly from Al_2O_3 Aluminium Oxide. Its maximum continuous operational temperature without mechanical load is 1200°C,

but for few minutes it can withstand as much as 1600°C . For these reasons it can be used as a very efficient and durable insulation layer. Research progressed in this thesis is focussed not just on CMC insulation capabilities, but assesses structural strength of cylindrical liner under the extreme conditions. It contains close proximity of extremely hot methane oxy-combustion flame, transpiration cooling, crushing pressure and axial compression from compensation springs and contact pressure.

Temperature gradient across liner's wall is the highest contributor to the load carried by the liner. The root cause of it is the thermal expansion fight between hot and cold fibres. In the steady state, heated surface tries to expand but is restrained by the colder fibres. As a consequence, compressive hoop stress is generated in hot fibers. On the other side, cold surface tries to contract, but is restrained by the expanded hot fibres. The higher thermal gradient, the higher thermal fight between hot and cold fibres resulting in stress increase.

Transient condition physics is similar to the steady state case, but thermal gradients at the acceleration phase are much higher, which leads to the stress overshoot. For the axisymmetric liner, the initial condition is ambient temperature across the wall, which results in zero stress. Soon after the ignition, heated surface fibers tries to expand, but are restrained by the full thickness of material at ambient temperature, which causes much higher thermal gradients in comparison to the steady state. After some time, thermal conduction inside CMC wall is going to spread smoothly thermal gradient across the entire thickness, which is effectively a steady state. Described phenomenon is the reason why stress overshoot occurs at the hot side. From the cooled surface point of view, stress overshoot does not exist, because thermal gradient next to it grows smoothly during the acceleration phase.

On top of the thermal gradient impact, CMC and any other material's properties weaken with the temperature growth. Applied Thermal FSI model couples all relevant physical processes such as combustion and water evaporation, so liners' thermal prediction is much more accurate than in the case of separate CFD and CSD approach. Temperature distribution inside liners' follows the pattern driven by swirlers and water spray diffusers, which form a 120° cyclic symmetry. They are three hotspots circumferentially and three cold spots between them. Stress pattern created by this is well reflected on the plot of Tsai-Wu Inverse Reserve Factor highlighting durability shortages. Tsai-Wu failure criterion compares resultant stresses against test results performed along and across fibers. Based on obtained results, some regions of CMC liner have Tsai-Wu Inverse Factor higher than one, so they are expected to be cracked. This applies to the hot and cold spots, where thermal gradient is the highest. This was obtained for 14g/s of water mass flow, 1.2g/s of methane mass flow and 4.8g/s of oxygen mass flow.

The second question is: "What is the impact of the evaporation process and the pressure surge on the structural and mechanical properties of the material during thermal load?"

Porous ceramic matrix composite (CMC) material is made from filaments of diameter between 10 and 12 μm and porous matrix filling gaps between them. For that reason pores' sizes are much smaller, with average size of few μm . On top of that, pores and filament distribution is a random parameter, which can be captured only with statistical description. For these reasons, explicit computational mesh would be too fine to be practical, so porous zone implicit definition is required to numerically model the flow inside micro pores. However, in the analysed Thermal FSI model porous zone is incompatible with combustion and discrete particle evaporation models, so it cannot be used. As an

alternative solution, cylindrical fluid domain was extracted to cover liners' boundary zone, where transpiration cooling flow evaporation is expected. This domain was defined as an uniform water vapour source and uniform evaporation latent heat sink. That approach is acceptable from the temperature prediction point of view, but it does not capture flow inside the porous zone. For that reason, analytical solution was applied to answer the question about evaporation process impact to porous zone.

In the numerical models, the pressure drop inside the porous media is modelled as the source term S_i added to the standard fluid flow equations, which has units of force per unit volume. It can be expressed by Equation 6.1 below.

$$S_i = -\frac{\Delta p_i}{t_i} = -\left(C_1 v_i + C_2 \frac{1}{2} \rho |\underline{v}| v_i\right) \frac{1}{t_i} = -\left(\frac{\mu}{\alpha} v_i + \frac{C_2}{t_i} \frac{1}{2} \rho |\underline{v}| v_i\right) \quad (6.1)$$

where Δp_i is the pressure drop in the direction i , t_i is porous zone thickness in the direction i , C_1 and C_2 are internal resistance factors, v_i is the velocity in the direction i , ρ is the fluid density, μ is the dynamic viscosity, α is the permeability.

Water evaporation is expected to happen at the surface of porous liner, because ceramics has low thermal conductivity and continuous liquid water flow towards the flame is a very efficient internal structure cooling system. On top of that, based on the Darcy's law presented on Equation 6.2, pressure required to pump fluid through the porous zone is proportional to the velocity and dynamic viscosity. To keep the same mass flow of water after the evaporation, its velocity has to increase 200 times. However, it is easier to pump gas, as its viscosity is reduced by the factor of 50. As a result, four times larger pressure difference would be required to pump vapour instead of liquid through the porous wall. This difference would act as a non-return valve, pushing vapour towards the flame.

$$\Delta p = -\frac{\mu}{\alpha} v \quad (6.2)$$

From the pressure growth perspective, its local increase inside subsurface pores is not going to cause any damage. During the scope of analysis, it was proved, that the CMC liner can withstand pressure difference as high as 5MPa. The most severe scenario to cause CMC liner damage is too high thermal gradient due to the cooling system malfunction.

The third question is: "What is the relationship between thermo-mechanical load and deterioration of structural and mechanical properties?".

Thermo-mechanical load exists in nearly every component of heat engines, due to the heat flow from the high to low source. Even if given element does not carry any external load, transient thermal gradients can cause dysfunction driven by the temporary differences in thermal expansion. The other phenomena leading to structure weakening at high temperature is linked with the molecular bonding, which drops when internal kinetic energy grows. Research progressed in this thesis refers to the elastic properties of applied materials. Other deterioration mechanisms like plasticity, creep, oxidation or contact rubbing are not taken into account.

The analysed wet combustion chamber is build mostly from isotropic, homogeneous materials such as steel and copper, which was used in the flame proximity to enhance cooling effectiveness. Steel elements which are mostly exposed to the high thermo-mechanical load form the outlet passage. Their cylindrical elements are washed internally with hot gas and cooled externally with cold water. This leads to the cross-wall thermal gradients as high as 200°C. Steady state peak worst principal stress occurs at the hole inside the flange edge, with stress significantly above 600 MPa. The lowest analysed value in that region is equal to 643MPa for passage thermal gradient equal to 75°C. That increases to

725 MPa for gradient equal to 200°C . Elastic analysis show extreme high stress there, which is much above yield strength of 225MPa for steel 304/1.4301. Due to the fact, that this hole has a very high stress concentration factor, in the real structure material will be plastically deformed.

Transient CSD analysis of wet combustion chamber assembly revealed, that tensile stress overshoot factor at the rear flange can be as high as 3.26 (358MPa/110MPa). This was calculated for the most pessimistic acceleration time of 1 second, however stress can be reduced below steel's yield strength of 225MPa, if acceleration is slow enough. Similar comparison was made for compressive stress overshoot, where point next to the swirlers experienced transient factor of 1.21 (-631MPa/-522MPa). That region is at the copper cap, which yield strength is equal to 137MPa. For that reason, this area will be heavily plastically deformed at the first cycle and work in cyclic plasticity regime until the dysfunction.

Bibliography

- [1] Advanced gas path upgrade for 9F gas turbines, General Electric, <https://www.ge.com/gas-power/services/gas-turbines/upgrades/advanced-gas-path-9f>, accessed: 10.11.2023.
- [2] P. Durbin, B. P. Reif, Statistical Theory and Modeling for Turbulent Flows, General Electric, John Wiley and Sons, 2011.
- [3] M. Waclawczyk, J. Pozorski, Modelling of turbulent flow in the near-wall region using pdf method, Journal of Theoretical and Applied Mechanics 41 (5) (1999) 327–336.
- [4] M. Froissart, Wet Combustion Chamber Liner Mechanical Analysis - Ceramic Matrix Composite Failure Prediction, Tricity Doctoral School, Polish Academy of Sciences, 2023.
- [5] M. Kunz, WHIPOX - Oxide Fiber Ceramics for industrial heat treatment and high temperature applications, WPX, <https://www.youtube.com/watch?v=pCyg0AWx0bU>, accessed: 16.11.2022.
- [6] E. Volkmann, K. Tushtev, D. Koch, C. Wilhelmi, G. Grathwohl, K. Rezwan, Influence of fiber orientation and matrix processing on the tensile and creep performance of nextel610 reinforced polymer derived ceramic matrix composites, Materials Science and Engineering A 614 (2014) 171–179.
- [7] N. Bansal, Handbook of ceramic composites, Kluwer Academic Publishers, Boston, Dordrecht, London, 2005.
- [8] T. Koyamav, S. Hayashi, A. Yasumori, K. Okada, M. Schmucker, H. Schneider, Microstructure and mechanical properties of mullite/zirconia composites prepared from alumina and zircon under various firing conditions, Journal of the European Ceramic Society 16 (1996) 231–237.
- [9] Y. Hirata, S. Matsushita, Y. Ishihara, H. Katsuki, Colloidal processing and mechanical properties of whiskerreinforced mullite matrix composites, Journal of the American Ceramic Society 74 (1991) 2438–2442.
- [10] K. K. Chawla, Composite materials, Science and Engineering, Springer, New York, 1998.
- [11] K. K. Chawla, Ceramic matrix composites, Kluwer Academic Publishers, Boston, 2003.
- [12] N. Eswara-Prasad, A. Kumar, J. Subramanyam, Chapter 16, Ceramic Matrix Composites (CMCs) for Aerospace Applications, Springer, DOI 10.1007/978-981-10-2134-3-16, 2016.

- [13] H. Schneider, M. Schmucker, J. Goring, B. Kanka, J. She, P. Mechnich, Porous aluminosilicate fiber/mullite matrix composites: Fabrication and properties, innovative processing and synthesis of ceramics, glasses, and composites iv, The American Ceramic Society 115 (2000) 415–434.
- [14] 3M Nextel Ceramic Textiles and Composites Maintaining excellent flexibility at highest temperatures. Product and Application Guide., 3M Deutschland GmbH, <https://multimedia.3m.com/mws/media/1026373O>, accessed: 22.09.2022.
- [15] J. She, P. Mechnich, H. Schneider, M. Schmucker, B. Kanka, Effect of cyclic infiltrations on microstructure and mechanical behavior of porous mullite/mullite composites, Materials Science and Engineering A325 (2002) 19–24.
- [16] M. Schmucker, A. Grafmüller, H. Schneider, Mesostructure of whisker-reinforced oxide composites, Composites A34 (2003) 613–622.
- [17] Y. Shi, N. Jain, D. Koch, Investigation and modeling of tensile failure properties of woven ceramic matrix composites, Composites Part A (114) (2018) 316–326. doi:<https://doi.org/10.1016/j.compositesa.2018.08.029>.
- [18] J. Goring, S. Hackemann, H. Schneider, Oxid/Oxid-Verbundwerkstoffe: Herstellung, Eigenschaften und Anwendungen, in: Keramische Verbundwerkstoffe, Wiley-VCH, Weinheim, 2003.
- [19] M. Schmucker, B. Kanka, H. Schneider, Temperature-induced fiber/matrix interactions in porous aluminosilicate ceramic matrix composites, Journal of the European Ceramic Society 20 (2000) 2491–2497.
- [20] A. Lefebvre, Gas Turbine Combustion, Hemisphere Publishing Corporation, Washington, 1983.
- [21] M. Froissart, P. Ziolkowski, W. Dudda, J. Badur, Heat exchange enhancement of jet impingement cooling with the novel humped-cone heat sink, Case Studies in Thermal Engineering 28 (101445) (2021) 1–13. doi:<https://doi.org/10.1016/j.csite.2021.101445>.
- [22] M. Froissart, P. Ziolkowski, J. Badur, A study of jet impingement cooling enhancement by concave and convex heat sink shape modifications, E3S Web of Conferences 323 (10) (2021) 1–14. doi:<https://doi.org/10.1051/e3sconf/202132300010>.
- [23] R. Pavri, G. Moore, Gas Turbine Emissions and Control, GER-4211 (03/01), GE Power Systems, ASME Turbo Expo, 11–15 June, Oslo, Norway.
- [24] Y. Pchelkin, Combustion Chambers of Turbine Engines, U.S. Air Force, Ohio, 1967.
- [25] D. Paxson, Pressure-Gain Combustion for Gas Turbines, NASA John H. Glenn Research Center, ASME Turbo Expo, 11–15 June, Oslo, Norway, 2018.
- [26] O. Zienkiewicz, R. Taylor, The Finite Element Method, Volume 3: Fluid Dynamics, Butterworth-Heinemann, Oxford, United Kingdom, 2000.
- [27] A. C. T. Material, Lecture 6, turbulence modeling, Introduction to Ansys Fluent (2010).
- [28] I. Ansys, Ansys Fluent Theory Guide, Ansys, Inc., 2023.

- [29] A. Wimshurst, The k-epsilon Turbulence Model, Fluid Mechanics 101, <https://www.youtube.com/watch?v=fOB91zQ7HJU>, accessed: 08.04.2022.
- [30] A. Wimshurst, The k-omega Turbulence Model, Fluid Mechanics 101, <https://www.youtube.com/watch?v=26QaCK6wDp8>, accessed: 10.05.2022.
- [31] B. Launder, B. Sharma, Application of the energy-dissipation model of turbulence to the calculation of flow near a spinning disc, Letters in heat and mass transfer Vol.1 (1974) 131–138.
- [32] W.P.Jones, B.E.Launder, The prediction of laminarization with a two-equation model of turbulence, International Journal of Heat and Mass Transfer Vol.15 (1972) 301–314.
- [33] B. Launder, D. Spalding, The numerical computation of turbulent flows, Computer methods in applied mechanics and engineering Vol.3 (1974) 269–289.
- [34] F. Menter, Two-equation eddy-viscosity turbulence models for engineering applications, AIAA Journal Vol.32 (8) (1994).
- [35] C. Rumsey, NASA Turbulence Modelling Resource, NASA Langley Research Center, <https://turbmodels.larc.nasa.gov/sst.html>, accessed: 29.02.2022.
- [36] D. Apsley, M. Leschziner, Advanced turbulence modelling of separated flow in a diffuser, Flow, Turbulence and Combustion Vol.63 (2000) 81–112.
- [37] A. Wimshurst, The k-omega SST Turbulence Model, Fluid Mechanics 101, <https://www.youtube.com/watch?v=myv-ityFnS4>, accessed: 02.06.2022.
- [38] R. Anderson, S. MacAdam, F. Viteri, D. Davies, A. Paliszewski, Adapting gas turbines to zero emission oxy-fuel power plants, Proceedings of ASME Turbo Expo 2008 GT2008-51377 (2008).
- [39] R. Anderson, F. Viteri, R. Hollis, M. Hebbbar, J. Downs, D. Davies, M. Harris, Application of existing turbomachinery for zero emissions oxy-fuel power systems, Proceedings of ASME Turbo Expo 2009 GT2009-59995 (2009).
- [40] R. Hollis, P. Skutley, C. Ortiz, V. Varkey, D. LePage, B. Brown, D. Davies, M. Harris, Oxy-fuel turbomachinery development for energy intensive industrial applications, Proceedings of ASME Turbo Expo 2012 GT2012-69988 (2012).
- [41] R. Anderson, C. Hustad, P. Skutley, R. Hollis, Oxy-fuel turbo machinery development for energy intensive industrial applications, Energy Procedia 63:511-523 (2014).
- [42] I. Saanum, M. Ditaranto, Experimental study of oxy-fuel combustion under gas turbine conditions, Energy and Fuels 31:4445-4451 (2017).
- [43] P. Ziółkowski, T. Ochrymiuk, J. Badur, Implementation of oxy-combustion for gas turbines - advantages and disadvantages of classic and innovative methods of steam cooling of wcc, NCO2PP WP1 Task 2 report 56 (2021).
- [44] P. Ziółkowski, W. Zakrzewski, J. Badur, O. Kaczmarczyk, Thermodynamic analysis of the double brayton cycle with the use of oxy combustion and capture of co2, Archives of thermodynamics 34 (2013).

- [45] P. Ziółkowski, J. Badur, H. Pawlak-Kruczek, J. Niedźwiecki, M. Kowal, K. Krochmalny, A novel concept of negative co₂ emission power plant for utilization of sewage sludge, *Proceedings Of The 6th International Conference On Contemporary Problems Of Thermal Engineering Cpote 2020* (2020).
- [46] P. Ziółkowski, J. Badur, A thermodynamic and technical analysis of zero-emission power plant for pomerania, *Technical Transactions* 3 (2017) 197–210.
- [47] P. Ziółkowski, Thermodynamic analysis of low-emission gas-steam cycles with the use of oxy-combustion, PhD thesis at IMP PAN (2018).
- [48] P. Ziółkowski, J. Badur, Porous structures in aspects of transpiring cooling of oxycombustion chamber walls, *AIP Conf. Proc.* 2077 (2019) 020065 (2019).
- [49] C. Liu, G. Chen, N. Sipocz, M. A. ans X. Bai, Characteristics of oxy-fuel combustion in gas turbines, *Applied Energy* 89 (2012) 387–394.
- [50] P. Kutne, B. Kapadia, W. Meier, M. Aigner, Experimental analysis of the combustion behavior of oxyfuel flames in a gas turbine model combustor, *Proceedings of the Combustion Institute* (2010).
- [51] T. Williams, C. Shaddix, R. Schefer, Effect of syngas composition and co₂-diluted oxygen on performance of a premixed swirl stabilized combustor, *Combust Sci Technol* 180 (2008) 64–88.
- [52] J. Badur, M. Karcz, T. Wysocki, Chemistry-turbulence coupling within a model of inhomogenously premixed combustion, *TASK Quarterly* 7 (2009) 335–344.
- [53] J. Badur, Numeryczne modelowanie zrównoważonego spalania w turbinach gazowych, Wydawnictwo IMP PAN (2003).
- [54] L. Laudau, E. Lifszyc, *Hydrodynamika*, PWN, Warszawa (1994).
- [55] R. Biliger, Turbulent flow with nonpremixed reactions, In Libby P.A. and Williams F.A. editors of *Turbulent Reacting Flows* Springer Verlag (1984).
- [56] C. Doparo, Recent developments in pdf methods, In Libby P.A. and Williams F.A. editors of *Turbulent Reacting Flows* Springer Verlag (1984).
- [57] B. Launder, D. Spalding, *Mathematical models of turbulence*, Academic Press (1972).
- [58] S. Pope, Pdf methods for turbulent reactive flows, *Progress in Energy and Combustion Science* 11 (1985) 119–192.
- [59] D. Spalding, A general theory of turbulent combustion, *Energy* 2 (1978) 16–23.
- [60] K. Kuo, *Principles of combustion*, John Wiley and Sons 56 (1986).
- [61] T. Ochrymiuk, J. Badur, Flameless oxidation at the gt26 turbine - numerical study via full chemistry, *TASK Quarterly - Computational Fluid Dynamics* 5/2 (2001) 239–246.
- [62] T. Ochrymiuk, M. Froissart, P. Madejski, J. Badur, Modelling of catalytic combustion in a deformable porous burner using a fluid–solid interaction (fsi) framework, *Materials* 16 (2023) 1–29. doi:<https://doi.org/10.3390/ma16052093>.

- [63] C. Hirsch, Numerical computation of internal and external flows, John Wiley and Sons 56 (1990).
- [64] I. Ansys, Ansys Fluent User's Guide, Ansys, Inc., 2023.
- [65] W. Sobieski, An efficient method of tortuosity estimation, Archives of Mechanics 74 (1) (2022) 1–26. doi:<https://doi.org/10.24423/aom.3861>.
- [66] M. Bramowicz, S. Kulesza, W. Sobieski, Characteristics of porous beds based on fractal parameters, Technical Sciences 20 (2) (2017) 171–179.
- [67] J. Oliver, Multimedia course: Continuum Mechanics for Engineers, Technical University of Catalonia, <http://oliver.rmee.upc.edu/xo>, accessed: 05.11.2022.
- [68] O. S. A. Boresi, R. Schmidt, Advanced mechanics of materials, John Wiley and Sons, INC., New York, Chichester, Brisbane, Toronto, Singapore, 1993.
- [69] T. Ochrymiuk, W. Dudda, M. Froissart, J. Badur, Principles of stress-strength modelling of the highly thermally loaded materials—the influence of an effect of strength differential on the material effort, Materials 14 (7449) (2021) 1–4. doi:<https://doi.org/10.3390/ma14237449>.
- [70] L. Xie, X. Wang, Z. Han, X. Yu, M. Alim, T. Manninen, Z. Tao, Post-fire stress-strain response of structural ferritic stainless steels, Journal of Constructional Steel Research 196 (107389) (2022) 1–17. doi:<https://doi.org/10.1016/j.jcsr.2022.107389>.
- [71] K. Symon, Mechanics, Addison-Wesley, Reading, Massachusetts, 1971.
- [72] C. Kassapoglou, Advanced design and optimisation of composite structures, Technical University Delft, Postbus 5, 2600 AA Delft, The Netherlands.
- [73] K. F. Hasan, P. G. Horvath, T. Alpar, Potential fabric-reinforced composites: a comprehensive review, Journal of Materials Science 56 (2021).
- [74] S. Burzyński, J. Chróscielewski, W. Witkowski, Geometrically nonlinear fem analysis of 6-parameter resultant shell theory based on 2-d cosserat constitutive model, Journal of Applied Mathematics and Mechanics 96 (2) (2016) 191–204. doi:<https://doi.org/10.1002/zamm.201400092>.
- [75] J. Chroscielewski, W. Pietraszkiewicz, W. Witkowski, On shear correction factors in the non-linear theory of elastic shells, International Journal of Solids and Structures 47 (2010) 3537–3545. doi:<https://doi.org/10.1016/j.ijsolstr.2010.09.002>.
- [76] M. Rucka, W. Witkowski, J. Chróscielewski, K. Wilde, Damage detection of a t-shaped panel by wave propagation analysis in the plane stress, Archives of Civil Engineering LVIII (1) (2012) 1–22. doi:<https://doi.org/10.2478/v.10169-012-0001-4>.
- [77] A. Kapadia, Non-destructive testing of composite materials - best practise guide, Journal of National Composites Network - WordPress (2013) 1–52.
- [78] J. Zheng, C. Maharaj, J. Liu, H. Chai, H. Liu, J. Dear, A comparative study on the failure criteria for predicting the damage initiation in fiber-reinforced composites, Mechanics of Composite Materials 58 (1) (2022).
- [79] R. Talreja, Assessment of the fundamentals of failure theories for composite materials, Composite Science and Technology 105 (2014).

- [80] C. Sun, B. Quinn, J. Tao, Comparative evaluation of failure analysis methods for composite laminates, DOT/FAA/AR-95/ 109 (1996).
- [81] A. Puck, H. Schurmann, Failure analysis of frp laminates by means of physically based phenomenological models, *Composite Science and Technology* 58 (1998).
- [82] A. Puck, H. Schurmann, Failure analysis of frp laminates by means of physically based phenomenological models, *Composite Science and Technology* 62 (2002).
- [83] K. Liu, S. Tsai, A progressive quadratic failure criterion of a laminate, *Composites Science and Technology* 58 (1998).
- [84] P. Zinoviev, S. Grigoriev, O. Lebedeva, L. Tairova, The strength of multi-layered composites under a plane-stress state, *Composite Science and Technology* 58 (1998).
- [85] P. Zinoviev, O. Lebedeva, L. Tairova, Coupled analysis of experimental and theoretical on the deformation and failure of laminated composites under a plane state of stress, *Composite Science and Technology* 62 (2002).
- [86] T. Bogetti, R. Hoppel, V. Harik, J. Newill, B. Burns, Predicting the nonlinear response and progressive failure of composite laminates, *Composite Science and Technology* 64 (2004).
- [87] T. Bogetti, R. Hoppel, V. Harik, J. Newill, B. Burns, Predicting the nonlinear response and failure of composite laminates: Correlation with experimental results, *Composite Science and Technology* 64 (2004).
- [88] R. Cuntze, A. Freund, The predictive capability of failure mode concept-based strength criteria for multidirectional laminates, *Composite Science and Technology* 64 (2004).
- [89] R. Cuntze, The predictive capability of failure mode concept-based strength criteria for multi-directional laminates - part b, *Composite Science and Technology* 64 (2004).
- [90] R. Talreja, Assessment of the fundamentals of failure theories for composite materials, *Composites Science and Technology* 105 (2014).
- [91] S. Tsai, Strength characteristics of composite materials, NASA/CR-224 (1965).
- [92] Z. Hashin, Failure criteria for unidirectional fiber composites, *Journal of Applied Mechanics* 47 (1980).
- [93] G. Catalanotti, P. Camanho, A. Marques, Three-dimensional failure criteria for fiber-reinforced laminates, *Composite Structures* 95 (2013).
- [94] C. Davila, Failure criteria for frp laminates in plane stress, NASA/TM-2003 0212663 (2003).
- [95] O. Hoffman, The brittle strength of orthotropic materials, *Journal of Composite Materials* 1 (1967).
- [96] Z. Hashin, A. Rotem, A fatigue failure criterion for fiber reinforced materials, *Composite Materials* 7 (1973).
- [97] I. Goldenblat, V. Kopnov, *Mekanika polimerov* 1 (70) (1965).

- [98] J. Echaabi, F. Trochu, R. Gauvin, Review of failure criteria of fibrous composite materials, *Polymer composites* 17 (6) (1996).
- [99] A. De-Luca, F. Caputo, A review on analytical failure criteria for composite materials, *AIMS Materials Science* 4 (5) (2017).
- [100] J. Chrosielewski, A. Sabik, B. Sobczyk, W. Witkowski, Examination of selected failure criteria with asymmetric shear stresses in the collapse analysis of laminated shells, *Composite Structures* 261 (113537) (2021) 1–15. doi:<https://doi.org/10.1016/j.compstruct.2020.113537>.
- [101] N. Nyambeni, B. Mabuza, Considerations of failure analysis in a multi-layered composite structure under thermomechanical loading, *Proceedings* 2 (447) (2018).
- [102] R. Koh, B. Madsenb, Strength failure criteria analysis for a flax fibre reinforced composite, *Mechanics of Materials* 124 (2018).
- [103] A. Puck, H. Schurmann, Failure analysis of frp laminates by means of physically based phenomenological models, *Composites Science and Technology* 62 (2002).
- [104] M. Hintona, A. Kaddourb, P. Sodenc, A comparison of the predictive capabilities of current failure theories for composite laminates, judged against experimental evidence, *Composites Science and Technology* 62 (2002).
- [105] K. Kodagali, Progressive failure analysis of composite materials using the puck failure criteria, Submitted in Partial Fulfillment of the Requirements For the Degree of Master of Science in Mechanical Engineering College of Engineering and Computing University of South Carolina (2017).
- [106] V. Las, R. Zemčík, T. Kroupa, R. Kottner, Failure prediction of composite materials, *Bulletin of Applied Mechanics* 4 (14) (2008).
- [107] GE Aviation and the Ceramic Matrix Composite Revolution, YouTube - GE Aerospace, <https://www.youtube.com/watch?v=is1BBilkyUM>, accessed: 30.02.2023.
- [108] P. Ladeveze, E. Baranger, M. Genet, C. Cluzel, Damage and lifetime modeling for structure computations, John Wiley and Sons, The Americal Ceramic Society, 2015.
- [109] Ansys Composites Tutorials on the LEAP Academic Portal for Australian and New Zealand engineers, LEAP Australia, <https://www.youtube.com/c/leapaustralia>, 2018.
- [110] Composite Materials Handbook, Volume 5: Ceramic Matrix Composites, Department of Defense, 2002.
- [111] Y. Gawayed, G. Ojard, R. Miller, U. Santhosh, J. Ahmad, R. John, Mechanical properties of MI SiC/SiC composites and their constituents, Air Force Research Laboratory, 2007.
- [112] J. Vlach, R. Doubrava, R. Ruzek, J. Raska, J. Hornas, M. Kadlec, Strain-field modifications in the surroundings of impact damage of carbon/epoxy laminate, *Polymers* 14 (3243) (2022) 1–17. doi:<https://doi.org/10.3390/polym14163243>.

- [113] F. Christin, CMC materials for space and aeronautical applications. Ceramic matrix composites, Wiley-VCH Verlag GmbH and Co. KGaA, 2008.
- [114] A. Kohyama, CMC for nuclear applications. Ceramic matrix composites., Wiley-VCH Verlag GmbH and Co. KGaA, 2008.
- [115] M. Gerendas, Y. Cadoret, C. Wilhelmi, T. Machry, R. Knoche, T. Behrendt, Improvement of oxide/oxide cmc and development of combustor and turbine components in the hipoc program., ASME 2011 Turbo Expo: Turbine Technical Conference and Exposition (2011) 477–490.
- [116] T. Behrendt, S. Hackemann, P. Mechnich, Y. Shi, S. Honig, S. Hofmann, Development and test of oxide/oxide cmc combustor liner demonstrators for aero engines., ASME 2016 Turbo Expo: turbine technical conference and exposition (2016).
- [117] A. E. T. Herbell, Ceramic matrix composites for rocket engine turbine applications, Journal of Engineering for Gas Turbines and Power 115 (1) (1993) 64–69.
- [118] S. Schmidt, S. Beyer, H. Knabe, H. Immich, R. Meistring, A. Gessler, Advanced ceramic matrix composite materials for current and future propulsion technology applications, Acta Astronaut 55 (2004) 409–420.
- [119] I. Low, Ceramic matrix composites: microstructure, properties and applications. Minerals and Mining, Woodhead Pub. and Maney Pub. on behalf of the Institute of Materials, England, 2006.
- [120] J. Goring, S. Hackemann, B. Kanka, Whipox (r): a fiber-reinforced oxide-ceramic matrix composite for long-term high-temperature applications, Materialwiss Werkstofftech 38 (9) (2007) 766–772.
- [121] F. Breede, R. Jemmali, H. Voggenteiter, D. Koch, Design and testing of a C/C-SiC nozzle extension manufactured via filament winding technique and liquid silicon infiltration. Design, development, and applications of structural ceramics, composites, and nanomaterials., John Wiley and Sons, 2014.
- [122] L. Xu, S. Kim, C. Ong, S. Ha, Prediction of material properties of biaxial and triaxial braided textile composites., Journal of Composite Materials 46 (18) (2012) 2255–2270.
- [123] L. Srikanth, R. Rao, Concurrent studies on braided and filament wound carbon fiber composites - a comparative appraisal., Journal of Reinforced Plastics and Composites 30 (16) (2011) 1359–1365.
- [124] J. Carey, M. Munro, A. Fahim, Longitudinal elastic modulus prediction of a 2-d braided fiber composite, Journal of Reinforced Plastics and Composites 22 (9) (2003) 813–831.
- [125] W. Zhao, P. Liaw, N. Yu, Computation of the lamina stacking sequence effect on elastic moduli of a plain-weave nicalon/sic laminated composite with a [0/30/60] lay-up., Journal of Nuclear Materials 253 (1-3) (1998) 10–19.
- [126] J. Lamon, Approach to microstructure–behavior relationships for ceramic matrix composites reinforced by continuous fibers., John Wiley and Sons, 2014.

- [127] K. Tushtev, J. Horvath, D. Koch, G. Grathwohl, Deformation and failure modeling of fiber reinforced ceramics with porous matrix., *Advanced Engineering Materials* 6 (8) (2004) 664–669.
- [128] A. Puck, H. Schurmann, Failure analysis of frp laminates by means of physically based phenomenological models., *Composites Science and Technology* 62 (12-13) (2002) 1633–1662.
- [129] S. Tsai, E. Wu, A general theory of strength for anisotropic materials., *Journal of Composite Materials* 5 (1) (1971) 58–80.
- [130] R. Sevenois, W. Van-Paepegem, Fatigue damage modeling techniques for textile composites: review and comparison with unidirectional composite modeling techniques., *Applied Mechanics Reviews* 67 (2) (2015) 021401.
- [131] W. Van-Paepegem, J. Degrieck, Calculation of damage-dependent directional failure indices from the tsai–wu static failure criterion., *Composites Science and Technology* 63 (2) (2003) 305–310.
- [132] N. Chawla, P. Liaw, E. Lara-Curzio, M. Ferber, R. Lowden, Effect of fiber fabric orientation on the flexural monotonic and fatigue behavior of 2d woven ceramic matrix composites., *Materials Science and Engineering: A* 557 (2012) 77–83.
- [133] N. Chawla, Y. Tur, J. Holmes, J. Barber, A. Szweda, High-frequency fatigue behavior of woven-fiber-fabric-reinforced polymer-derived ceramic-matrix composites., *Journal of the American Ceramic Society* 81 (5) (2005) 1221–1230.
- [134] N. Chawla, Effect of laminate stacking sequence on the high frequency fatigue behavior of scs-6 fiber-reinforced si₃n₄ matrix composites., *Metallurgical and Materials Transactions A* 28 (11) (1997) 2423–2427.
- [135] Y. Shi, N. Jain, R. Jemmali, S. Hofmann, D. Koch, S. Hackemann, Prediction of elastic properties for a wound oxide ceramic matrix composite material., *International Journal of Applied Ceramic Technology* 12 (2015) 99–110.
- [136] Y. Shi, S. Hofmann, R. Jemmali, S. Hackemann, D. Koch, Determination of elastic properties for a wound oxide ceramic composite., *Journal of Ceramic Science and Technology* 5 (1) (2013) 31–38.
- [137] R. Cuntze, A. Freund, The predictive capability of failure mode concept-based strength criteria for multidirectional laminates., *Composites Science and Technology* 64 (3-4) (2004) 343–377.
- [138] A. Puck, J. Kopp, M. Knops, Guidelines for the determination of the parameters in puck’s action plane strength criterion., *Composites Science and Technology* 62 (3) (2002) 371–378.
- [139] M. Hinton, A. Kaddour, P. Soden, Failure criteria in fibre reinforced polymer composites: the World-Wide Failure Exercise., UK: Elsevier Science Ltd., Oxford, 2004.
- [140] M. Hinton, A. Kaddour, The background to the second world-wide failure exercise., *Journal of Composite Materials* 46 (19-20) (2012) 2283–2294.
- [141] A. Kaddour, M. Hinton, P. Smith, S. Li, The background to the third world-wide failure exercise., *Journal of Composite Materials* 47 (20-21) (2013) 2417–2426.

- [142] K. Rohwer, Predicting fiber composite damage and failure., *Journal of Composite Materials* 49 (21) (2015) 2673–2683.
- [143] D. Koch, K. Tushtev, G. Grathwohl, Ceramic fiber composites: Experimental analysis and modeling of mechanical properties, *Composites Science and Technology* 68 (2008) 1165–1172. doi:<https://doi.org/10.1016/j.compscitech.2007.06.029>.
- [144] E. Volkmann, K. Tushtev, D. Koch, C. Wilhelmi, J. Goring, K. Rezwan, Assessment of three oxide/oxide ceramic matrix composites: Mechanical performance and effects of heat treatments, *Composites Part A* (68) (2015) 19–28. doi:<https://doi.org/10.1016/j.compositesa.2014.09.013>.
- [145] D. Munz, T. Fett, *Ceramics – mechanical properties, failure behaviour, materials selection.*, Springer-Verlag, Berlin Heidelberg New York Tokyo, 1999.
- [146] G. Hou, D. Shang, L. Zuo, L. Qu, M. Xia, S. Wu, G. Hao, Fatigue life prediction of needled ceramic matrix composite under variable amplitude loading, *International Journal of Fatigue* 156 (2022) 106690. doi:<https://doi.org/10.1016/j.ijfatigue.2021.106690>.
- [147] G. Fang, X. Gao, S. Zhang, J. Xue, Y. Song, F. Wang, A residual strength model for the fatigue strengthening behavior of 2d needled cmcs, *International Journal of Fatigue* 80 (2015) 298–305. doi:<https://doi.org/10.1016/j.ijfatigue.2015.06.019>.
- [148] G. Yu, Y. Jia, C. Xie, J. Du, X. Gao, F. W. Y. Song, Transverse tensile mechanical experimental method and behavior of ceramic matrix mini-composites, *Composite Structures* 297 (2022) 115923. doi:<https://doi.org/10.1016/j.compstruct.2022.115923>.
- [149] G. Hou, D. Shang, L. Zuo, L. Qu, M. Xia, S. Wu, X. Yin, C. Chen, Fatigue life prediction method for central hole of needled ceramic matrix composite, *Ceramics International* 48 (2022) 31438–31448. doi:<https://doi.org/10.1016/j.ceramint.2022.07.053>.
- [150] Y. Shi, P. Dileep, B. Heidenreich, D. Koch, Determination and modeling of bending properties for continuous fiber reinforced c/c-sic sandwich structure with grid core, *Composite Structures* 204 (2018) 198–206. doi:<https://doi.org/10.1016/j.compstruct.2018.07.086>.
- [151] S. Zhang, Y. Feng, X. Gao, Y. Song, F. Wang, S. Zhang, Modeling of fatigue failure for sic/sic ceramic matrix composites at elevated temperatures and multi-scale experimental validation, *Journal of the European Ceramic Society* 42 (2022) 3395–3403. doi:<https://doi.org/10.1016/j.jeurceramsoc.2022.02.049>.
- [152] Z. Yang, J. Sun, J. Yang, T. Liu, H. Liu, Mechanical behavior of woven cmcs under non-uniform stress and strain fields, *Composite Structures* 299 (2022) 116097. doi:<https://doi.org/10.1016/j.compstruct.2022.116097>.
- [153] W. Xiang, X. Li, H. Ni, B. Liu, Micromechanical analysis of fiber-reinforced ceramic matrix composites by a hierarchical quadrature element method, *Composite Structures* 300 (2022) 116143. doi:<https://doi.org/10.1016/j.compstruct.2022.116143>.
- [154] L. Li, Hysteresis-based identification approach for crack opening and closure stress in sic/sic fiber-reinforced ceramic-matrix composites, *International Journal of Fatigue* 162 (2022) 106945. doi:<https://doi.org/10.1016/j.ijfatigue.2022.106945>.

- [155] F. Rebillat, Advances in self-healing ceramic matrix composites, in: in: Advances in ceramic matrix composites, Elsevier, 2014.
- [156] G. Bellezza, G. Couegnat, M. Ricchiuto, G. Vignoles, A 2d image-based multiphysics model for lifetime evaluation and failure scenario analysis of self-healing ceramic-matrix mini-composites under a tensile load, *Journal of the European Ceramic Society* 42 (2022) 6391–6403. doi:<https://doi.org/10.1016/j.jeurceramsoc.2022.07.037>.
- [157] X. Lva, M. Yuc, W. Yanga, X. Fengc, X. Li, Y. Wange, J. Wanga, J. Zhanga, J. Wanga, Tunable strength of sicf/b-yb2si2o7 interface for different requirements in sicf/sic cmc: Inspiration from model composite investigation, *Journal of Materials Science and Technology* 67 (2021) 165–173. doi:<https://doi.org/10.1016/j.jmst.2020.05.071>.
- [158] S. Hackemann, F. Flucht, W. Braue, Creep investigations of alumina-based all-oxide ceramic matrix composites, *Composites Part A* (41) (2010) 1768–1776. doi:<https://doi.org/10.1016/j.compositesa.2010.08.012>.
- [159] Y. Zhaoa, Y. Chenb, C. Heb, S. Aib, D. Fanga, A damage-induced short-circuit diffusion model applied to the oxidation calculation of ceramic matrix composites (cmcs), *Composites Part A* (127) (2019) 105621. doi:<https://doi.org/10.1016/j.compositesa.2019.105621>.
- [160] J. Schichtel, A. Chattopadhyay, Modeling the two-way coupling of stress, diffusion, and oxidation in heterogeneous cmc microstructures, *Journal of the European Ceramic Society Journal pre-proof* (2022). doi:<https://doi.org/10.1016/j.jeurceramsoc.2022.09.046>.
- [161] K. Ramachandran, B. Chaffey, C. Zuccarini, J. Bear, D. Jayaseelan, Experimental and mathematical modelling of corrosion behaviour of cmcs coated oxide/oxide cmcs, *Ceramics International Article in press* (2022). doi:<https://doi.org/10.1016/j.ceramint.2022.09.294>.
- [162] X. Wang, *Fundamentals of Fluid-Solid Interactions: Analytical and Computational Approaches*, Elsevier, Amsterdam, 2008.
- [163] D. Hodges, G. Pierce, *Introduction to Structural Dynamics and Aeroelasticity (Vol.15)*, Cambridge University Press, Cambridge, 2011.
- [164] E. Dowell, *A Modern Course in Aeroelasticity*, vol. 720., Springer, New York, 2004.
- [165] P. Ziolkowski, T. Ochrymiuk, V. Eremeyev, Fluid–solid interaction on a thin platelet with high-velocity flow: vibration modelling and experiment, *Continuum Mechanics and Thermodynamics* 35 (2023) 1495–1521.
- [166] J. Talaga, P. Duda, Identification of the liquid turbulent flow based on experimental methods, *Archives of Thermodynamics* 41 (3) (2020) 91–102. doi:<https://doi.org/10.24425/ather.2020.134573>.
- [167] P. Duda, Felkowski, Negative impact of thermal loads on pressure and non-pressure boiler parts, *Energies* 16 (5768) (2023) 1–9. doi:<https://doi.org/10.3390/en16155768>.
- [168] J. Donea, A. Huerta, J. Ponthot, A. Rodriguez-Ferran, Chapter 14: Arbitrary Lagrangian–Eulerian Methods, John Wiley and Sons, 2004.

- [169] K. Czechowicz, J. Badur, K. Narkiewicz, Two-way fsi modelling of blood flow through cca accounting on-line medical diagnostics in hypertension, *Journal of Physics: Conference Series* 530 (2014).
- [170] J. Badur, M. Karcz, R. Kucharski, A. Wisniewski, M. Kekana, *Coupled modelling of the cooling processes and the induced thermo-corrosive fatigue within a gas turbine*, Crackow TU Press, 2003.
- [171] P. Sarkar, G. Ghigliotti, J. Franc, M. Fivel, Fluid–structure modelling for material deformation during cavitation bubble collapse, *Journal of Fluids and Structures* 106 (103370) (2021).
- [172] T. Ochrymiuk, M. Banaszkiewicz, M. Lemanski, T. Kowalczyk, P. Ziolkowski, P. Ziolkowski, R. Hyrzynski, M. Stajnke, M. Bryk, B. Kraszewski, S. Kruk-Gotzman, M. Froissart, J. Badur, Fluid solid interactions – a novelty in industrial applications, *Archives of thermodynamics* 43 (2) (2022) 75–96.
- [173] P. Ziolkowski, T. Ochrymiuk, V. Eremeyev, Adaptation of the arbitrary lagrange–euler approach to fluid–solid interaction on an example of high velocity flow over thin platelet, *Continuum Mechanics and Thermodynamics* 33 (2021) 2301–2314.
- [174] L. Margolin, Introduction to an arbitrary lagrangian-eulerian computing method for all flow speeds, *Journal of Computational Physics* 135 (1997) 198–202.
- [175] P. Duda, Heat transfer coefficient distribution—a review of calculation methods, *Energies* 16 (3683) (2023) 1–21. doi:<https://doi.org/10.3390/en16093683>.
- [176] P. Duda, M. Konieczny, An iterative algorithm for the estimation of thermal boundary conditions varying in both time and space, *Energies* 15 (2686) (2022) 1–13. doi:<https://doi.org/10.3390/en15072686>.
- [177] C. S. University, Chemical Equilibrium Calculator, Colorado State University, Bioanalytical Microfluids Program, Chemical and Biological Engineering, <https://navier.engr.colostate.edu/code/code-4/index.html>, accessed: 06.12.2021.
- [178] L. Hylton, M. Mihelc, E. Turner, D. Nealy, R. York, *Analytical and Experimental Evaluation of the Heat Transfer Distribution Over the Surfaces of Turbine Vanes*, NASA Lewis Research Center, 1983.
- [179] M. Froissart, T. Ochrymiuk, Thermal-fluid–solid coupling—parametrical numerical analysis of hot turbine nozzle guide vane, *Materials* 14 (7313) (2021) 1–21. doi:<https://doi.org/10.3390/ma14237313>.
- [180] M. Froissart, Numerical simulation of combustion process in combustor chambers. Selected problems in mechanical engineering 2022., Tricity Doctoral School, Polish Academy of Sciences, 2022.
- [181] P. J. W, H. Toral, Temperature and composition measurements in a research gas turbine combustion chamber, *Combustion Science and Technology* 31 (1983) 249–275.
- [182] P. J. W, H. Toral, Numerical simulation of oxy-fuel combustion for gas turbine applications, *Applied Thermal Engineering* 78 (2015) 471–481.

- [183] 3 Nexte Ceramic Fibers and Textiles - Technical Reference Guide, 3M Advanced Materials Division, 3M Center, St. Paul, MN 55144 USA, <https://multimedia.3m.com/mws/media/1327055O/3m-nextel-technical-reference-guide.pdf>, accessed: 26.09.2023.
- [184] M. Froissart, T. Ochrymiuk, Novel wet combustion chamber concept cfd studies with triple water inlet, *Energy* 278 (127854) (2023) 1–7. doi:<https://doi.org/10.1016/j.energy.2023.127854>.